Imperial College London

Department of Earth Science and Engineering

Fold growth in the South Caspian Sea Basin: Mechanisms and interaction with deep-water lacustrine sediments

Andrew Liam Procter

Submitted in fulfilment of the requirements for the degree of Doctor of Philosophy

May 2022

Declaration of originality

I certify that this thesis is the result of my own research carried out under the supervision of Dr. Lidia Lonergan and Dr. Mike Mayall. All published and unpublished material used in this thesis has been appropriately referenced. None of this work has been previously submitted to Imperial College London or any other academic institution for a degree, diploma or any other publication.

Andrew Liam Procter

2022

Copyright Declaration

The copyright of this thesis rests with the author. Unless otherwise indicated, its contents are licensed under a Creative Commons Attribution-NonCommercial 4.0 International Licence (CC BY-NC).

Under this licence, you may copy and redistribute the material in any medium or format. You may also create and distribute modified versions of the work. This is on the condition that: you credit the author and do not use it, or any derivative works, for a commercial purpose.

When reusing or sharing this work, ensure you make the licence terms clear to others by naming the licence and linking to the licence text. Where a work has been adapted, you should indicate that the work has been changed and describe those changes.

Please seek permission from the copyright holder for uses of this work that are not included in this licence or permitted under UK Copyright Law.

Abstract

Growth strata analysis, finite element modelling and mapping of a lacustrine turbidite channel network utilizing a high-quality 3D seismic reflection dataset have been used to explore the Plio-Pleistocene growth history of the Shafag – Asiman fold structure, within the centre of the South Caspian Basin. For the first time, I document the amplification of fold growth in response to shortening and sediment loading of a mobile shale in the South Caspian Basin. 2D finite element modelling results suggest that atypical growth strata geometries can be explained by tectonic shortening and sediment loading of a mobile visco-plastic layer (Maykop shale) with a viscosity of 10^{18} Pa.s and a porosity of 30%. Fold geometries are controlled by the distribution of sediment between the crest and flanks of the fold structures, determined by the relative amounts of shortening and sediment input. The location and initial growth of the fold structure is controlled by a deep basement fault. However, detailed growth strata analyses record anti-clockwise rotation of the fold axes through the Pleistocene as the structures formed in response to transpressive dextral shear above the mobile shale. Shortening and subsequent transpression is caused by the relative NNW and SW motion of the basin with respect to Eurasia and Iran. The interaction of deep-water lacustrine turbidites with growing fold structures is documented for the first time, revealing the alternating dominance of the Shafag and Asiman fold crests on seafloor topography through the Pleistocene to recent times. Novel growth strata analysis, defined as sediment accumulation indices, and lacustrine turbidite channel mapping demonstrate the complex interaction of the channel network and growing fold structures. Channel characteristics such as density, sinuosity and avulsion points are controlled by the interaction of the channels with the growing structures. The results show that sediment accumulation indices have the potential to be applied as a predictive tool for other deep-water sedimentary systems.

Acknowledgements

Firstly, I would like to thank my supervisors Lidia Lonergan and Mike Mayall for their continuous support throughout my PhD, especially during the difficult period of the last two years. I thank Lidia for her ability to enthuse and motivate me throughout and for all her efforts to help me whenever I needed it. She has been a key influence on my development as a researcher for which I will always be appreciative. I would like to thank Mike for his knowledge and expertise, which always inspired me. I also thank him for always being available and having the ability to cheer me up, even after another English batting collapse.

I would like to thank Alex Whittaker for always being open for a chat and offering support whenever I asked as well as helping me with my research even though he had no obligation to give me his time. I thank Dan Roberts at Rockfield for his tireless efforts and help with numerical modelling, especially with the difficulty of communicating exclusively over teams. I thank Simon Grant for the early support and development of my project as well as Steve Dee, Ken McCaffrey and Richard Jolly for help during the research.

I am grateful to bp for providing me with the dataset as well as the NERC CDT for sponsoring my PhD and providing enjoyable training courses from which I have met lifelong friends.

Thanks to my Imperial friends: Hamish, Marco, Vic, David, Sophie, Gaetano, old man Rob and Kartik for keeping me fuelled with Union beers throughout my PhD and my friends outside of Imperial for giving me an escape from the post-graduate life (Kyle, Jackson and Eggy).

I would like to thank my parents for all their love and support, especially for putting up with me living at home during the lockdowns, and their encouragement of my academic journey, even if they have no idea what my research is about.

And last but not least, thank you Nele for everything these past couple of years, keeping me motivated and focussed on work, even when you're incredibly bored and 'geology is ruining your life'.

Contents

1. Introduction 1

1.1 Motivation 1

1.2 The South Caspian Basin 3

1.2.2 Tectonics 3

1.2.3 Stratigraphy 14

1.3 Shale Tectonics 22

1.4 Lacustrine Turbidite Systems 28

1.5 Thesis Aims and Objectives 31

1.6 Thesis Outline and Structure 33

2. Data set and methods 35

2.1 Seismic Dataset 35

2.2 Seismic interpretation 39

2.3 Methods 46

3. Constraints on fold orientations within the South Caspian Basin 49

3.1 Introduction 49

3.1.1 Introduction to South Caspian Basin 49

3.1.2 Geological History 51

3.1.3 Stratigraphy 52

3.1.4. Folding in the South Caspian Basin 53

3.1.5 Datasets 55

3.2 Methodology 56

3.2.1 Regional folds (work by Ken McCaffrey) 56

3.2.2 Shafag-Asiman fold 56

3.3 Results 59

3.3.1 Regional fold mapping 59

3.3.2 Shafag-Asiman fold structure 60

3.4 Discussion 68

3.4.1 Formation of the Shafag-Asiman fold structure 68

3.4.2 Regional Context 71

3.5. Conclusions 76

4. The geometry of the Shafag-Asiman fold from growth strata, using novel techniques 77

4.1 Introduction 77

4.2 Methods 79

4.2.1 Sediment Accumulation Indices 79

4.2.2 Uncertainties of Sediment Accumulation Index calculations 82

4.3 Results 83

4.3.1 2D Sediment Accumulation Indices 83

4.3.2 1D Sediment Accumulation Indices 85

4.3.3 3D Sediment Accumulation Indices 89

4.3.4 Mud Volcanism 95

4.4 Discussion 99

4.5 Conclusions 102

5. Numerical modelling the mechanical properties and influences of sediment load on a mobile shale cored fold structure. 103

5.1 Introduction 103

5.2 Methods 104

5.3 Results 110

5.3.1 Experiment 1a: Viscosity and Porosity/Density of Shale layer 110

5.3.2 Experiment 1b: Shafag Model 120

5.3.3 Experiments of Sensitivity analysis 122

5.4 Discussion 128

5.5 Conclusions 131

6. Deep-water lacustrine turbidite system of the South Caspian Basin and interaction with structures 132

6.1 Introduction 132

6.2 Methodology 136

6.3 Results 140

6.3.1 Unit A (Hz120 – Hz110) 141

6.3.2 Unit B (Hz130 – Hz120) 144

6.3.3 Unit C (Hz140 – Hz 130) 147

6.3.4 Unit D (Hz150 – Hz140) 150

6.3.5 Unit E (Hz160 – Hz150) 153

6.3.6 Channel Architecture 156

6.4 Discussion 166

6.4.1 Influence of Shafag-Asiman on the channel network 167

6.4.2 Structures outside of the dataset 171

6.4.3 Tectonic controls 174

6.4.4 Climatic controls 174

6.4.5 Comparison with Marine Systems 176

6.4.6 Comparison with Lacustrine Systems 177

6.5 Conclusions 182

7. Discussion 183

7.1 Summary of novel findings 183

7.2 Influence of sediment loading on fold development 185

7.3 Evolving numerical models of fold growth in the South Caspian Basin and beyond 193

7.4 The application of sediment accumulation indices on structural development and turbidite architecture 196

7.5 Future Work 203

8. Conclusions 206

References 210

Appendix 237

List of Figures

Figure 1.1: Map of the South Caspian Sea, surrounded by the Greater Caucuses, Talysh, Kopeh Dagh and Alborz mountains. Bathymetry/Topography data are from GeomapApp…….3

Figure 1.2: Structural elements of the South Caspian Sea and surrounding areas from Smith-Rouch 2006 (modified from Nalivkin, 1976; Adamia et al., 1977; Berberian and King, 1981; Philip et al., 1989 Devlin et al., 1999) The study area for this these is highlighted by the red box. …….....4

Figure 1.3: A section from Abdullayev et al. (2017) showing gravity modelling with observed (dotted line) and modelled (solid line) results. Density model below showing the oceanic crust in red brown. Density values are in g/cm3. Inset: Bouguer gravity anomaly map, Red = high, blue = low……5

Figure 1.4: Interpretation of the crustal structure shown over the depth to basement map. The map shows a comparison of B-factors derived from modelling of 2D lines and 1D strain-rate inversion. From Abdullayev et al. (2017).……5

Figure 1.5: Regional 2D seismic line from SSW to NNE across the Absheron Ridge, where the ACG fold is located. The subduction of the ocean like crust and subsequent accretionary prism is interpreted. The deep-water central part of the South Caspian basin is on the left of the image. The seismic section has 6x vertical exaggeration, with the inset top left showing no vertical exaggeration. From Stewart and Davies, (2006)…….6

Figure 1.6: Sketches describing the present-day active tectonics of the South Caspian Basin from Jackson et al. (2002). a) The present-day configuration of the basin showing S to SW underthrusting in the Talysh, Alborz and Greater Caucases and north dipping thrusting in the centre, under the location of the Absheron Ridge, where the South Caspian Basin is undergoing subduction. The white arrow indicates the relative motion of the basin relative to Iran, and the black arrow with respect to Eurasia. b) shows the velocity triangle between Iran, Eurasia and the South Caspian Basin, modified from Walker et al. (2021) ……8

Figure 1.7: The deep earthquakes of the South Caspian region from Jackson et al. (2002). Black spheres show events deeper than 30km (km depths in bold). Grey spheres are Harvard CMT solutions with reported depths of >33km, numbers next to the spheres are depths in km from Engdahl et al. (1998). Small circles are earthquakes deeper than 60km between 1964 – 1998 from Engahl et al. (1998). The inset is an enlarged area, shown by the black box……...9

Figure 1.8: Map of the best quality shallow earthquake focal mechanisms in the South Caspian Region, from Jackson et al. (2002). Black focal spheres show earthquakes that are less than 30 km with depths shown in bold. Grey spheres are Harvard centroid moment tensor solutions for events Mw ≥ 5.3. Light grey spheres show focal mechanisms recorded from long-period

instruments. Small black circles are hypocentres of 1964 - 1998 from Engahl et al. (1998). Large grey and black circles are epicentres of earthquakes > Ms 6.0 and > Ms 7.0 for large sized circles from 1900 to 1962 and post-1963. A and B in the east are the epicentres of the 1895 Krasnovodsk and the 1983 Kum Dag earthquakes respectively. The grey region offshore shows bathymetry greater than 500m……...10
Figure 1.9: Map of the structural orientations of the South Caspian Region. From Jackson 2002…...12
Figure 1.10: Regional 2D seismic line across the centre of the South Caspian Basin showing fold structures and mud volcanoes. From Narimanov (1997). Location on figure 1.9…….12
Figure 1.11: Stratigraphic column for the South Caspian Basin with major geological events and local stratigraphic stages (suites) indicated. Modified rom Abdullayev et al. (2017). Stratigraphic ages are from Popov et al. (2006), Hudson et al. (2008), Lazarev et al. (2019) and Van Baak et al. (2019)…….14
Figure 1.12: Thickness map of the Oligo-Miocene sequence. This is a depth isochore map between the Base Productive Series depth surface and the near-Base Maykop depth surface. From Green et al. (2009)…….15
Figure 1.13: Schematic map of possible sources of sediment deposited in palaeodeltas prograding into the South Caspian Basin during deposition of the Pliocene Productive Series. From Smith-Rouch (2006)…….16
Figure 1.14: Depositional model for the Productive Series from Green et al. (2009). The location is shown on the inset map. The evaporite facies of the Surakhany within the centre of the South Caspian Basin are shown in green (4) and pink (5)……..17
Figure 1.15: Paleogeographic maps for the Plio-Pleistocene Pontocaspian region. A) Middle Pliocene Productive Series; B) Late Pliocene Akchagyl; C) Early Pleistocene Absheron; D) Middle Pleistocene Bakunian. The South Caspian can be seen as deep water from the Akchagyl through to the present-day. From Krijgsman et al. (2019)…….18
Figure 1.16: Thickness map of the Late Pliocene–Recent sequence. This is a depth isochore map constructed between the present-day Caspian seafloor and the Top Productive Series depth surfaces. Thinning over the crests of the folds in the South Caspian Basin can be seen. From Green et al. (2009)……19
Figure 1.17: Unlocated seismic line in the Turkmenistan shelf in the east of the South Caspian Basin, showing channel systems that supplied sediment to the deep-water turbidites of the Pleistocene to Recent stratigraphy. CLS = channel levee system. From Abdullayev (2000)……19
Figure 1.18: Seismic facies and depositional systems map of the base of the Pleistocene Absheron Formation. Depositional infill is uniform in character and interpreted as onlap-fill mud-rich turbidites (diagonal dotted pattern) and hemipelagics (vertical solid lines). From Abdullayev (2000)…….20

Figure 1.19: Line drawing of an interpreted seismic profile from the Eastern margin of the South Caspian Basin, showing progradation of the Palaeo-Amu Darya in the Absheron to Recent. Location is shown in red on the inset map. Offlap-break curve is shown in red (dashed line indicates the uncertainty in the location of the offlap break). Inset map shows the location of the river deltas during the Absheronian, with the Palaeo-Amu Darya further west than the present-day. Grey arrows show onlap. Black arrows show downlap and white arrows show truncation. From Abreu and Nummedal (2007)……20

Figure 1.20: Seismic facies and depositional system map of facies within the Bakunian. Thick clinoforms were formed in the southeast with slides and slumps (black and white dotted area).in the deep part of the basin. Drape facies and turbidite infill are vertical solid lines. From Abdullayev (2000)……...21

Figure 1.21: Location of mud volcanoes within the South Caspian Basin interpreted using regional 2D seismic lines. From Yusifov and Rabinowitz, (2004)……25

Figure 1.22: Cross section through the southern Caspian Sea region showing stratigraphy and structure from the Kura Basin in Azerbaijan eastward through the Apsheron-Pribalkhan Zone into western Turkmenistan. The mobile shale of the Maykop Formation can be seen in green. Note that the vertical scale in kilometers is 10× the horizontal scale. From Smith-Rouch 2006……...26

Figure 1.23: Seismic dip-line from a fold in the western offshore part of the South Caspian Basin (a) and interpreted (b). A collapsed mud diapir is found in the fold crest, bounded by normal faults. Vertical scale is in real depth (in kilometres with no vertical exaggeration. From Santos Betancor and Soto (2015)……...27

Figure 1.24: Lake-basin type phase diagram showing existence and character of nonmarine strata in general and lacustrine strata in particular as a function of both sediment+water supply and potential accommodation. Interaction of these two controls is reflected in the lithology, stratal stacking, biota, and geochemistry of lake deposits. Potential accommodation is the space available for sediment accumulation below the basin's outlet or spillpoint (a key difference from marine systems) (Carroll and Bohacs, 1995), and it is mainly influenced by basin tectonics, along with sill uplift and erosion, and inherited topography. Sediment + water supply is primarily a function of climatic humidity, along with seasonality, local relief, and bedrock geology. From Bohacs et al. (2000)…….30

Figure 2.1: Map of anticline structures within the South Caspian Basin (yellow) and recent mud volcanism (triangles) from Santos-Betancor and Soto (2015). The Shafag – Asiman fold structure is highlighted by the red box……35

Figure 2.2: Outline of the seismic data for the pre-stack depth migrated (PSDM) data and the broadband seismic data (dashed line). The projection is WSG 84/UTM zone 39N……36

Figure 2.3: Frequency of the PSDM seismic dataset between 1000 m/s and 3500 m/s depth……..37

Figure 2.4: RMS amplitude maps showing channels in a) PSDM and b) broadband seismic datasets with corresponding sections showing the channel image quality in section view in c) PSDM and d) broadband seismic datasets. The RMS window is shown by the yellow lines in c) and d)…….38
Figure 2.5: Slice through a) Discontinuity cube and b) Dip-corrected Discontinuity cube imaging faults over a fold crest……39
Figure 2.6: Seismic stratigraphic column describing the horizons interpreted, reflector characteristics and a brief description of the intervals. The ages are shown on the left as well as ages and formation names used in this study. The formation tops are supplied by bp and are tied to regional seismic lines. The Surakhany Formation is the top of the Productive Series. The Akchagyl, Absheron and Baku Formations constitute the Post-Productive Series. Ages given are based on Van Baak et al. (2019), Lazarev et al. (2019), Lazarev et al. (2021), Vasiliev et al, (2022)……..40
Figure 2.7: Depth to seabed map with locations of mud volcanoes and seismic lines. Of the three mud volcanoes in the dataset, only MV1 is active on the present-day seabed……42
Figure 2.8: Seismic section through a) Asiman and b) Shafag fold structure showing the horizon interpretation as well as the seismic wipe out in the crest due to the mobile mud core. H/V exaggeration is 1:3…….43
Figure 2.9: a) Active mud volcano visible on the present-day seabed, up to 4 km wide. The area of seismic wipe-out reaches up to 5 km down to 3 km depth. There is significant thinning of the Surakhany Formation below the mud volcano. b) extinct mud volcano north of Shafag situated on Hz100, the Surakhany Formation. c) extinct mud volcano west of Asiman showing periodic activity up until Hz170 -Hz160, with no reflectivity preserved in the data below this. H/V exaggeration is 1:3……...44
Figure 2.10: a) Seabed dip map showing slumping off the flanks of the Shafag and Asiman fold structures. b) Section displaying thrusts within the mass transport deposits showing a flow direction to the south, sourced from outside the area to the north…….45
Figure 2.11: Workflow of the channel analysis. The software used to conduct the analysis was Landmark DecisionSpace software (yellow boxes), Ellis Paleoscan software (blue boxes), ArcGIS (green boxes), MATLAB (pink box) and Stereonet (grey box). The thick black boxes are the results used within the channel analysis. 1 Pauget et al. (2009). 2 Bechtold (2016) (code used to create violin plots). 3 Allmendinger et al. (2011). 4 Cardozo and Allmendinger (2013)…….46
Figure 2.12: Schematic diagram showing how isoproportional slices can be used for a) no growth strata and b) growth strata. Where there are growth strata, horizons a and b, isoproportional horizons (red box) do not map the correct geometry of the reflectors and therefore channel maps will not be correct…….47

Figure 2.13: a) Seismic cube, b) geomodel calculated from the seismic cube and horizon extracted from the geomodel. From Pauget et al. (2009)……48
Figure 3.1: Structural map of the South Caspian Basin. Structures taken from Jackson 2002. The Shafag-Asiman fold structure analysed in this study is indicated by the red box. Bathymetry/Topography data are from GeomapApp…….50
Figure 3.2: Generalised stratigraphic column of the South Caspian Basin. Modified from Abdullayev et al. (2017). Ages are from Popov et al. (2006), Hudson et al. (2008), Lazarev et al. (2019) and Van Baak et al. (2019)…….53
Figure 3.3: a) Map of the seabed of the Shafag-Asiman fold structures, with inset location of map within the South Caspian Basin. The three mud volcanoes MV1, MV2 and MV3 are highlighted in white circles. MV1 is presently active on the seafloor, whereas MV2 and MV3 are extinct. Seismic sections through b) Asiman and c) Shafag highlighting the stratigraphy of the Shafag-Asiman fold structures. Vertical exaggeration = 3.2x…….58
Figure 3.4: a) Dip azimuth map of the northern South Caspian Basin and b) map of interpreted folds. The colour scale is shown beneath the map where the colours indicate the dip direction (azimuth) of the mapped horizon. Fold anticlinal axes are in black dashed lines and synclinal axes are in red dashed lines. Four fold domains have been interpreted, Talysh, central basin, ACG and Alov. From McCaffery (pers. com). Inset map from Jackson et al. (2002)……59
Figure 3.5. Isopach maps for intervals from a) Hz110 – Hz100, b) Hz120 - Hz110, c) Hz130 – Hz120, d) Hz140 – Hz130. White circles are due to seismic wipe out from mud volcanoes. The axial trace location during each interval is shown by a black dashed line……...62
Figure 3.6: Depth slice at 2200m, showing the two major fault styles observed within the Post-Productive Series. En-Echelon crestal normal faults and normal ring faults……..63
Figure 3.7: En-Echelon normal faults that extend along the fold crests. The yellow horizon is used to indicate the fault displacement. Section location indicated in figure 3.6……64
Figure 3.8: Ring faults around the large mud volcano that erupts onto the surface between the Shafag and Asiman fold crests. Section located on figure 3.6……65
Figure 3.9: a) Depth map of a pre-Maykop horizon and b) interpretation of faults which display shortening A large fault lies beneath the fold structures as well as smaller faults thar trend in a N-S orientation around Shafag and NE-SW near Asiman. c) section showing the large deep basement fault beneath the AMykop shale which underlies the Shafag – Asiman fold structures ……...66
Figure 3.10: Interpretation of fold axial traces from isopach maps from Hz100 to Hz140 showing anticlockwise rotation and inferred dextral shear of the Shafag – Asiman fold structures..69

Figure 3.11: Block diagram demonstrating the a) pre-dextral transpression and b) post-dextral transpression, showing the anti-clockwise rotation of the fold axis and development of en-echelon crestal normal faults (red)…….70

Figure 3.12: Map view of structures formed during dextral transpression. C = compression axis σ1, E = extensional axis σ3, T = thrusts faults, N =normal faults, F =fold axis, V =veins or extensional fractures. R = Riedel shears. Both the orientation of the fold axis and crestal extensional faults in relation to σ1 displayed in the transpressional model are observed on Shafag-Asiman. Taken from Sanderson and Marchini (1984)……..71

Figure 3.13: Section through the Chirag fold of the ACG fold structure showing the deep faults of the accretionary prism controlling the location of the ACG folds. From Robinson et al. (2005)…… 73

Figure 3.14: Examples of models from Ghosh et al. (1995) of pure constriction of clay with total radial shortening of a) 18.8 % b) 17.7 % and c) 29.4 % and d) Interpreted plan view of a clay model showing anticlines (white) and syncline (dotted) areas which resembles the fold pattern obsereved within the central Caspian region where Shafag-Asiman is located. Taken from Ghosh et al. (1995)……..74

Figure 3.15: Depth map of the basement underneath the ACG structure in the north of the South Caspian Basin showing the current ACG structure, shown by the red peaks and the older E-W basement structure shown by the dashed white line. Surface mapped by Ken. McCaffrey…….76

Figure 4.1: a) Summary of the terminology for a detachment fold and growth strata, b) – e) models of overlap, offlap and onlap based on the ratio of uplift to sediment accumulation. From Burbank and Vergés (1994)……...77

Figure 4.2: A model of growth strata formed during deposition of a detachment fold. The first two layers are deposited with uplift greater than sedimentation rate, the last two layers are deposited with sedimentation rate greater than uplift. From Poblet et al. (1997)……..78

Figure 4.3: An illustration of the sediment accumulation index. A larger index equates to more sediment thickening on the fold limb relative to the fold crest and therefore increased fold growth, if a constant sedimentation rate is assumed……...80

Figure 4.4: Sections through a) Asiman and b) Shafag highlighting the intervals and sequences analysed using sediment accumulation indices. The locations on the limb from which true stratigraphic sediment thickness was measured for the 1D analysis is shown on the northern and southern limbs. MTD = mass transport deposits. Asiman H/V = 1:3. Shafag H/V = 1:3.2……81

Figure 4.5: Illustration of the effect of compaction on sediment thickness showing the present-day compacted sediment to be thinner than the true decompacted sediment thickness…….82

Figure 4.6: Sediment accumulation indices for a section across the Asiman fold axis for Hz120 – Hz110 (black) and Hz180 – Hz170 (red) showing the variation in sediment growth between the two packages using sediment accumulation indices. The intervals both show an asymmetry, with higher indices in the southeast……83

Figure 4.7: Sediment accumulation indices for a section across the Shafag fold axis for intervals between Hz110 and Hz160 showing the variation in sediment growth between the two packages using sediment accumulation indices. The data are taken from sediment accumulation maps. Hz160-Hz150 values does not reach 1.0 on the fold crest since Asiman had thinner sediment over the crest at this time……..84

Figure 4.8: 1D sediment accumulation indices for a) Asiman, b) Shafag and c) both southern limbs. Location of the limb thicknesses located on figure 4.4…….……..88

Figure 4.9: a) 1D sediment accumulation indices from the southern limbs of Asiman and Shafag. Hz 120 – Hz110 is highlighted in black. B) Sediment accumulation index map created using 190 data points measured across Hz120 – Hz110. C) Sediment accumulation index map calculated using every point from isopach map for Hz120 - Hz110. The two black dots are the locations from which the 1D indices were calculated in a)……...90

Figure 4.10: Sediment accumulation index maps for intervals between the top Absheron formation and top Surakhany Formation, Hz100 to Hz160. a) = oldest, f) = youngest. Each map is scaled to the same colour bar for comparison. The white circles are where mud volcanoes cause seismic wipe out in the data……92

Figure 4.11: Sediment accumulation index map for Hz170 – Hz160, the oldest interval of the mass transport deposits……...93

Figure 4.12: Sediment accumulation index maps for intervals between the Seabed and the Top Absheron Formation, Hz200 – Hz160. Each map is scaled to the same colour bar for comparison. The white circles are where mud volcanoes cause seismic wipe out in the dataset…….94

Figure 4.13: a) uninterpreted and b) interpreted seismic section of an extinct mud volcano in the north of the area, MV3. H/V = 1:3……...96

Figure 4.14: Palaeo mud cones of a mud volcano to the west of Asiman, showing mud volcano activity from Hz110 -Hz100 up to Hz170 – Hz160. H/V = 1:3……...97

Figure 4.15: a) Sediment accumulation maps around the central mud volcano, MV1, which is active on the present-day seabed, showing sediment growth around the volcano. b) Seismic section across the central mud volcano showing the lack of seismic response in the feeder pipe and sediment growth around the pipe. …….98

Figure 4.16: Isopach map of the Post-Productive Series from Green et al. (2009). Thinning of the strata can be seen in the yellow colours southeast of Shafag (S) and northwest of Asiman (A)..101

Figure 5.1: Simple model geometry used for sensitivity analysis with constant sedimentation rate based on values measured from seismic reflection data of the Shafag fold……...108

Figure 5.2: Fold geometries at end of model run in Experiment 1a for viscosities of 1018 (red), 1019 (blue) and 1020 (green) for (a) 35% (b) 30% and (c) 25% porosity……..111
Figure 5.3: Contours showing accumulated displacement in x for a model with 30% visco-plastic layer porosity and 1018 Pa.s viscosity through time…….113
Figure 5.4: Distance of particle movement in x for the model of 30% porosity and 1018 Pa.s viscosity for the visco-plastic layer at three starting locations from the fold axis in the centre of the model, 16000m in red, 10000m in blue and 4000m in green. Applied tectonic shortening is shown at 16000m starting location by tracking within the elasto-plastic sand layer (grey dashed line)……..114
Figure 5.5: Distance of particle movement in x for models of 35%, 30% and 25% porosity of the visco-plastic layer at viscosities of 1018 and 1020 at three starting locations, from the fold axis in the centre of the model, 16000m in red, 10000m in blue and 4000m in green. Applied tectonic shortening is shown at 16000m location by tracking within the elasto-plastic sand layer, in grey……116
Figure 5.6: Particle distance moved in x through time within the visco-plastic layer for viscosities between 1018-1022 at the 16000m, 10000m and 4000m starting position for visco-plastic layer porosities of 35%, 30% and 25%.....117
Figure 5.7: Sediment Accumulation Index (SAI) explanation. A larger index number means more thickening on the edge of the fold than over the crest. …….118
Figure 5.8: Sediment Accumulation Index (SAI) for viscosities of 1022-1018 for 35% (red), 30% (blue) and 25% (green) porosity of the visco-plastic layer……...119
Figure 5.9: Displacement in x for the visco-plastic layer for models with the Shafag model geometry (variable sedimentation rate) and the simple model geometry (constant sedimentation rate)……..121
Figure 5.10: Displacement in x for the visco-plastic layer for models set with original initial visco-plastic layer thickness: 1200m, increased thickness: 1800m and decreased thickness: 600m.……...123
Figure 5.11: Displacement in x for the visco-plastic layer for models set with original applied tectonic shortening h=1400m w=5000m, increased applied tectonic shortening h=2100 w=7500, and decreased applied tectonic shortening h=700m w=2500m. h=perturbation height and w= shortening applied to both edges of the model……..125
Figure 5.12: Displacement in x for the visco-plastic layer for models set with original overburden thickness 3000m, increased overburden thickness 4000m, and decreased overburden thickness 2000m……..127
Figure 6.1: Present-day seabed bathymetry showing the Shafag-Asiman fold complex and associated mud volcano (MV1). Inset: location of the study area within the South Caspian Sea…...133

Figure 6.2: Bathymetry and topography map for the South Caspian Basin and surrounding areas showing the three river sources into the South Caspian Basin as well as the clinoforms prograding from the Turkmenistan Shelf as interpreted from 2D seismic data by Abdullayev (2000)……...134

Figure 6.3: Line drawing of an interpreted seismic profile from the Eastern margin of the South Caspian Basin, showing progradation of the Palaeo-Amu Darya in the Absheron to Recent. Location is shown in red on the inset map. Offlap-break curve is shown in red (dashed line indicates the uncertainty in the location of the offlap break). Inset map shows the location of the river deltas during the Absheronian, with the Palaeo-Amu Darya further west than the present-day. Grey arrows show onlap. Black arrows show downlap and white arrows show truncation. From Abreu and Nummedal (2007)……..134

Figure 6.4: Model of channel architecture used when interpreting deep water marine depositional systems, highlighting the detail that occur in most channels. The model emphasizes three orders of channel systems, complexes and individual channel elements. In this study we use this terminology to describe the channel network. From Mayall and Kneller (2021).136

Figure 6.5: Section through Asiman fold axis with the six regional horizons, Hz160 – Hz110 interpreted for this study and units. Line location is labelled on figure 6.1……...137

Figure 6.6. An RMS amplitude map calculated with a 50m window (yellow) from within Unit A and corresponding section showing the channels. The map shows the truncation of reflectors around the Shafag fold since the window from which the RMS amplitude was calculated is based on the horizon interpretation. Described in chapter 2……..138

Figure 6.7: Example RMS amplitude map taken from a 50m window above and below a horizon within Unit B interpreted from a Palaeoscan geomodel. 28 RMS maps are used to interpret a total of 259 channels used in this study. The black circles are the mud volcanoes…….138

Figure 6.8: Point bar scrolls from Interval B showing a flow direction in a north westerly direction..139

Figure 6.9: Map of channels interpreted within Unit A, colour coded for each horizon. N = 71. Channel orientations are plotted on equal area rose diagrams in 10° bin. The mean vector is shown as an arrow with 95% confidence interval. The outer circle is 30% of the data. Statistics are shown in table 6.2. The white circles on the map are areas of poor data quality due to mud volcanism. The locations of the Asiman (A) and Shafag (S) fold crests have been superimposed from the Unit A sediment accumulation index map…….. 142

Figure 6.10: Maps produced for Unit A showing: a) sediment accumulation index (SAI). b) Sediment accumulation index overlain by the channel interpretations. c) Channel density calculated within 2 km x 2 km areas. Dark blue areas show a high concentration of channels, white areas show a low concentration of channels. Violin plots for d) Asiman and b) Shafag calculated by comparing the mean SAI with the channel density for the 2km x 2km shown in c). White circles on the maps are areas of poor data quality due to mud volcanism…..143

Figure 6.11: Map of channels interpreted within Unit B, colour coded for each horizon. N = 71. Channel orientations are plotted on equal area rose diagrams in 10° bin. The mean vector is shown as an arrow with 95% confidence interval. The outer circle is 30% of the data. Statistics are shown in table 6.3. The white circles on the map are areas of poor data quality due to mud volcanism. The locations of the Asiman (A) and Shafag (S) fold crests have been superimposed from the Unit B sediment accumulation index map……...145

Figure 6.12: Maps produced for Unit B showing: a) sediment accumulation index (SAI). b) Sediment accumulation index overlain by the channel interpretations. c) Channel density calculated within 2 km x 2 km areas. Dark blue areas show a high concentration of channels, white areas show a low concentration of channels. Violin plots for d) Asiman and b) Shafag calculated by comparing the mean SAI with the channel density for the 2km x 2km shown in c). White circles on the maps are areas of poor data quality due to mud volcanism…..146

Figure 6.13: Map of channels interpreted within Unit C, colour coded for each horizon. N = 40. Channel orientations are plotted on equal area rose diagrams in 10° bin. The mean vector is shown as an arrow with 95% confidence interval. The outer circle is 30% of the data. Statistics are shown in table 6.4. The white circles on the map are areas of poor data quality due to mud volcanism. The locations of the Asiman (A) and Shafag (S) fold crests have been superimposed from the Unit C sediment accumulation index map……...148

Figure 6.14: Maps produced for Unit C showing: a) sediment accumulation index (SAI). b) Sediment accumulation index overlain by the channel interpretations. c) Channel density calculated within 2 km x 2 km areas. Dark blue areas show a high concentration of channels, white areas show a low concentration of channels. Violin plots for d) Asiman and b) Shafag calculated by comparing the mean SAI with the channel density for the 2km x 2km shown in c). White circles on the maps are areas of poor data quality due to mud volcanism…..149

Figure 6.15: Map of channels interpreted within Unit D, colour coded for each horizon. N = 43. Channel orientations are plotted on equal area rose diagrams in 10° bin. The mean vector is shown as an arrow with 95% confidence interval. The outer circle is 30% of the data. Statistics are shown in table 6.5. The white circles on the map are areas of poor data quality due to mud volcanism. The locations of the Asiman (A) and Shafag (S) fold crests have been superimposed from the Unit D sediment accumulation index map……..151

Figure 6.16: Maps produced for Unit D showing: a) sediment accumulation index (SAI). b) Sediment accumulation index overlain by the channel interpretations. c) Channel density calculated within 2 km x 2 km areas. Dark blue areas show a high concentration of channels, white areas show a low concentration of channels. Violin plots for d) Asiman and b) Shafag calculated by comparing the mean SAI with the channel density for the 2km x 2km shown in c). White circles on the maps are areas of poor data quality due to mud volcanism…..152

Figure 6.17: Map of channels interpreted within Unit E, colour coded for each horizon. N = 35. Channel orientations are plotted on equal area rose diagrams in 10° bin. The mean vector is shown as an arrow with 95% confidence interval. The outer circle is 30% of the data. Statistics are shown in table 6.6. The white circles on the map are areas of poor data quality due to mud volcanism. The locations of the Asiman (A) and Shafag (S) fold crests have been superimposed from the Unit E sediment accumulation index map……...154

Figure 6.18: Maps produced for Unit E showing: a) sediment accumulation index (SAI). b) Sediment accumulation index overlain by the channel interpretations. c) Channel density calculated within 2 km x 2 km areas. Dark blue areas show a high concentration of channels, white areas show a low concentration of channels. Violin plots for d) Asiman and b) Shafag calculated by comparing the mean SAI with the channel density for the 2km x 2km shown in c). White circles on the maps are areas of poor data quality due to mud volcanism…..155

Figure 6.19: Normalised cumulative frequency of sediment accumulation index measured at each Avulsion point and 100k random points for Units A and B with K-S test statistics. At the 80% confidence level, Dmax > Dcrit so the null hypothesis is rejected suggesting that the distributions are not drawn from the same probability distribution……..158

Figure 6.20 RMS map of a horizon within Unit A showing lateral avulsion points of a channel elements from a channel complex at locations 1 and 2……159

Figure 6.21: RMS map of a channel complex within Unit B showing point avulsions up-dip of the fold crest and lateral avulsions downdip of the fold crest. Avulsion points are highlighted in red. Labels 1 (oldest) – 5 (youngest) indicate the relative age of the channel elements. Uninterpreted and interpreted seismic sections for three sections A-A', B-B' and C-C' along the channel profile, showing a change from lateral migration and aggradation to isolated channel elements……..160

Figure 6.22: RMS map of a channel complex within Unit B showing point avulsions up-dip of the fold crest and lateral avulsions downdip of the fold crest. Avulsion points are highlighted in red. Labels 1 (oldest) – 4 (youngest) indicate the relative age of the channel elements…161

Figure 6.23: Channel complexes within Unit B overlain on to the unit equivalent sediment accumulation index map…… 162

Figure 6.24: Channel complexes within Unit D overlain onto the unit equivalent sediment accumulation index map…… 163

Figure 6.25: Sections showing onlap (black arrows) within units D and B across Shafag (a) and (b) and Asiman (c)…….... 165

Figure 6.26: 3D depositional model of the deep water lacustrine turbidite system within the deep-water South Caspian Sea Basin……170

Figure 6.27: Isopach map of the Late Pliocene to recent sediments modified from Green et al., (2009). The Asiman and Shafag structures are labelled A and S respectively. The location of the seismic line from figure 6.26 is shown by the black line……...172
Figure 6.28: Regional 2D seismic line across the centre of the South Caspian Basin showing fold structures and mud volcanoes. The 'Alov' structure is labelled. The strata show significant thinning onto the structure From Narimanov (1997). Location on figure 6.25…….173
Figure 6.29: Regional bathymetry map of the deep-water South Caspian Sea Basin around the Shafag - Asiman data set (black box). Fold structures on the present-day seabed are shown in grey. Red arrows show possible channel sources from the Paleo Amu-Darya. Dashed lines show channels entering Shafag – Asiman before the Alov structure blocked the flow path. The blue arrow shows the likely source area for the SW trending channels within Unit D. The black channel shows a possible channel complex splitting into channel elements on a structure outside of the dataset…….173
Figure 6.30: Comparison of deep water turbidite systems between (a) marine from Mayall and Kneller (2021) and b) Shafag-Asiman……..177
Figure 6.31: Active continental rift depositional system from Gawthorpe and Leeder (2000). Footwall scarp lacustrine turbidites are highlighted by the red box…….178
Figure 6.32: Lake types from Bohacs et. al. (2000). The deep water turbidites of the South Caspian Basin are deposited in an overfilled lake……..179
Figure 6.33: Seismic images a) and b) from the Songliao Basin, China showing deep-water turbidites and lobes in a similar depositional setting to the South Caspian Basin. From a) Zhi-Qiang (2010) and b) Pan (2020). c) RMS amplitude map taken from unit B of this study scaled to match the map in b)……..181
Figure 7.1: a) interpretation of a seismic section of a fold structure in the west of the South Caspian Basin from Santos-Betancor and Soto (2015) and comparison with b) numerical model with double shortening from chapter 5 showing similar fold geometries…….189
Figure 7.2: Fold wavelengths found within deep-water fold and thrust belts, including both salt and shale detachments. The Zagros Mountains are for comparison with an orogenic fold and thrust belt. The South Caspian Sea Basin is highlighted in red and contains the largest mean fold wavelenth of all fold belts included..From Morley et al. (2011)……..191
Figure 7.3: Fold wavelength vs. stratigraphic thickness for a range of deep-water fold and thrust belts. The South Caspian Basin is highlighted in red and shows both the highest fold wavelengths and stratigraphic thickness. From Morley et al. (2011)……192
Figure 7.4: a) Seismic section through the Absheron fold from Blouin et al. (2019) and b) an interpretation of a seismic section through the Shah Deniz fold from Fowler et al. (2000). Both structures are in the deepwater part of the South Caspian Basin, to the north of the Shafag-Asiman fold structure and have similar overlapping strata of the Absheron and are

therefore ideal structures to implement and replicate the methods used within this thesis……198

Figure 7.5: Seismic section through the Mexican Ridges fold belt showing overlapping growth strata across the fold belt. Fold structures on the north-eastern extent of the belt appear to look similar to the Shafag-Asiman fold structure, however, the fold wavelengths are narrower in the Mexican Ridges fold belt. From Yarbuh and Contreras (2017)……..200

Figure 7.6: Isochron maps (a, b c and d) and corresponding channel interpretations (a', b', c' and d') for seismic intervals 1 (a and a'), 2 (b and b'), 3 (c and c') and 4 (d and d') from Howlett et al. (2021). A growing salt cored topographic high is highlighted in a black box. I have calculated sediment accumulation indices from the isochron maps based on the thin value on the crest of the salt cored structure. Indices are shown in red. The sediment accumulation indices show the relative growth of the structure as well as showing that high indices coincide with highly sinuous channel complexes and lower indices coincide with low sinuosity complexes, similar to what I have observed at Shafag-Asiman……..202

List of Tables

Table 5.1: Parameter values used in the model set up for each experiment……...109

Table 6.1: A summary of the units, highest relative fold growth of Asiman and Shafag, the thickness of each unit and the number of maps from which the channels were interpreted from within each unit……...137

Table 6.2: Channel statistics and observations for each horizon interpreted within Unit A and the total for the unit……141

Table 6.3: Channel statistics and observations for each horizon interpreted within Unit B and the total for the unit……144

Table 6.4: Channel statistics and observations for each horizon interpreted within Unit C and the total for the unit……147

Table 6.5: Channel statistics and observations for each horizon interpreted within Unit D and the total for the unit……151

Table 6.6: Channel statistics and observations for each horizon interpreted within Unit E and the total for the unit. ……..153

Table 6.7: Total number of Avulsion points and number of avulsion points per horizon within each unit……...156

Table 6.8: Summary of the main observations made of the channel network within each unit……166

1. Introduction

1.1 Motivation

The South Caspian Basin is a tectonically complex basin which contains one of the thickest sedimentary successions of any basin in the world, containing a 20 km thick sedimentary succession with the topmost 10 km deposited within the last 6 Ma (Devlin et al., 1999, Allen et al., 2002). The rapid sedimentation rates generate abnormal conditions, such as low temperature gradients (Abrams and Narimanov, 1997) and over-pressured sediments including a thick organic-rich shale (Narimanov, 1993, Nadirov et al., 1997). The thick sedimentary layer is deposited during rapid subsidence, due to the basin being underlain by an 'oceanic type' crust within a zone of complex plate convergence (Berberian, 1983, Zonenshain and Pichon, 1986, Mangino and Priestley, 1994, Jackson et al., 2002, Allen et al., 2003, Green et al., 2009, Egan et al., 2009, Abdullayev et al., 2017). A major tectonic reorganisation originating in the Pliocene formed shale-cored anticlines, as buckle folds, above the over-pressured shale within a deep-water lacustrine environment (Shikalibeily and Grigoriants, 1980, Devlin et al., 1999, Allen et al., 2002, Allen et al., 2003, Brunet et al., 2003, Green et al., 2009, Santos-Betancor and Soto, 2015). Evidence suggests that mobile shale movement is directly linked to the folding, with mud evident within the cores of anticlines in the west of the basin (Santos-Betancor and Soto, 2015) or piercing of fold crests at Shah Deniz in the north of the deep-water basin focussed above deep structural highs (Fowler et al., 2000, Yusifov and Rabinowitz, 2004). Mud volcanoes are widespread within the basin (Yusifov and Rabinowitz, 2004), highlighting the regional significance of mobile shale tectonics.

Historically, folds within the South Caspian Basin are thought to form in response to tectonic shortening (Devlin et al., 1999). However, the rapid deposition of large volumes of sediment into the basin upon an over-pressured mobile shale may have also contributed to fold growth, by the gravitational loading of the weak underlying shale. Whilst the regional tectonics of the South Caspian Basin have been widely examined, only recently have individual fold histories been studied, since the acquisition of high-quality 3D seismic reflection data within the basin (Santos-Betancor and Soto, 2015). However, the role of sediment loading of the over-pressured shale has not been directly studied.

Understanding the influence of mobile shale tectonics during fold growth is important since the structural history of 65 regions across the world are affected by mobile shale tectonics, including the Niger Delta, the Gulf of Mexico, and the Caribbean Basin (Soto et al., 2021a). Previous attempts to understand the role of sediment loading of mobile shales include discrete element modelling of fold and thrust belts such as the Niger Delta (e.g. Dean 2014, Dean et al., 2015), however, there have been no attempts to model sediment loading of shale in the South Caspian Basin.

I have been provided with a 3D seismic reflection dataset by bp, located over two-fold structures, Shafag-Asiman, in the deep-water part of the South Caspian Basin. The high-quality seismic dataset provides me with the opportunity to study the mechanics of fold growth in a tectonically active basin influenced by shale tectonics. I investigate the mode of formation of the Shafag-Asiman fold structure and address the role of sediment loading as well as tectonic shortening in their genesis. I put the understanding of the fold growth of the Shafag-Asiman fold structures into a wider regional context with respect to other folds within the South Caspian Basin.

The folds grew within the deep-water South Caspian Basin during the Pleistocene, a time in which lacustrine turbidites were deposited (Abdullayev, 2000). Very little is known about deep-water lacustrine turbidites and in particularly how these interact with growing structures, historically due to the lack of high-quality 3D seismic surveys conducted within these environments. In this thesis I use the high-quality 3D seismic reflection dataset shot over Shafag-Asiman to comprehensively map the lacustrine turbidites. I investigate how the turbidite channels interact with the growing fold structures as well as improving our understanding of lacustrine turbidite systems and how they vary compared with marine turbidite systems.

1.2 The South Caspian Basin

The South Caspian Basin is located in the southern-most part of the Caspian Sea, the world's largest inland body of water, with a present-day area of 371,000 km^2. The basin lies within Azerbaijan, Iran and Turkmenistan. and covers an area of approximately 189,000 km^2 with a maximum water depth of approximately 1000m (Smith-Rouch, 2006). The basin is surrounded by mountain belts, with the Greater Caucasus to the north, Talysh to the West, Alborz to the South and Kopeh Dagh to the east (figure 1.1).

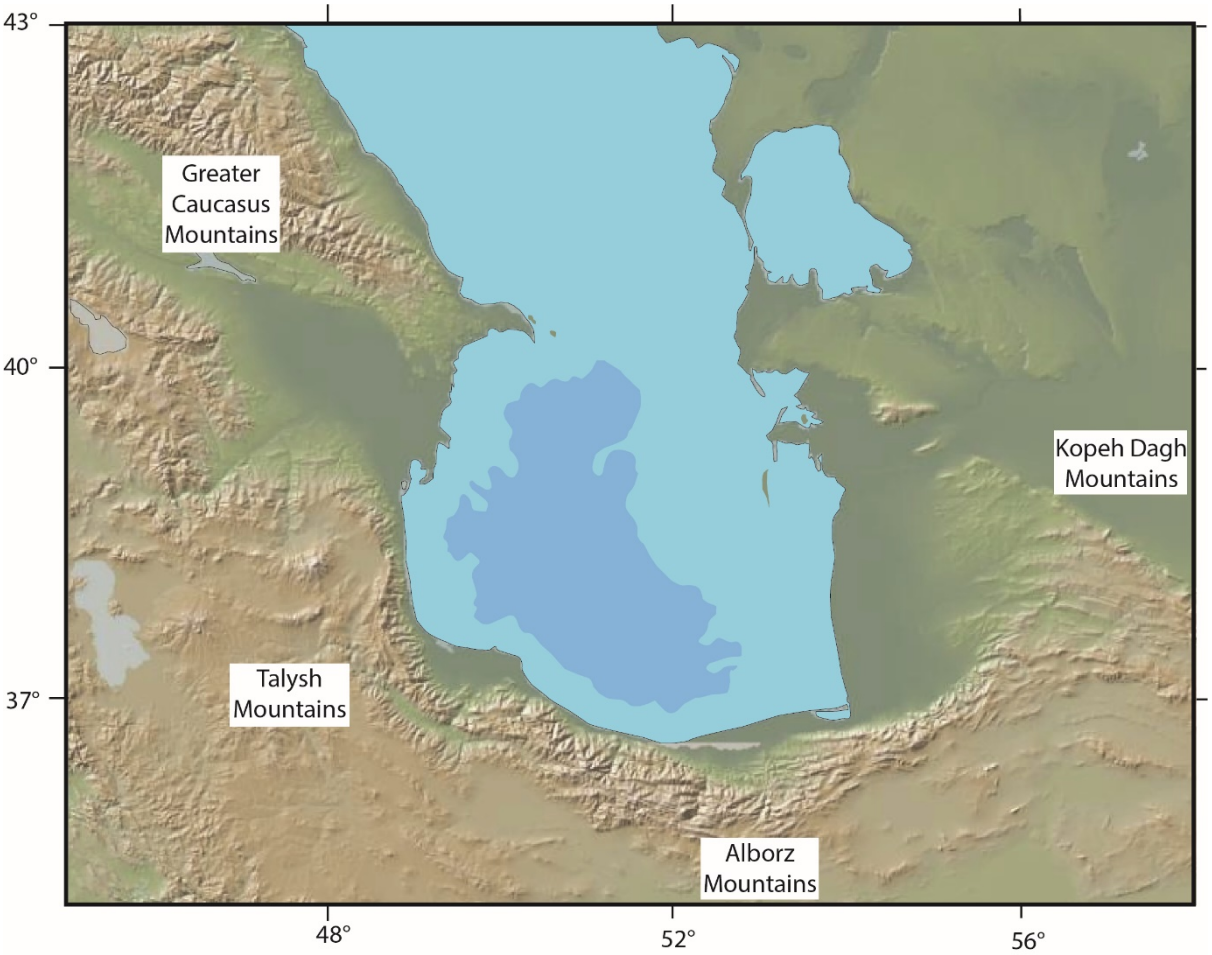


Figure 1.1: Map of the South Caspian Sea, surrounded by the Greater Caucuses, Talysh, Kopeh Dagh and Alborz mountains. Bathymetry/Topography data are from GeomapApp.

1.2.2 Tectonics

The South Caspian Basin is tectonically complex with numerous fault zones and folds (figure 1.2). In this section I will discuss the current understanding of the structural development and structural history of the basin.

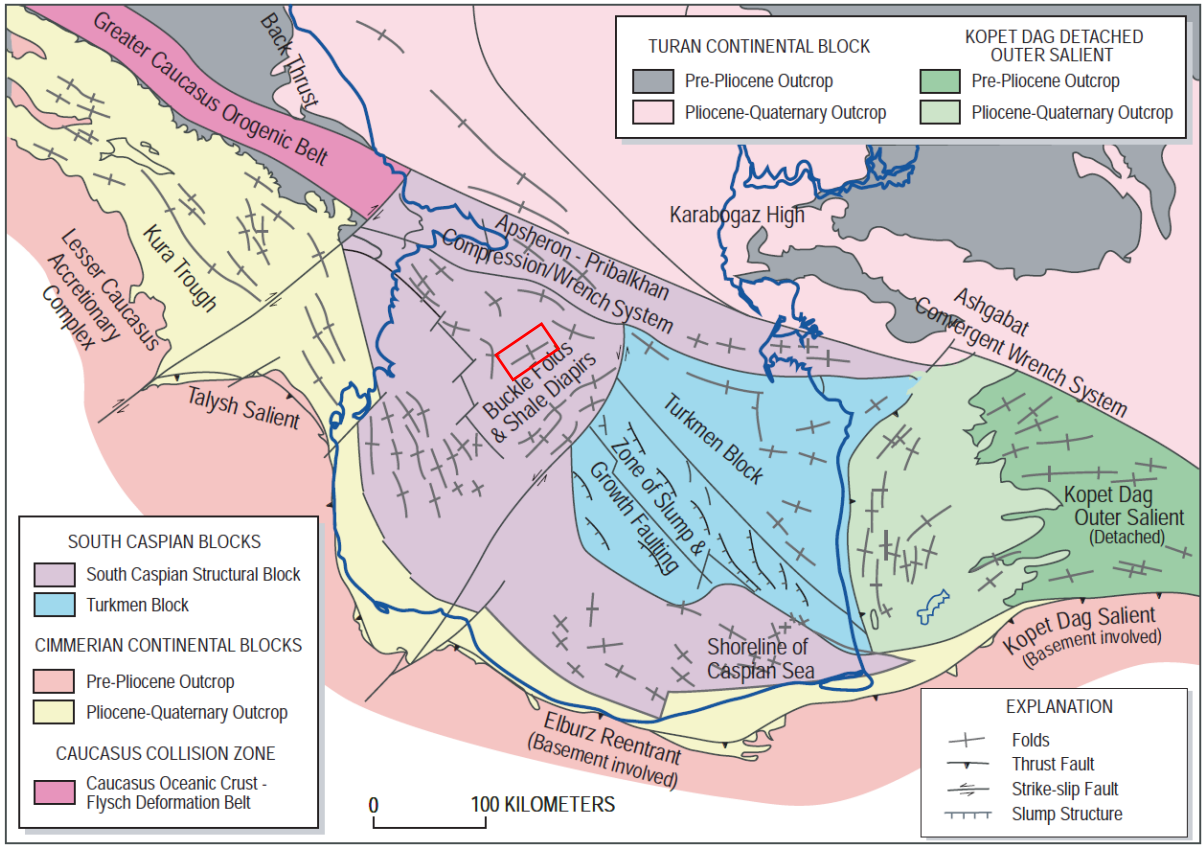


Figure 1.2: Structural elements of the South Caspian Sea and surrounding areas from Smith-Rouch 2006 (modified from Nalivkin, 1976; Adamia et al., 1977; Berberian and King, 1981; Philip et al., 1989 Devlin et al., 1999). The study area for this these is highlighted by the red box.

Geophysical data shows the basement of the South Caspian Basin to have high P-wave velocities of 6.5 – 7.1 km/s and has been interpreted by many authors to indicate 'oceanic like' crust (Rezanov and Chamo, 1969, Berberian, 1983, Zonenshain and Pichon, 1986, Priestley et al., 1994, Mangino and Priestley, 1994, Devlin et al., 1999, Jackson et al., 2002, Brunet et al., 2003, Knapp et al., 2004, Guest et al., 2007, Green et al., 2009, Egan et al., 2009, Kadirov and Gadirov, 2014, Abdullayev et al., 2017). The 'oceanic like' crust was likely formed in the Jurassic due to back-arc rifting, with evidence given from Jurassic aged volcanics (Berberian, 1983, Zonenshain and Pichon, 1986, Devlin et al., 1999, Brunet et al., 2003, Egan et al., 2009, Green et al., 2009, Abdullayev et al., 2017). It has also been postulated that the basin may have formed during the Cretaceous, as a pull-apart basin due to strike-slip in the Caucusus (Şengör, 1990). Gravimetric models show that the 'oceanic-like' crust exists in the northern part of the South Caspian Basin with continental crust surrounding the 'oceanic-like' crust (figure 1.3). Abdullayev et al. (2017) suggest that there is rift depocenter which is constrained to

the east by a block of continental crust, with a NE-SW feature that is possibly a transform fault (figure 1.4).

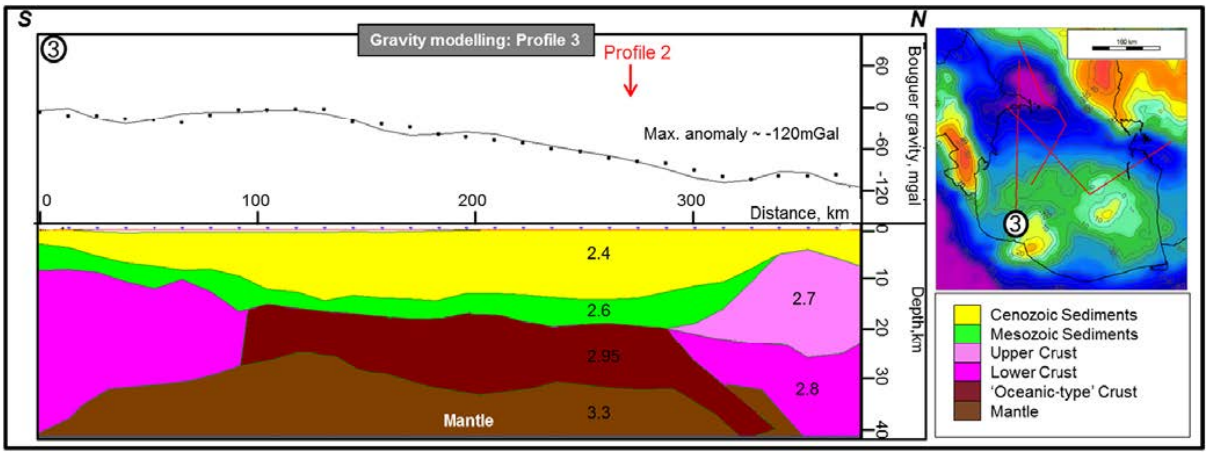


Figure 1.3: A section from Abdullayev et al. (2017) showing gravity modelling with observed (dotted line) and modelled (solid line) results. Density model below showing the oceanic crust in red brown. Density values are in g/cm^3. Inset: Bouguer gravity anomaly map, Red = high, blue = low.

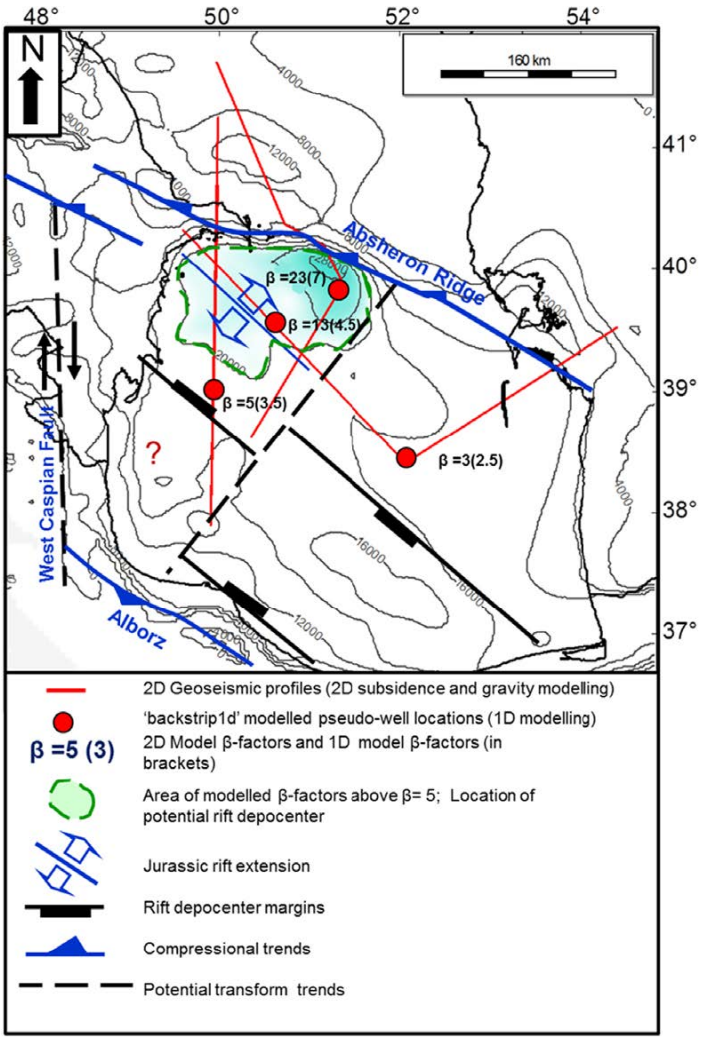


Figure 1.4: Interpretation of the crustal structure shown over the depth to basement map. The map shows a comparison of B-factors derived from modelling of 2D lines and 1D strain-rate inversion. From Abdullayev et al. (2017).

After the Jurassic back-arc rifting, there is a long period of post-rift thermal subsidence (Egan et al., 2009) until the Oligocene – Miocene 'Early Arabian' compression (Green et al., 2009, Egan et al., 2009) and then a later phase initiated in the Late Miocene – Early Pliocene, 'Late Arabian' compressional phase, when a significant increase in subsidence occurred (Khalilov et al., 1987, Allen et al., 2003, Brunet et al., 2003, Knapp et al., 2004, Egan et al., 2009, Green et al., 2009). This subsidence coincides with a significant tectonic reorganisation of the basin and an acceleration of the Arabian-Eurasian collision, causing building of mountain belts surrounding the basin as well as subduction of the basin beneath the Central Caspian in a subduction zone to the north of the basin known as the Absheron Ridge (Allen et al., 2002, Knapp et al., 2004, Khain et al., 2007, Hollingsworth et al., 2008, Egan et al., 2009, Green et al., 2009). The Absheron Ridge is formed by submarine NW-SE trending anticlines (Allen et al., 2002) described as an accretionary prism (Stewart and Davies, 2006,

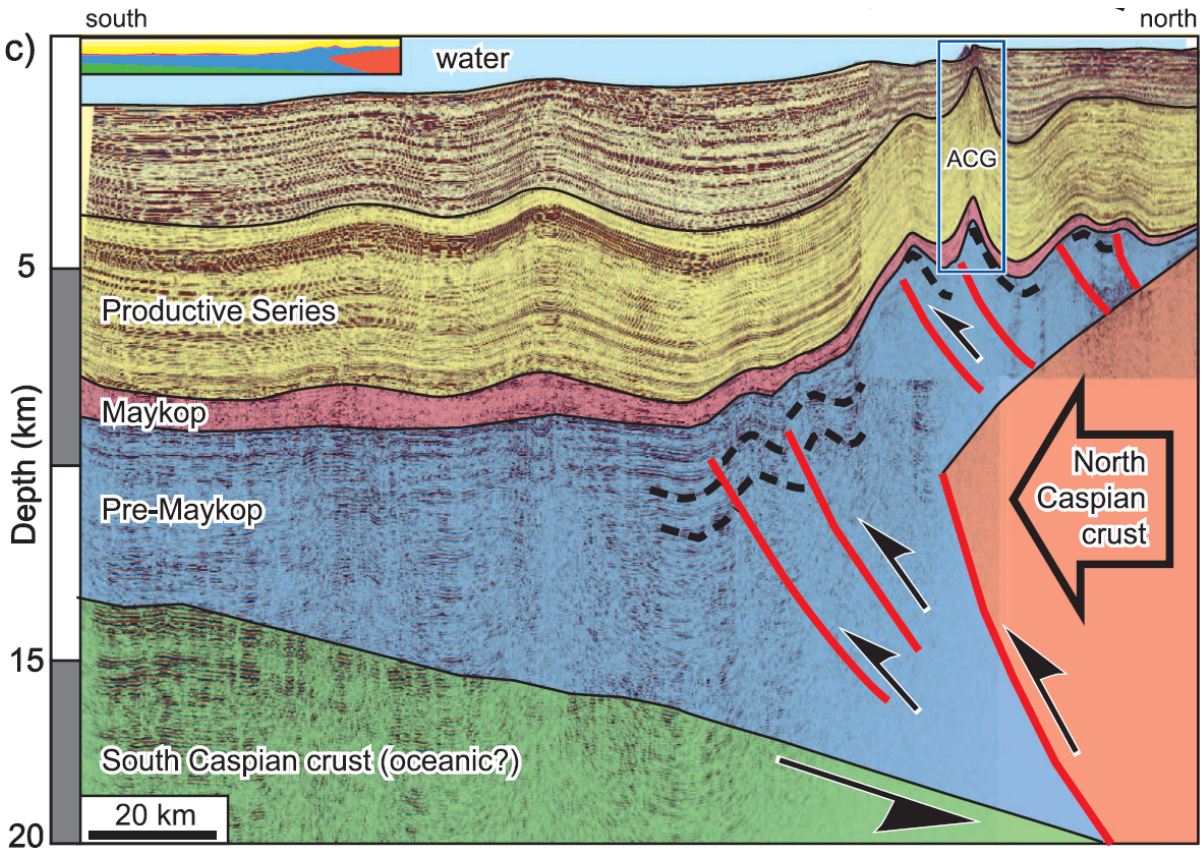


Figure 1.5: Regional 2D seismic line from SSW to NNE across the Absheron Ridge, where the ACG fold is located. The subduction of the ocean like crust and subsequent accretionary prism is interpreted. The deep-water central part of the South Caspian Basin is on the left of the image. The seismic section has 6x vertical exaggeration, with the inset top left showing no vertical exaggeration. From Stewart and Davies, (2006).

Green et al., 2009) (figure 1.5) where the sediment - basement contact is between 26 km – 28 km deep (Knapp et al., 2004).

The sedimentary succession deposited since the Jurassic is up to 20 km thick in the basin (Nadirov et al., 1997, Allen et al., 2003), however the uppermost 10 km has been deposited within the last 6 My (Devlin et al., 1999) as a result of the acceleration of the Arabian-Eurasian collision. Previous studies have attempted to understand how rapid subsidence could have developed and created the accommodation space for such a thick package of sediment. Allen et al. (2002) use back stripping to suggest that the Pliocene to recent subsidence rate of the basin is caused by the subduction of the 'oceanic like' South Caspian Basin crust beneath the Central Caspian Basin, with subsidence rates 1.5 – 10 times that of typical foreland basins. The authors suggest that the faster subsidence rates relative to typical foreland basins is due to the rigidity of the subducting South Caspian basement. More recent studies have used modelling to explain the rapid subsidence rate and determine that the subsidence is due to thermal subsidence and sediment loading of the 'oceanic like' crust due to the rapid deposition of the Pliocene to recent succession as a result of a 1 km – 2 km base-level fall approximately 6 Ma (Green et al., 2009, Egan et al., 2009, Kadirov and Gadirov, 2014, Abdullayev et al., 2017) Whilst Green et al. (2009) do not include the effect of tectonics or subduction in their study, Egan et al. (2009), Kadirov and Gadirov (2014) and Abdullayev et al. (2017) are all in agreement that subduction and uplift of the surrounding mountain belts increase the total subsidence (Brunet et al., 2003), causing local variations in subsidence, in particular an increase directly south of the subduction zone under the Absheron Ridge.

The increase in shortening that occurs in the Pliocene continues to the present-day, with uplift of the mountain belts surrounding the basin, the Greater Caucasus, Talysh, Kopeh Dagh and Alborz Mountains (Dewey et al., 1986, Jackson et al., 2002, Allen et al., 2003, Brunet et al., 2003, Knapp et al., 2004). Current earthquake focal plane solutions and GPS data indicate that the basin is moving north with respect to the Eurasian Plate and south-west with respect to the Iranian Plate (Jackson et al., 2002, Vernant et al., 2004, Reilinger et al., 2006, Copley and Jackson, 2006) which will lead to the destruction of the basin by subduction or under thrusting (Priestley et al., 1994, Jackson et al., 2002). Jackson et al. (2002) use earthquake focal mechanisms to suggest that the South Caspian Basin moves 7-10 mm/yr

north of 300° relative to Eurasia and 13-17 mm/yr in a direction of 210° relative to Iran. However, the authors do not include GPS data within their measurements, leading to an overestimation of the motion of the basin relative to Iran (Allen et al., 2004). Copley and Jackson (2006) include GPS measurements (Vernant et al., 2004, Reilinger et al., 2006) to interpret the South Caspian Basin to move 11 ± 2 mm/yr towards 330° - 340° relative to Eurasia and 6 – 8 mm/yr relative in a direction of 225°. Recent plate motions calculated using slip-rates along a large 200 km long dextral strike-slip fault in the Kopeh Dagh show that the Caspian moves 10.4 ± 1.1 mm/yr in a direction of 333° ± 5° relative to Eurasia and moves 4.8 ± 0.8 mm/yr in a direction of 236° ± 14° relative to Iran (Walker et al., 2021) in-line with the results of Copley and Jackson (2006) (figure 1.6).

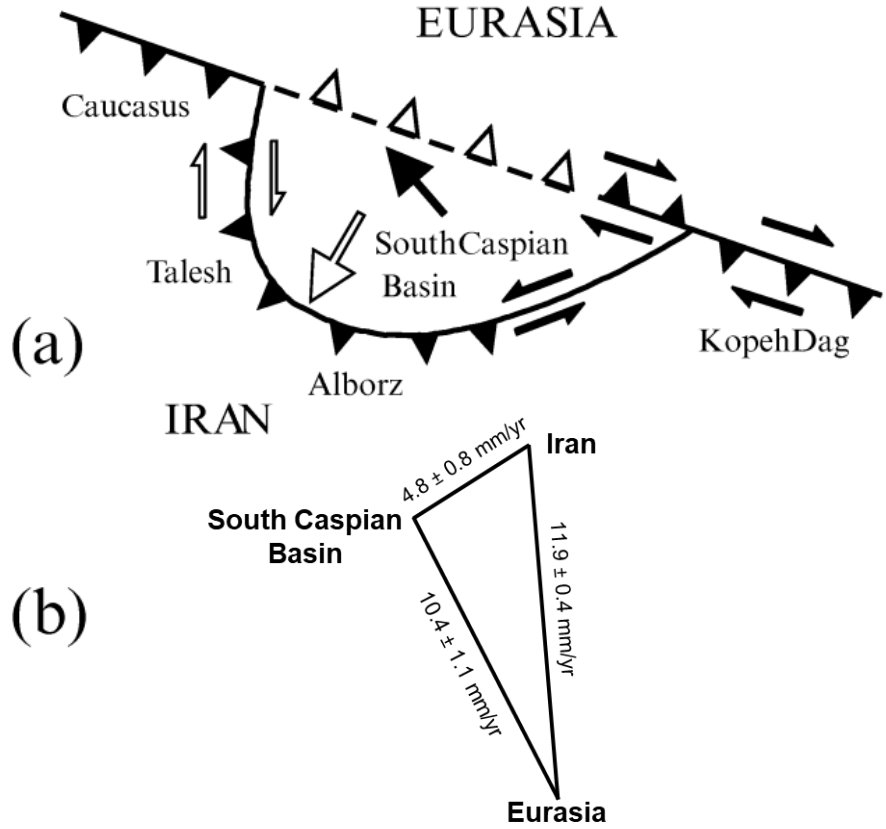


Figure 1.6: Sketches describing the present-day active tectonics of the South Caspian Basin from Jackson et al. (2002). a) The present-day configuration of the basin showing S to SW underthrusting in the Talysh, Alborz and Greater Caucusus and north dipping thrusting in the centre, under the location of the Absheron Ridge, where the South Caspian Basin is undergoing subduction. The white arrow indicates the relative motion of the basin relative to Iran, and the black arrow with respect to Eurasia. b) shows the velocity triangle between Iran, Eurasia and the South Caspian Basin, modified from Walker et al. (2021)

The presently active tectonics of the South Caspian Basin can be inferred using earthquake locations within the surrounding mountain belts. Although located within the centre of a zone of continental convergence, the basin is largely aseismic (Priestley et al., 1994, Jackson et al., 2002), with

deep earthquakes focussed beneath the Absheron Ridge most likely due to subduction of the South Caspian on the northern margin (Khalilov et al., 1987, Priestley et al., 1994, Jackson et al., 2002, Knapp et al., 2004) (figure 1.7). Shallow earthquakes occur within the Alborz and Kopeh-Dagh mountains and can happen deeper in the Talysh (Jackson et al., 2002) (figure 1.8). Within the Alborz, left-lateral strike slip faults are presently active (Jackson et al., 2002, Allen et al., 2003) whilst N-S shortening is accommodated by thrust faults as the Iranian Plate is trust over the South Caspian Basin (Allen et al., 2004). The Talysh Mountains, towards the west of the basin, are formed as a fold and thrust belt, with active thrusts trending N-S and dipping west, showing that the South Caspian Basin is over-thrust by the basement of the Talysh (Jackson et al., 2002, Allen et al., 2004, Allen et al., 2003). The Kopeh-Dagh to the east of the basin trends NW-SE with focal mechanisms showing strike slip motion as well as reverse faulting (Jackson et al., 2002, Allen et al., 2003). The focal mechanisms show evidence of

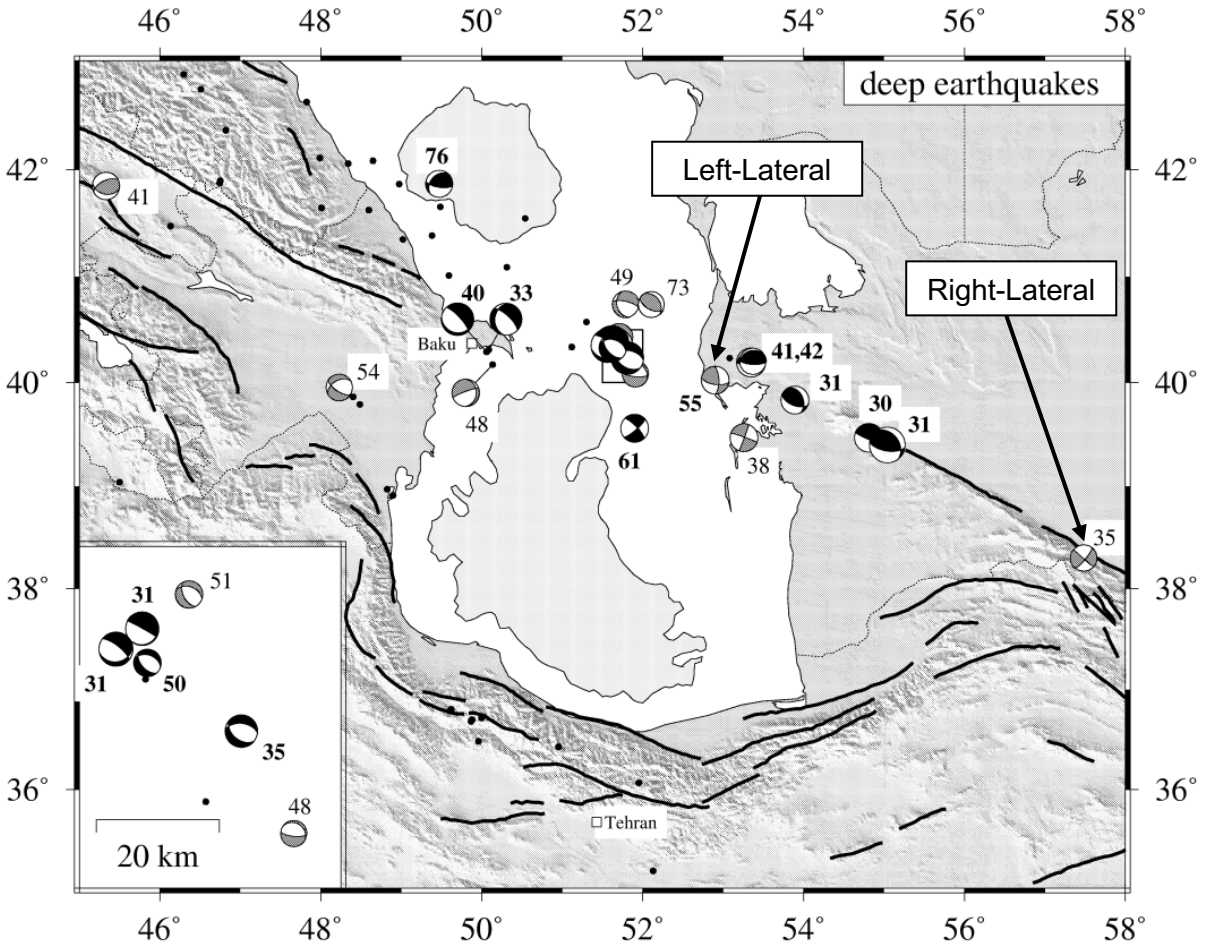


Figure 1.7: The deep earthquakes of the South Caspian region from Jackson et al. (2002). Black spheres show events deeper than 30km (km depths in bold). Grey spheres are Harvard CMT solutions with reported depths of >33km, numbers next to the spheres are depths in km from Engdahl et al. (1998). Small circles are earthquakes deeper than 60km between 1964 – 1998 from Engahl et al. (1998). The inset is an enlarged area, shown by the black box.

left lateral motion in the west of the Kopeh-Dagh and right-lateral motion in the eastern mountain range of the Kopeh-Dagh (Jackson et al., 2002, Ritz et al., 2006, Shabanian et al., 2009, Robert et al., 2004). The right-lateral motion can be observed in outcrop data along the strike-slip faults (Walker et al., 2021).

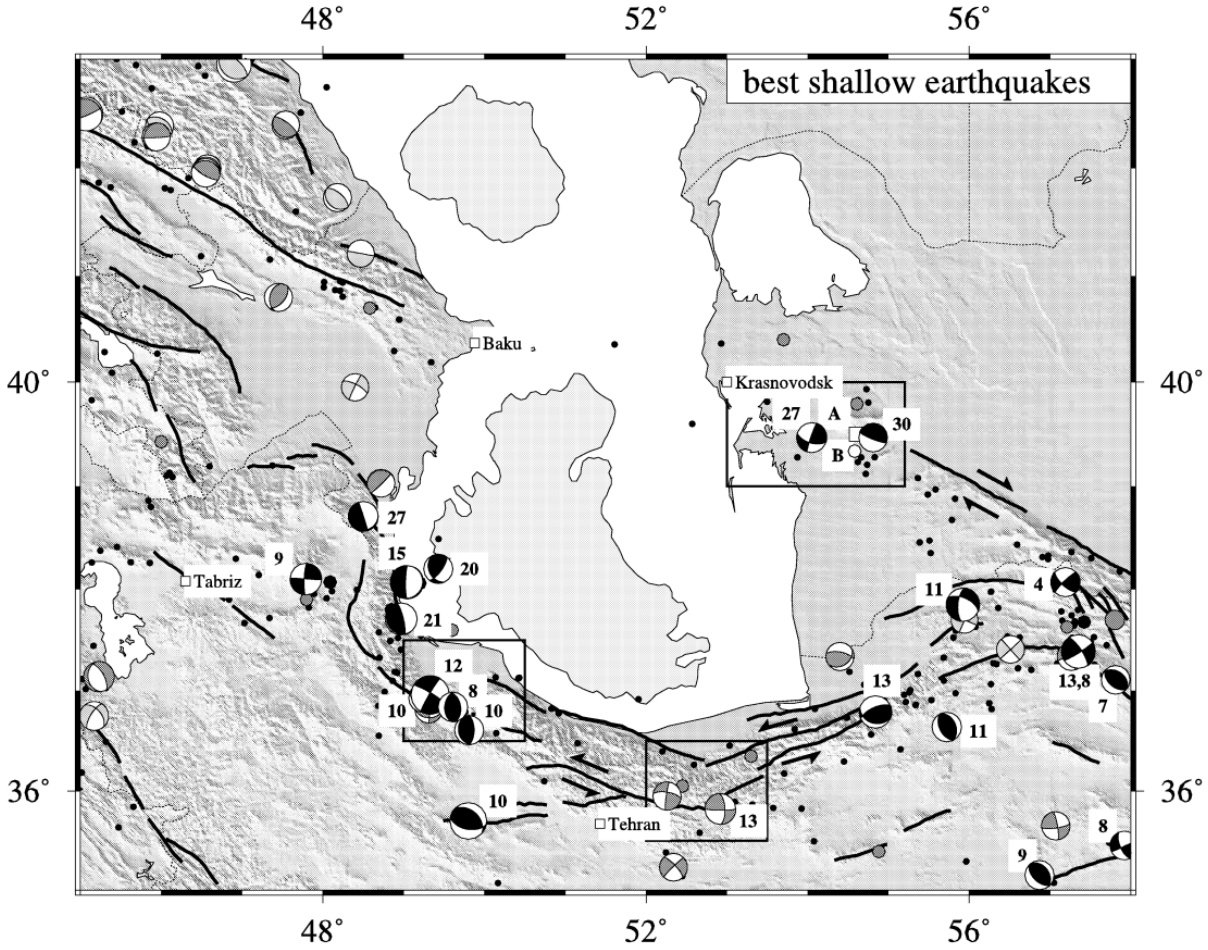


Figure 1.8: Map of the best quality shallow earthquake focal mechanisms in the South Caspian Region, from Jackson et al. (2002). Black focal spheres show earthquakes that are less than 30 km with depths shown in bold. Grey spheres are Harvard centroid moment tensor solutions for events $M_w \geq 5.3$. Light grey spheres show focal mechanisms recorded from long-period instruments. Small black circles are hypocentres of 1964 - 1998 from Engahl et al. (1998). Large grey and black circles are epicentres of earthquakes > M_s 6.0 and > M_s 7.0 for large sized circles from 1900 to 1962 and post-1963. A and B in the east are the epicentres of the 1895 Krasnovodsk and the 1983 Kum Dag earthquakes respectively. The grey region offshore shows bathymetry greater than 500m.

The initial Arabian-Eurasian collision may have taken place as long as 40 Ma (Hempton, 1987) or earlier, 12 Ma (Dewey et al., 1986). Both ages are significantly earlier than the present-day tectonic setting and the widespread folding within the basin which occurred at the time of increased Alpine compression in the Late Pliocene (Aliev, 1960, Devlin et al., 1999, Abdullayev, 2000, Green et al., 2009). Some studies have suggested that the greatest folding intensity in the basin occurs in the

Quaternary (Narimanov et al., 2019). The age of the present-day tectonic origin and relative westward movement of the basin has been debated. Allen et al. (2004) suggest westward movement occurred 7 - 3 Ma, in-line with estimates of 5 ± 2 Ma by Axen et al. (2001) and 3.4 Ma by Devlin et al. (1999). An earlier date has been postulated of 10 Ma, based on strike-slip faulting in the Kopeh-Dagh (Hollingsworth et al., 2008). A later age for the onset has been more widely reported. Ritz et al. (2006) suggest that the basin rotated clockwise and moved NW relative to Eurasia approximately 1.5 Ma adding that the subduction northward started in the Mid-Miocene and Pliocene, with a westward motion associated with a clockwise rotation added during the Pleistocene (Ritz, 2009). Cifelli et al. (2015) use paleomagnetic data from the Alborz Mountains to agree with the more recent timing of westward motion and rotation, suggesting it began 3 - 0.7 Ma. Mattei et al. (2019) use paleomagnetic data from the Kopeh-Dagh to agree with this conclusion, suggesting that the westward motion initiated as early as 2 Ma. More recently, Walker et al. (2021) also agree with the later timing, suggesting a time of 5 - 3 Ma, based on strike-slip and shortening rates of the 200 km long Main Kopeh Dagh Fault. Although it is generally agreed that the later timing is most likely, these studies emphasise the challenges of understanding the structural complexity and deformation history of the South Caspian Basin.

Fold trace orientations vary across the basin, as do fold geometries (Jackson et al., 2002, Allen et al., 2003) in response to the active tectonics of the mountain belts. The main fold orientations observed generally trend parallel to the large mountain ranges onshore and continue offshore: N-S in the west parallel to the Talysh Mountains, NW-SE in the Greater Caucasus and along the Absheron Ridge and E-W parallel to the Alborz in the south (figure 1.9). Within the deep-water part of the basin, folds trend NW-SE and NE-SW. The NE-SW trend of the large folds in the centre of the basin may be due the inversion of a Jurassic rift transform fault (Abdullayev et al., 2017). The folds are documented as large buckle folds detached upon a shale detachment, the Oligo - Miocene Maykop Formation (Devlin et al., 1999, Allen et al., 2003, Santos-Betancor and Soto, 2015) (figure 1.10).

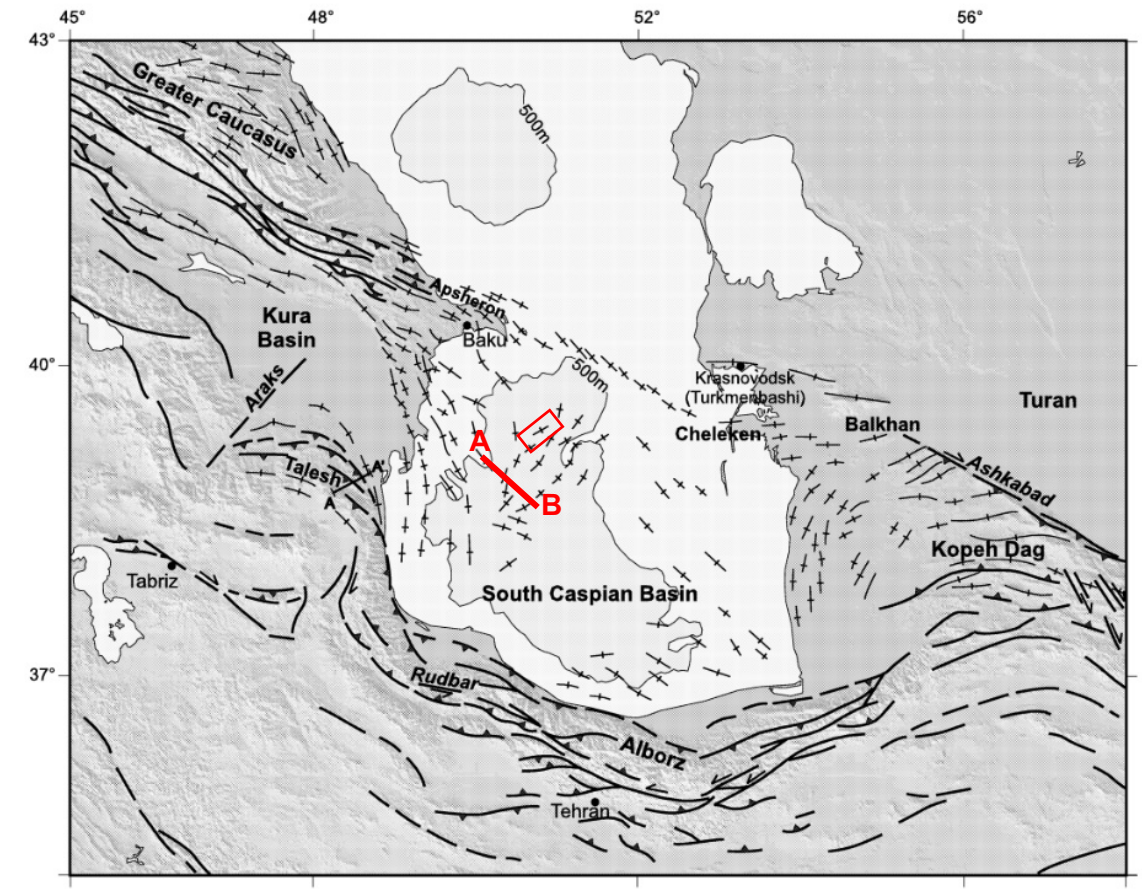


Figure 1.9: Map of the structural orientations of the South Caspian Region. From Jackson 2002. The study area for this thesis is shown by the red box.

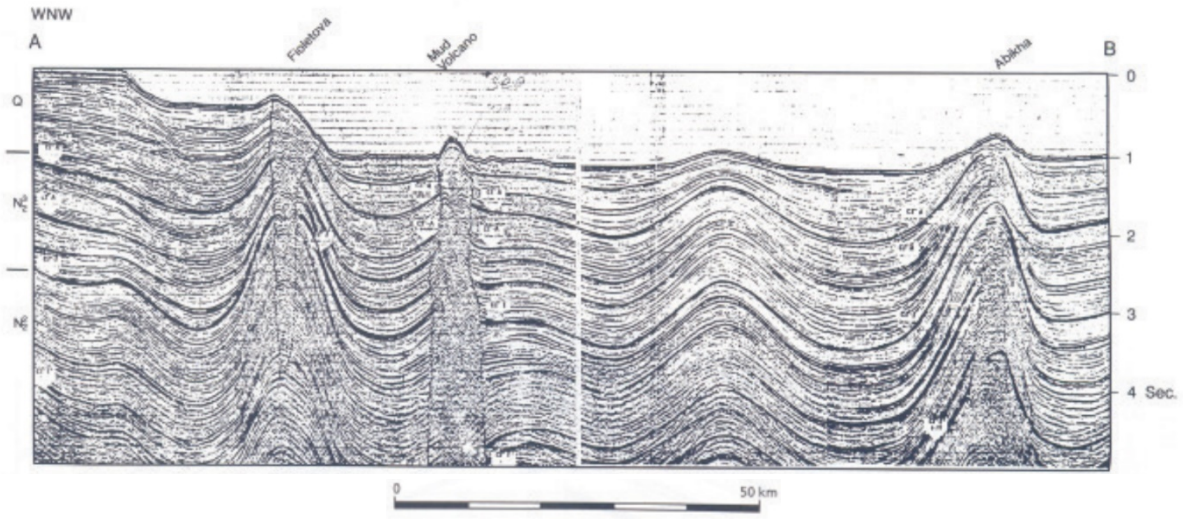


Figure 1.10: Regional 2D seismic line across the centre of the South Caspian Basin showing fold structures and mud volcanoes. From Narimanov (1997). Location on figure 1.9.

Whilst there have been many studies on the regional tectonics of the South Caspian Basin, there have been very few in depth studies on growth of individual folds within the basin using 3D seismic data. Fowler et al. (2000) describe the offshore Shah Deniz fold structure in the north of the basin, 70 km southeast of Baku using 3D seismic reflection data. They interpret a deep pre-Oligocene thrust fault coring the structure along its strike as well as a reverse fault that detaches into the Maykop shale. Extensional crestal faults sole out into Pliocene Surakhany Formation evaporites. However, the most important studies to date were completed by Santos-Betancor and Soto (2015) and Sánchez-Borrego et al. (2016). Santos-Betancor and Soto (2015) who used 3D seismic reflection data imaged over the Kurdashi-Araz Deniz fold structure, offshore the western margin of the basin, to understand the fold growth through time. They demonstrate that the 7 km wavelength fold has two culminations cut by mud diapirs, but rather than being symmetrical it has an east-vergent forelimb and has thrusts on both limbs. The authors proposed that the detachment fold structures developed above a linked normal fault system with a component of dextral strike-slip motion, and that the later phases of the growth were enhanced by flow of mud along the strike of the fold into the structures.

1.2.3 Stratigraphy

Since the formation of the South Caspian Basin in the Jurassic, there has been 10 - 15 km of basin fill (Brunet et al., 2003), reaching a maximum of 28 km (Knapp et al., 2004). In this thesis I focus on the Pleistocene to recent successions (figure 1.11).

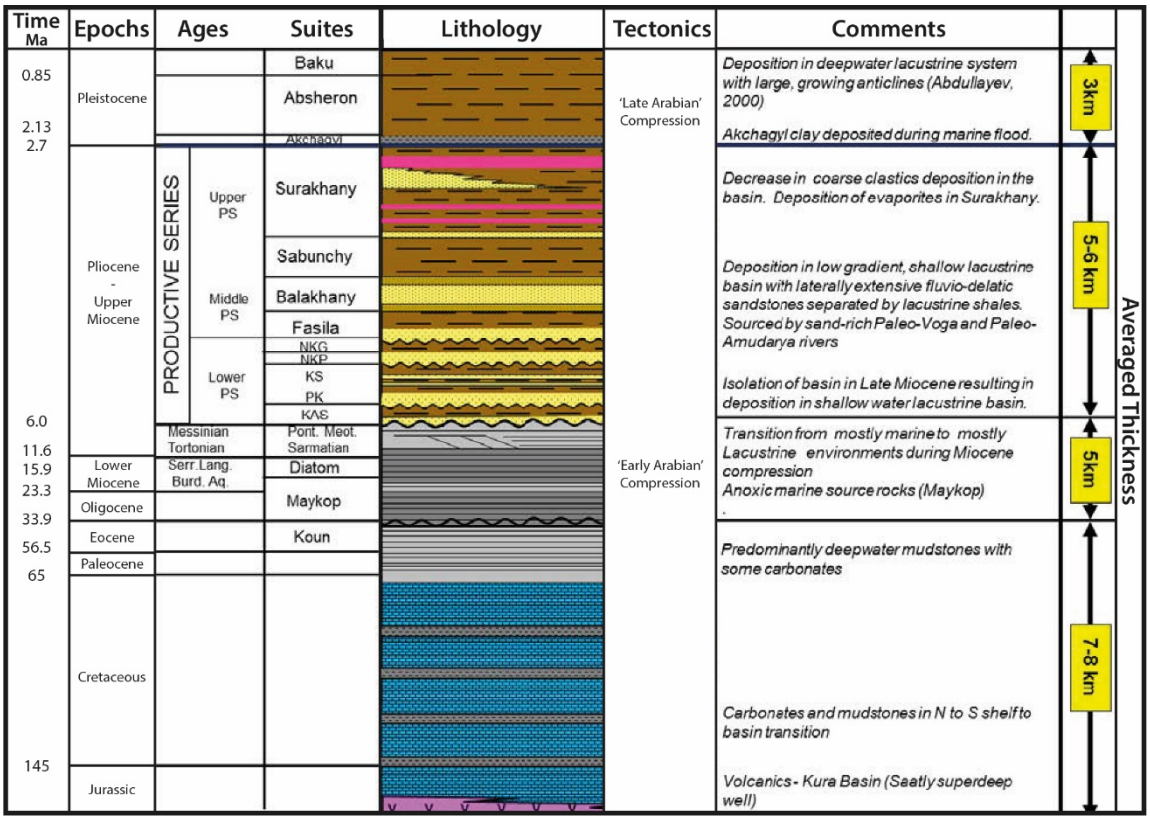


Figure 1.11: Stratigraphic column for the South Caspian Basin with major geological events and local stratigraphic stages (suites) indicated. Modified rom Abdullayev et al. (2017). Stratigraphic ages are from Popov et al. (2006), Hudson et al. (2008), Lazarev et al. (2019) and Van Baak et al. (2019).

From the basin formation to the Neogene, deposition of calcareous and diatomaceous black shales occurred as the basin had episodic marine restriction (Abrams and Narimanov, 1997). The Jurassic to Cretaceous sequence is not encountered offshore since it is too deep, with the first mappable horizon of the basin interpreted to be the Top Cretaceous event (Green et al., 2009). The thickness of sediment up to the base Oligocene ranges from 5 km in the basin to 20 km to the south of the Absheron Ridge (Green et al., 2009). During the Late Oligocene, the South Caspian was still within a marine setting, connected to the Black Sea (Steininger and Rögl, 1984) in which the regional Oligo-Miocene Maykop and Diatom suites were deposited. The Maykop Formation consists of a series of dark grey, organic rich shales (Jones and Simmons, 1996, Inan et al., 1997, Hudson et al., 2008). The formation

reaches up to 3000m thick in the basin (Smith-Rouch, 2006) and shows inconsistent thickness in the centre of the basin, varying from 1500m to 3000m (Green et al., 2009) (figure 1.12).

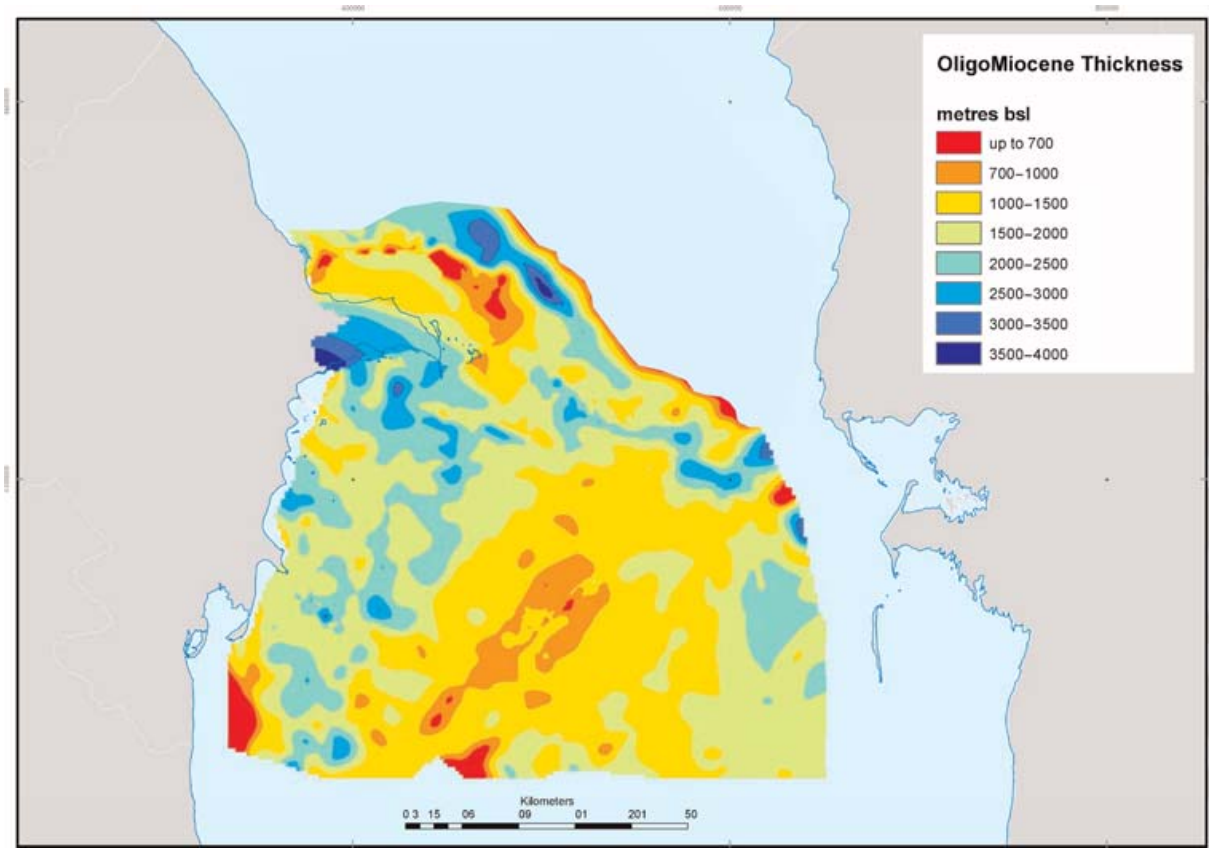


Figure 1.12: Thickness map of the Oligo-Miocene sequence. This is a depth isochore map between the Base Productive Series depth surface and the near-Base Maykop depth surface. From Green et al. (2009).

In the Late Miocene there was a significant change in the depositional system, with the complete isolation of the basin from the global ocean between 6 – 5.3 Ma and a significant drop of base level, between 600m and 1500m (Kerimov et al., 1992, Jones and Simmons, 1996, Reynolds et al., 1998, Green et al., 2009, Abdullayev et al., 2012, Forte and Cowgill, 2013). This period coincides with the tectonic reorganisation of the basin as the mountain belts grew due to the Neogene plate convergence (Jackson et al., 2002, Brunet et al., 2003, Vernant et al., 2004). Erosion from surrounding mountain belts caused a significant increase in sedimentation to the basin, which was deposited into a land-locked topographic depression with a base-level 1.5 km below the global sea level (Green et al., 2009). A package of fluvio-deltaic sandstones up to 6 km thick were deposited, known as the Productive Series. The Productive Series was deposited at a rate of 3.9 km/My in the centre of the basin, with a large

increase in sedimentation rate occurring at 4 Ma, concordant with a change in the global climate at the time (Peizhen et al., 2001) and enhanced by the tectonic reorganisation and isolation of the Caspian since 5.38 Ma (Abdullayev et al., 2018). The sediments were sourced primarily from the, the Palaeo-Volga River systems, as well as from the Palaeo-Kura River to the west and the Palaeo-Amu-Darya River to the east (Reynolds et al., 1998, Morton et al., 2003, Hinds et al., 2004, Smith-Rouch, 2006, Abreu and Nummedal, 2007) (figure 1.13).

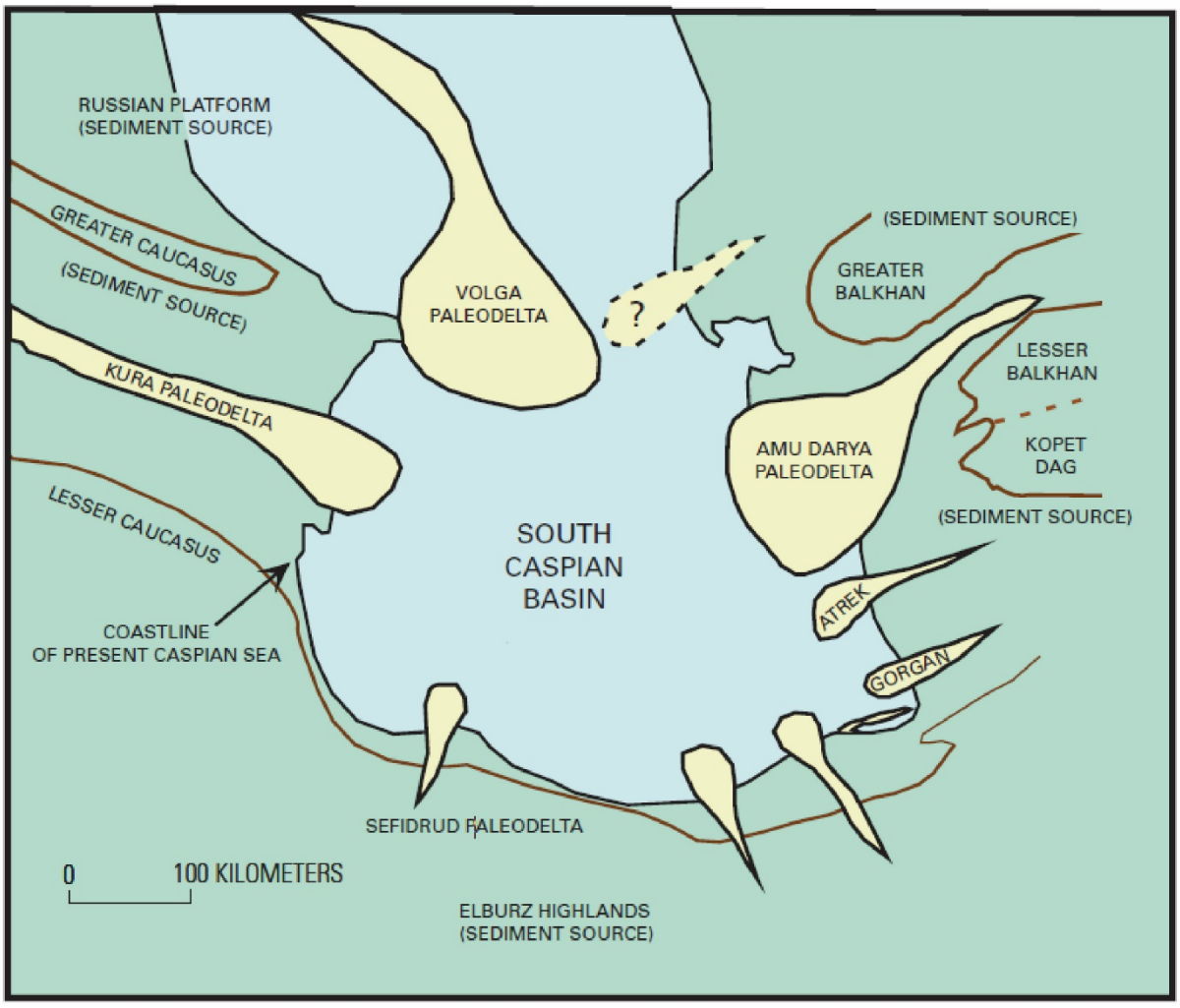


Figure 1.13: Schematic map of possible sources of sediment deposited in palaeodeltas prograding into the South Caspian Basin during deposition of the Pliocene Productive Series. From Smith-Rouch (2006).

At the time of the base-level shift, the Palaeo-Volga River system migrated 700 km south and deposited sediment into the South Caspian Basin (Green et al., 2009). The early deposition of the Productive series was dominantly sourced by the Palaeo-Volga, with an increased source from the Palaeo Kura and Palaeo-Amu Darya in the youngest part of the succession (Green et al., 2009,

Abdullayev and Leroy, 2016). The youngest formation of the Productive Series, the Surakhany Formation, is up to 2.5 km thick in the centre of the basin and is deposited as a fine grained succession of thick shales with evaporites deposited in the centre of the basin, indicating a playa lake environment (Green et al., 2009) (figure 1.14).

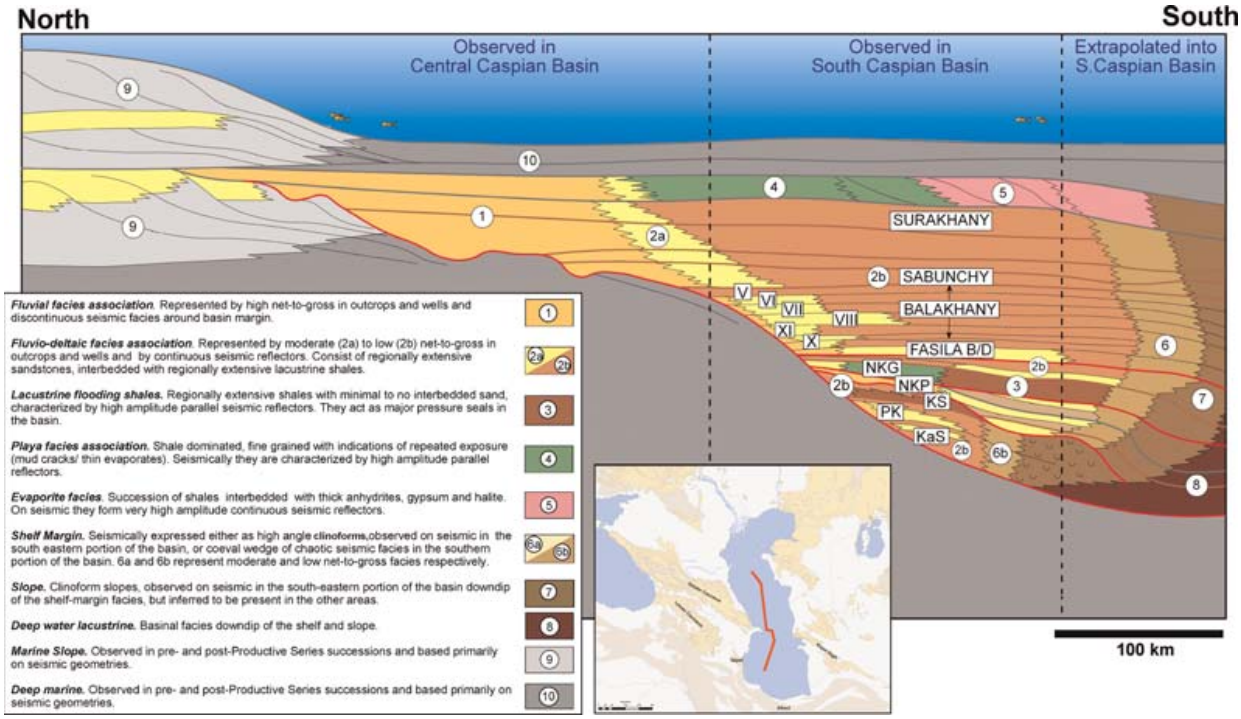


Figure 1.14: Depositional model for the Productive Series from Green et al. (2009). The location is shown on the inset map. The evaporite facies of the Surakhany within the centre of the South Caspian Basin are shown in green (4) and pink (5).

In the Late Pliocene, after deposition of the Surakhany Formation, the end of the Productive Series, a hemi-marine system was developed as the Akchagylian Sea flooded the basin (Popov et al., 2006). The age of this marine transgression is debated, with estimates of 3.4 Ma (Morton et al., 2003), 2.6 Ma (Reynolds et al., 1998, Hinds et al., 2004, Abdullayev et al., 2012) or more recently 2.7 Ma (Van Baak et al., 2019) and 2.75 Ma (Hoyle et al., 2021, Vasiliev et al., 2022). During the marine incursion, up to 500 m of deep-water sediments were deposited within the centre of the basin, known as the Akchagyl Formation (Popov et al., 2006). At the top of the Akchagyl, a regression took place as the basin became a deep-water lake, similar to the present-day lake, with water depths up to 1000 m (Abdullayev, 2000, Krijgsman et al., 2019) (figure 1.15). The regression coincides with the timing of the increase in Alpine-Himalayan compression and the formation of the folds within the basin (Devlin et al., 1999, Fowler et al., 2000, Abdullayev, 2000, Allen et al., 2002, Green et al., 2009, Egan et al.,

2009). The dating of this has been suggested as 1.8 Ma (Green et al., 2009) or more recently 2.13 Ma (Lazarev et al., 2019, Lazarev et al., 2021, Vasiliev et al., 2022) and 2.46 Ma (Hoyle et al., 2021).

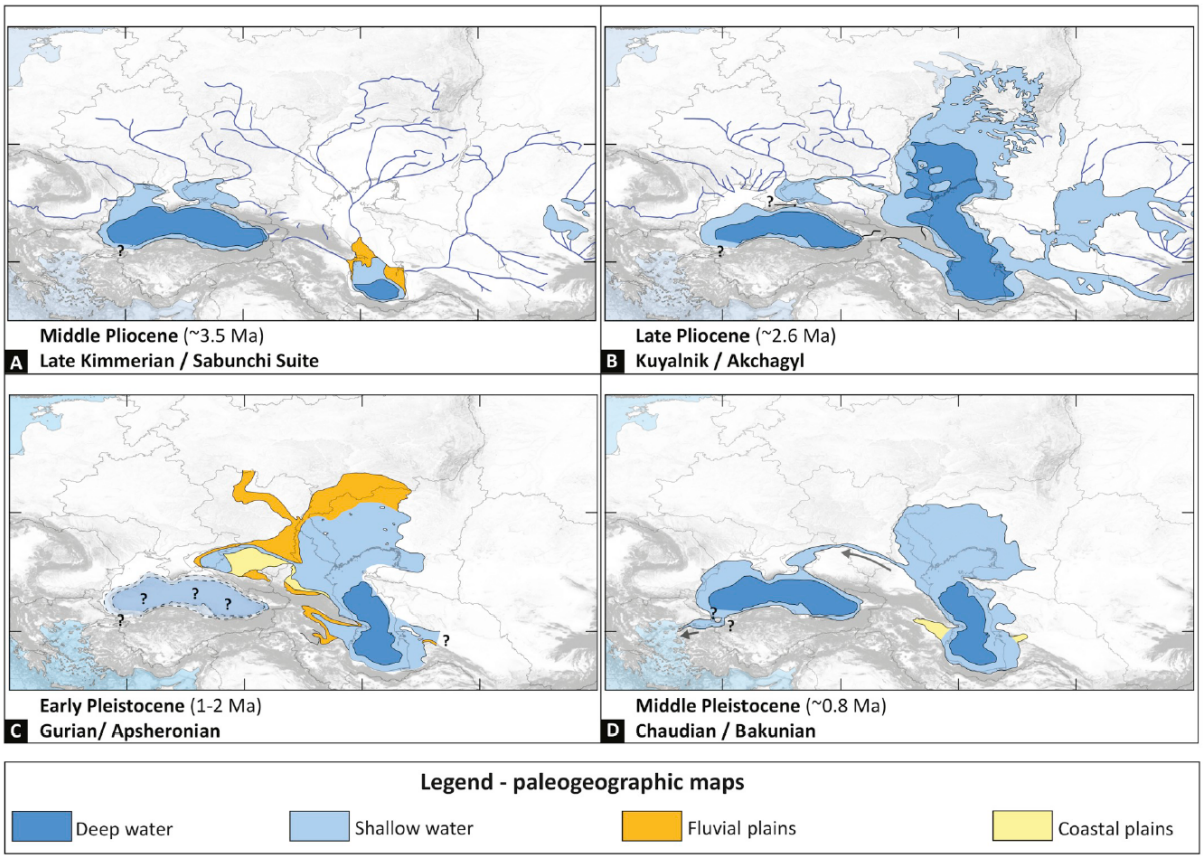


Figure 1.15: Paleogeographic maps for the Plio-Pleistocene Pontocaspian region. A) Middle Pliocene Productive Series; B) Late Pliocene Akchagyl; C) Early Pleistocene Absheron; D) Middle Pleistocene Bakunian. The South Caspian can be seen as deep water from the Akchagyl through to the present-day. From Krijgsman et al. (2019).

The thinning of strata deposited over the growing folds can be seen within the Pleistocene to Recent sequence (Green et al., 2009) (figure 1.16). Regional 2D seismic lines show large clinoforms and channels up to 15 km wide on the Turkmenistan Shelf in the east, likely supplied by the Palaeo-Amu Darya River (Abdullayev, 2000, Abreu and Nummedal, 2007) (figure 1.17). Within the Absheronian, deep-water turbidites were deposited in the basin (Abdullayev, 2000) (figure 1.18). The deposition is significantly affected by lake level and climate, controlled by glacial periods and orbital forcing (Abreu and Nummedal, 2007, Forte and Cowgill, 2013) (figure 1.19). The deep-water turbidites are known as the Absheron Formation and are the primary sequence studied within this thesis.

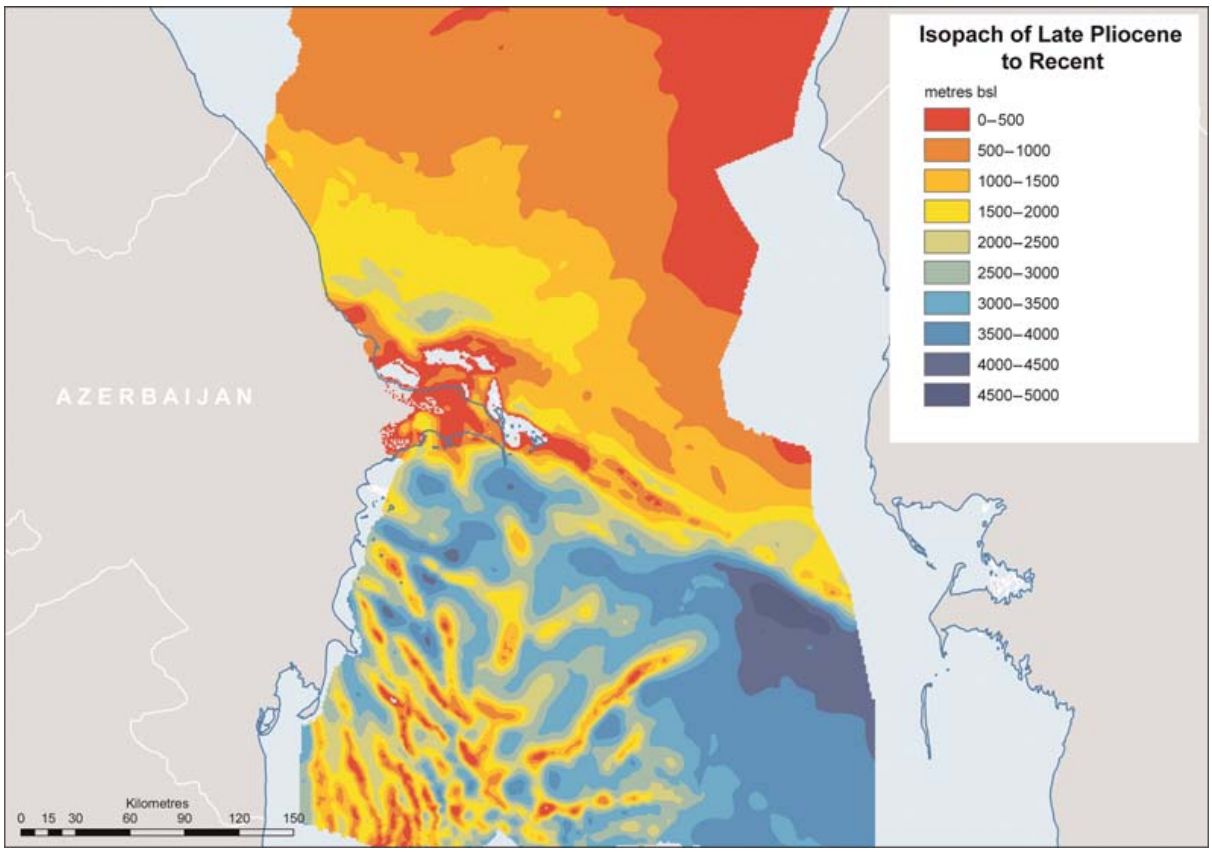


Figure 1.16: Thickness map of the Late Pliocene–Recent sequence. This is a depth isochore map constructed between the present-day Caspian seafloor and the Top Productive Series depth surfaces. Thinning over the crests of the folds in the South Caspian Basin can be seen. From Green et al. (2009).

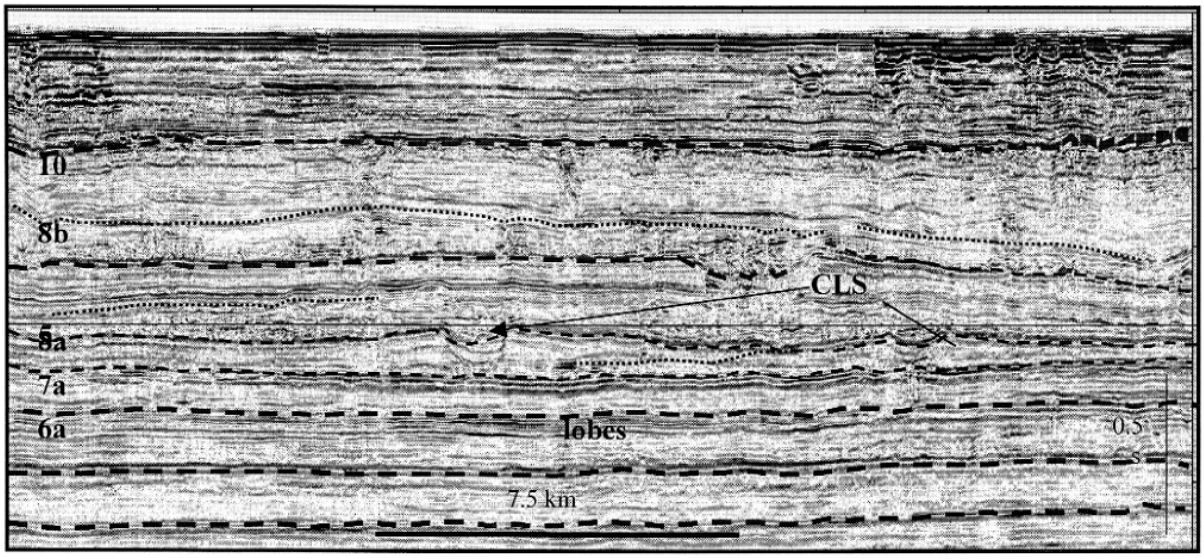


Figure 1.17: Unlocated seismic line in the Turkmenistan shelf in the east of the South Caspian Basin, showing channel systems that supplied sediment to the deep-water turbidites of the Pleistocene to Recent stratigraphy. CLS = channel levee system. From Abdullayev (2000).

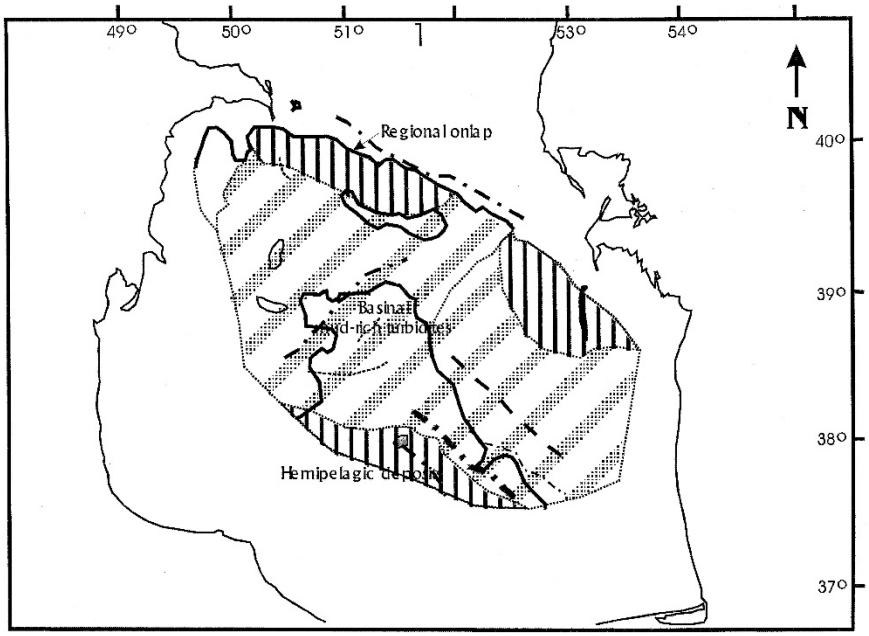


Figure 1.18: Seismic facies and depositional systems map of the base of the Pleistocene Absheron Formation. Depositional infill is uniform in character and interpreted as onlap-fill mud-rich turbidites (diagonal dotted pattern) and hemipelagics (vertical solid lines). From Abdullayev (2000).

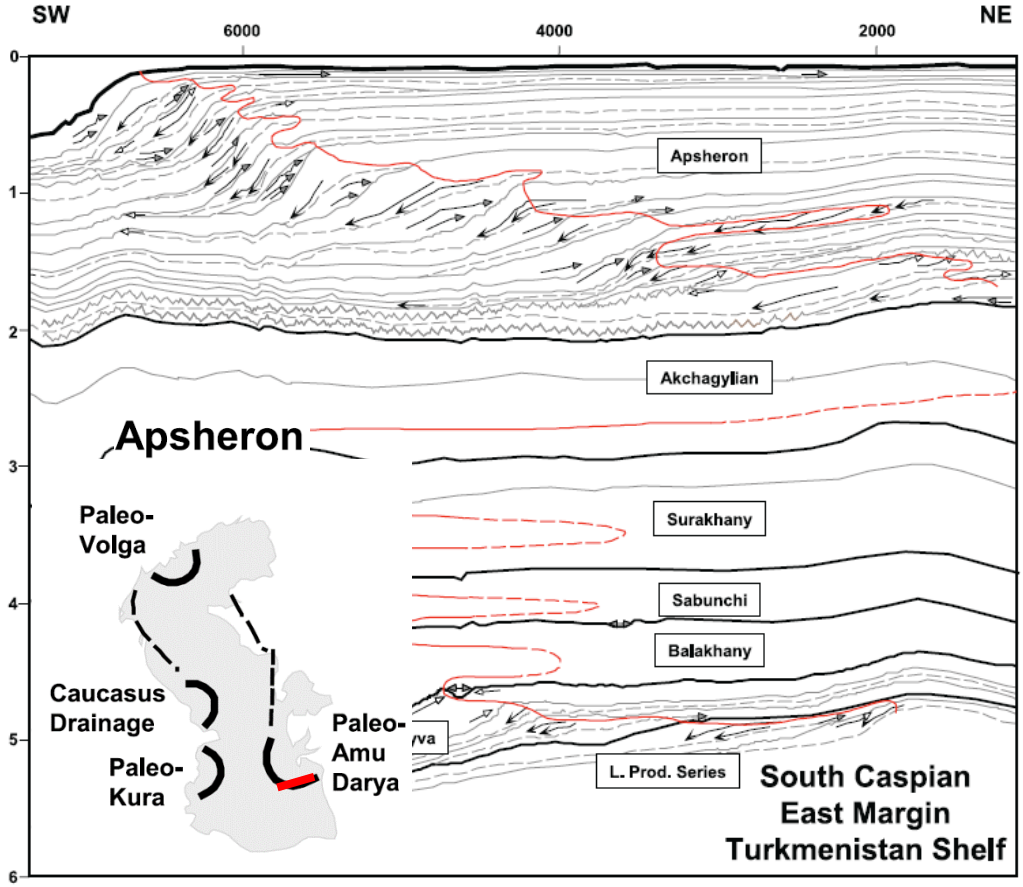


Figure 1.19: Line drawing of an interpreted seismic profile from the Eastern margin of the South Caspian Basin, showing progradation of the Palaeo-Amu Darya in the Absheron to Recent. Location is shown in red on the inset map. Offlap-break curve is shown in red (dashed line indicates the uncertainty in the location of the offlap break). Inset map shows the location of the river deltas during the Absheronian, with the Palaeo-Amu Darya further west than the present-day. Grey arrows show onlap. Black arrows show downlap and white arrows show truncation. From Abreu and Nummedal (2007).

The section from the top of the Absheron to the present-day is dominated by mass transport deposits in the central part of the basin, composed of slides and slumps, with turbidites in the southeastern part (figure 1.20), separated by a large NE-SW trending structure known as Abikha or Alov (Abdullayev, 2000). These deposits are initially deposited within the Bakunian and therefore in this thesis I describe the sequence as the Bakunian Formation. The change in facies within the centre of the basin from the deep-water turbidites of the Absheron to the mass transport deposits of the Bakunian may be influenced by the re-routing of the Palaeo Amu-Darya from the Caspian Sea to the Aral Sea, causing a decrease in clastic input (Yunov and Martirosyan, 1996). 3D seismic data from the deep-water structures within the South Caspian Basin show many types of mass transport deposits around the folds and that they are sourced from along the basin slope as well as from the flanks of growing anticlines (Richardson et al., 2011, Santos-Betancor et al., 2014).

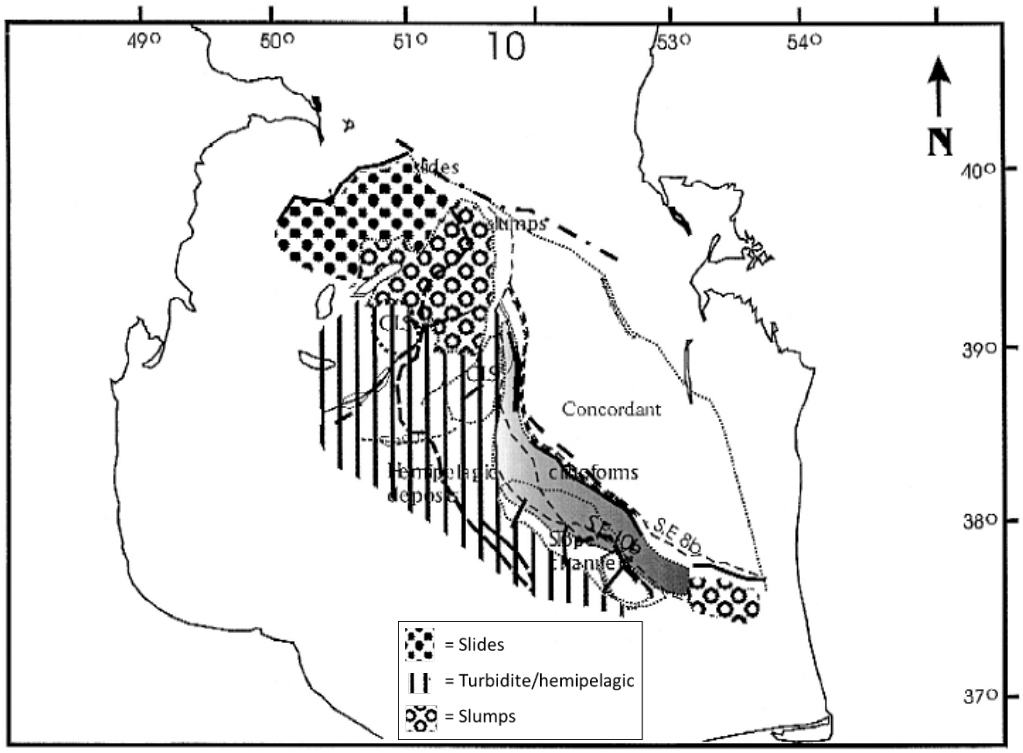


Figure 1.20: Seismic facies and depositional system map of facies within the Bakunian. Thick clinoforms were formed in the southeast with slides and slumps (black and white dotted area) in the deep part of the basin. Drape facies and turbidite infill are vertical solid lines. From Abdullayev (2000)

1.3 Shale Tectonics

Detachment fold geometries have been widely documented with much work published in the 1990s (Dahlstrom, 1969, Jamison, 1987, Dahlstrom, 1990, Epard and Groshong Jr, 1993, Epard and Groshong Jr, 1995, Poblet and McClay, 1996) with these folds applied to either salt or mobile shale detachments. Shale tectonics was documented to have many similarities with salt tectonics, for example, mud can act as a detachment layer and cause thin-skinned tectonic deformation and both salt and mud can form diapirs (Morley and Guerin, 1996). Unlike salt tectonics, shale tectonics, and more specifically mobile shales have only been of significant research interest since the turn of the century, such as the 2006 AAPG conference on Mobile Shale Basins and the related AAPG memoir published in 2011. Wood (2011) is a compilation of many publications of shale tectonics from basins across the world. The increased work since the turn of the century has built on our knowledge and understanding of mobile shales and how most standard salt tectonic models cannot be directly applied to them, with recent detailed reviews of shale detachment zones and shale characteristics in Morley et al. (2017), Morley et al. (2018), Soto et al. (2021a) and Soto et al. (2021b).

Although salt and mobile shale both move in response to extension, compression and load (Jackson and Talbot, 1986, Wu et al., 2000, Graham and Pepper, 2008) , the intrinsic properties of both mediums mean that they act and respond differently depending on the local conditions (Jackson and Vendeville, 1994). Salt does not compact at depth and acts as a fluid compared to compacted sediments (Morley and Guerin, 1996), with viscosities of between 10^{17} and 10^{19} Pa (Jackson, 1990). In contrast, shale mobility is significantly affected by compaction and depth (Ewy et al., 2020) as movement is dependent on the degree of overpressure within the pore fluids within the shale (Morley and Guerin, 1996). To create significant overpressure, rapid burial is required to restrict fluid escape from the pore space. This in turn creates a pore pressure that is greater than the hydrostatic pressure. The pore fluids within the shales can be generated through smectite-illite transition (Bruce, 1984) or more importantly, hydrocarbon generation (Barker, 1990, Osborne and Swarbrick, 1997). Recent publications question whether deeply buried shales can display viscous behaviour (Morley et al., 2017 and references therein e.g. Day-Stirrat et al., 2010, Morley et al., 2011) because above 80 °C (at ~ 2-3km burial depth)

chemical compaction and cementation should lithify shale. Very recently Soto et al. (2021a) and references therein, suggest that when high fluid pressures build up in shales they can behave in a viscous way at greater depths. Hydrocarbon generation in these deeper shales are therefore a significant cause for high pore fluid pressures, especially in the South Caspian Basin where the mobile shales within the basin are well known for producing oil and gas (Jones and Simmons, 1998). Soto et al. (2021b) compare mobile shale characteristics from basins all around the world, which shows a unique decrease in shale density below 5 km in the South Caspian Basin, which is likely caused by generation of thermogenic methane at depth (Feyzullayev and Lerche, 2009).

The ability for the pore fluid pressure to change over time, either due to fluid escape or hydrocarbon generation is a key factor that differentiates shale tectonics from salt tectonics. The properties of the mud therefore varies not only across basins globally, but also within individual basins both spatially and with time. Thus, the structures formed due to active shale tectonics varies depending on the properties of the shale. For example, a moderately over-pressured shale acts similarly to salt whereas a very over-pressured shale acts like a low viscosity fluid and is therefore very mobile and acts somewhat like magma and is hence prone to forming mud volcanoes (Graham and Pepper, 2008). Shale does not become mobile until the frictional resistance to slip is overcome, which can be reduced by an increase in fluid pressure (Rowan et al., 2004).

Recent work by Soto et al. (2021a) state that shale moves once the 'critical state' is reached and define mobile shales as "bodies of clay-rich sediment or sedimentary rock undergoing penetrative, (visco-) plastic deformation at the critical state". In this thesis I use the term mobile shale based on this definition. The authors suggest that shales become mobile once shear stress becomes greater than shear strength and the critical state conditions are met. Tectonic forces can increase the shear stress and in the case of the South Caspian Basin, the forces are compressional. The magnitude of the compressional load will determine the initiation timing and the rate at which the shale will become mobile. Once shortening has initiated, a significant thickness of overburden is required to build up fluid pressures, therefore it is likely that folding above a shale detachment does not occur until the overburden is sufficiently thick enough to allow the shale to reach critical state. This varies from salt, which theoretically can deform and act as a detachment immediately after deposition (Rowan et al., 2004).

Once the shale reaches critical state and becomes mobile, the mud can form different structures, such as ridges and diapirs, as seen in the Niger Delta (Wu et al., 2000) and South Caspian Basin (Santos-Betancor and Soto, 2015), and diatremes/mud volcanoes offshore Brunei (Van Rensbergen et al., 1999), offshore Trinidad (Barboza and Boettcher, 2000, Deville et al., 2003), offshore Nigeria (Graue, 2000) and are very common in the South Caspian Basin, with over 300 observed (Kadirov et al., 2003) both onshore and offshore (Fowler et al., 2000, Yusifov and Rabinowitz, 2004, Stewart and Davies, 2006). The shape and size of mud volcano is determined by both the properties of the mud (Planke et al., 2003) and also the width of the conduit (Kopf, 2002). Higher pore fluid pressures cause the formation of larger volcanoes since the mud has a lower viscosity and therefore erupts more violently and frequently (Yusifov and Rabinowitz, 2004). Large scale (km wide) volcanoes frequently appear to be fed by wide conduits (Kopf, 2002). However, conduits are reported to be narrow in width (10's m) (Stewart and Davies, 2006), much like in igneous systems (Lorenz, 1975). Recent work by Hudec and Soto (2021) agrees with the similarity to igneous systems, suggesting that mobile shales may rise through the overburden through fractures and faults. The authors also suggest that shale viscosities can be so low to cause rapid expulsion of mud at the surface, leading to collapse calderas, as observed in the South Caspian Basin (Stewart and Davies, 2006). During ascent, mud-fluids intrude and replace country rock as seen by fragments brought up to the surface onshore (Kopf et al., 2003). The fluid can infiltrate the pores of the sediments surrounding the conduit. This causes problems in seismic data as the reflectors become noisy and uninterpretable away from the conduit.

Modelling the effects of sedimentation upon salt has been document frequently, however numerical modelling of sediment loading of mobile shales has not been as common. Waltham (1997) presents mathematical models showing how differential sediment loading and buoyancy can significantly enhance fold growth upon a salt detachment. Numerical modelling the impact of differential loading by progradation upon a salt detachment has been presented by Cohen et al. (1996) and Gemmer et al. (2004). Analogue modelling by Warsitzka et al. (2013) demonstrates the importance of loading to salt diapirism. In the late 1990's the influence of differential loading on mobile shales was documented using seismic reflection data in the Western Alboran Sea (Pérez-Belzuz et al., 1997) and offshore Brunei (Van Rensbergen et al., 1999). Albertz et al. (2010) implement numerical modelling of

a visco-plastic Bingham fluid which shows the influence of differential loading due to delta progradation of the Niger Delta. Dean et al. (2015) then present the results from their discrete element modelling to show the effect of sediment loading of a mobile shale in a fold and thrust belt based on the Niger delta. There has been very little documentation of numerical modelling of shale tectonics and, to my knowledge, no documentation of models that model the effect of sediment loading on fold growth in the South Caspian Basin.

Shale tectonics of the South Caspian Basin

The South Caspian Basin has many mud volcanoes, with 99 mud volcanoes in the deep-water part of the basin with 70 occurring at the crests of anticlines, with the rest, mainly in the south of the deep-water centre of the basin, developed on the flanks of anticlines, possibly due to deep structures (Fowler et al., 2000, Yusifov and Rabinowitz, 2004) (figure 1.21).

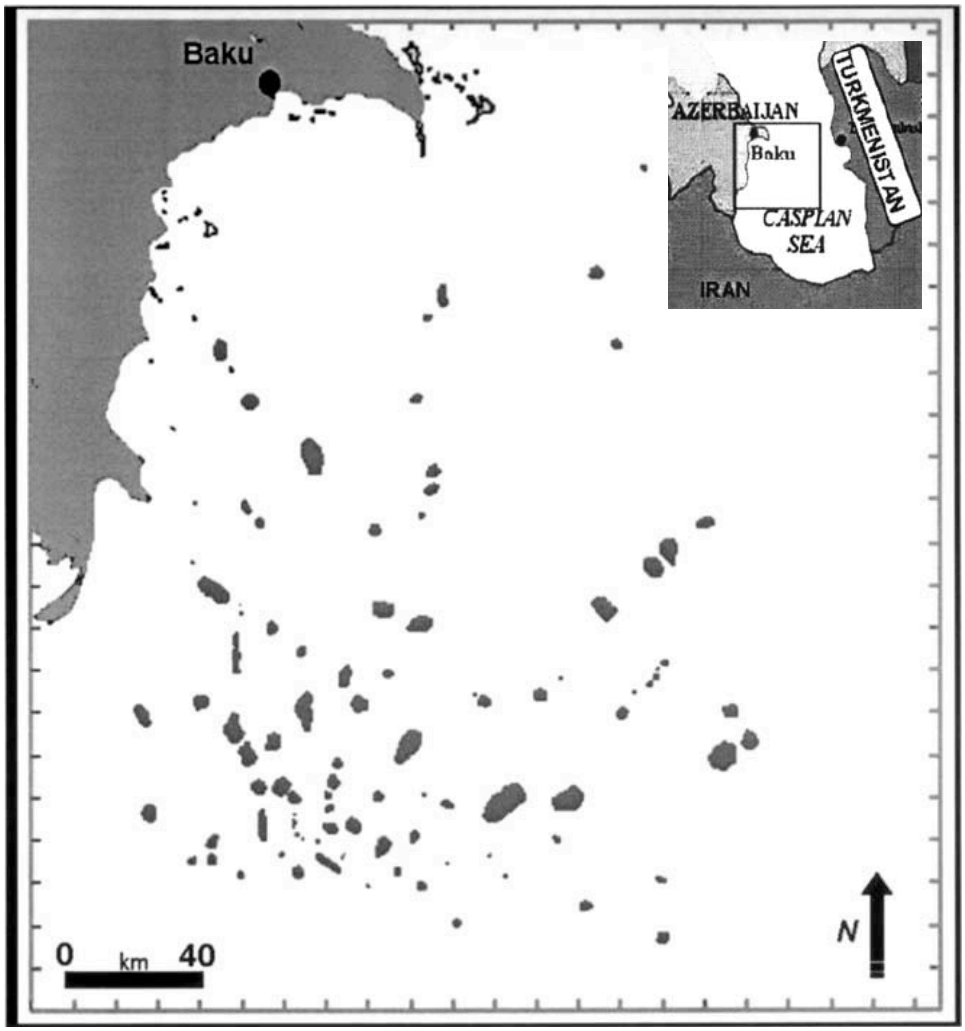


Figure 1.21: Location of mud volcanoes within the South Caspian Basin interpreted using regional 2D seismic lines. From Yusifov and Rabinowitz, (2004).

The source of the mud volcanoes is most likely from the Oligo-Miocene Maykop Formation (Inan et al., 1997, Abrams and Narimanov, 1997, Kopf et al., 2003, Stewart and Davies, 2006, Evans et al., 2007) (figure 1.22).

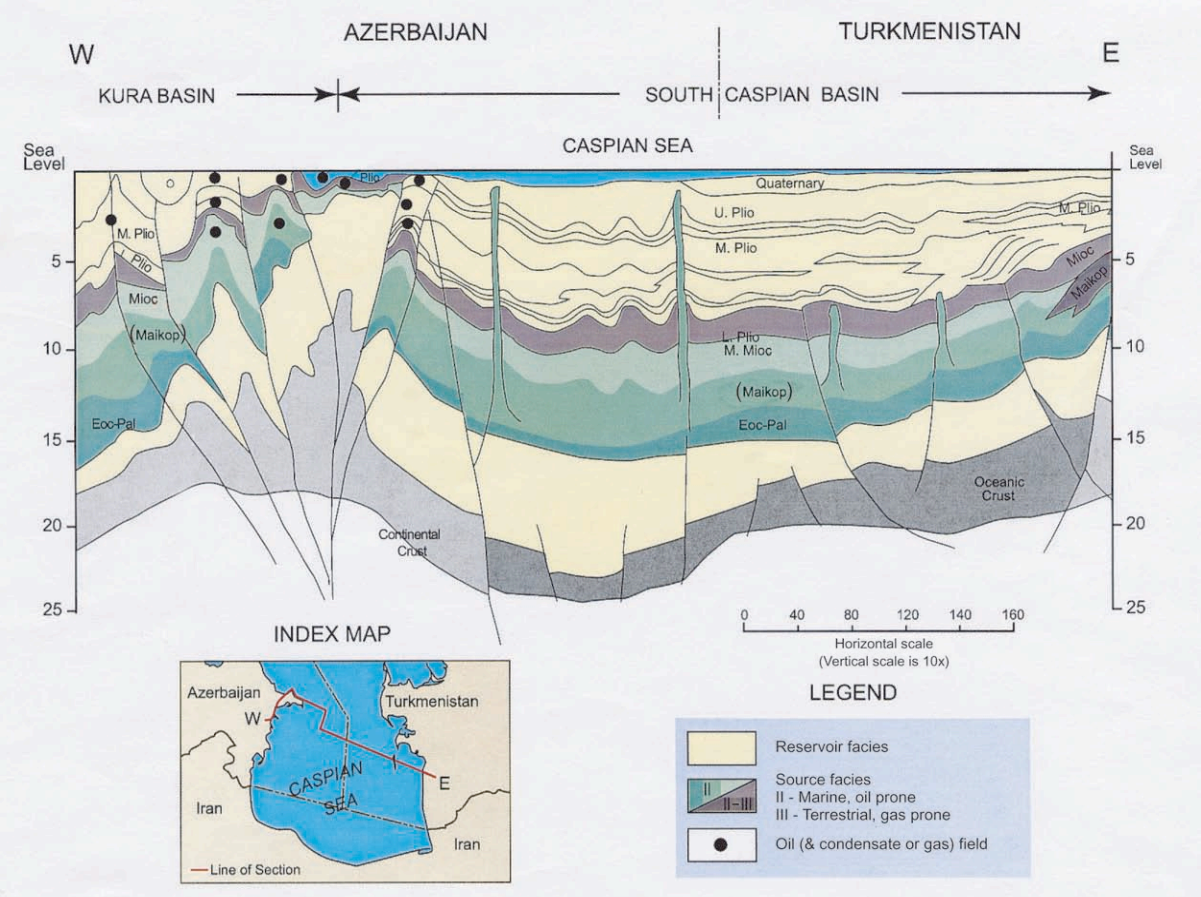


Figure 1.22: Cross section through the southern Caspian Sea region showing stratigraphy and structure from the Kura Basin in Azerbaijan eastward through the Apsheron-Pribalkhan Zone into western Turkmenistan. The mobile shale of the Maykop Formation can be seen in green. Note that the vertical scale in kilometers is 10× the horizontal scale. From Smith-Rouch 2006.

The mud may also be sourced from shallower sections (Yusifov and Rabinowitz, 2004, Blouin et al., 2019), such as the Surakhany Formation at the top of the Productive Series, as gases produced from the Maykop Formation move up into the Surakhany Formation and saturates the clays, leading to the formation of overpressured sediments and the eruption of a mud volcano (Blouin et al., 2019). Evidence of gas saturation within the erupted mud can be shown from breccia samples, where 35% of the volume is massive gas hydrate, significantly impacting the buoyancy of the mud during ascent (Ginsburg and Soloviev, 1994, Kopf, 2002). Mud volcano activity initiated in the Pliocene, approximately 4.33 Ma, with the greatest amount of active mud volcano activity occurring during the Late Quaternary, from 0.75 Ma (Yusifov and Rabinowitz, 2004). The mobile shale within the basin has

also been shown to influence the growth of the folds within the basin, with shale inflating the core of folds and producing mud diapirs (Santos-Betancor and Soto, 2015) (figure 1.23)

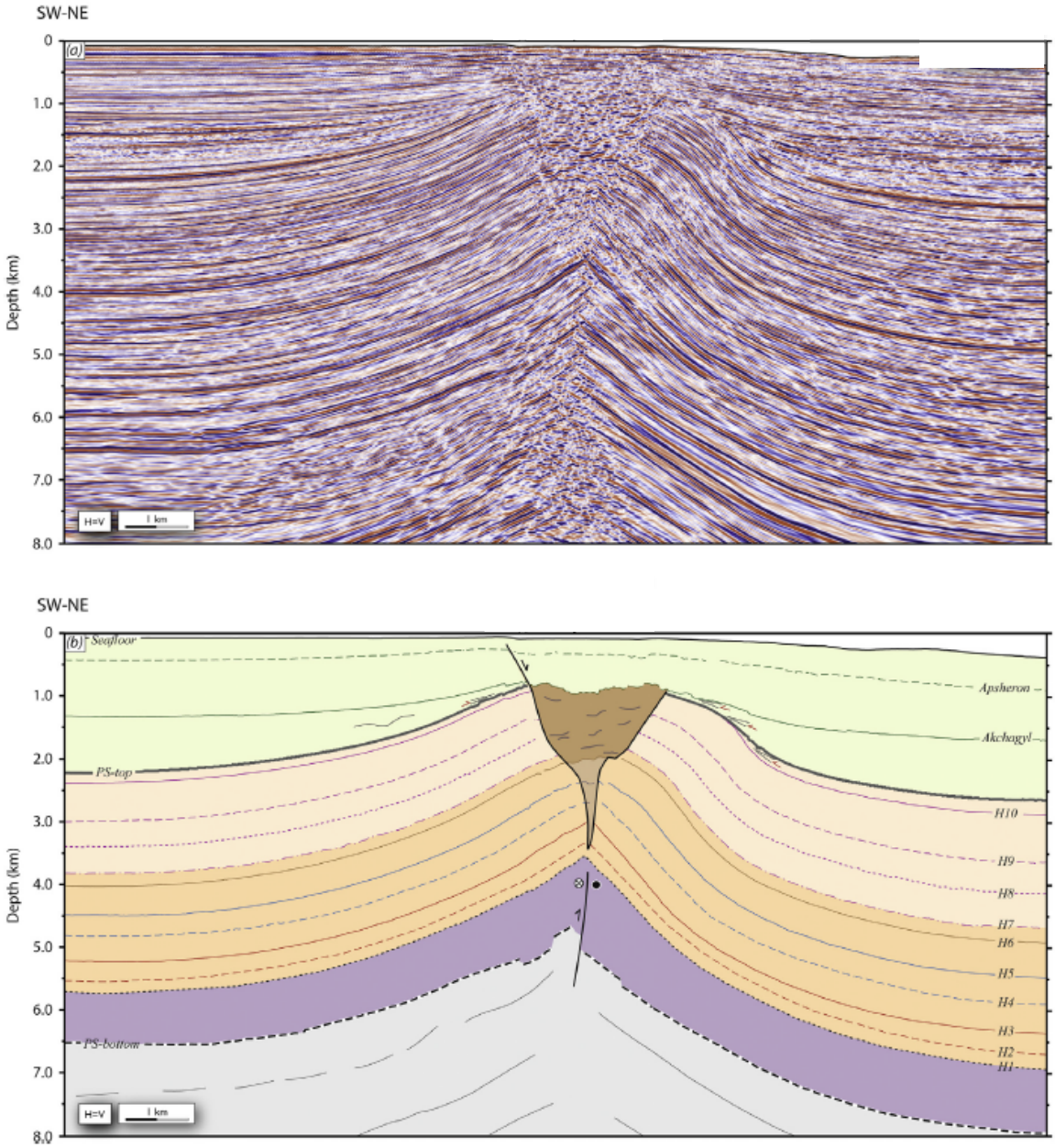


Figure 1.23: Seismic dip-line from a fold in the western offshore part of the South Caspian Basin (a) and interpreted (b). A collapsed mud diapir is found in the fold crest, bounded by normal faults. Vertical scale is in real depth (in kilometres with no vertical exaggeration. From Santos Betancor and Soto (2015).

The South Caspian Basin is an ideal basin for research into shale tectonics due to the very thick overburden (Devlin et al., 1999), the mobile shale is up to 9 km deep (Green et al., 2009) with many mud volcanoes (Yusifov and Rabinowitz, 2004), large folds (Devlin et al., 1999) and the formation of hydrocarbons (Feyzullayev and Lerche, 2009). All of these components of the basin lead to the possibility of differential loading affecting the fold growth history.

1.4 Lacustrine Turbidite Systems

Whilst there have been many studies on deep water marine channel systems (e.g. Mutti et al. 2003, Posamentier and Kolla 2003, Sprague et al. 2005, Mayall et al. 2006, Porter et al. 2006, McHargue et al. 2011, Janocko et al. 2013), the number of published examples on lacustrine sedimentary systems has been very limited. Research and interest into lacustrine depositional systems came into focus at the start of the 1990's, led by the AAPG conference 'Lacustrine Basin Exploration – Case Studies and Modern Analogues' in 1988 and the subsequent publication of the AAPG Memoir 50, edited by Barry J. Katz (Katz, 1990b). Studies within memoir mainly focussed on the deposition of source rocks within lakes (Barron, 1990, Katz, 1990a, Mello and Maxwell, 1990, Huc et al., 1990, Imbus et al., 1990) and lacustrine rift basins from Angola, Brasil, North America and East Africa (Lambiase, 1990, Abrahao and Warme, 1990, McHargue, 1990) as well as fluvio-deltaic systems in North America (Liro and Pardus, 1990, Castle, 1990) and lacustrine depressions in China that include deep-water lacustrine shales (Desheng and Ming, 1990) .

At the turn of the century, some of the most important and widely used models used within the topic of lacustrine sedimentology were published (Carroll and Bohacs, 1999, Bohacs et al., 2000). The authors use studies completed during the 1990s (Anadón et al., 1991, Horsfield et al., 1994, Renaut and Last, 1994, Katz, 1995, Scholz, 1995) to present models of lake basin type and the characteristic stratigraphy expected within each type. They state that lake basins differ from marine systems, primarily due to lake systems being more sensitive to changes in accommodation space and climate than in marine systems and therefore require their own sequence-stratigraphic models. They present three types of lake basin: overfilled, balanced filled and underfilled (figure 1.24). The lake type is dependent on the relative

fill of the basin by water and sediment compared to the potential accommodation space driven by basin subsidence. Lake basin types are often classified using these three types. Up to the early 2000's, most lacustrine research was focussed on source rock formation. In 2004 a Hedberg Conference focussing on lacustrine sandstone stratigraphy and reservoirs took place and was and compiled in the 2012 AAPG Memoir 95 'Lacustrine Sandstone Reservoirs and Hydrocarbon Systems' (Baganz et al., 2012a). The memoir includes papers from compressional regimes, extensional regimes, and modern analogues, including many studies on lacustrine reservoirs of the South Caspian Basin (Abdullayev et al., 2012, Nummedal et al., 2012, Sylvester et al., 2012, Baganz et al., 2012b), However, these studies focussed on fluvio-deltaic depositional systems. At this point in time, there were very few studies aiming to understand the sedimentology of deep-water lacustrine turbidites. Within the last decade there have been more studies focussing on deep water lacustrine turbidite systems, mostly by utilising 3D seismic datasets. Zhang and Scholz (2015) use seismic reflection data from East African rift lakes to demonstrate how deep water lacustrine turbidite channels, overbank levees and lobes are controlled by rift topography and syn-rift tectonism. Recently, studies focusing on lacustrine turbidite systems in China have been published. The Cretaceous Songliao Basin and Triassic Ordos Basin are intra-cratonic sag basins (Yang et al., 2005, Zhi-qiang et al., 2010). Seismic reflection data images deep water turbidite channels within the Songliao Basin (Zhi-qiang et al., 2010, Pan et al., 2020). Liu et al. (2021) recently showed how deep-water lacustrine lobes within the Eocene Weixinan Depression, China, are controlled by relay ramps influencing the lake floor topography. To my knowledge, there are no studies utilising 3D seismic reflection data to analyse the depositional system of deep-water lacustrine turbidites effected by structures formed within a compressional basin setting.

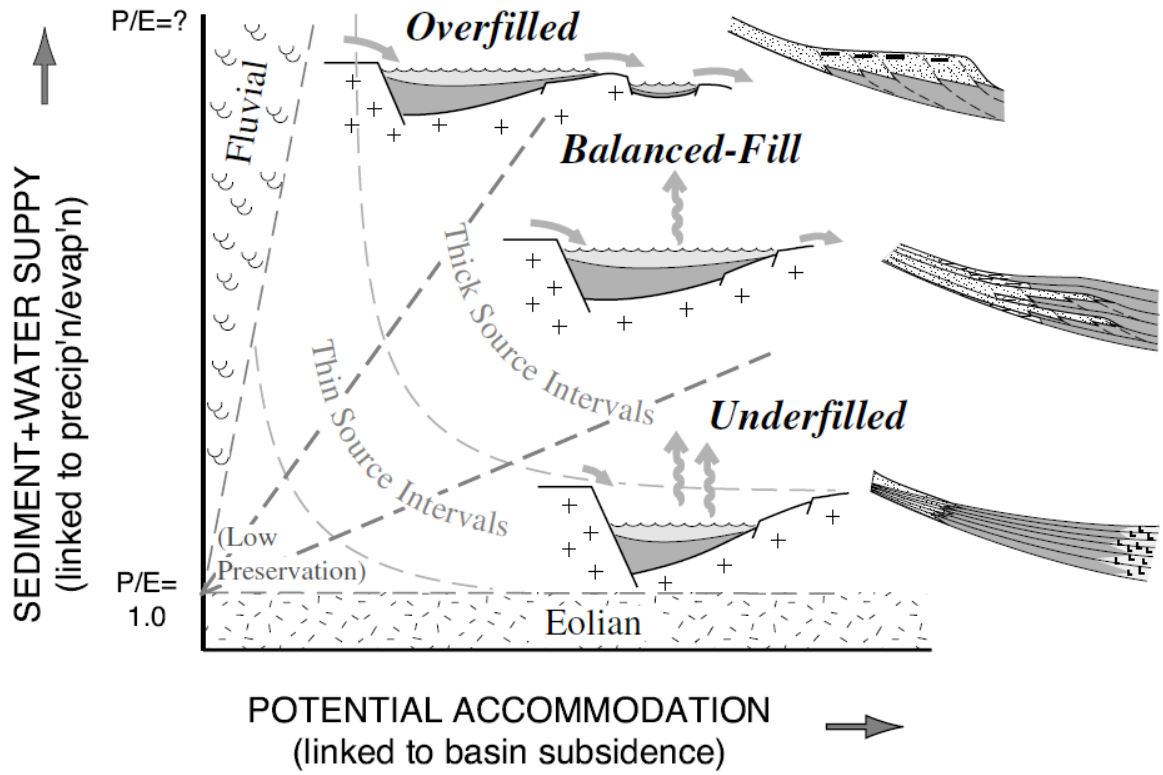


Figure 1.24: Lake-basin type phase diagram showing existence and character of nonmarine strata in general and lacustrine strata in particular as a function of both sediment+water supply and potential accommodation. Interaction of these two controls is reflected in the lithology, stratal stacking, biota, and geochemistry of lake deposits. Potential accommodation is the space available for sediment accumulation below the basin's outlet or spillpoint (a key difference from marine systems) (Carroll and Bohacs, 1995), and it is mainly influenced by basin tectonics, along with sill uplift and erosion, and inherited topography. Sediment+water supply is primarily a function of climatic humidity, along with seasonality, local relief, and bedrock geology. From Bohacs et al. (2000).

1.5 Thesis Aims and Objectives

The intention of this thesis is to investigate the fold growth of a structure within the deep-water South Caspian Basin, known as Shafag – Asiman, focussing on the Pleistocene to recent times. Deep-water lacustrine turbidite channel analysis will aid this investigation as well as further understand turbidite systems within deep-water lacustrine environments. In order to achieve the goals of this thesis, I set out the following aims and subsequent objectives to complete these aims:

1. Understand the growth history of the Shafag - Asiman fold structure within the deep-water South Caspian Basin and put the structure into context of the wider regional basin tectonic regime.
    1.1. Interpret the Pleistocene tectonic history of the Shafag-Asiman fold structure in the deep-water South Caspian Basin, utilising isopach maps created from 3D seismic interpretation.
    1.2. Relate the Shafag-Asiman fold growth to regional fold patterns and determine the main controls on fold development within the South Caspian Basin

2. Analyse the growth history of the Shafag-Asiman fold structure through time and space using novel sediment growth strata analysis.
    2.1. Understand the Pleistocene to recent fold growth history of the Shafag-Asiman fold structure using a novel approach, defined as sediment accumulation indices.
    2.2. Determine the potential controls on the growth of the fold structure using the distribution of 3D growth strata.

3. Examine the impact of mobile shale tectonics on the growth history of the Shafag – Asiman fold structure using numerical modelling.
    3.1. Numerically model a mobile shale cored anticline based on the Shafag – Asiman fold geometries.
    3.2. Determine the properties of a mobile shale required to realistically reproduce the Shafag – Asiman fold geometry.

3.3. Understand the principal influences on sediment loading of a shale cored anticline.

4. Investigate the extent to which growing fold structures interact with the depositional system of deep-water lacustrine turbidites.
   4.1. Understand the channel network within the Pleistocene lacustrine turbidites around the Shafag-Asiman fold structure through mapping of a 3D seismic dataset.
   4.2. Analyse and interpret channel network characteristics, such as orientation, sinuosity and channel architecture.
   4.3. Compare the channel network characteristics with sediment accumulation indices to infer the structural influence on the channel network.
   4.4. Develop a depositional model for lacustrine turbidite deposition around the Shafag – Asiman fold structures.
   4.5. Compare the observations of the deep-water lacustrine to other deep-water lakes and marine systems.

1.6 Thesis Outline and Structure

This thesis consists of a data and methods chapter, four research chapters, a discussion chapter, and a conclusion chapter. To achieve the aims as discussed above, the research of this thesis was conducted to analyse the fold growth of an individual fold structure in the South Caspian Basin, firstly on a regional scale and then focussing on a more local scale. The research chapters are presented in a way from which they can be adapted into stand-alone contributions, with the intention of submitting for publication. Each research chapter contains the following sections: introduction, methods, results, discussion, and conclusions. The discussion chapter synthesises the novel findings of the thesis and brings together the results and analysis of the four research chapters.

Chapter 2 introduces the Shafag-Asiman fold structure in the deep-water part of the South Caspian Basin and describes the 3D seismic reflection dataset studied in this thesis. The chapter presents the stratigraphic interpretation of the seismic dataset, with emphasis on the Pleistocene to recent stratigraphy. The chapter also introduces the techniques used in the subsequent research chapters, which are discussed further in the relevant research chapters.

Chapter 3 focusses on the growth of the Shafag-Asiman fold structure with respect to the wider regional development of the basin. Regional fold axis trends are mapped by Ken McCaffrey which has only previously been presented in an AAPG presentation in 2007 (McCaffrey and Jolly, 2007). I investigate the structural and stratigraphic development of the Shafag – Asiman fold structure to show how the structure forms and relate the fold structure to the wider context of the regional development of the basin using the interpretation of the regional fold axis trends. This chapter is written as a draft of a paper as it documents, for the first time, fold axis rotation due to torquing through time in response to transpressive dextral shear. Authors listed as Andrew Procter, Ken McCaffrey, Lidia Lonergan and Richard Jolly.

Chapter 4 focusses on the growth of the Shafag-Asiman fold structure through time, with emphasis on the Pleistocene to recent Post-Productive Series. The novel method defined as sediment accumulation indices are presented, used to analyse the distribution of growth strata across the folds. I demonstrate how the complex growth history of the Shafag - Asiman fold structures, in combination

with active mud volcanism since the Pliocene Productive Series, leads to the hypothesis that the Shafag – Asiman fold growth has been influenced by sediment loading of a mobile shale.

Chapter 5 addresses the hypothesis presented in Chapter 4 by using 2D finite element modelling. Numerical models are set-up using the geometry of the Shafag-Asiman fold structure to determine the material properties of the mobile shale under the fold structures. Realistic material properties are then used to test parameter sensitivities such as the mobile shale thickness, total amount of applied shortening and sedimentation rate. The chapter documents the role of sediment loading in the development of the Shafag – Asiman fold structure.

Chapter 6 presents the comprehensive mapping of the deep-water lacustrine turbidite channel network of the Pleistocene Absheron Formation. This chapter integrates the results of chapter 4 to demonstrate how the channel network is influenced by the growing fold structures. I also discuss the channel network in terms of the regional aspect of the basin as well as how the channel network compares to other lacustrine turbidites in basins globally as well as in marine settings.

In **Chapter 7,** I synthesise the novel findings of the research chapters and integrate these into an overall discussion. I discuss key cross-cutting themes from the thesis which includes the influence and timing of the Shafag - Asiman fold structure and how these results are pertinent to other fold structures in both the South Caspian Basin and globally. I discuss how the results of the 2D finite element modelling opens the door to further model evolution and present a potentially predictive tool for deep-water sedimentary systems using sediment accumulation indices. I then present potential future research suggestions that the results presented within this thesis have facilitated.

The thesis is closed with **Chapter 8**, in which I present the key conclusions from the research.

2. Data set and methods

2.1 Seismic Dataset

In this thesis I make use of a 3D seismic reflection data set, supplied by bp. No wells have been drilled in the area and therefore no well data are available. The data has been shot as a 3D seismic volume over two fold structures known as Shafag and Asiman in the deep water South Caspian Basin, where water depth is between 700 m – 900 m (figure 2.1). The folds lie to the east of the Zafar Marshal fold structure, the structure of which can be partially seen to the west of the data set. Three 3D seismic data cubes have been provided.

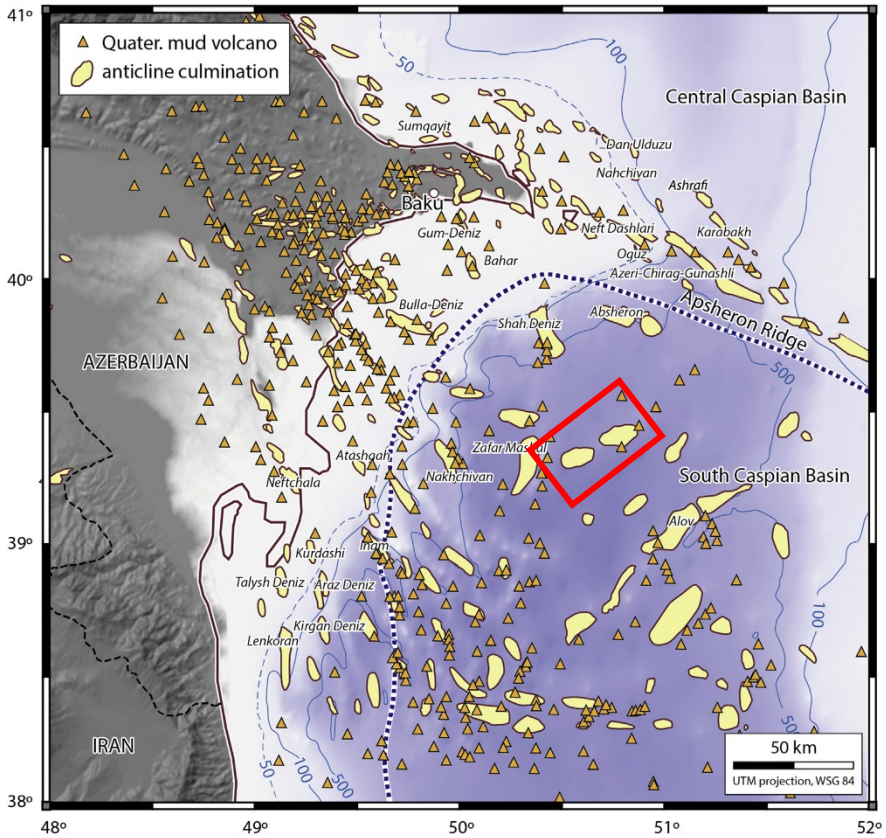


Figure 2.1: Map of anticline structures within the South Caspian Basin (yellow) and recent mud volcanism (triangles) from Santos-Betancor and Soto (2015). The Shafag – Asiman fold structure is highlighted by the red box.

Two are depth converted and one is a time cube. The first 3D seismic cube provided was a 3D broadband depth cube with a line spacing of 12.5 m by 6.25m and a 2 ms sample rate. The data is short offset data and therefore only images to 3.5 km. The broadband cube allows for the removal of 'ghosts'

and shows an extended band of frequencies between 2 Hz and 200 Hz. The low and high frequencies are boosted, removing ghosts and giving clearer signals at finer scales, for example thin beds (Amundsen and Landrø, 2014). During the project, two further seismic reflection data sets were supplied, one pre-stack depth migrated (PSDM) 3D volume and one time volume. This data is taken

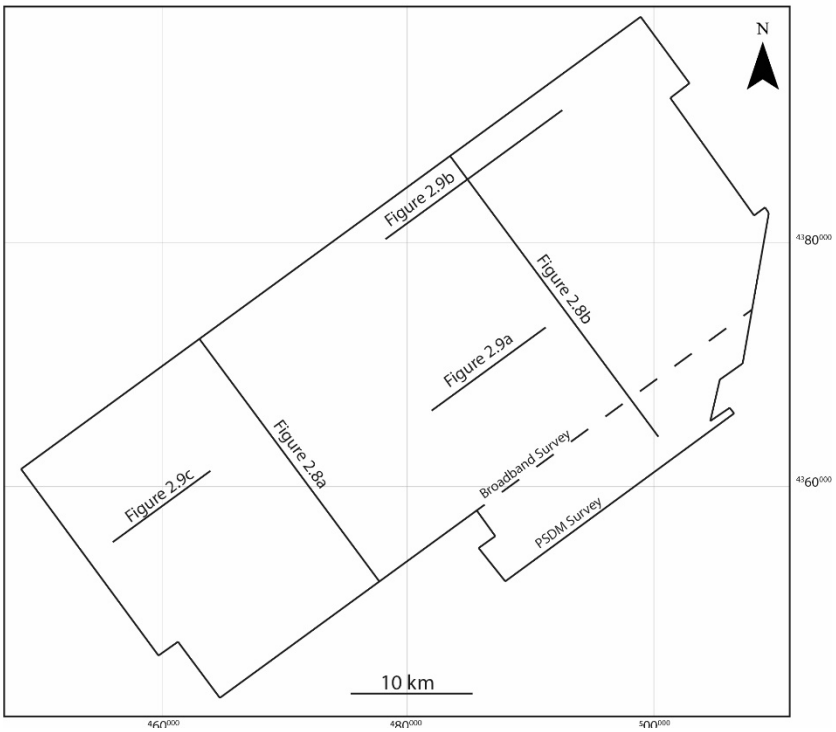


Figure 2.2: Outline of the seismic data for the pre-stack depth migrated (PSDM) data and the broadband seismic data (dashed line). The projection is WSG 84/UTM zone 39N.

from a different survey to the broadband data, covering 1655 km^2, a larger area than the survey in which the broadband data was collected, 1400 km^2 (figure 2.2). The PSDM volume is full stack and images to a depth of 13 km. The PSDM data is the original data processed and used by bp in 2012. The broadband data were acquired and processed after the PSDM data. The depth cube was depth converted using bp's velocity model, where the velocity model was built using average velocities derived from original interval velocities using the Dix equation (Dix, 1955). Since there are no well data the seismic volume is not calibrated and therefore there are likely to be small depth errors. Within the PSDM dataset, the line and trace spacing is 25m with a sample rate of 4 ms. The time cube was used to calculate the vertical resolution using the average velocities from the velocity model for the shallow section of 3500m. The frequency content from 1000 – 3500 m/s is 25 Hz – 50 Hz and an average of 40 Hz (figure 2.3). Using

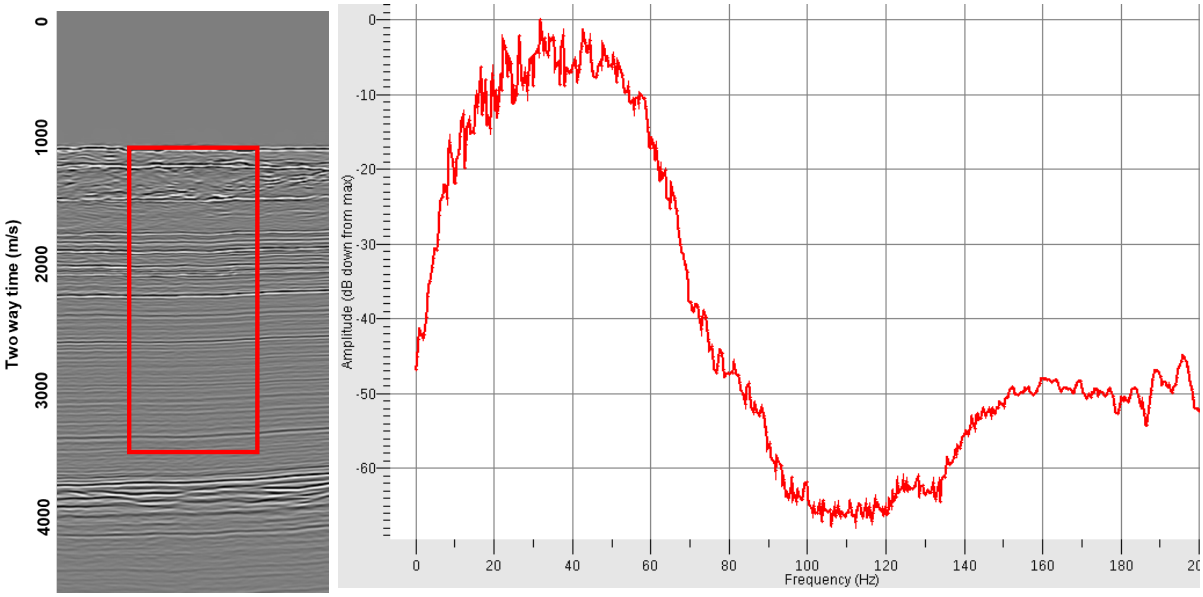


Figure 2.3: Frequency of the PSDM seismic dataset between 1000 m/s and 3500 m/s depth.

a velocity of 1800 m/s and a frequency of 40 Hz gives a vertical resolution of 11.25m. The data are in SEG normal polarity, with an increase in acoustic impedance displayed in blue or black.

Faults were interpreted using the broadband data. All faults within the PSDM data are all imaged by the broadband data. Since the PSDM data covers a larger area, this is the data set that was used for the horizon interpretation and channel imaging. Although this is of a lower resolution than the broadband data, channels are still imaged in high quality. A comparison between the PSDM data (figure 2.4a) and the broadband data (figure 2.4b). shows that although the broadband data has better resolution in cross section (figure 2.4d), in map view, the channels are almost as equally well resolved in both data sets (figure 2.4c).

To interpret the structure within the dataset, the broadband seismic cube was converted into a discontinuity cube. The Landmark DecisionSpace software was used for seismic interpretation and to create the discontinuity cubes. Two discontinuity cubes were created, a discontinuity cube and a dip-corrected discontinuity cube. In DecisionSpace, the discontinuity cube is based on an extension of Bahorich and Farmer (1995) method of calculating a correlation discontinuity which is also similar to a semblance discontinuity and comparable to coherency (Marfurt et al., 1998, Gersztenkorn and Marfurt, 1999). The original coherence algorithm (Bahorich and Farmer, 1995, Bahorich and Farmer, 1996) uses only three traces, to cross correlate each trace with its in-line and cross-line. Marfurt et al.

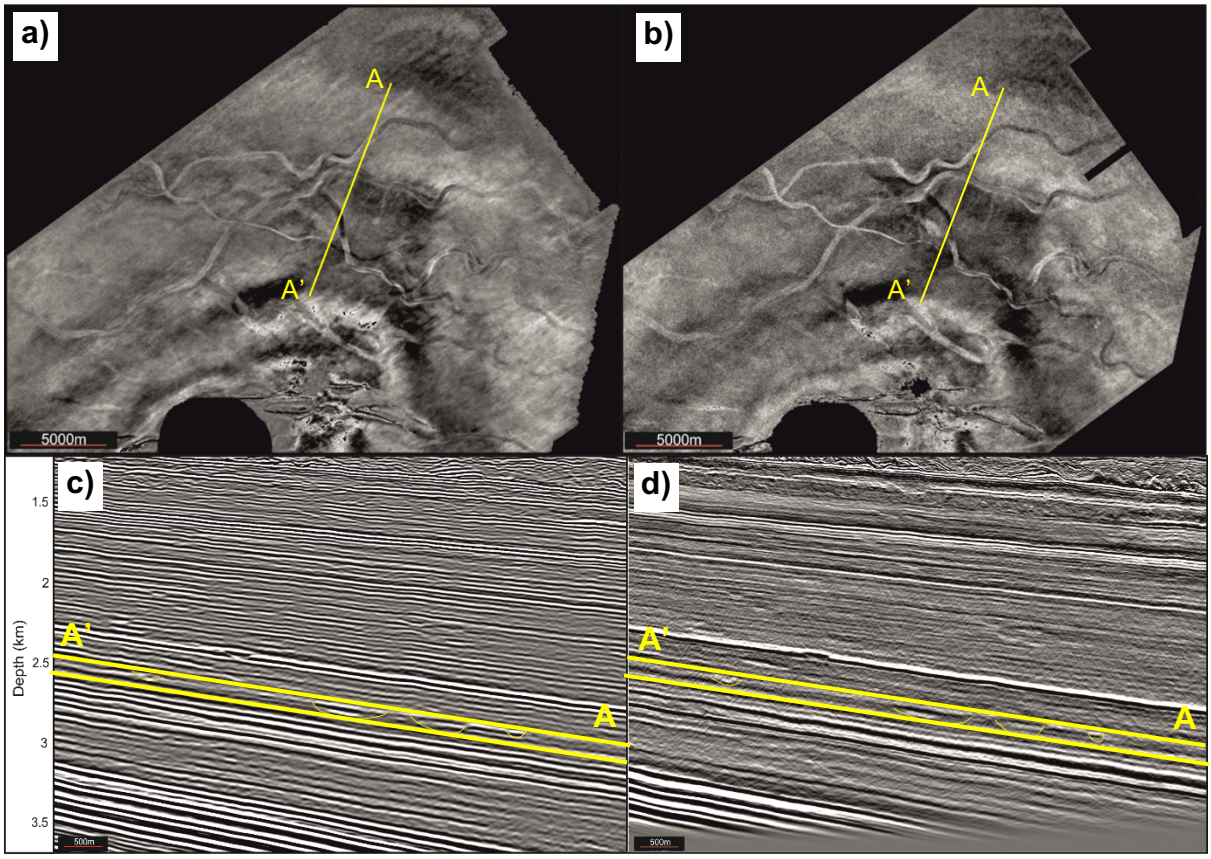


Figure 2.4: RMS amplitude maps showing channels in a) PSDM and b) broadband seismic datasets with corresponding sections showing the channel image quality in section view in c) PSDM and d) broadband seismic datasets. The RMS window is shown by the yellow lines in c) and d).

(1998) improved upon the algorithm by using a multi-trace algorithm, which reduces the noise of the discontinuity cube. The last improvement to the algorithm was produced by Gersztenkorn and Marfurt (1999) which is also multi-trace but uses the eigenstructure of the matrix to reduce noise. In DecisonSpace, this method is further modified by weighting the constituent correlations to produce a weighted correlation discontinuity attribute (figure 2.5a)

The dip-corrected discontinuity cube in DecisionSpace is based on Randen et al. (2000). The cube is computed using a gradient-squared tensor, which produces three eigenvalues. The three eigenvalues are measured in three orthogonal axes. The largest is the maximum squared gradient normal to the reflections (λ_1). The second is along an axis parallel to the reflections in the direction of the maximum gradient change (λ_2), whilst the third is in the axis parallel to the reflections in the direction of least change (λ_3) (Barnes, 2016). A fault within a clean seismic volume has a very minimal λ_3 and so is not used within the DS algorithm. The discontinuity, *D*, for the dip-corrected discontinuity is based on Hale (2009) and is:

$$D = \frac{(\lambda 2)}{(\lambda 1)}$$

The discontinuity-along-dip cube gives better images for steep discontinuities, which has advantages for structures around diapirs however the images generally have a lower resolution than the standard discontinuity cube but can be clearer (figure 2.5a, b).

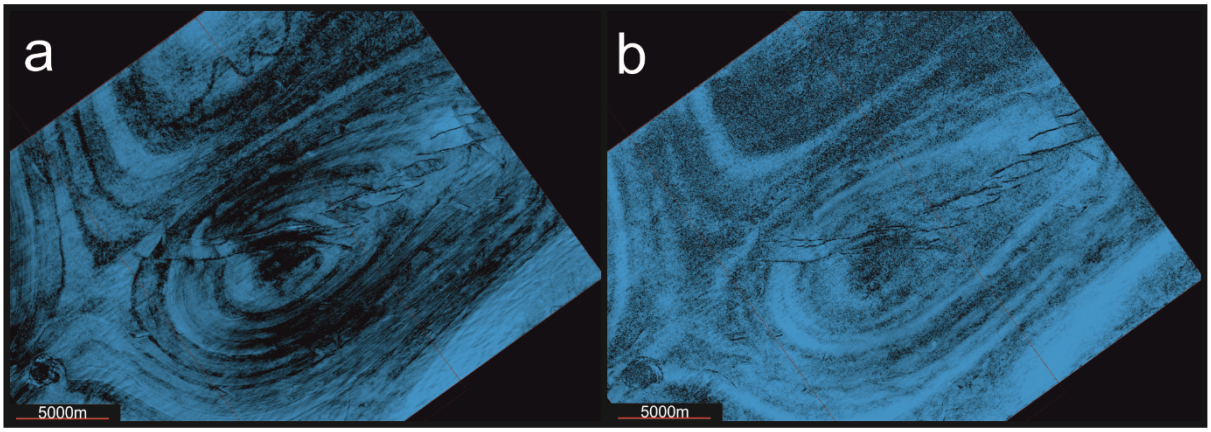


Figure 2.5: Slice through a) Discontinuity cube and b) Dip-corrected Discontinuity cube imaging faults over a fold crest.

2.2 Seismic interpretation

Fault interpretation was conducted within the upper 4 km of data using the broadband seismic data and is discussed within Chapter 3. Since there are no well data available, the stratigraphy was interpreted using seismic characteristics such as reflection geometries (e.g. onlap), amplitude variation and correlating the horizons with known regional stratigraphy of the basin with information for formation tops supplied by bp. These formation tops are: Top Surakhany Formation, Top Akchagyl Formation and the Top Absheron Formation. Between the Top Absheron and Top Akchagyl Formations, five intervals have been interpreted. Between the seabed and the Top Absheron Formation, four intervals have been interpreted (figure 2.6). Horizons were selected based on regional continuity of the reflectors, strength of reflectors, reflection geometry and chaotic reflectivity. For simplicity, the horizons are labelled Hz100 (top Surakhany), up to Hz200 (seabed) (figure 2.6). Lacustrine turbidite channels are present within the Absheron Formation, between Hz110 – Hz160. The channels within the Absheron Formation are studied and analysed within Chapter 6. The uppermost units, between Hz160 – Hz200 consist of mass transport deposits, which were not studied in any detail for this research.

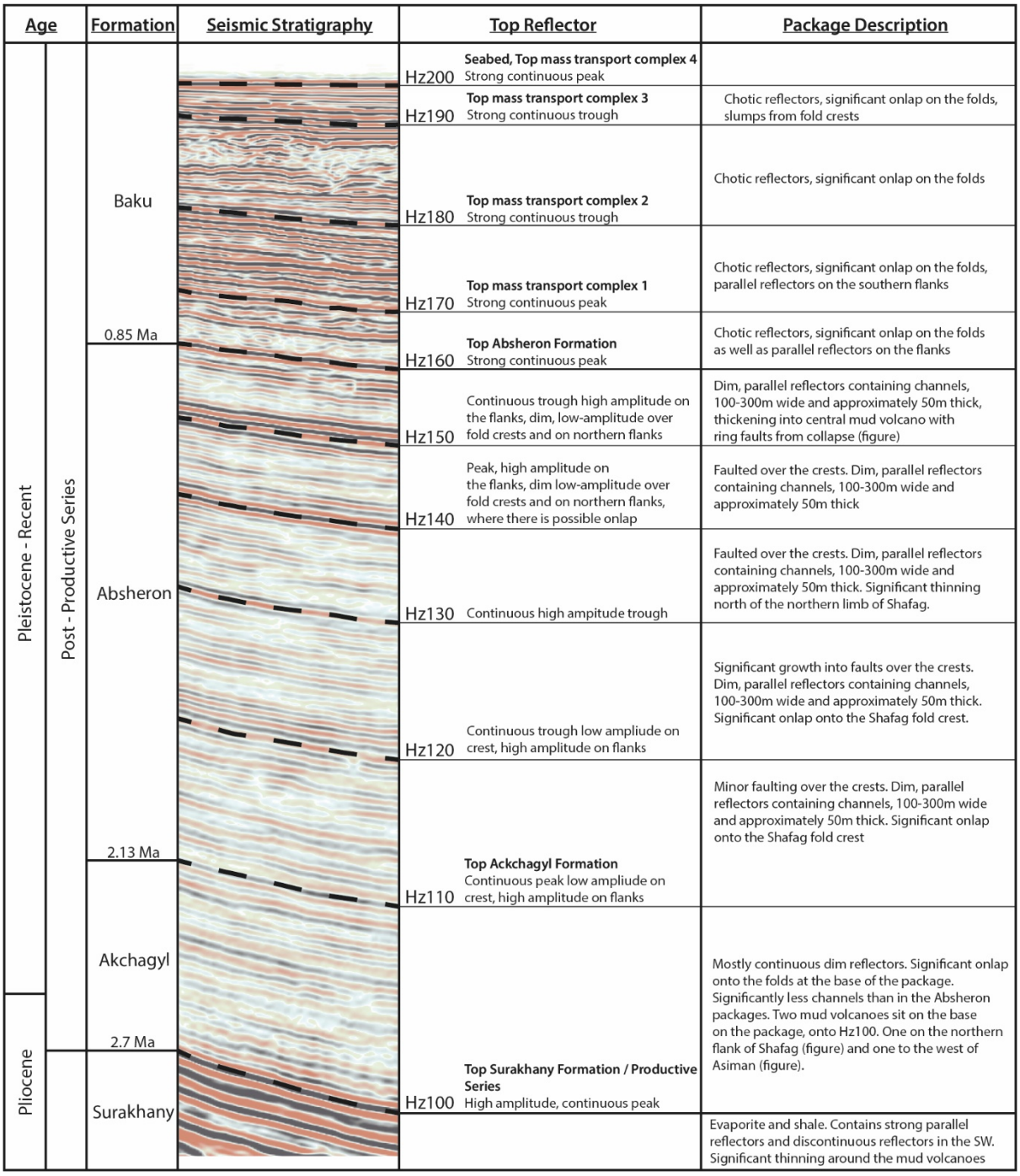


Figure 2.6: Seismic stratigraphic column describing the horizons interpreted, reflector characteristics and a brief description of the intervals. The ages are shown on the left as well as ages and formation names used in this study. The formation tops are supplied by bp and are tied to regional seismic lines. The Surakhany Formation is the top of the Productive Series. The Akchagyl, Absheron and Baku Formations constitute the Post-Productive Series. Ages given are based on Van Baak et al. (2019), Lazarev et al. (2019), Lazarev et al. (2021), Vasiliev et al, (2022).

The Asiman and Shafag fold structures are both visible on the present-day seabed (figure 2.7). Both the Asiman (figure 2.8a) and Shafag (figure 2.8b) structures are shale cored, causing a disruption of the seismic reflectors. Evidence for mobile shale is shown by the presence of three mud volcanoes within the dataset (figure 2.9). The most prominent mud volcano can be seen on the present-day seabed, MV1 (figure 2.7). It is up to 4 km wide on the seabed and causes the seismic data to be wiped-out throughout the sequence (figure 2.9a). One mud volcano, MV3, located to the north of Shafag has an edifice approximately 4.5 km wide and lies on the Top Surakhany (Hz100) (figure 2.9b). It has a feeder zone of opaque seismic data indicating that mud comes from below the Surakhany Formation. A third mud volcano is located to the west of Asiman (MV2), with intermittent mud flows visible from the Top Surakhany (Hz100) up to Hz170 in the mass transport deposits (figure 2.9c). The mud is seismically opaque and causes the feeders and surrounding data to lack any reflectivity, causing an area of seismic 'wipe out' (figure 2.9). Therefore, throughout this thesis maps from within the Post-Productive Series will exclude the area of limited seismic data below the central mud volcano and the mud volcano in the west of the area.

Although the mass transport deposits of the Bakunian (Hz160 – Hz200) are not studied in detail within this thesis, the broadband seismic data images the deposits in high detail, both on the seabed (figure 2.10a) and in section (figure 2.10b). Slumping is visible on the seabed, on the flanks of the fold structures (figure 2.10a). However, in section, the mass transport deposits contain small thrusts which can be used to infer the flow direction (Alsop et al., 2017), showing that, to the north of Shafag, the deposits are mostly sourced from outside the area, flowing from north to south (figure 2.10b).

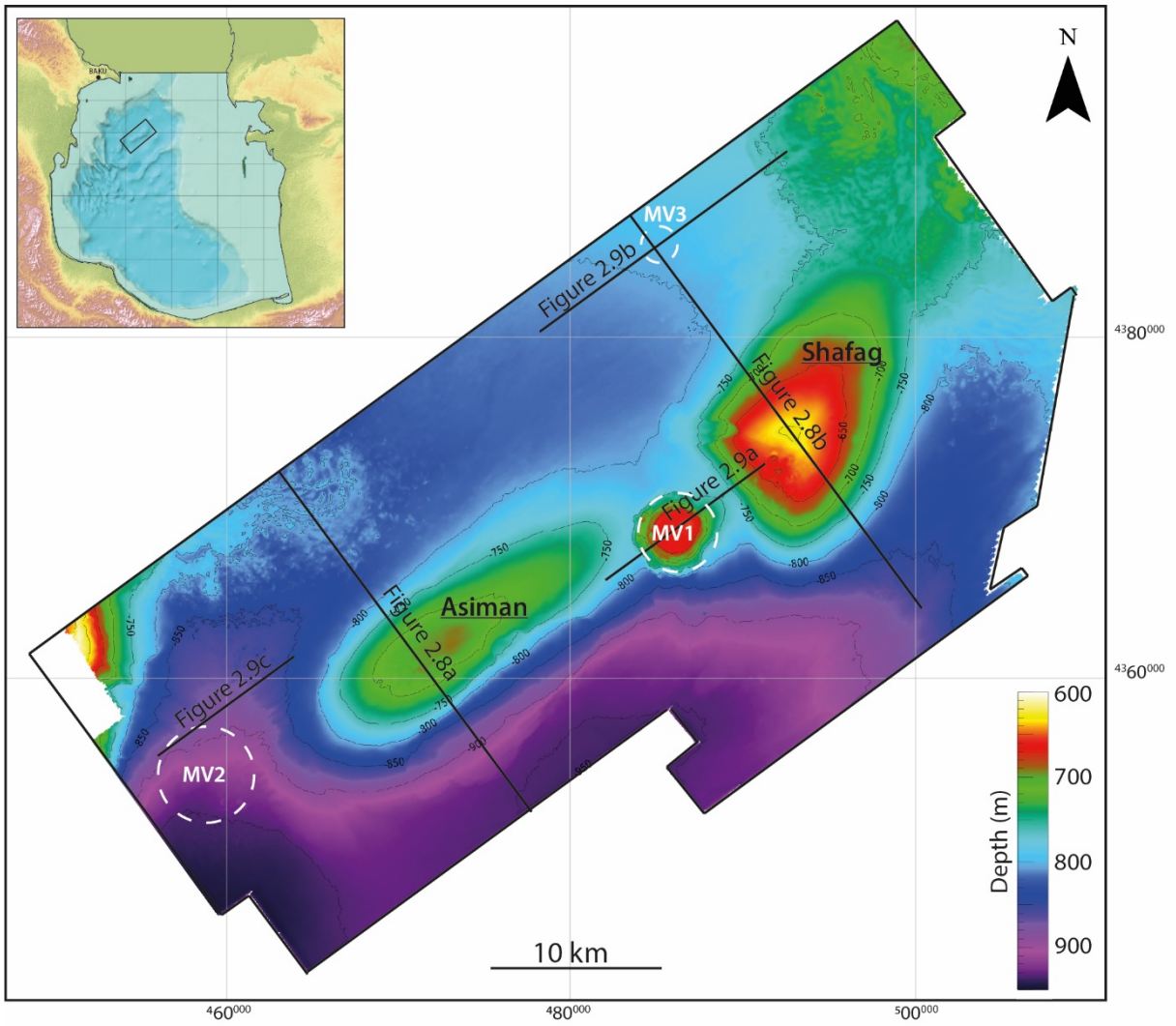
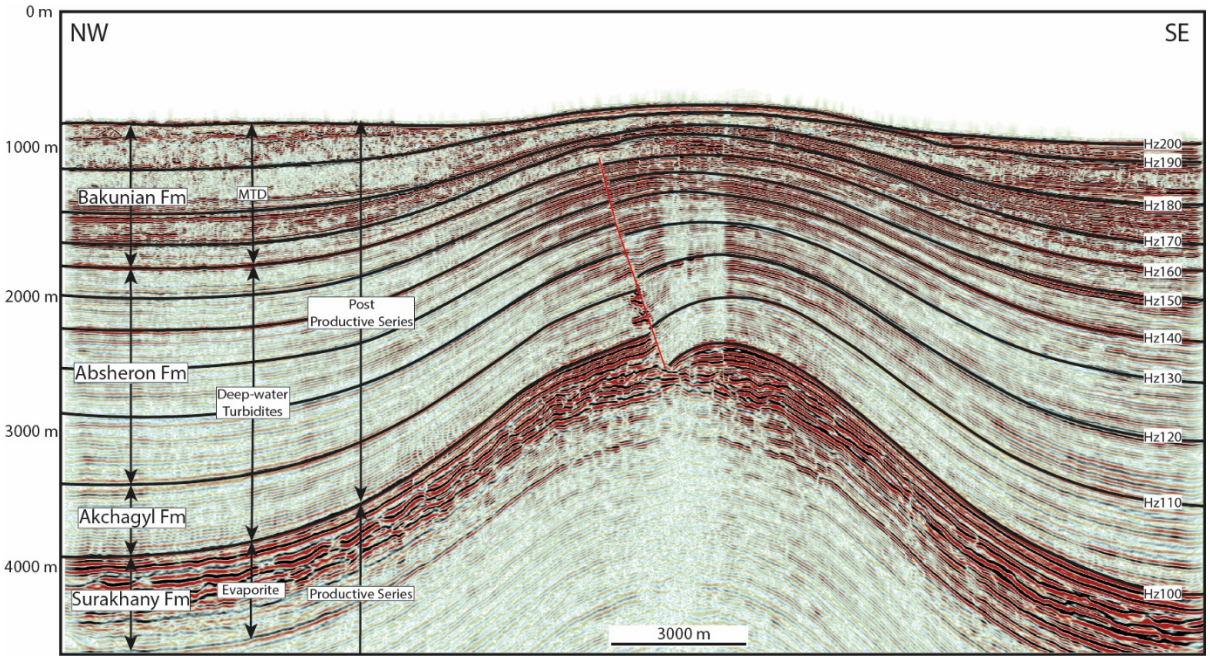


Figure 2.7: Depth to seabed map with locations of mud volcanoes and seismic lines. Of the three mud volcanoes in the dataset, only MV1 is active on the present-day seabed.

a) Asiman



b) Shafag

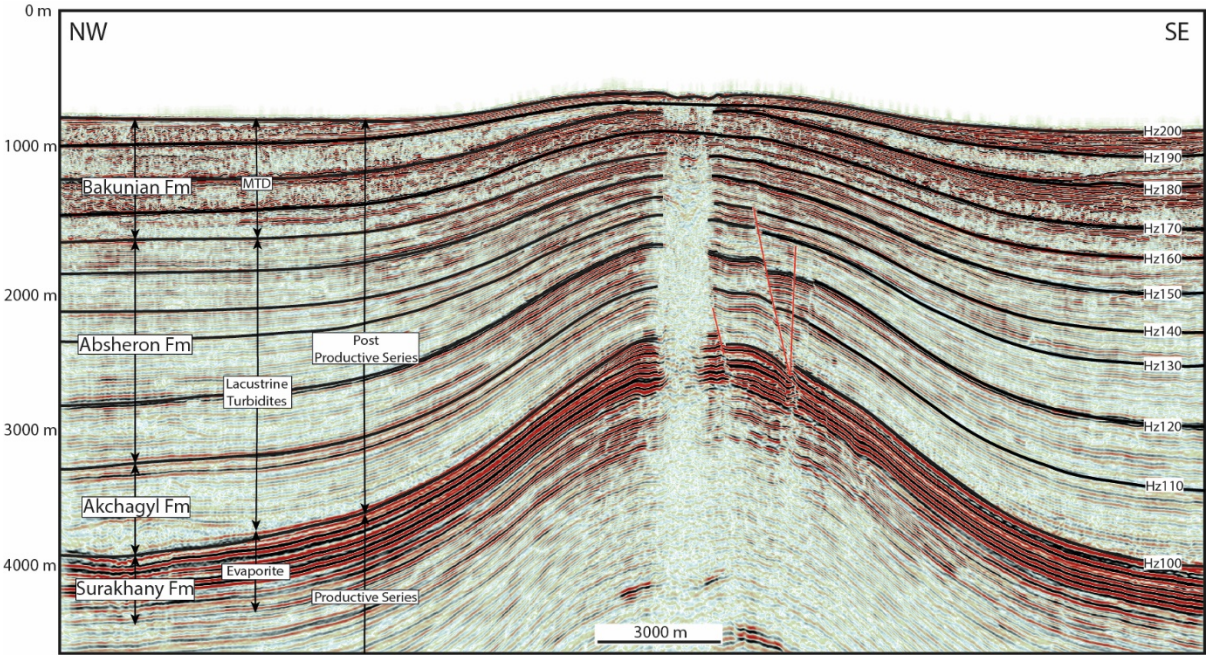


Figure 2.8: Seismic section through a) Asiman and b) Shafag fold structure showing the horizon interpretation as well as the seismic wipe out in the crest due to the mobile mud core. H/V exaggeration is 1:3.

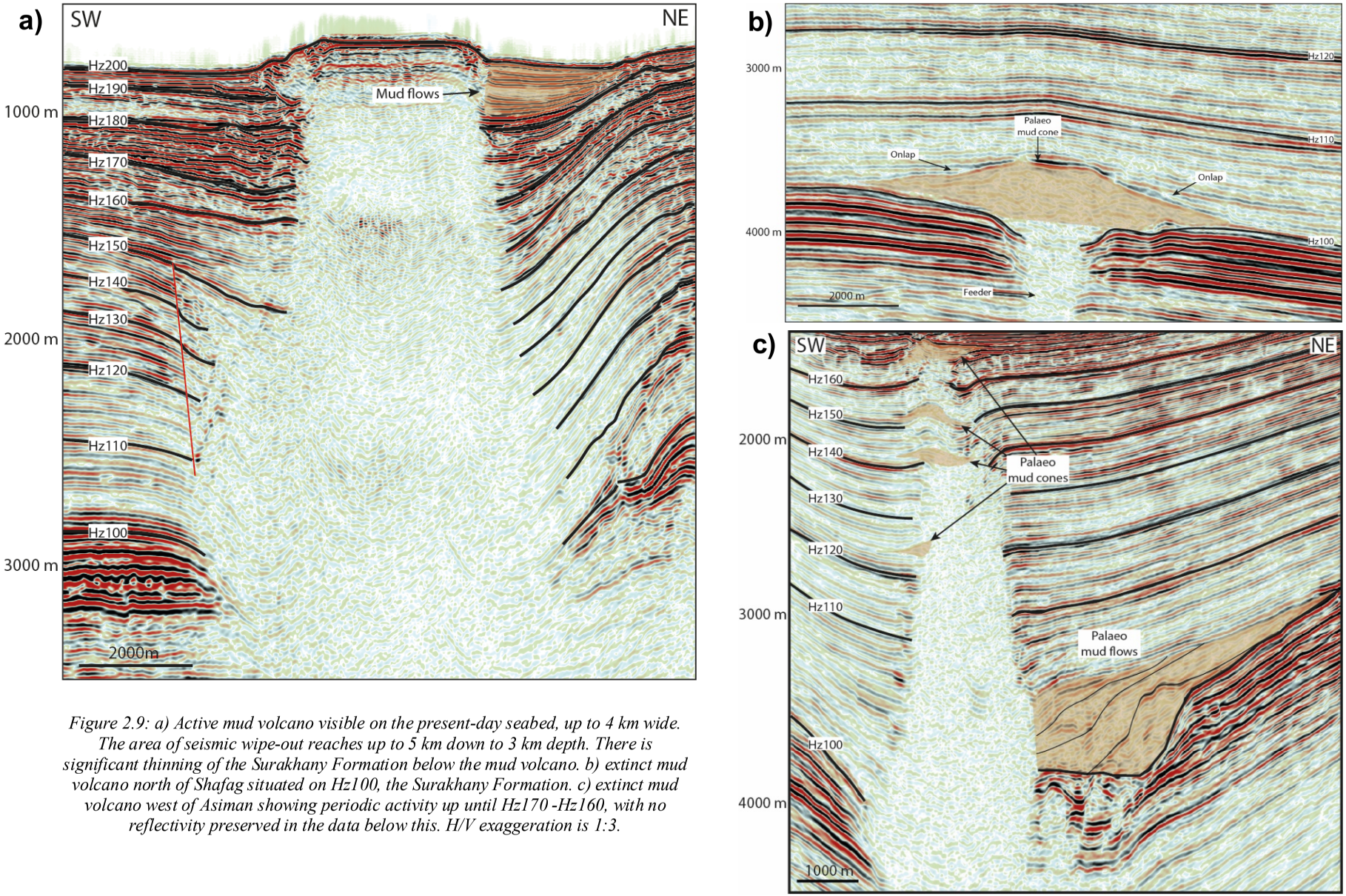


Figure 2.9: a) Active mud volcano visible on the present-day seabed, up to 4 km wide. The area of seismic wipe-out reaches up to 5 km down to 3 km depth. There is significant thinning of the Surakhany Formation below the mud volcano. b) extinct mud volcano north of Shafag situated on Hz100, the Surakhany Formation. c) extinct mud volcano west of Asiman showing periodic activity up until Hz170 -Hz160, with no reflectivity preserved in the data below this. H/V exaggeration is 1:3.

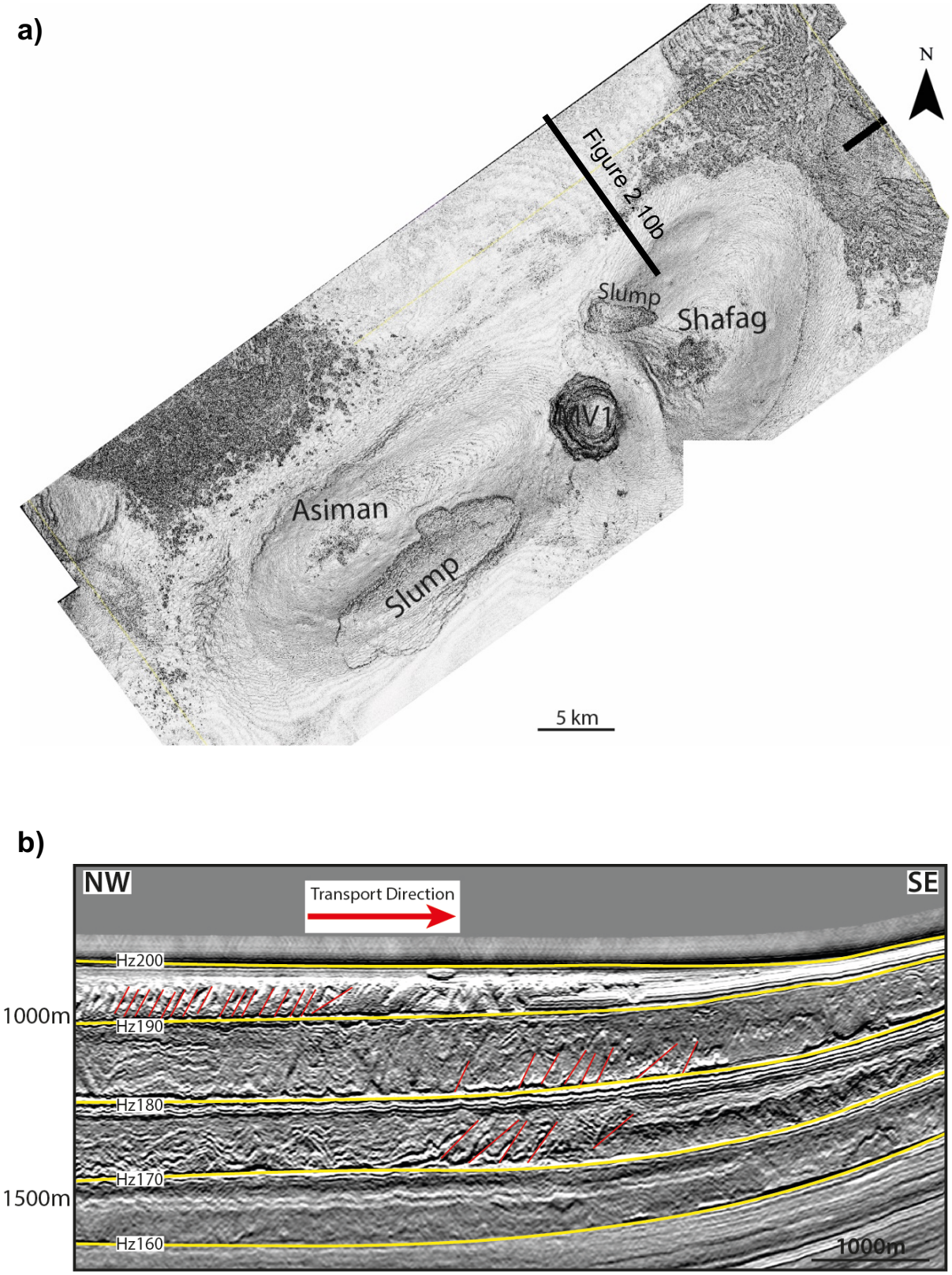


Figure 2.10: a) Seabed dip map showing slumping off the flanks of the Shafag and Asiman fold structures. b) Section displaying thrusts within the mass transport deposits showing a flow direction to the south, sourced from outside the area to the north.

2.3 Methods

Using the horizon interpretation, I created regional isopach maps (true stratigraphic thickness) which were used to understand the history of the fold growth through time (Chapter 3) and to conduct a novel analysis of the fold growth, focussing on the past 2.7 Ma within the Post - Productive Series (Chapter 4). The workflow for the horizon interpretation, isopach maps and deep-water turbidite analysis is shown in figure 2.11.

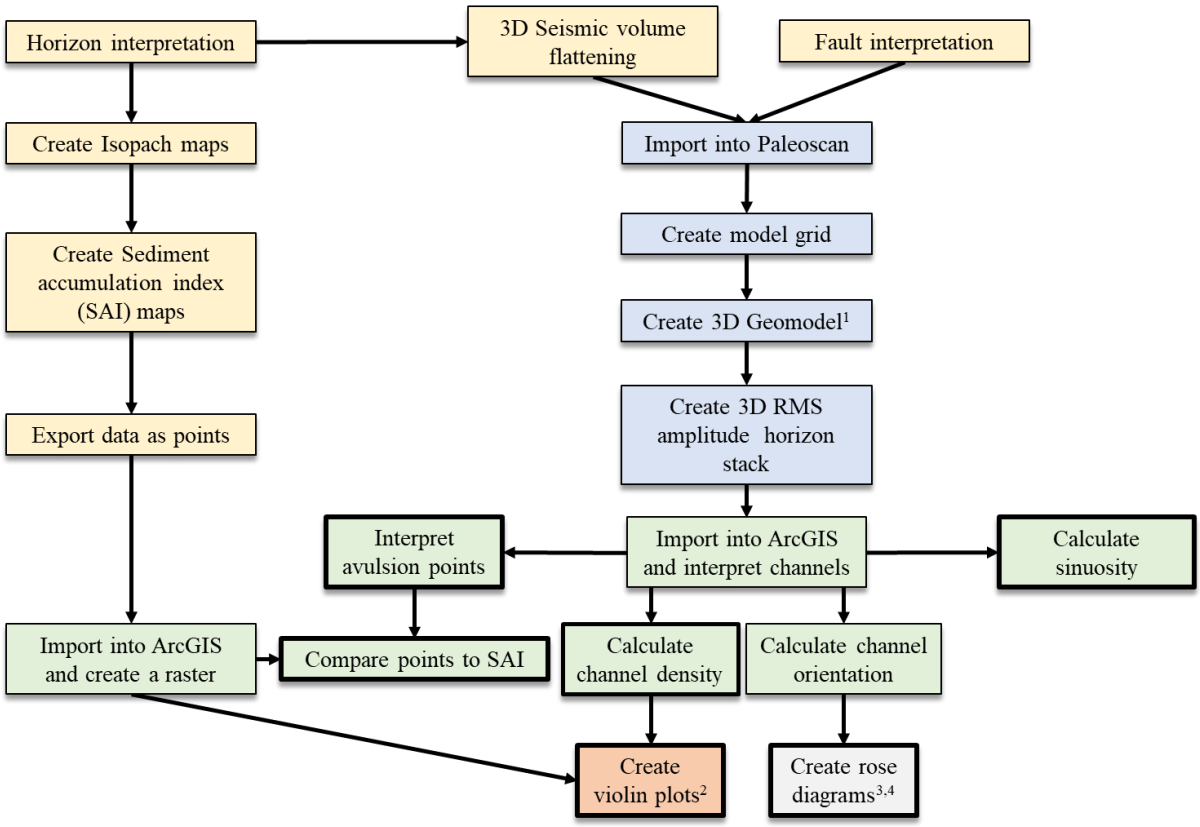


Figure 2.11: Workflow of the channel analysis. The software used to conduct the analysis was Landmark DecisionSpace software (yellow boxes), Ellis Paleoscan software (blue boxes), ArcGIS (green boxes), MATLAB (pink box) and Stereonet (grey box). The thick black boxes are the results used within the channel analysis. [1] Pauget et al. (2009).[2] Bechtold (2016) (code used to create violin plots). [3] Allmendinger et al. (2011). [4] Cardozo and Allmendinger (2013).

For the deep-water turbidite analysis (Chapter 6), I manually interpreted channels imaged from Root Mean Square (RMS) amplitude maps, which were created using the Paleoscan software from Ellis (Pauget et al., 2009). Frequently for dipping strata with minor amounts of growth, isoproportional horizons can be constructed from which to extract amplitudes within an interval constrained by well imaged reflections. Due to the complexity of growth strata expansion and difficulty of interpreting horizons between the mapped surfaces (figure 2.12), I choose to use Paleoscan for better imaging of the

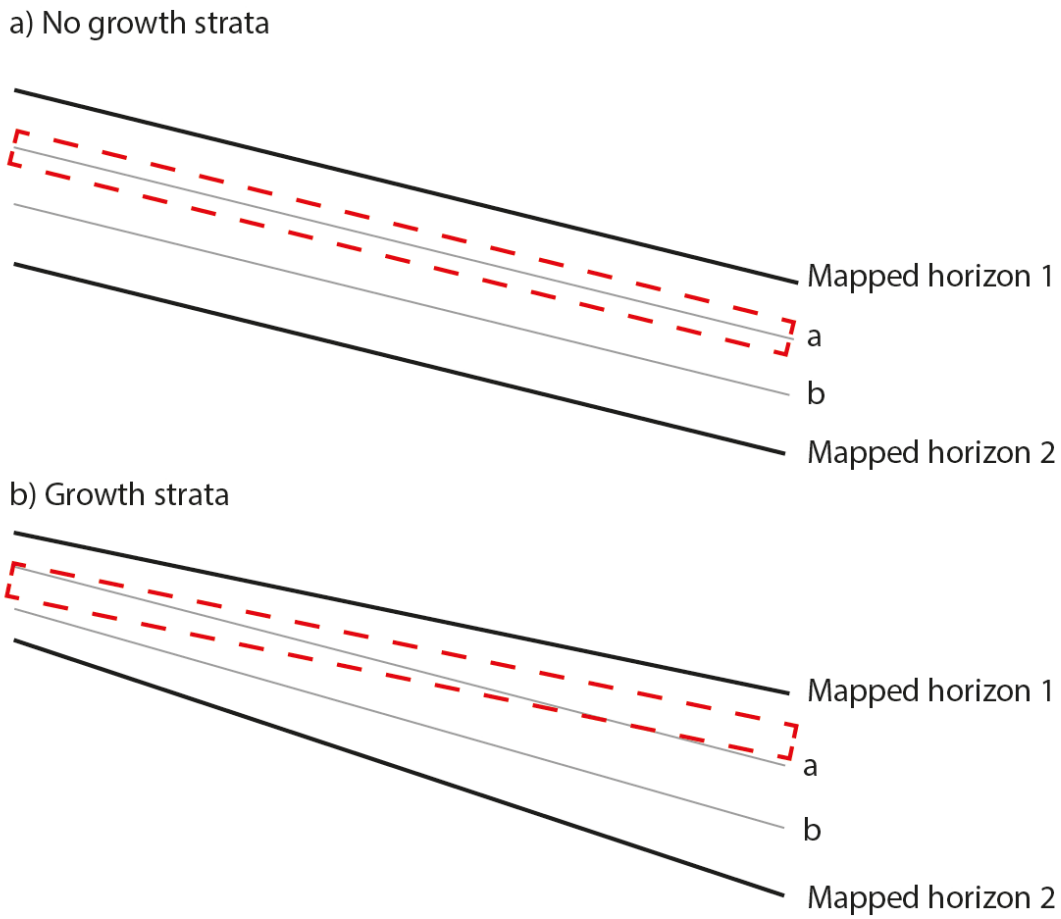


Figure 2.12: Schematic diagram showing how isoproportional slices can be used for a) no growth strata and b) growth strata. Where there are growth strata, horizons a and b, isoproportional horizons (red box) do not map the correct geometry of the reflectors and therefore channel maps will not be correct.

channels. The Paleoscan software attempts to map detailed events throughout the dataset, allowing a higher resolution amplitude extraction. To produce RMS amplitude maps from Paleoscan, the horizon interpretation was used to flatten the seismic data as a 3D volume between two horizons and exported from Landmark's Openworks and imported into Paleoscan. The analysis was conducted between Hz110 and Hz160, hence flattened volumes were used for the Paleoscan analysis. The faults interpreted within DecisionSpace were imported into Paleoscan. Within Paleoscan, a 3D geomodel was created for each flatted volume. The geomodel is produced based on methods from Pauget et al. (2009) (figure 2.13) The geomodel parameters were set to model the horizons within each interval, between my initial manual regional interpretation of the seven horizons of the Absheron Formation. The models were used to create a horizon stack, where 40 RMS amplitude horizons were output from within each interval. RMS amplitudes were extracted over a window of 50 m for each horizon. These horizons were then interpreted with channel analysis conducted within ArcGIS.

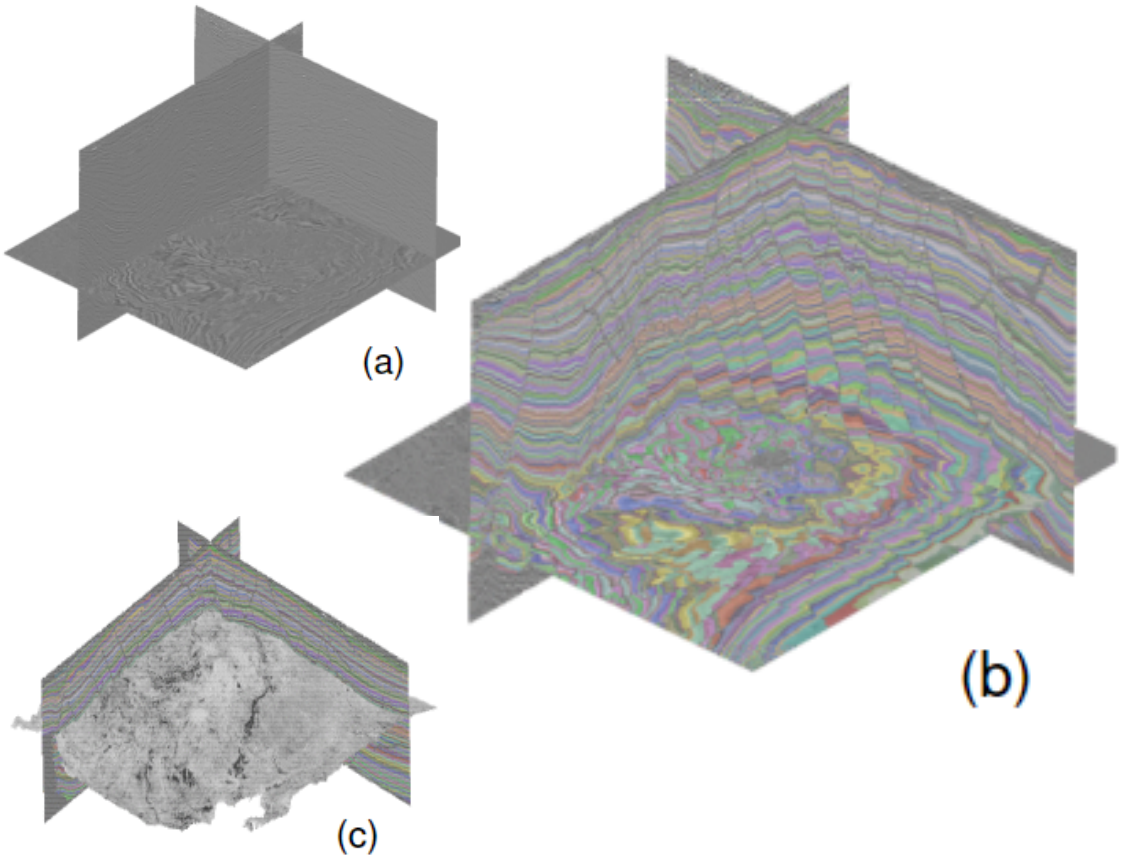


Figure 2.13: a) Seismic cube, b) geomodel calculated from the seismic cube and horizon extracted from the geomodel. From Pauget et al. (2009).

For the 2D numerical modelling of the fold structure (Chapter 5), plane-strain finite-element models were designed and run using the Elfen numerical codes from Rockfield Global (Rockfield, 2010). This software allowed modelling of the folds with the ability to vary input parameters such as mechanical rock properties with relative ease. Initial models were run with a basement fault to create the initial fold perturbation, however this created instability in the model and so a simpler predefined perturbation was used. The depths of the Maykop Formation, which is modelled as the mobile shale layer, was taken from bp p-wave velocity data since no wells penetrate the formation. More information on the methodology of the modelling is included within Chapter 5.

3. Constraints on fold orientations within the South Caspian Basin

This chapter is presented as a draft for a paper. Authors: Andrew Procter, Ken McCaffrey, Lidia Lonergan, Richard Jolly. Regional maps and fold trend orientations were made by Ken McCaffrey during the 2000's whilst on a research fellowship at bp, published in an AAPG presentation, McCaffrey and Jolly (2007).

3.1 Introduction

3.1.1 Introduction to South Caspian Basin

The South Caspian Basin is a tectonically complex, land-locked basin containing a 20 km thick sedimentary succession, one of the thickest successions of any basin on the planet (Allen et al., 2002). The topmost 10 km of its sedimentary fill has been deposited within the last 6 Ma (Devlin et al., 1999) and the rapid sedimentation rates generate abnormal conditions, such as low temperature gradients (Abrams and Narimanov, 1997) and overpressured sediments (Narimanov, 1993, Nadirov et al., 1997). It lies within a zone of complex plate convergence, with the boundaries of the basin constrained by the Great Caucausus, Talysh, Alborz and Kopeh-Dagh mountain ranges to the north, west, south, and east respectively (figure 3.1), see also Chapter 1. The northern limit between the Great Caucausus and the Kopeh-Dagh is defined by a structure known as the Absheron Ridge; with NW-SE trending folds and is interpreted as an accretionary prism (Green et al., 2009). Current earthquake focal plane solutions and GPS data indicate that Iran (Arabian plate) is moving to the N with respect to Eurasia at a rate of 16mm/yr and the Caucasus block is moving NNE with respect to Eurasia at a rate of 13mm/yr (Reilinger et al., 2006). The South Caspian Basin appears to behave as a rigid block, with most of the plate convergence deformation being taken in the surrounding mountain belts (Jackson et al., 2002, Reilinger et al., 2006).

Although located within the centre of a zone of continental convergence, the basin is largely aseismic (Priestley et al., 1994, Jackson et al., 2002), with deep earthquakes focussed beneath the Absheron Ridge and Talysh mountains, most likely due to subduction of the South Caspian on the northern margin and thrusting on the western margin (Khalilov et al., 1987, Priestley et al., 1994,

Jackson et al., 2002, Knapp et al., 2004). Despite this, the sedimentary fill is deformed by young, large amplitude folds which are suggested to detach on an Oligocene – Early Miocene, over-pressured shale, known as the Maykop Formation (Devlin et al., 1999, Brunet et al., 2003, Allen et al., 2003). The folds exhibit a range of trends; including N-S in the west of the basin, E-W in the south, NE-SW in the centre

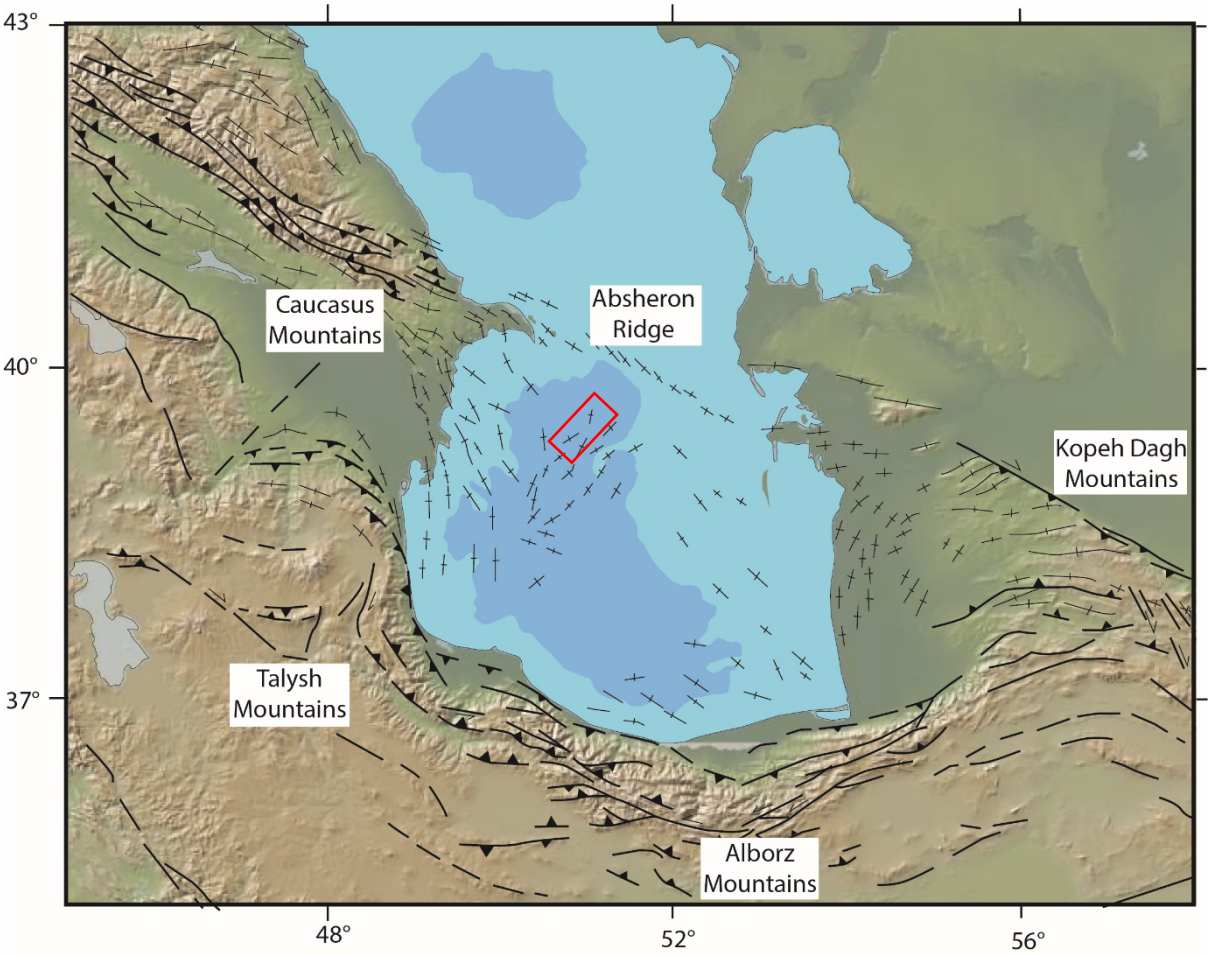


Figure 3.1: Structural map of the South Caspian Basin. Structures taken from Jackson 2002. The Shafag-Asiman fold structure analysed in this study is indicated by the red box. Bathymetry/Topography data are from GeomapApp.

and NW-SE along the Absheron Ridge to the north west, which extends into the dextral Kopeh Dagh fault zone in Turkmenistan (Jackson et al., 2002, Allen et al., 2003) (figure 3.1).

In this chapter we investigate the relative importance of far field tectonics and basement inheritance on fold formation. We show how the interaction of the controls influenced the style and geometry in different parts of the South Caspian basin. We then focus on one fold, the Shafag-Asiman structure (red box in figure 3.1), in more detail as an example of how the folds in the deep-water part of the basin have formed. By analysing the growth strata, we show that the Shafag-Asiman fold formed

in a regime of dextral transpression with 'rotation' or torquing of its axis as it grew, but that its location is constrained by the presence of an underlying ENE-WSW trending basement fault.

3.1.2 Geological History

Geophysical data shows the basement of the South Caspian Basin to have high P-wave velocities of 6.8 – 7 km/s, likely indicating oceanic crust (Rezanov and Chamo, 1969, Berberian, 1983, Zonenshain and Pichon, 1986, Priestley et al., 1994, Mangino and Priestley, 1994). Deep seismic reflection data shows the oceanic crust to be 10 km thick, with the sediment contact at 26-28 km deep (Knapp et al., 2004). There remains some debate as to the origin of the oceanic crust with two models being proposed. The first suggests that the South Caspian basin formed in the Jurassic as a back-arc basin to the north of the subducting Tethyan ocean (Zonenshain and Pichon, 1986, Devlin et al., 1999, Allen et al., 2002, Brunet et al., 2003, Green et al., 2009), and the second suggests it is a remnant of Tethyan oceanic crust left after closure of the during the Black and Caspian Seas in the Tertiary (Berberian, 1983, Nadirov et al., 1997).

The Arabia-Eurasian shortening may have begun as early as 40 Ma (Allen et al., 2003), however, there are two main shortening phases: Oligocene – Miocene Early Arabian compression and Pliocene - Present day Late Arabian compression (Allen et al., 2003, Abdullayev et al., 2012). The Arabian and Iranian plates collided during the early phase, causing the formation and uplift of the Great Caucasus, in the north, and Kopeh Dag, in the south east, orogens (Zonenshain and Pichon, 1986). The tectonic rearrangement that initiated during the Late Arabian phase, ca. 5.5 Ma, caused the onset of subduction beneath the Absheron Ridge and subsequent rapid subsidence of the oceanic crust and creation of accommodation space (Khalilov et al., 1987, Priestley et al., 1994, Jackson et al., 2002, Allen et al., 2002, Knapp et al., 2004). Late Arabian shortening continues to the present day, with uplift of the surrounding Greater Caucuses, Talysh, Kopeh-Dagh and Alborz mountains and the formation of the folds we observe in the present day (Dewey et al., 1986, Jackson et al., 2002, Allen et al., 2003, Brunet et al., 2003, Knapp et al., 2004, Abdullayev et al., 2012). The early Pliocene reorganisation is also expressed as north-south dextral strike-slip faults in the Talysh, and eastern Kopeh Dagh, with sinistral

strike-slip faults in the western Kopeh-Dagh and Alborz (Jackson et al., 2002, Allen et al., 2003, Robert et al., 2014, Santos-Betancor and Soto, 2015).

3.1.3 Stratigraphy

From the Late Jurassic through to the Eocene the South Caspian Sea area formed part of larger seaway that contained connected smaller basins that extended to the Black Sea (Steininger and Rögl, 1984, Popov et al., 2006). During this time, up to 10 km of Cretaceous carbonates and muds were deposited in the basin (Devlin et al., 1999, Green et al., 2009). The collision of the Eurasian and Arabian plate during the 'Early Arabian Compression', in Oligo-Miocene times (Zonenshain and Pichon, 1986) led to regional uplift and episodic restriction of marine conditions (Khain et al., 1991, Inan et al., 1997). During these euxinic conditions, the organic rich black shales of the Oligocene to Lower Miocene Maykop Formation were deposited (Inan et al., 1997). The Maykop Formation is significant as it acts as both the hydrocarbon source rock for the basin (Jones and Simmons, 1998) as well as the detachment surface for the large folds in the area (Shikalibeily and Grigoriants, 1980, Devlin et al., 1999) and source for the numerous mud volcanoes found throughout the basin and onshore in Azerbaijan (Fowler et al., 2000, Kopf et al., 2003). The Early Arabian compression continued into the Late Miocene leading to the closure of the seaway and the basin becoming an inland lake as the South Caspian Sea became isolated (Kerimov et al., 1992, Reynolds et al., 1998).

The Early Arabian compression phase ended at the end of the Miocene and major delta systems (Paleo-Kura, Amu-Darya and Volga) fed clastic material into the basin, forming fluvio-deltaic deposits of the 'Productive Series'- the reservoir interval for the main producing hydrocarbon fields (Reynolds et al., 1998, Abreu and Nummedal, 2007). In places the Productive Series is over 5000m in thickness (Abrams and Narimanov, 1997).

At the end of Productive Series deposition, sediment input to the basin centre decreased and thick evaporites within the Surakhany Formation were deposited within a playa lake in parts of the basin (Green et al., 2009). As reconnection was established to the global ocean via the Black Sea the Akchagyl Formation was deposited during the marine transgression, 2.7 Ma (Devlin et al.,

1999, Green et al., 2009, Lazarev et al., 2019). In the northern part of the centre of the deep-water basin the Akchagyl can reach up to 700m thick (Smith-Rouch, 2006). At ~2.13 Ma (Lazarev et al., 2019) (documented as 1.8 Ma by Green et al. 2009) the basin returned to isolation from the Black Sea and the centre of the basin became the site of extensive, thick, deep-water lacustrine deposition with clastic sediment mainly sourced from the prograding Amu-Darya delta to the east (Abdullayev, 2000) (figure 3.2).

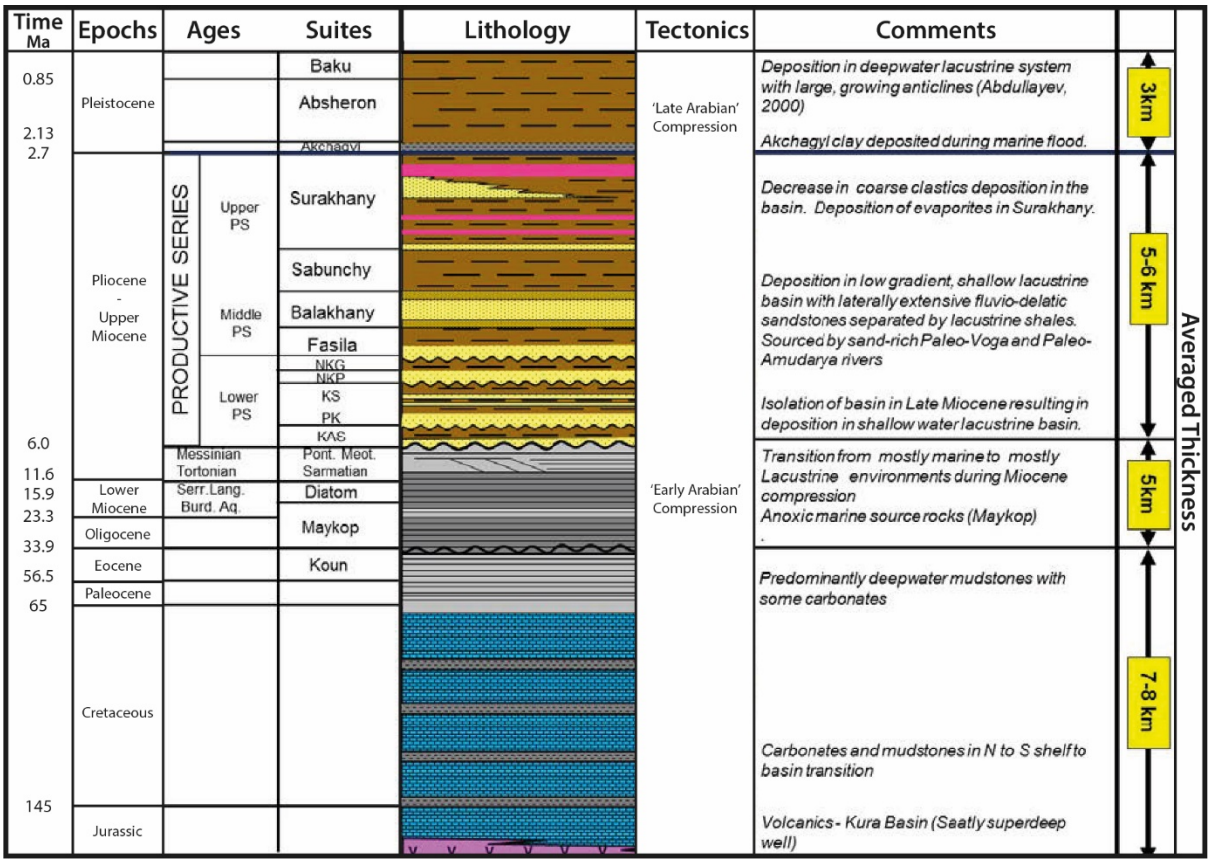


Figure 3.2: Generalised stratigraphic column of the South Caspian Basin. Modified from Abdullayev et al. (2017). Ages are from Popov et al. (2006), Hudson et al. (2008), Lazarev et al. (2019) and Van Baak et al. (2019).

3.1.4. Folding in the South Caspian Basin

Although growth strata shows evidence for fold growth in the Productive Series onshore (Aliev, 1960), seismic data shows that widespread folding in the basin commenced in late Pliocene times (Devlin et al., 1999), at close to the top of the Productive Series (Fowler et al., 2000). The folds are long, linear, domal anticlines, often pierced by mud volcanoes or mud diapirs and with expression

on the modern-day seabed (Devlin et al., 1999, Fowler et al., 2000, Allen et al., 2003, Santos-Betancor and Soto, 2015). From regional 2D seismic reflection data the folds have been described as buckle folds detaching on the underlying Maykop Formation, which also fills the core of some of the folds (Devlin et al., 1999) (Chapter 1).

Fold axis orientations vary across the basin, as do fold geometries (figure 3.1) (Jackson et al., 2002, Allen et al., 2003). The main fold orientations observed generally trend parallel to the large mountain ranges onshore and continue offshore: N-S in the west parallel to the Talysh Mountains, NW-SE in the Greater Caucasus and along the Absheron Ridge and E-W parallel to the Alborz in the south. Folds in the Absheron Peninsular, near Baku, have curved axial traces which are associated with thick Plio-Pliocene strata, akin to the basin offshore (Allen et al., 2003). Within the deep-water part of the basin, where Shafag-Asiman is located, we see puzzling fold axis trends of NW-SE.

Devlin et al., (1999) describe relatively symmetrical folds, with crestal normal faults in the shallowest stratigraphy near the fold, with low-angle reverse faults in the deeper parts of the fold, formed by bedding plane slip and detaching on the Maykop at 10 - 12 km depth. A more recent study by Santos Betancor and Soto (2015) using 3D seismic reflection data imaged a fold offshore the western margin of the basin, the Kurdashi-Araz Deniz structure. The authors demonstrate that the 7 km wavelength fold has two culminations cut by mud diapirs, but rather than being symmetrical, it has an east-vergent forelimb and has thrusts on both limbs. The authors proposed that the detachment fold developed above a normal fault with a component of dextral strike-slip motion, and that the later phases of the growth were enhanced by flow of mud along the strike of the fold into the culmination. Fowler et al., (2000) describe the Shah Deniz fold structure offshore in the north of the basin, 70 km southeast of Baku using 3D seismic reflection data. They interpret a deep pre-Oligocene thrust coring the structure along its strike as well as a reverse fault that detaches into the Maykop series. Extensional crestal faults sole out into the Surakhany Formation evaporites.

In this chapter, the relative importance of far field tectonics and basement inheritance is investigated by: a) examining the differing fold patterns and geometries on regional maps based on the interpretation of 2D seismic reflection (max 8s TWT) data shot over the western part of the basin (McCaffrey and Jolly, 2007) (b) investigating one of the NW-SE folds in the centre of the basin in more detail, Shafag-Asiman fold structure, and showing how its trend is partially constrained by the trend of an underlying basement structure and that the fold has rotated right-laterally as it has grown.

3.1.5 Datasets

Regional fold patterns are mapped from a regional grid of 2D seismic lines covering the South Caspian Basin. Seismic data used to image subsurface folds of the South Caspian are based on 1995 vintage good quality 2D seismic reflection data (McCaffrey and Jolly, 2007).

The detailed fold was studied on a 3D seismic reflection pre-stack depth migrated depth dataset over the Shafag-Asiman structure (figure 3.1) (Chapter 2), located approximately 100 km south of Baku in water depths of approximately 900 m. The cube covers an area of 1655 km^2 and images to a total depth of 13 km, the top 4 km which is the focus of this thesis. The data are standard polarity with an inline and crossline spacing of 25 m by 25 m with a sample rate of 4 ms and a vertical resolution of approximately 11.25 m, yielding high quality data of standard polarity. There are no well data available from the block.

3.2 Methodology

3.2.1 Regional folds (work by Ken McCaffrey)

The regional fold patterns were analysed by mapping key stratigraphic events on the regional 2D seismic reflection data. These data were tied to wells at the margins of the basins. The fold patterns are analysed on a map within the Productive Series. These horizons were viewed as surfaces in GoCAD™ and the dip azimuth attribute calculated to illustrate the fold patterns.

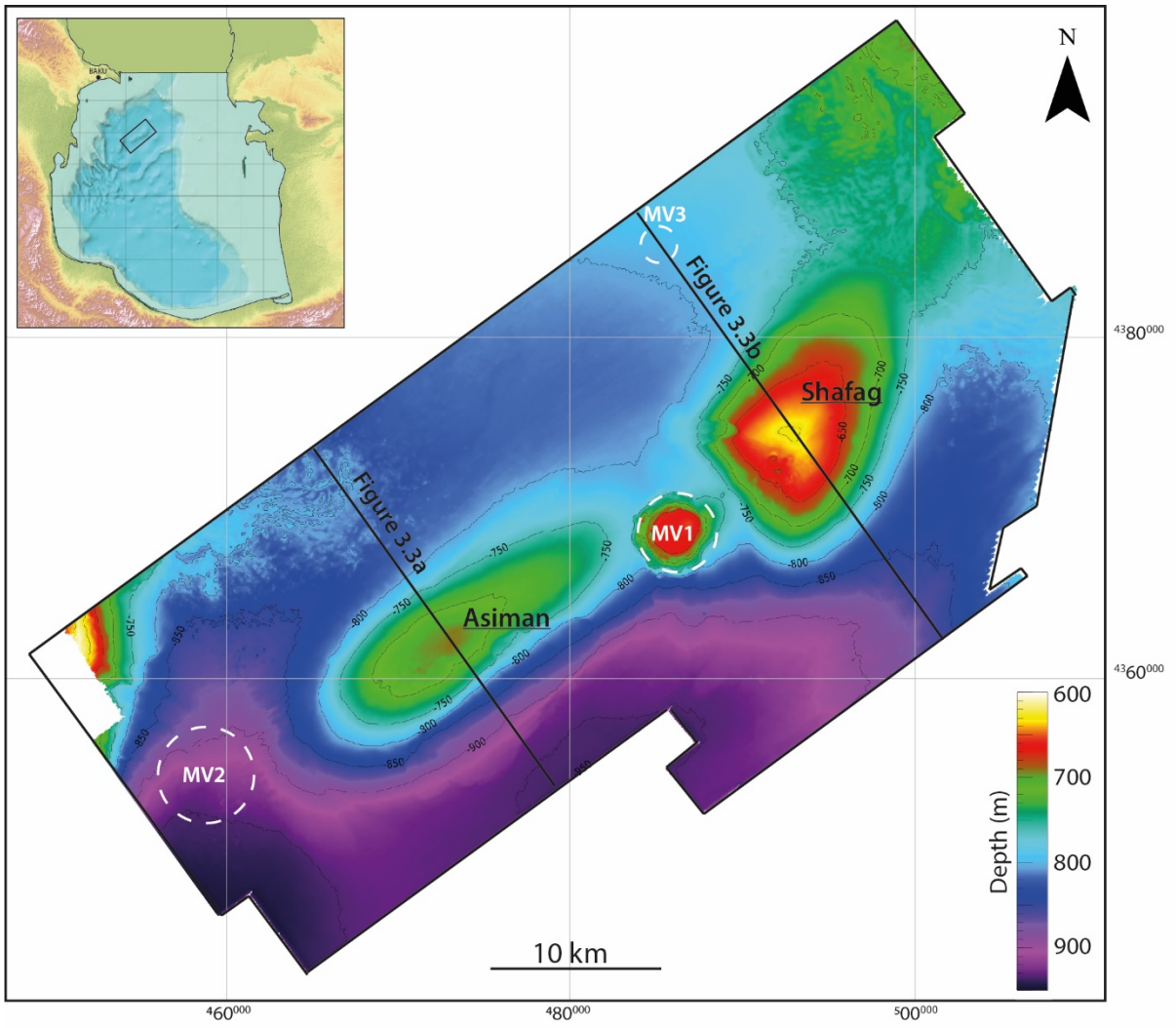
3.2.2 Shafag-Asiman fold

The dataset images two fold accumulations (figure 3.3a), Asiman to the west (figure 3.3b) and Shafag to the east (figure 3.3c) as well as three mud volcanoes, two of which, MV2 and MV3 are not active on the present day seabed (figure 3.3a), The period of significant fold development occurred after the Productive Series and therefore we focussed our analysis on the Plio-Pleistocene Akchagyl and Absheron Formations, which encompass an age range of approximately 2.7 Ma – 0.85 Ma (Lazarev et al., 2019, Jorissen et al., 2020).

Seven horizons were mapped based on seismic character and continuity within the Akchagyl and Absheron Formations. Additionally, one deep horizon beneath the Oligo-Miocene Maykop Formation was mapped to assist with understanding whether there is any basement control on the fold formation. Based on regional correlations from well ties outside of the study area, we interpret the lowest Post-Productive Series horizon, Hz 100, to represent the base Akchagyl Formation, Hz 110 the base of the Absheron Formation. and Hz 160 the top of the Absheron Formation. Horizons were then used for the creation of isopach maps which can used to demonstrate the development of the folds through time. For a simple symmetrical buckle fold growing during sediment deposition, isopach maps would be expected to demonstrate similar contour shapes through time. The absolute thickness values would change due to varying sedimentation rates, but the contour shapes would be self-similar through the structure. Any deviation from this simple fold model gives an insight into how the fold has grown through time. Faults were interpreted on the standard amplitude data as well as with a dip-discontinuity cube (chapter 2).

Since there are no well data, we can only assign ages to the base Akchagyl (Hz 100), 2.7 Ma (Van Baak et al., 2019), and the base (Hz 110) and top (Hz 160) Absheron, 2.13 Ma and 0.85 Ma respectively (Lazarev et al., 2019, Jorissen et al., 2020). Across the fold, changes in stratal thickness occur within the Absheron Formation, (Figure 3.3b and 3.3c), showing that the fold was growing during formation deposition. We mapped high amplitude events within the Absheron Formation. that continue over the fold to map, Hz 100 - Hz 160. True stratigraphic thickness maps are presented for intervals between Hz110 – Hz150.

a)



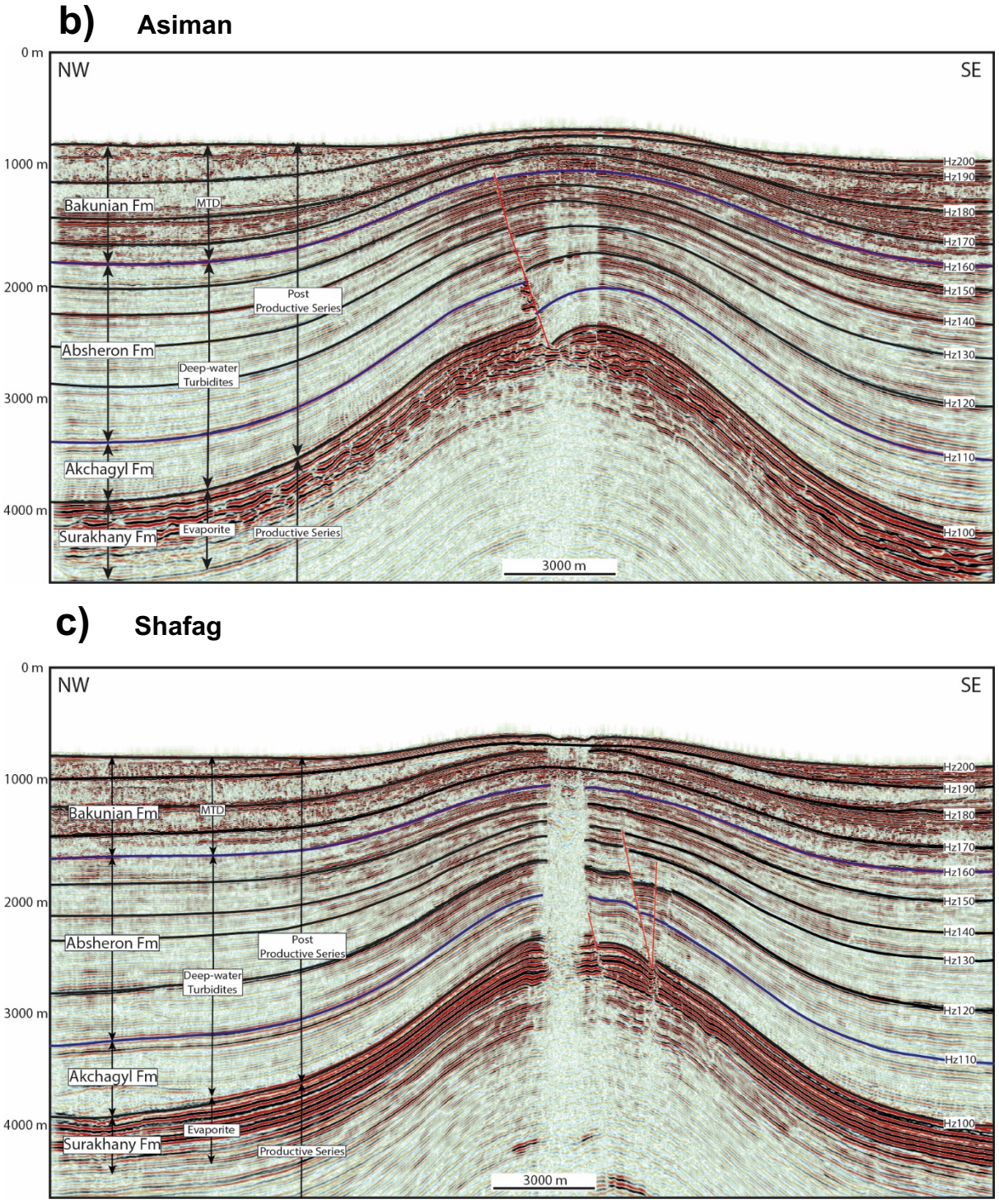


Figure 3.3: a) Map of the seabed of the Shafag-Asiman fold structures, with inset location of map within the South Caspian Basin. The three mud volcanoes MV1, MV2 and MV3 are highlighted in white circles. MV1 is presently active on the seafloor, whereas MV2 and MV3 are extinct. Seismic sections through b) Asiman and c) Shafag highlighting the stratigraphy of the Shafag-Asiman fold structures. Vertical exaggeration = 3.2x.

3.3 Results

3.3.1 Regional fold mapping

A dip-azimuth map calculated from a horizon mapped within the Productive Series illustrates fold limb dips very clearly and allows fold axes to be mapped (figure 3.4). The dip direction (azimuth) is shown on a varying colour bar from 0 to 360 degrees (figure 3.4a). East to southeast dipping limbs of the mapped surface are shown in yellow-green colours, whereas southwest to northwest dipping

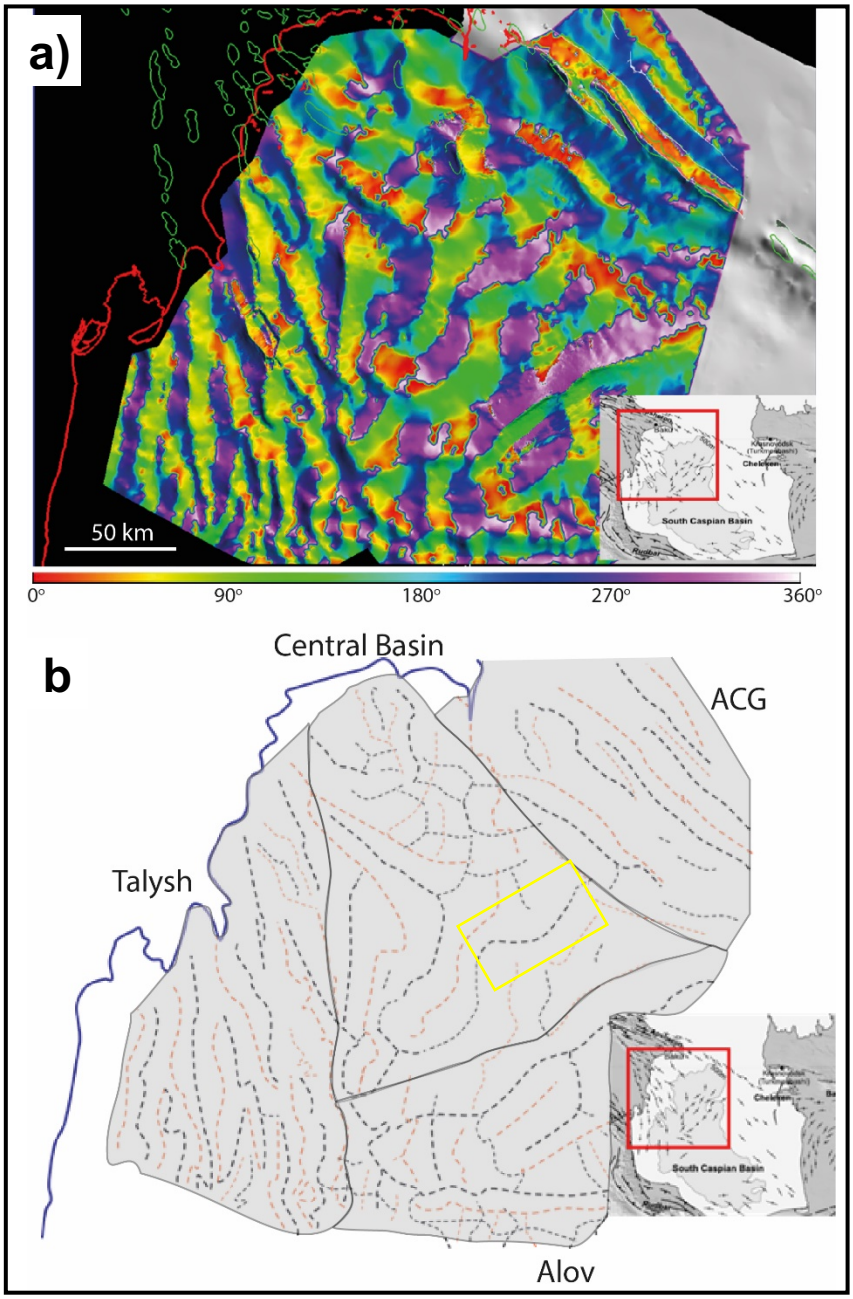


Figure 3.4: a) Dip azimuth map of the northern South Caspian Basin and b) map of interpreted folds. The colour scale is shown beneath the map where the colours indicate the dip direction (azimuth) of the mapped horizon. Fold anticlinal axes are in black dashed lines and synclinal axes are in red dashed lines. Four fold domains have been interpreted, Talysh, central basin, ACG and Alov. Work of Ken McCaffery. Inset map from Jackson et al. (2002). The Shafag-Asiman dataset is shown by the yellow box.

limbs are in blue-purple colours. North dipping fold limbs are in red (figure 3.4a). The anticlinal (black dashes) and synclinal (red dashes) axes are interpreted from the dip directions (figure 3.4b).

From the dip azimuth map, four fold domains have been identified, three zones are dominated by broadly linear, sub parallel folds. In contrast the central part of the northern South Caspian Basin has a very complex fold pattern.

Talysh (western sector of the basin): The area is dominated by N-NW to N trending fold hinge traces up to 100 km in length but predominantly shorter, c. 30 km. There are some E–W trending fold axes (zones of red, north dipping limbs) that link the N-S trending folds, acting as transfer structures.

ACG (north-eastern sector of the basin): This area of the basin is dominated by large ESE-WNW trending folds with axes that extend up to 80 km. Fold traces are parallel to the Absheron Ridge.

Alov (southern sector of the basin): The zone is dominated by some long (first order) NE-SW to E-W trending folds, up to 80 km long. It also contains a number of short fold hinges which trend N-S which appear to be second order forming cross-links between the first order folds.

Central Basin (central sector of the basin): This zone is broadly triangular, flanked by the other three zones. Folds patterns are more inconsistent often giving short dip panels with a variety of orientations. There are NE-SW trending folds in the south and eastern part of the area, which includes the Shafag – Asiman fold axis. N-S trending folds occur in the west and the northern part of the area is dominated by egg-box shape structures, where domes of three anticlinal axis meet and circular basinal synclines form with intervening anticlines that show annular patterns.

3.3.2 Shafag-Asiman fold structure

3.3.2.1 Fold Geometry

The seismic reflection data covers two culminations known as the Shafag and Asiman fold structures. Presently, the fold hinge of Asiman trends at 060 and Shafag at 020 (figure 3.3a). The folds are elliptical in map view and have a saddle between the two crests which is 26 km long which includes a 4.5 km wide mud volcano (figure 3.3a). The Asiman axial trace is 25 km long and the Shafag trace is

18 km long. The folds are broad and have a wavelength of approximately 40 km. Measured at the Absheron level, the folds have an amplitude of 900m although this decreases towards the seabed. The folds are upright, detachment folds which deform the entire stratigraphy, appearing symmetrical (figure 3.3).

The growth strata between Hz100 to Hz160 consist of packages that thin over the fold crest but events can be mapped that overlap the fold as well as thin over the fold crest (figure 3.3). The onlapping events show that there were periods where the fold must have had a seabed expression, but onlapping shows times when the fold was buried due to either increased sedimentation rate or reduced fold growth rate. The growth strata thicknesses are asymmetrical across the folds, for example on Asiman between Hz100 – Hz160, the sediment is 2 km thick in the northern syncline and 2.3 km thick on the southern syncline (figure 3.3b).

3.3.2.2 Isopach Maps

Four isopach maps are displayed in figure 3.5, consisting of the base Akchagyl Formation, Hz100, to the Top Absheron Formation, Hz110 and demonstrate the changes of sediment thickness distribution within the Plio-Pleistocene and document the timing of activity of crestal faults. The isopach maps provide a very interesting insight into how the shape of the fold changes as it grows. The isopach maps can display the fold axis at the time of deposition, with sediment thinning onto the crest of the fold. The distribution of the sediment along the fold, both by thinning over the crest and the elliptical distribution of the sediment can allow for the orientation of the fold axis to be interpreted. Whilst interpretation of the fold axis from a depth structure map using dip measurements will give a more accurate fold axis orientation for the present day, interpreting the historical fold axis orientation from isopach maps can be used to show changes in fold geometry through time.

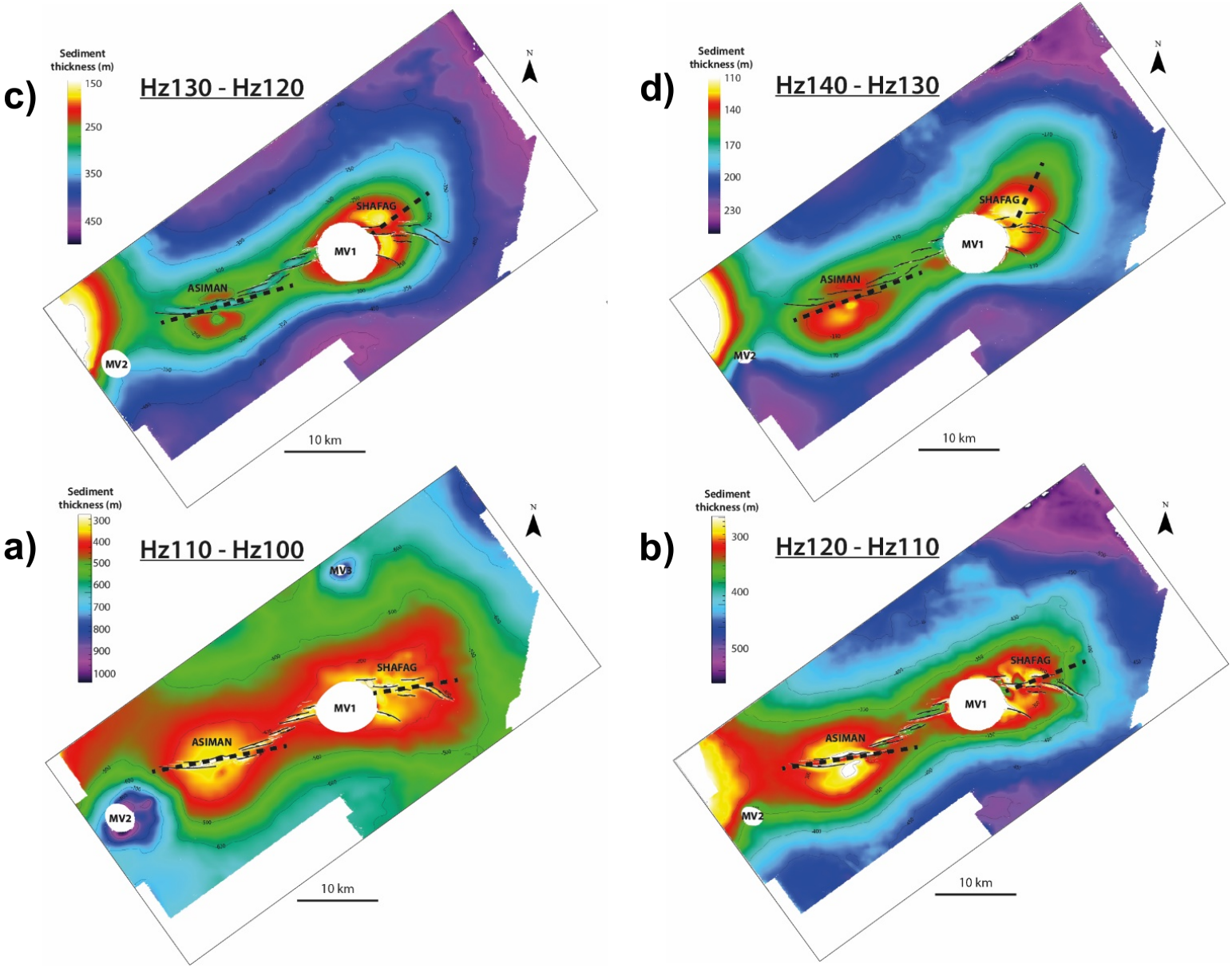


Figure 3.5. Isopach maps for intervals from a) Hz110 – Hz100, b) Hz120 - Hz110, c) Hz130 – Hz120, d) Hz140 – Hz130. White circles are due to seismic wipe out from mud volcanoes. The axial trace location during each interval is shown by a black dashed line.

The Hz110 – Hz100 isopach map within the Akchagyl Formation shows that at this time, the fold axial traces were oriented 080 for both folds (Figure 3.5a). Moving up the stratigraphy, from the isopach for Hz120 – Hz110, the orientation of the Asiman fold crest remains the same, but the axial trace for the Shafag fold has changed to approximately 070 (figure 3.5b). From isopach Hz130 – Hz120 both fold axes rotate anticlockwise, with the Asiman axis rotating to 070 and the Shafag axis rotating more significantly, to 045 (figure 3.5c). The fold axes rotate to the present-day orientation within interval Hz140 – Hz130, with Asiman orientated at 060 and Shafag at 020 (figure 3.5d).

3.3.2.3 Post-Productive Series Faults

Two sets of normal faults are found in the Post-Productive series (figure 3.6). The first set occur along the crest of the folds and the second set are ring faults associated with the large mud volcano located between the two folds.

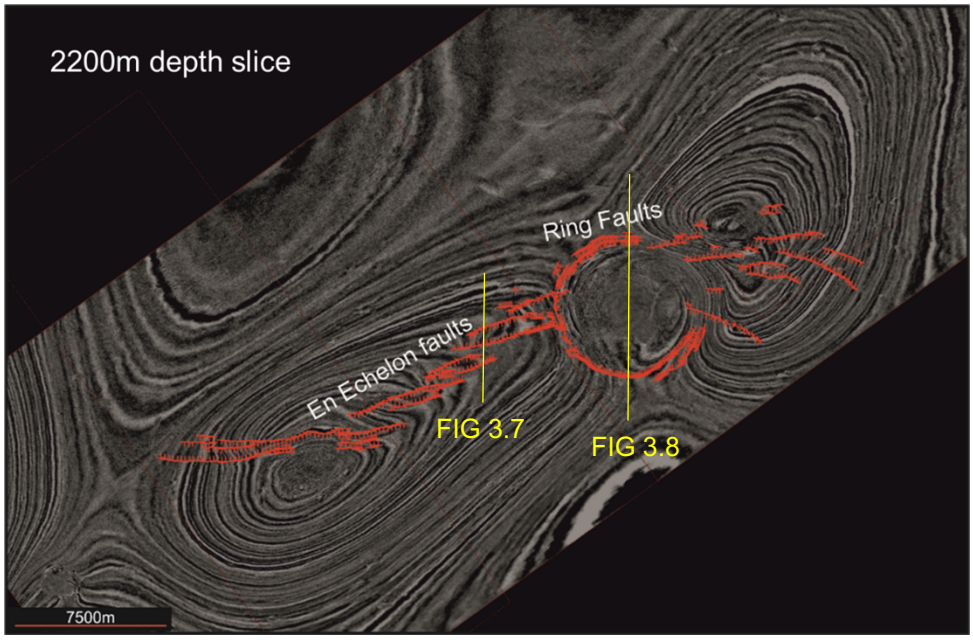


Figure 3.6: Depth slice at 2200m, showing the two major fault styles observed within the Post-Productive Series. En-Echelon crestal normal faults and normal ring faults.

The normal faults located across the crests of the folds generally trend E-W (Figure 3.6). They are located between 1.5 km and 4 km depth in the seismic reflection data and die out into the evaporites of the Surakhany Formation (top of Productive Series) (figure 3.7). They have small throws, between 50-200 m. The faults trend east-west over the Asiman crest and form en-echelon grabens within an

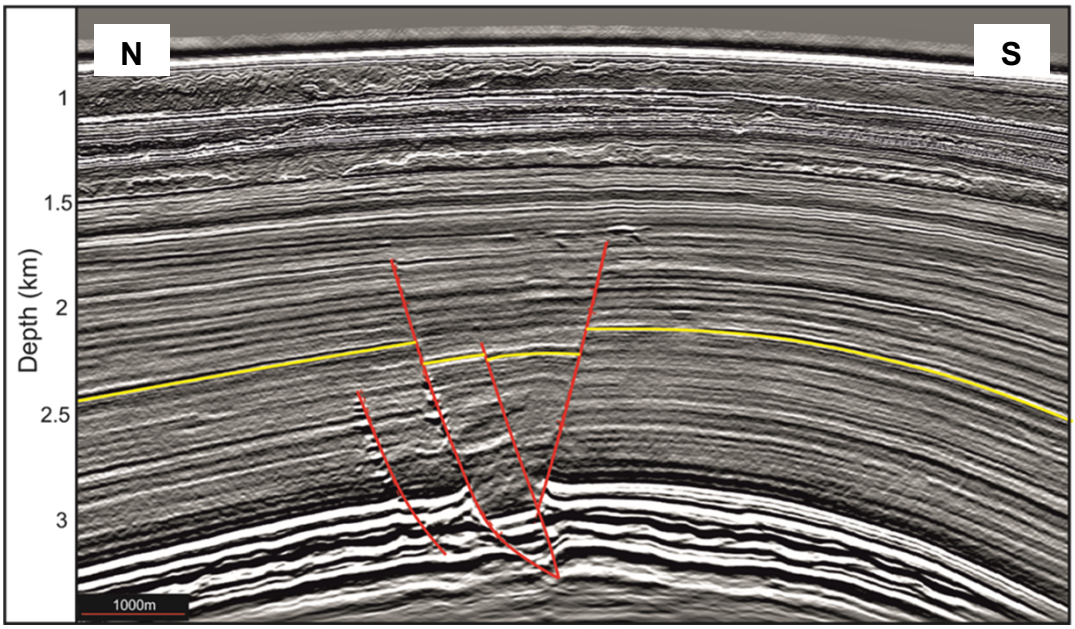


Figure 3.7: En-Echelon normal faults that extend along the fold crests. The yellow horizon is used to indicate the fault displacement. Section location indicated in figure 3.6.

overall NE-SW trending zone, terminating at the mud volcano. Over the Shafag structure the faults are more diffuse and swing round to trend E-W with three faults trending NW-SE (figure 3.6). In plan view, the entire set are en-echelon and sigmoidal (Figure 3.6). Isopach maps show sediment growth into the crestal normal faults (figure 3.5). Growth within the grabens of the faults initiates within Hz120 – Hz110, with growth of 30 – 40 m (figure 3.5b). Sediment growth into the faults continues within Hz130 – Hz120, reaching up to 100 m on the crest of Asiman (figure 3.5c). Moving into Hz140 - Hz130, the sediment growth into the faults continues, however the thickness decreases to a maximum of 20m (figure 3.5d).

The ring faults form around the flanks of the 4 km wide mud volcano that is situated between the Shafag and Asiman fold crests. The mud volcano is currently active on the present-day seabed (figure 3.3a). They are located between 1.5 km and 4 km depth and are densely spaced, creating half grabens tens of metres apart (Figure 3.8). Although sediment growth occurs in a peripheral trough around the mud volcano, the ring faults do not show any sediment growth (figure 3.5 and 3.8)

The sigmoidal fault pattern suggests that there is an element of shear taking place during fold formation, rather than purely compressional forces. The sigmoidal pattern of the extensional faults demonstrates that the fold was being affected by dextral transtension. More evidence for the shear is the apparent horsetail splay pattern to the east, over Shafag. Other folds within the basin with similar

crestal normal faults have been interpreted as outer-arc extension on a buckle fold with layer parallel shear (Devlin et al., 1999, Santos-Betancor and Soto, 2015). The ring faults situated around the large mud volcano are due to mud evacuation and subsequent collapse of the strata to produce a caldera-like feature. This is evidence for shale movement within the fold evolution history.

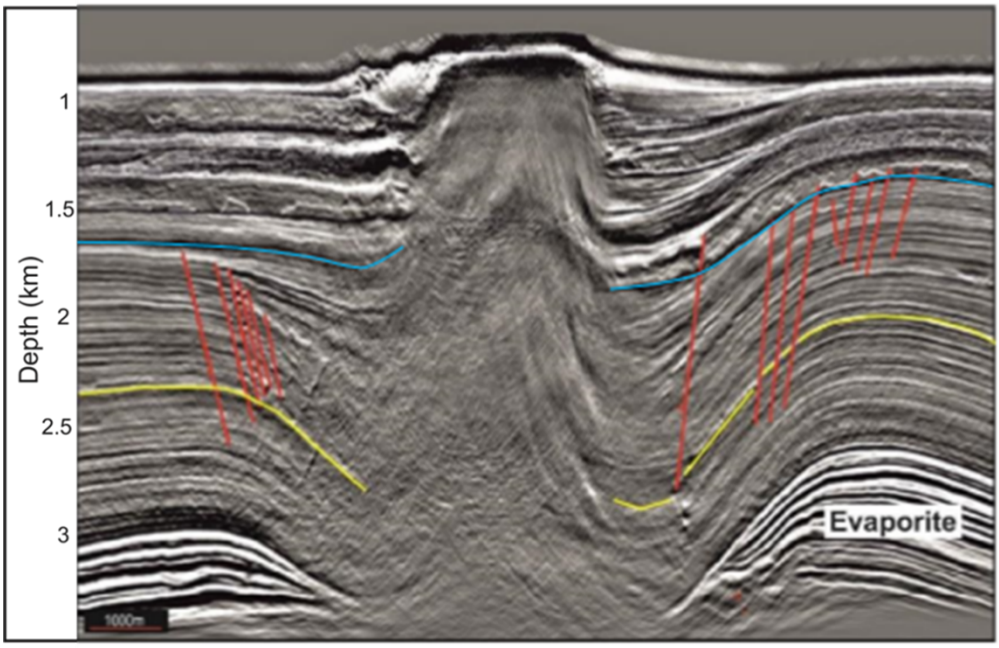


Figure 3.8: Ring faults around the large mud volcano that erupts onto the surface between the Shafag and Asiman fold crests. Section located on figure 3.6.

3.3.2.4 Pre-Productive Series Faults

A large, deep, NW-SE trending fault ~ 40 km in length occurs beneath the Shafag-Asiman fold structure. It dies out at approximately 10 km depth in the dataset beneath the Productive Series. It extends to the base of the seismic dataset, deforming the Maykop and deep pre-Maykop stratigraphy. The fault is best observed on a depth-structure map of a horizon lying beneath the interpreted Maykop Formation (Figure 3.9a, b) and shows the Asiman fold and part of the Shafag fold form directly above this fault. A section through the seismic data images the fault beneath the Maykop (figure 3.9c) Since the fault continues to greater depths than the seismic reflection dataset, it is difficult to describe the fault in considerable detail as it is likely that it is the tip of the fault that is imaged (figure 3.9c). Data at this depth is of poor quality so there is significant uncertainty in the depth map interpretation. From the depth map and section, the fault can be interpreted to dip to the NW and appears to be an inverted normal fault and possibly has a throw of up 1 km (figure 3.9c).

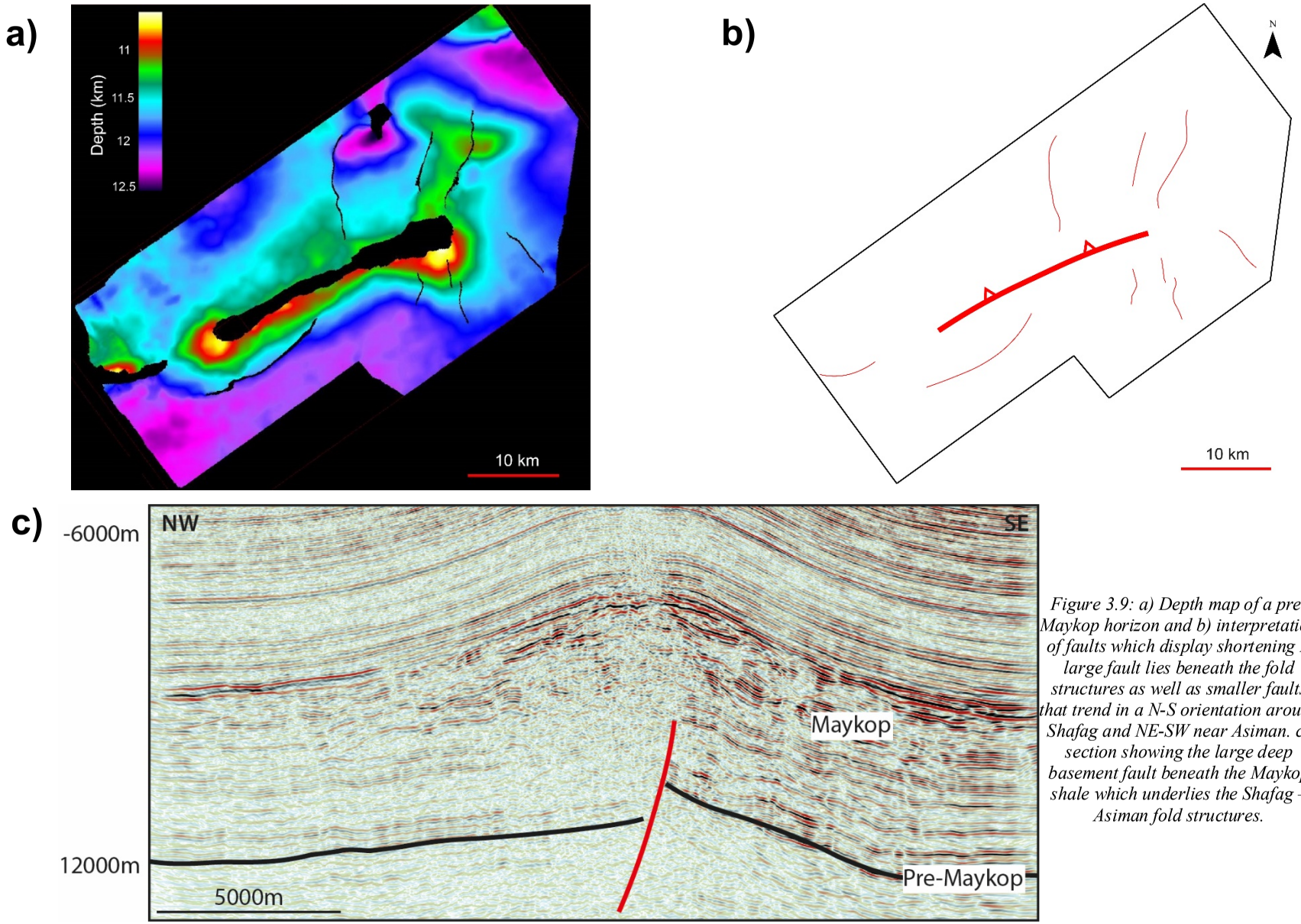


Figure 3.9: a) Depth map of a pre-Maykop horizon and b) interpretation of faults which display shortening A large fault lies beneath the fold structures as well as smaller faults that trend in a N-S orientation around Shafag and NE-SW near Asiman. c) section showing the large deep basement fault beneath the Maykop shale which underlies the Shafag – Asiman fold structures.

Due to the lack of data available, the reverse fault is interpreted to be either an inverted normal fault or thrust fault and may possibly display strike-slip movement It can be concluded however that some degree of shortening has occurred along the fault. A series of smaller faults trend broadly north-south (figure 3.9a, b) are associated with the large fault. These faults are concentrated in the east, under the Shafag fold. The largest of these faults trends NNW-SSE, which is the same as the present day Shafag axial trace.

The deep faults lie below the Productive Series, in the Pre-Miocene stratigraphy. The largest fault runs directly beneath the Asiman fold and appears to be controlling the orientation of the fold. Some previous workers have described similar folds as buckle folds upon a mud detachment, which developed in the Post-Productive series (Devlin et al., 1999, Allen et al., 2003). However, other studies have also described folds in the basin to be controlled and initiated by shortening along the deep-lying Mesozoic faults (Abrams and Narimanov, 1997, Fowler et al., 2000, Santos-Betancor and Soto, 2015). Fowler et al. (2000) describe the Pre-Productive Series faults below Shah Deniz, a NNW-SSE trending fold 50 km north of Shafag-Asiman, to be thrusts. Santos-Betancor and Soto (2015) describe the faults below a NNW-SSE trending fold 120 km west of Shafag-Asiman to be reactivated normal faults, with a likely element of strike-slip. These studies have similar limitations to our study as the seismic reflection data do not image the entirety of the faults. Our analysis of the Shafag-Asiman structure suggests that the fold has developed above a thick (over 1 km thick) mud detachment, directly overlying an older, deeper fault but we cannot conclusively state whether the fault was a thrust or a reactivated, older Pre-Maykop normal fault. We can conclude, however, that the fault has undergone shortening. The large fault does not extend fully under the Shafag fold axis. A smaller fault lies directly beneath Shafag and is parallel to the present-day fold axial trace. This small fault appears to have a much smaller throw than the large fault under Asiman and does not appear to control the orientation of Shafag as much as the large fault controls the location of Asiman, since it lies beneath the 1-2 km scale thickness of the Maykop and is detached from the folds.

The three mud volcanoes within the dataset are all located above the deep lying faults, a feature also observed at Shah Deniz (Fowler et al., 2000). Sediment thickening around the volcanoes during the Post-Productive Series (figure 3.5a) suggests that there is shale movement during the formation of

the fold structures, and this may be why we see asymmetry of growth strata on the flanks of the fold. Shale movement may be significant in the development and amplification of the Shafag-Asiman fold, as has been proposed by Santos-Betancor and Soto (2015). The impact and timing of shale movement and sediment loading on fold growth is discussed in subsequent chapters.

To summarise, the Shafag-Asiman structure is a non-cylindrical fold with two culminations, with an anticlinal hinge trace that broadly trends NE-SW over Shafag at the present day but that has rotated as the structure has grown, implying that fold axial plane is not planar but torqued. Whilst a complex fault pattern that deforms the Pre-Productive Series lies beneath the folds, younger strata are deformed by sigmoidal, en-echelon normal faults in graben sets that were active as the folds were growing.

3.4 Discussion

3.4.1 Formation of the Shafag-Asiman fold structure

At its simplest, the area is dominated by a large, broad, NE-SW trending anticline and one would predict that it formed due to SE-NW oriented compression. However, the existence of en-echelon crestal normal faults along the fold hinge suggests that there is transtension on the fold crest and a component of strike-slip shear associated with the fold formation, and hence the fold has formed due to transpression. The orientation of the en-echelon faults, and their overall sigmoidal geometry indicate that the main fold is forming within a zone of broad dextral transpression, that trends NE-SW, broadly parallel to the present day Asiman and Shafag axial traces. The increased dextral shear causes the torsion of the fold axial plane as the fold attempts to align perpendicular to the local dextral principal stress (Sanderson and Marchini, 1984)(Pollard and Segall, 1987), which is why, perhaps counterintuitively, the fold axes rotate anticlockwise through time (Section 3.2.2) (figure 3.10).

The weak underlying detachment acts as a free surface, which probably contributes to the fold being able to rotate, or more accurately torque, as it grows (figure 3.11). A shale intrusion along the

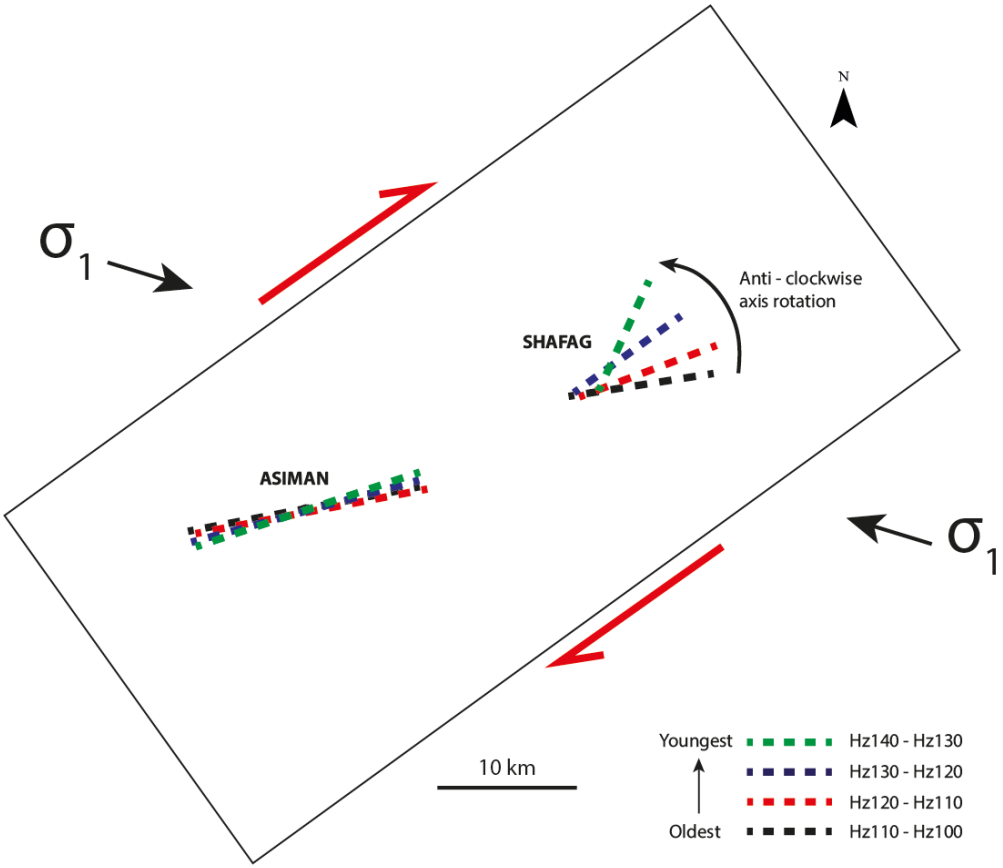


Figure 3.10: Interpretation of fold axial traces from isopach maps from Hz100 to Hz140 showing anticlockwise rotation and inferred dextral shear of the Shafag – Asiman fold structures.

axial plane will create a weakness, so dextral shear will be induced with a very small angle of obliquity. This may mean that the regional horizontal maximum stress is still SE-NW as indicated by Jackson et al. (2002) but due to the weak core, the fold locally rotates slightly anticlockwise in response to the dextral transpression (Sanderson and Marchini, 1984) (figure 3.12).

If new smaller folds were to develop within the zone, we would expect them to form in an en-echelon pattern and be oriented NNE-SSW. They would be likely to show sigmoidal dextral rotation as per the many studies of shear zone structures that exist in the literature (Moody and Hill, 1956, Harland, 1971, Harding, 1973, Wilcox et al., 1981, Sanderson and Marchini, 1984). Similarly, if strike-slip tectonics dominated the area and the Shafag and Asiman fold structures themselves were forming within

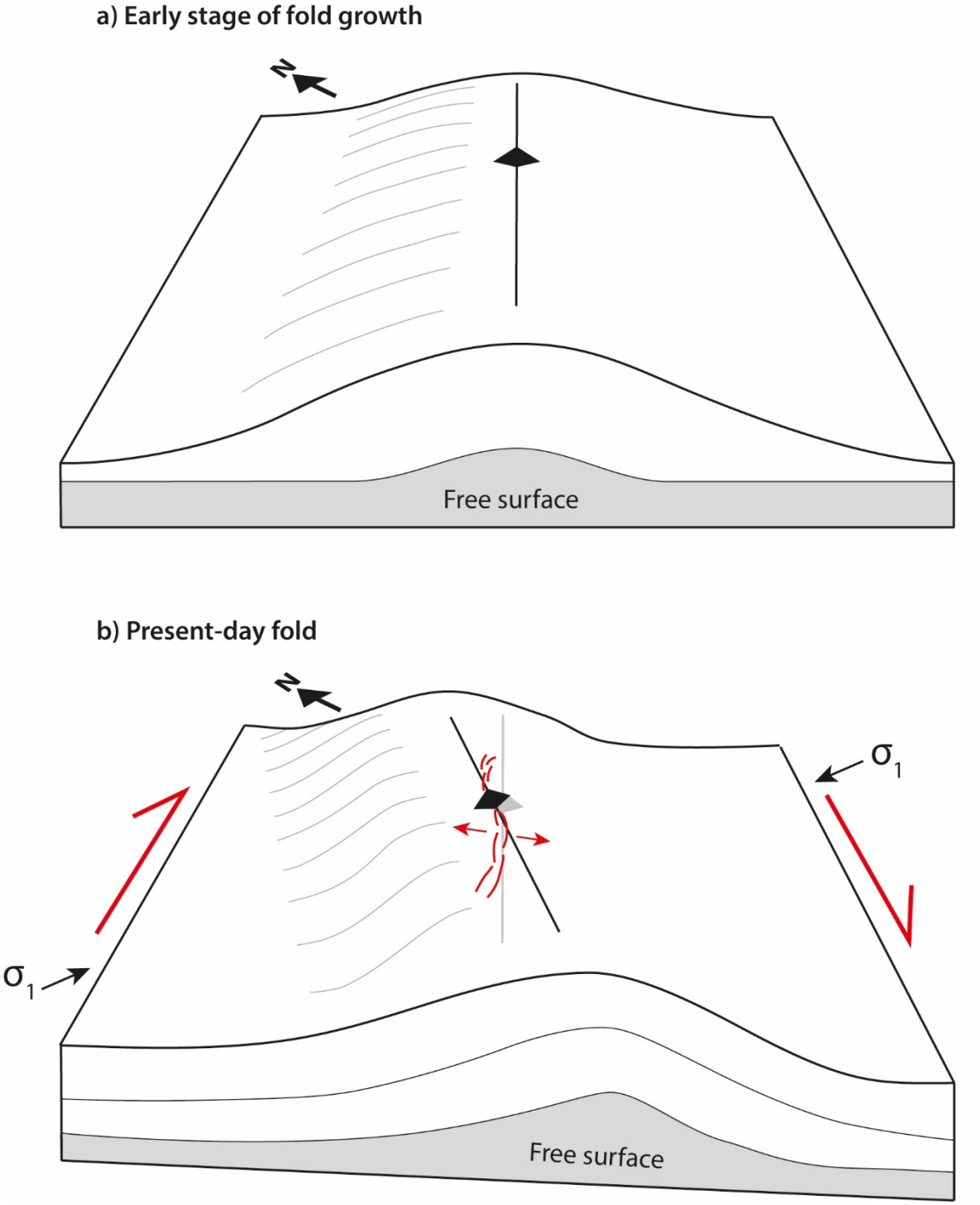


Figure 3.11: Block diagram demonstrating the a) pre-dextral transpression and b) post-dextral transpression, showing the anti-clockwise rotation of the fold axis and development of en-echelon crestal normal faults (red).

a large dextral shear zone, then we would expect their individual axes to have been oriented N-S and the folds to have formed as separate en-echelon structures as opposed to two collinear structures. These observations further support our conclusion that shortening dominates the regional deformation, with a component of dextral transpression.

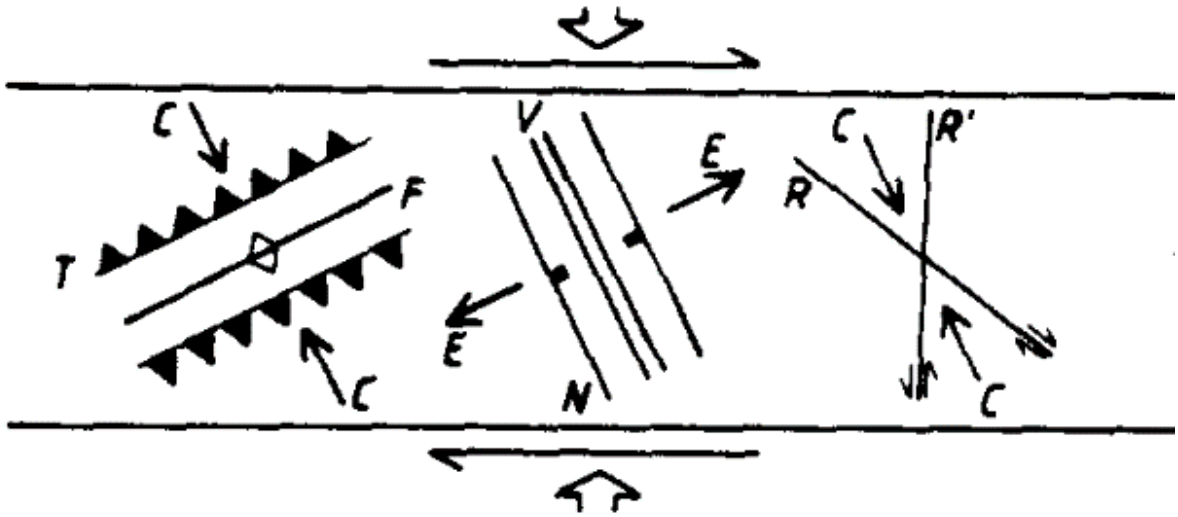


Figure 3.12: Map view of structures formed during dextral transpression. C = compression axis σ_1, E = extensional axis σ_3, T = thrusts faults, N =normal faults, F =fold axis, V =veins or extensional fractures. R = Riedel shears. Both the orientation of the fold axis and crestal extensional faults in relation to σ_1 displayed in the transpressional model are observed on Shafag-Asiman. Taken from Sanderson and Marchini (1984).

We think that this may be the first time that the torquing of a fold axial surface with an apparent opposite sense of rotation to the rotation in the zone of the transpression has been documented. We suspect that it is a function of previously not having full 3D imaging of large folds, as this 3D seismic reflection volume has afforded us. The fact that such clear growth strata are also preserved, also assisted us in making the observations, because each isopach interval recorded the fold crest for that specific time interval and gave us a proxy for mapping the axial trace of the fold hinge.

3.4.2 Regional Context

The observations and interpretations we make about the Shafag-Asiman fold suggest that there is a complex structural history in the deep-water South Caspian Basin. The regional observations also show that complex fold patterns occur across the entire basin. As stated previously, we classify the structures in the basin into four regional domains. The domains are based on the fold geometries and orientations, and we suggest that they are formed by two main factors which vary in importance for each domain: 1) far field tectonic control and 2) basement control (pre-existing thrusts, inverted normal faults).

3.4.2.1 Controls on Regional Fold Patterns

Initial basin formation was likely caused by Jurassic rifting (Brunet et al., 2003, Green et al., 2009), with compressional forces likely not affecting the central part of the basin until the Oligo-Miocene, due to N-S convergence of Eurasia and Arabia. As stated previously, the deep fault that we interpret under Shafag-Asiman, which may have initially formed as a normal fault, has experienced shortening, and possibly inversion, during the shortening. The shortening could have occurred as either the reactivation of basin forming Jurassic normal faults during the Oligo-Miocene early Arabian compression or as thrust faults formed during the early Arabian compression. If the fault is a reactivated normal fault, it could be a reactivated transform fault which was formed during Jurassic rifting (Abdullayev et al., 2017) as is postulated for the large Alov structure to the south which trends in a similar orientation to the deep Shafag-Asiman fault. The deep fault consequently controls the location of the Shafag-Asiman fold. Therefore, basement control is critically important for forming the fold patterns observed within the Shafag Asiman area. Santos-Betancor and Soto (2015) also show that in the Talysh domain, in the west of the basin, deep Pre-Productive Series normal faults control the N-S orientation of the fold patterns. We suggest that the control is due to the interaction of the early phase of Arabian shortening, from the Oligocene – Miocene with the pre-existing basement faults, as the northward movement of the Alborz mountains generated shortening on the faults (Abdullayev et al., 2012). In the ACG domain, the fold orientations are controlled by the location of deep accretionary prism under the Absheron Ridge which was also initiated due to early Arabian shortening prior to the deposition of the Productive Series (Jackson et al., 2002, Knapp et al., 2004, Robinson et al., 2005, Stewart and Davies, 2006) (figure 3.13).

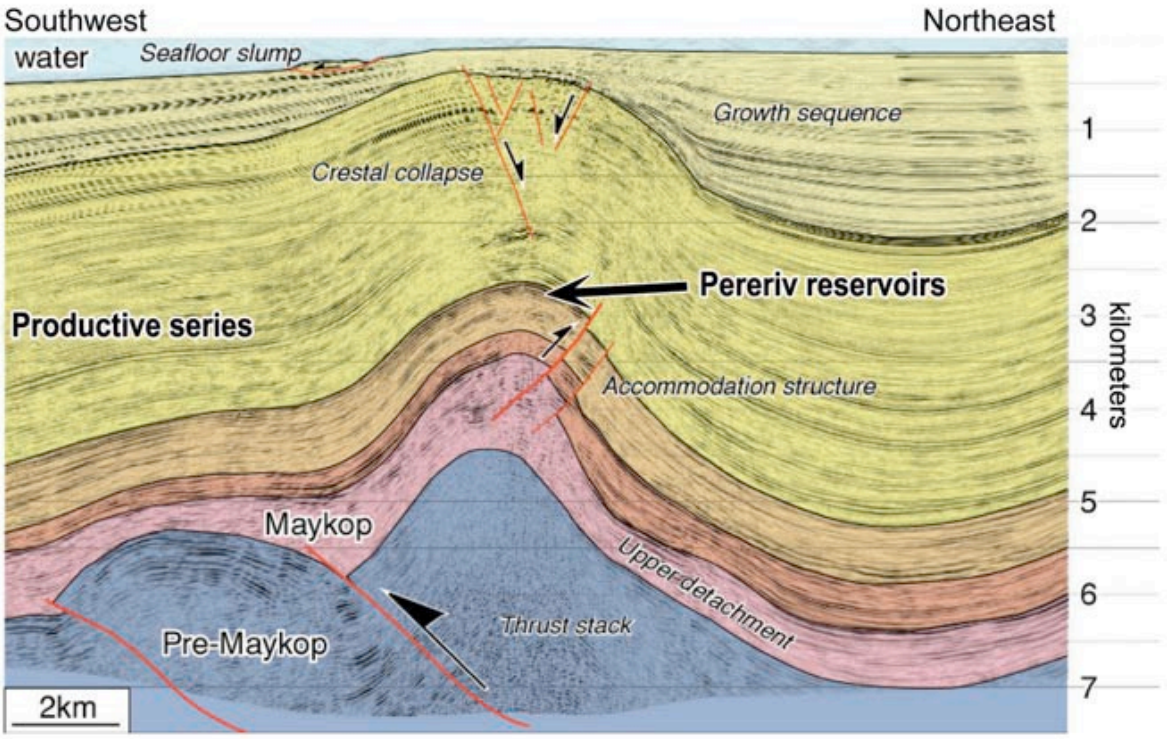


Figure 3.13: Section through the Chirag fold of the ACG fold structure showing the deep faults of the accretionary prism controlling the location of the ACG folds. From Robinson et al. (2005).

The Talysh pattern can be explained by its proximity to large fault zones caused by the SW movement of the basin relative to the Arabian plate (Jackson et al., 2002). The large NE-SW folds of the Alov domain can be explained by the relative NW motion of the basin compared to Eurasia reactivating potential transform faults, as previously mentioned (Abdullayev et al., 2017). The fold patterns of the central basin domain are more complex, however, they can be explained by a constrictional fold pattern, as modelled and described by Ghosh et al. (1995) (figure 3.14). Radial shortening could be generated by N-S shortening contemporaneous with E-W shortening generated by the relative movement of the basin with respect to the Arabian and Eurasian plates. This explains the circular synclines that occur in the northern part of the central basin region of the regional fold patterns (figure 3.14). Ghosh et al. (1995) models show that within constrictional settings synclinal basins can be rounded and can form an ‘ameoboidal shape’ when synforms link up which is what we see in the northern part of the central basin area.

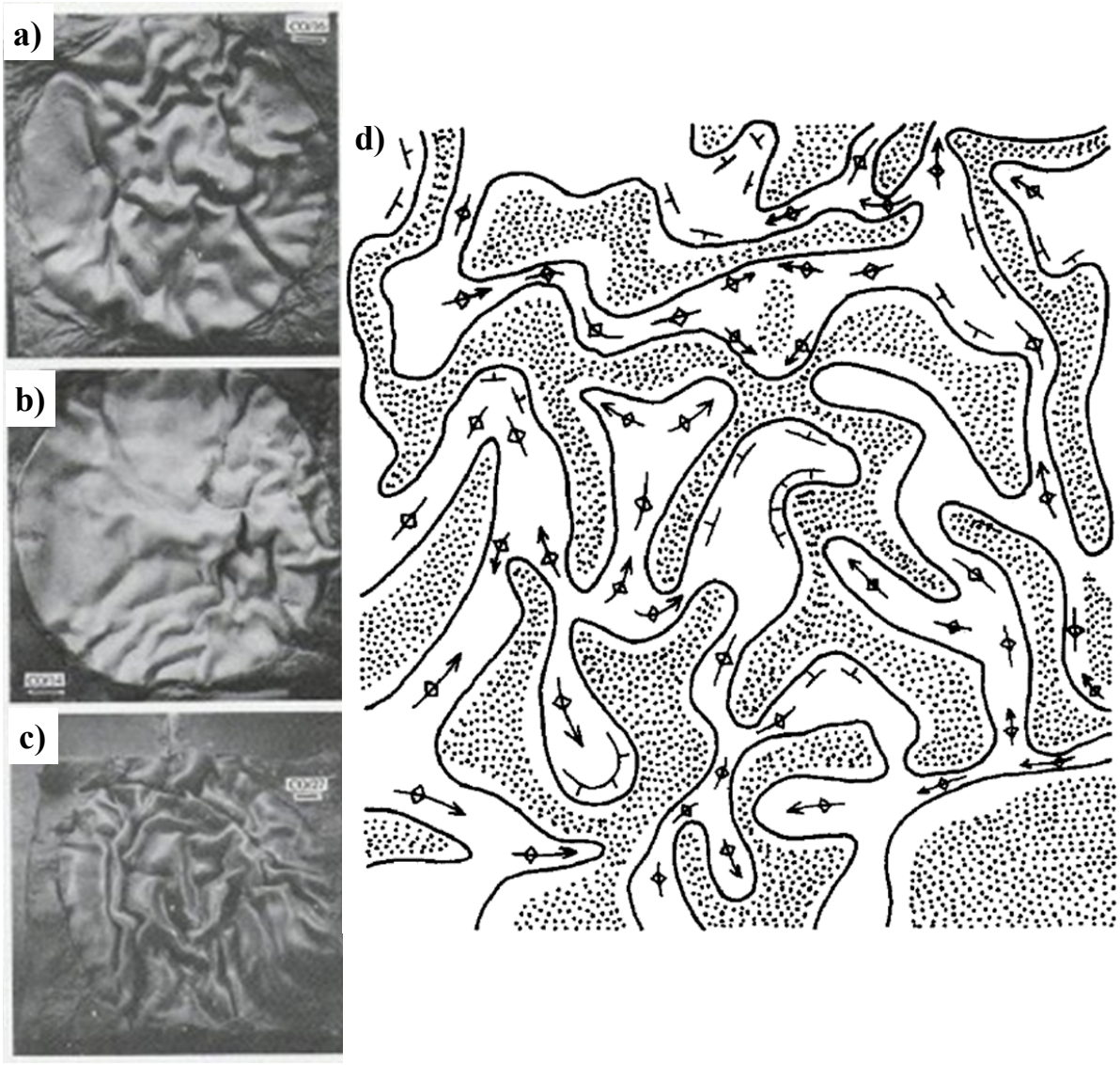


Figure 3.14: Examples of models from Ghosh et al. (1995) of pure constriction of clay with total radial shortening of a) 18.8 % b) 17.7 % and c) 29.4 % and d) Interpreted plan view of a clay model showing anticlines (white) and syncline (dotted) areas which resembles the fold pattern obsereved within the central Caspian region where Shafag-Asiman is located. From Ghosh et al. (1995)

3.4.2.2 Controls on Shafag-Asiman development

The main growth of the Shafag-Asiman fold occurs in the Pliocene-Pleistocene which corresponds to the late phase of Arabian shortening (Abdullayev et al., 2012). This shortening causes the rapid uplift of the Great Caucasus, Kopet Dagh and Alborz mountains, whilst subduction of the basin continues underneath the Absheron ridge and under thrusting below the Talysh mountains (Jackson et al., 2002, Knapp et al., 2004). This is due to a reorganisation of the tectonic plates, with the basin currently moving NW relative to Eurasia and SW relative to Iran (Priestley et al., 1994, Jackson et al., 2002, Walker et al., 2021). The plate reorganisation leads to the formation of strike slip faults

occurring on the rim of the basin, with dextral strike-slip in the Kopeh-Dagh mountains, sinistral strike-slip in the Alborz (Berberian, 1983, Jackson et al., 2002) and it has been suggested that dextral strike-slip occurs in the Talysh (Allen et al., 2003), with evidence of this seen below fold structures offshore (Santos-Betancor and Soto, 2015). The dextral shear component that occurs during the development of the Shafag-Asiman structure occurs during this 'Late Arabian shortening' phase, in the Plio-Pleistocene, as the plates reorganise. Within the published literature, there has been debate over the timing of the initiation of westward motion of the South Caspian Basin relative to the Iranian plate. Hollingsworth et al. (2008) suggested it occurs up to 10 Ma but the general consensus is that it occurs since about 3-5 Ma (Axen et al., 2001, Allen et al., 2004, Cifelli et al., 2015, Walker et al., 2021) and potentially within the last 2 My (Ritz et al., 2006, Mattei et al., 2019). The timing of the Shafag-Asiman fold axis rotation and growth of the sigmoidal crestal faults within the Pleistocene may be evidence to support the interpretation of an earlier timing for the westward movement since the dextral shear is likely caused by this plate motion.

The dextral shear may be caused by the deep fault accommodating the shear stresses initiated by the relative plate motion vectors of the basin. As mentioned in section 3.4.2.1, under the ACG fold structures, there are deep thrust faults related to an accretionary prism as the South Caspian Basin subducts beneath the Central Caspian (figure 3.13). These control the location of the fold structures. However, mapping of the ACG structure shows that the basement trend is E-W and the present ACG fold structure is oblique to this basement structure with a WNW-ESE trend (figure 3.15). This is due to dextral transpression occurring along the Absheron Ridge as late Arabian far field shortening, which is oblique to the E-W basement accretionary prism (McCaffery pers. comm). Santos-Betancor and Soto (2015) also find evidence for a deep fault beneath a fold accommodating shear stresses in the form of strike-slip movement.

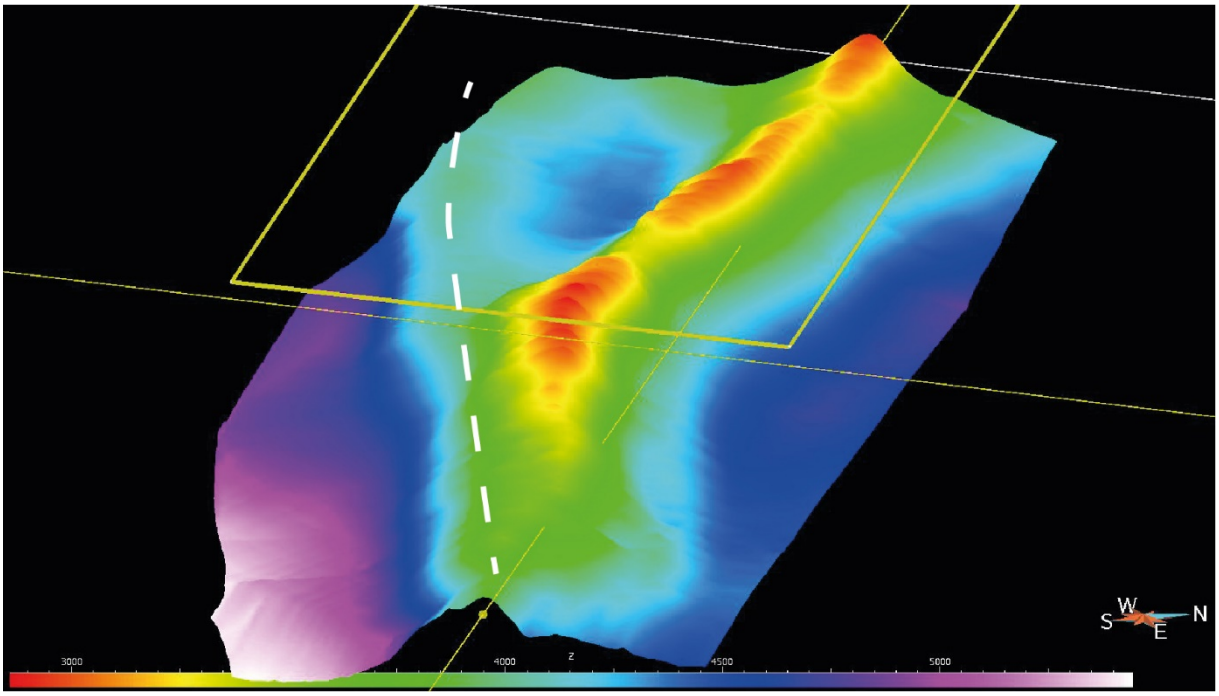


Figure 3.15: Depth map of the basement underneath the ACG structure in the north of the South Caspian Basin showing the current ACG structure, shown by the red peaks and the older E-W basement structure shown by the dashed white line. Surface mapped by Ken McCaffrey.

3.5. Conclusions

Within the central South Caspian Basin, far-field plate tectonic convergence directions interacting with existing orientations of basement structures is the primary control on fold orientation in the Talysh, ACG and north central areas of the South Caspian Basin. Whilst the Shafag-Asiman fold location and orientation is controlled by a deep basement fault, anti-clockwise fold axis rotation during the Pleistocene occurs in response to dextral transpression, with the Maykop shale detachment allowing this to take place by acting as a free surface. Although the Shafag – Asiman fold is controlled by basement faults, we suggest the complex varying fold orientations within the northern area of the South Caspian Basin may be controlled by constrictional deformation, forming domes and circular basinal synclines due to the interaction of the NW - SE and NE - SW active tectonic motions.

Local shale withdrawal around mud volcanoes in the Shafag-Asiman area indicate that mobile shale is present undeath the fold structures. Thick amounts of sediment are rapidly deposited onto the mobile shale which is likely to have contributed to the growth history of individual folds. In the subsequent chapters, the hypothesis that sediment loading may influence the fold history of the Shafag-Asiman fold structure is investigated and tested.

4. The geometry of the Shafag-Asiman fold from growth strata, using novel techniques

4.1 Introduction

The interaction between fold uplift and sediment deposition can be used to provide a history of fold development. Syn-kinematic sedimentation, defined as growth strata, acts as a record of the fold growth and seabed topography at the time of deposition (Decelles et al., 1991, Suppe et al., 1992). The relative rate of sediment accumulation and uplift can be determined using growth strata and can be used to predict the geometries of syn-kinematic strata (Burbank and Vergés, 1994) (figure 4.1). The use of

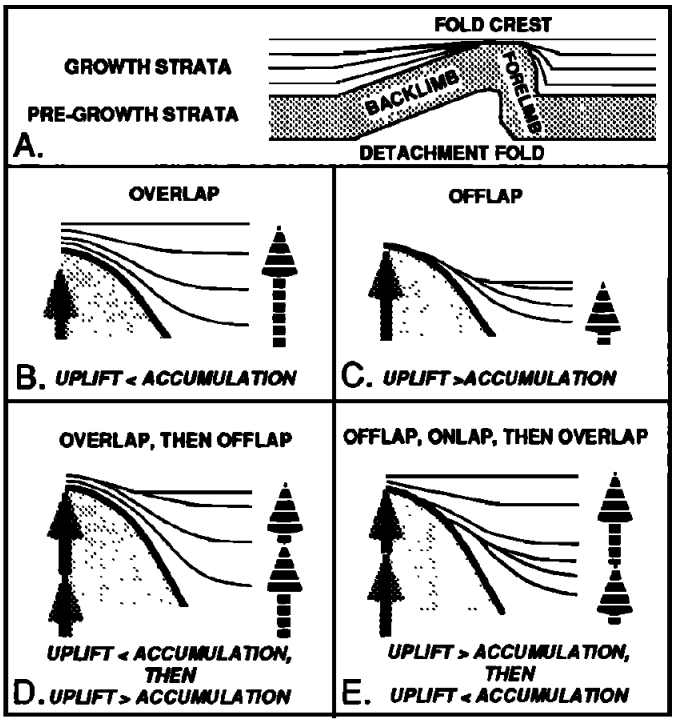


Figure 4.1: a) Summary of the terminology for a detachment fold and growth strata, b) – e) models of overlap, offlap and onlap based on the ratio of uplift to sediment accumulation. From Burbank and Vergés (1994).

growth strata as an aid to describe fold history was developed in the 1990's, with many of the early studies focussed on using kinematic models to: 1) predict fold geometry from growth strata or 2) predict growth strata geometries from geometrical models of different fold types e.g. fault bend folds, fault propagation folds, detachment folds and trishear folds (Erslev, 1991, Suppe et al., 1992, Hardy and Poblet, 1994, Hardy and Poblet, 1995, Poblet et al., 1997, Suppe et al., 1997, Hardy and Ford, 1997, Allmendinger, 1998). Models have been used to predict fault-bend and fault propagation folding,

modelling kink band migration, limb rotation and hinge migration (e.g. Suppe et al., 1992, Hardy and Poblet, 1994, Salvini and Storti, 2002, amongst many others). Growth strata related to the formation of

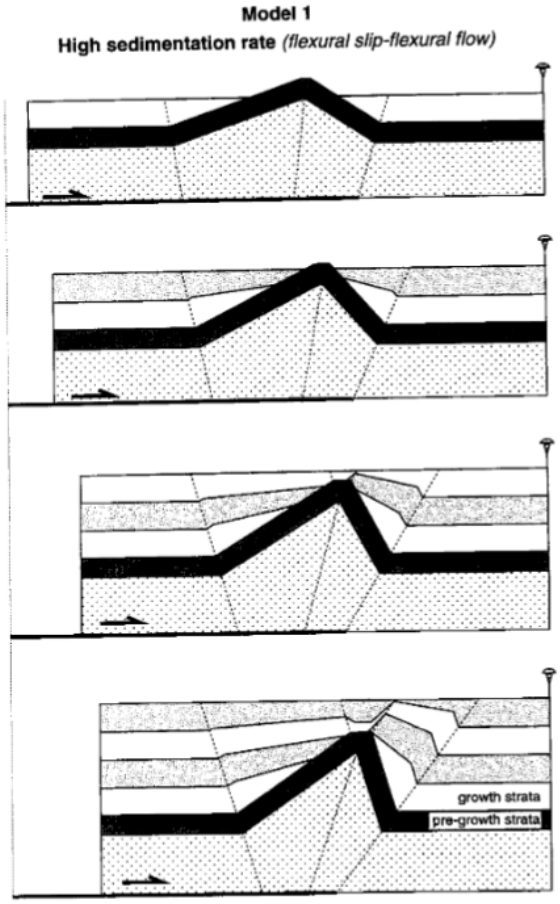


Figure 4.2: A model of growth strata formed during deposition of a detachment fold. The first two layers are deposited with uplift greater than sedimentation rate, the last two layers are deposited with sedimentation rate greater than uplift. From Poblet et al. (1997)

detachment folds have been forward modelled and compared with individual folds in the Spanish Pyrenees Mountains and show how limb rotation commonly occurs throughout growth (Hardy and Poblet, 1995, Poblet et al., 1997) (figure 4.2). Detailed fieldwork of growth strata has also been used to describe the fold history, with a tri-shear model proposed for fold growth of the Sant. Llorenç frontal structure in the eastern Spanish Pyrenees, rather than simple kink band migration (Ford et al., 1997).

The 2D kinematic models are too simplistic for understanding fold growth through time since they do not include mechanical properties and out of plane motion and therefore 3D models are more appropriate (Cristallini and Allmendinger, 2001, Salvini and Storti, 2002, Hardy and Finch, 2005, Guzofski et al., 2009, Vidal-Royo et al., 2012, Brandes and Tanner, 2014). Isopach maps of the Shafag – Asiman fold structure show that the folds have a complex three-dimensional geometry (chapter 3).

The complex three-dimensional nature suggests that the fold structures are not as simple as those predicted by numerical models commonly used to analyse growth strata and predict geometry (e.g. Salvini and Storti, 2002).

Consequently, in this chapter, I take a different approach to investigate the growth strata, by calculating the ratio of relative sediment thickness on the fold limb compared to the fold crest between stratal intervals. I define this as the sediment accumulation index. Sediment growth indices have previously been used as to analyse growth into extensional faults and have been defined as expansion indices (Thorsen, 1963, Cartwright et al., 1998, Childs et al., 2003), however, stratal growth indices have not been used to describe growth strata over a fold in three dimensions.

4.2 Methods

4.2.1 Sediment Accumulation Indices

The sediment accumulation index is calculated by dividing the thickness of sediment on the limb by the thickness of the sediment on the fold crest. The thickness measurement on the limb is calculated at the inflection point of the fold limb. The crestal thickness is calculated at the location of the crest for each interval. This gives a ratio that can be compared between stratal intervals in time and space to determine which interval had the most fold growth if sedimentation rate remained constant. A sediment accumulation index value = 1 shows the sediment thickness on the fold crest and limb are the same thickness, with no sediment growth (figure 4.3). A value < 1 shows that the sediment is thicker on the crest than over the limb and one of the products of this might be by ductile shearing on the limbs of the fold formed (figure 4.3). An index value > 1 shows increasing stratal growth on the fold limb relative to the crest, which is inferred to show growth of the fold crest during sediment deposition (figure 4.3). Therefore, the higher the value of the sediment accumulation index, the greater the thickness of sediment on the limb relative to the crest. Therefore, it can be inferred that the higher the sediment accumulation index, the higher the relative fold growth rate at that time. To compare the index between the horizon intervals, a constant sedimentation rate through time is assumed, from Hz100 to Hz200 (seabed). The sediment accumulation indices allow for the comparison of growth rate through time for intervals with no age data.

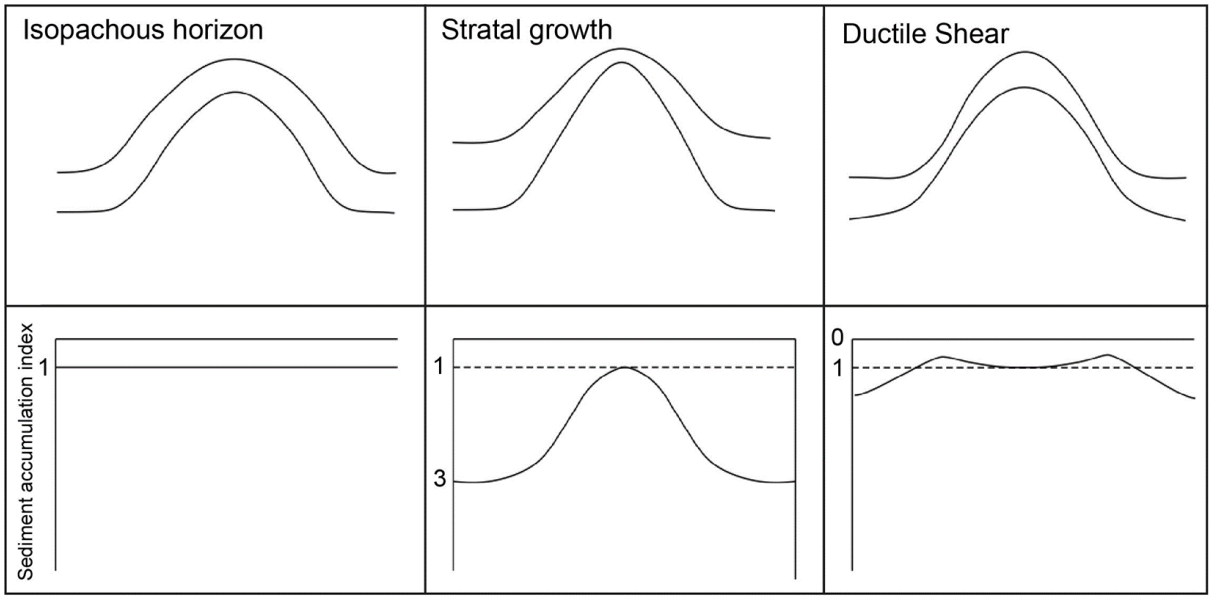


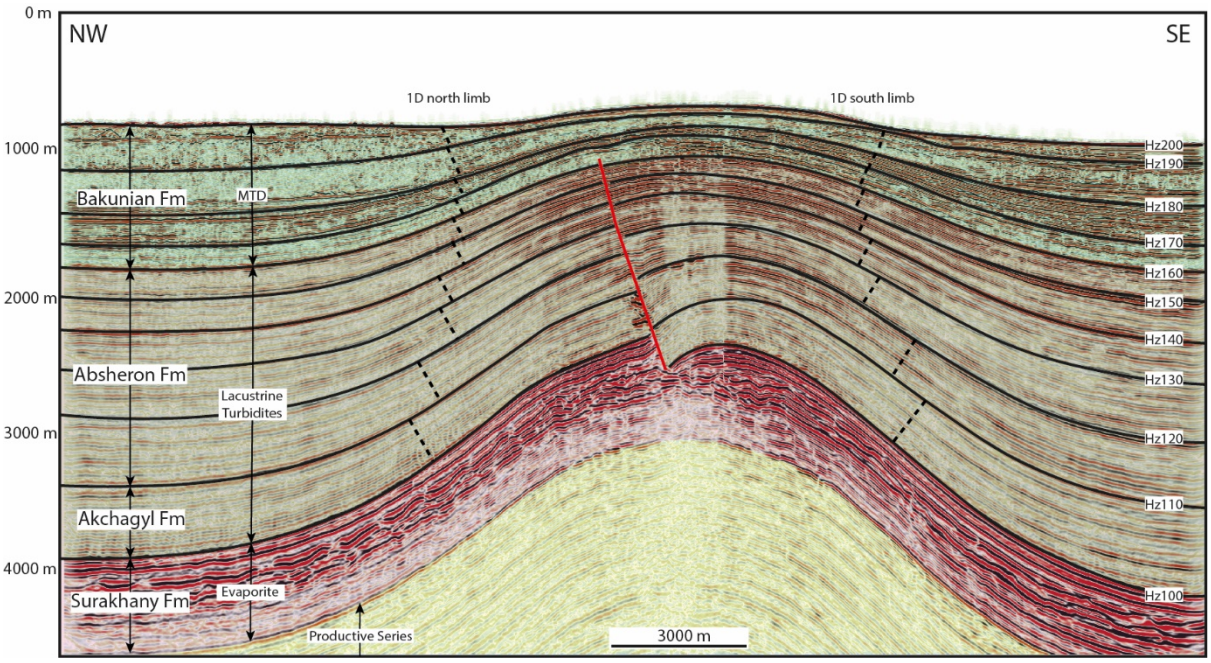
Figure 4.3: An illustration of the sediment accumulation index. A larger index equates to more sediment thickening on the fold limb relative to the fold crest and therefore increased fold growth, if a constant sedimentation rate is assumed.

The Pleistocene Absheron turbidite succession was deposited syn-kinematically over Shafag - Asiman, with onlapping strata within each interval. The sediment accumulation index is therefore used to infer which fold was growing most during the lacustrine turbidite and mass transport deposit intervals (figure 4.4). A thinner sediment package over the fold crests indicate that the fold structure created greater seabed topography at the relevant time. By comparing the sediment thickness between the Shafag and Asiman structures, the relative fold growth of the structures can be determined. Thickness variations between the two folds can indicate which fold had the greatest seabed topography during each interval. To compare the relative fold growth through time, isopach maps of the horizon intervals are used to calculate the relative sediment thickness on the fold crests relative to the fold limbs.

I calculate the sediment accumulation index for regionally continuous overlapping intervals from the base of the Productive Series (Hz 40), through the Surakhany evaporite (Hz 100) then the deep-water facies of the Akchagyl and Absheron times, Hz100 – Hz160 (2.13 Ma to 0.85 Ma) and then the mass transport deposits of the Bakunian to recent, Hz160 – Hz200 (0.85 Ma – 0 Ma). Initially the indices are calculated using a fixed point on the crest and limb of the Shafag and Asiman folds (figure 4.4). This provides a 1D sediment accumulation index and can be used to give an indication of the relative fold growth through time, between both fold crests spatially and through time. To get a better understanding of the spatial development of the folds within the Post-Productive Series, the indices

were then calculated across isopach maps to create a sediment accumulation index map. This was calculated by dividing each value of stratigraphic thickness in the isopach grid (at 25m spacing) by the thinnest value on the Shafag or Asiman fold crest, whichever had the thinnest value during each interval. From these both 2D and 3D representation of fold growth can be observed.

a) Asiman



b) Shafag

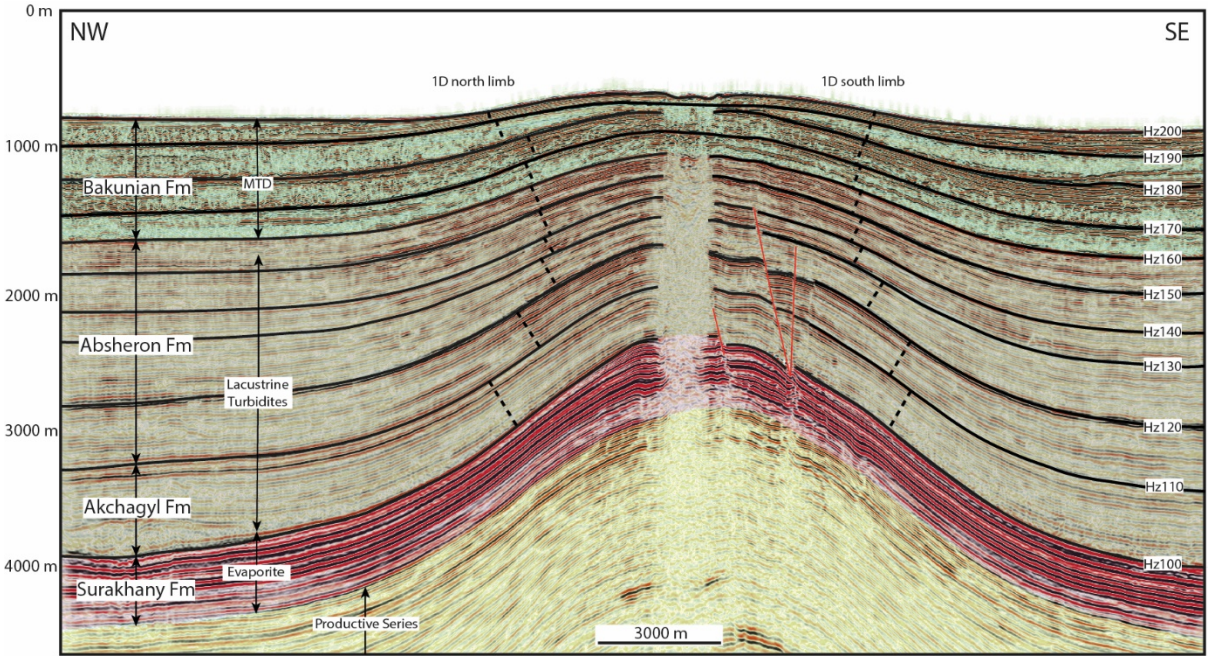


Figure 4.4: Sections through a) Asiman and b) Shafag highlighting the intervals and sequences analysed using sediment accumulation indices. The locations on the limb from which true stratigraphic sediment thickness was measured for the 1D analysis is shown on the northern and southern limbs. MTD = mass transport deposits. Asiman H/V = 1:3. Shafag H/V = 1:3.2.

4.2.2 Uncertainties and Assumptions of Sediment Accumulation Index calculations

Sediment accumulation indices can be used as a proxy for seabed topography, however, there may be errors associated with the index calculation when comparing the indices between layers. Firstly, one assumption that is made is that there is a constant sedimentation rate throughout the interval since there is no age data for the mapped surfaces between the top and base Absheron. A varying sedimentation rate will alter the sediment accumulation index if the fold growth stays constant. Therefore, if sedimentation rates vary significantly, the sedimentation accumulation index will not provide an accurate representation of fold growth when comparing intervals through time. When age data is not available, the sediment accumulation index will provide an indication of fold growth through time when sedimentation rates are constant. Fluctuations in sedimentation rate within the lacustrine turbidites are visible from the shelf edge (Abreu and Nummedal, 2007), however these are high frequency and sections from the shelf edge do not indicate phases of more rapid sedimentation from the Palaeo-Amu Darya River.

After sediment is deposited, it will undergo compaction over time, losing porosity and therefore layer thickness with depth (Sclater and Christie, 1980). This can cause errors within isopach maps since the oldest, deepest interval will have undergone more compaction than the youngest interval (figure 4.5). The tendency, therefore, is for the sediment accumulation indices to be artificially lower in the deeper intervals. Although this effect will take place on the Shafag-Asiman fold structure, drilling results within the deep-water part of the South Caspian Basin show that the Post-Productive Series is undercompacted due to very high sedimentation rates (Feyzullayev and Lerche, 2009). Therefore, although compaction will cause errors in the sediment accumulation indices at Shafag-Asiman, these are likely to be minor. There is also no systematic trend with sediment accumulation index with depth.

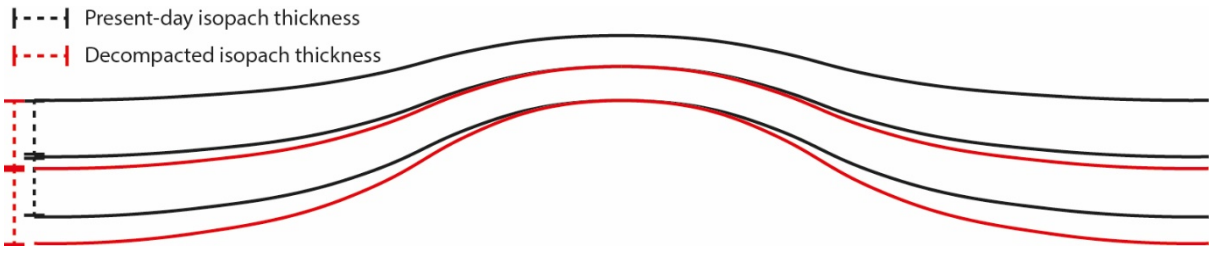


Figure 4.5: Illustration of the effect of compaction on sediment thickness showing the present-day compacted sediment to be thinner than the true decompacted sediment thickness.

Small errors may be caused by flexural flow and ductile shearing on the flanks of the folds, where ductile incompetent layers flow into the hinges of the folds, causing thinning of the fold limb. Errors in sediment thickness may also occur due to the depth conversion of the seismic data. However, these errors are likely to be small compared to the potential errors produced by assuming a constant sedimentation rate.

4.3 Results

4.3.1 2D Sediment Accumulation Indices

To demonstrate the sediment accumulation indices across a fold structure, I calculate sediment accumulation indices at 10 locations across the Asiman fold, for the oldest interval of the Absheron Formation, Hz120 – Hz110 and an interval within the mass transport deposits, Hz180 – Hz170 (figure 4.6). The mass transport deposit interval is significantly thicker on the limbs of the fold relative to the crest compared to Hz120-Hz110 in the lacustrine turbidite interval, as indicated by the higher sediment accumulation indices. The mass transport deposits fill in depressions on the seabed and onlap into the structure (Chapter 2), whereas the turbidites show more overlap on the structure. Both the intervals have a higher sediment accumulation index on the south-eastern fold limb, showing an asymmetry in the growth strata.

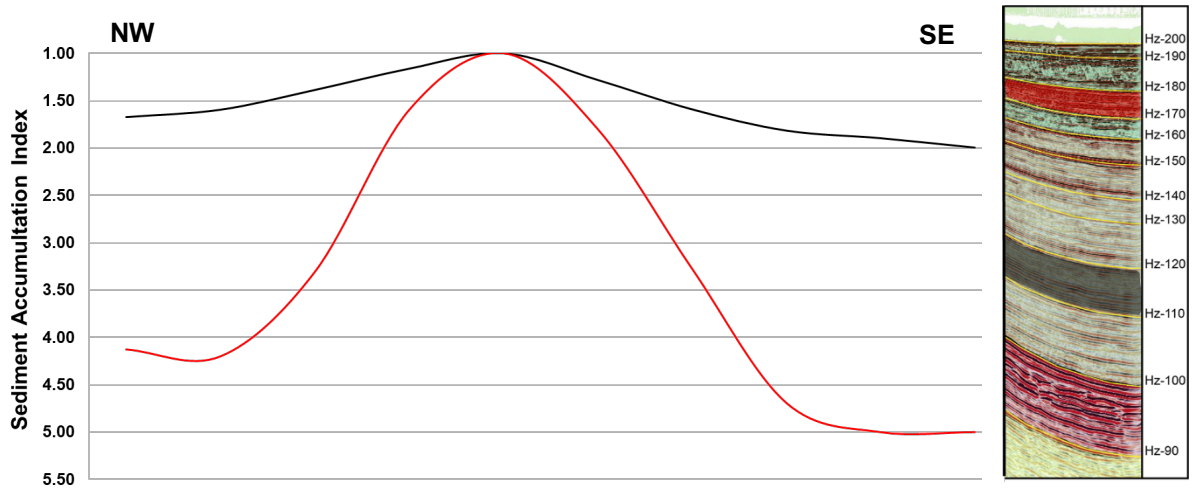


Figure 4.6: Sediment accumulation indices for a section across the Asiman fold axis for Hz120 – Hz110 (black) and Hz180 – Hz170 (red) showing the variation in sediment growth between the two packages using sediment accumulation indices. The intervals both show an asymmetry, with higher indices in the southeast.

To compare the relative fold growth through time, I have calculated sediment accumulation indices through the Absheron Formation, for intervals between Hz160 – Hz110 (figure 4.7). In this example, indices were calculated through a 2D profile at 25m intervals across the Shafag fold crest using sediment accumulation index maps. Interval Hz160 – Hz150 and Hz120 – Hz110 do not reach an index value of 1 on the crest since the thinnest sediment, and the value of 1.0, was over Asiman during these intervals. Whilst most of the intervals have an index of 1.8 – 2.0 on the flanks of the Shafag fold, interval Hz130 – Hz120 has a significantly higher index value on both the northern and southern limbs, up to 2.6. The intervals all show a slight asymmetry, except for Hz130 – Hz120, with a higher index value on the southern limb than the northern limb. The narrow increase in index value on the fold crest is due to active growth within crestal normal faults.

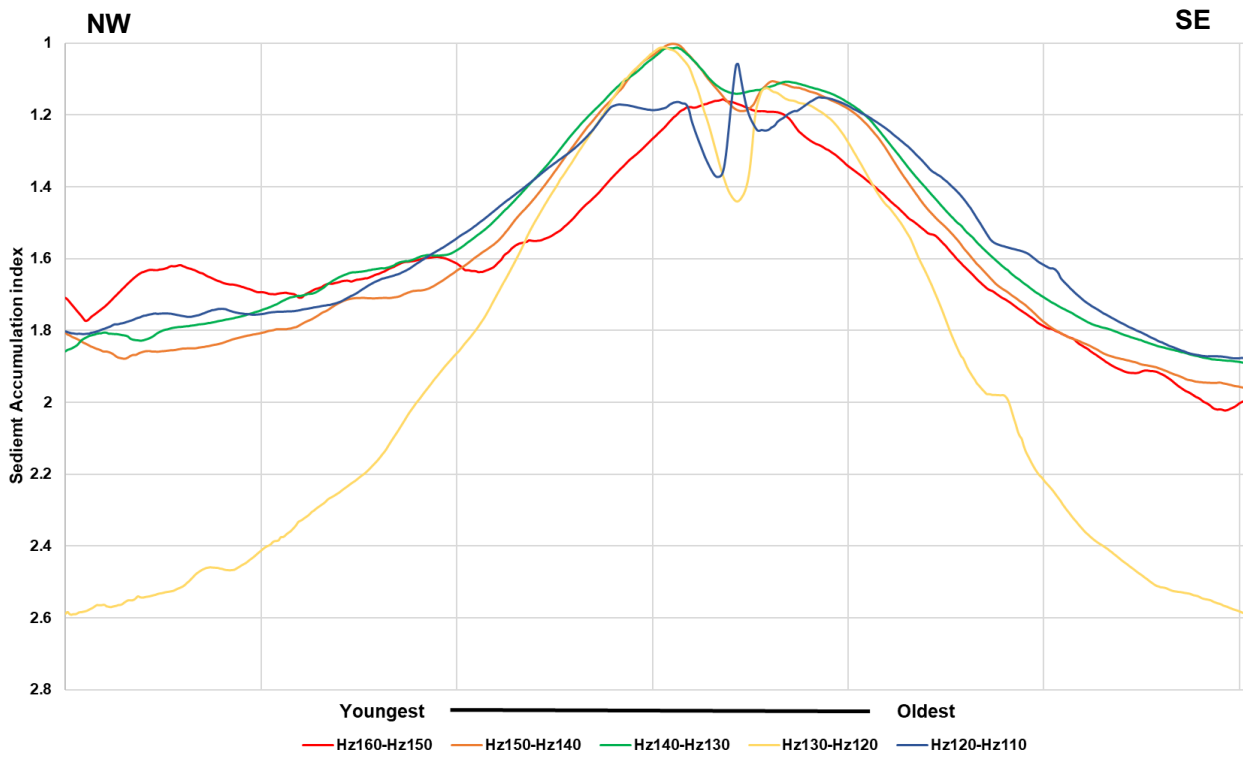


Figure 4.7: Sediment accumulation indices for a section across the Shafag fold axis for intervals between Hz110 and Hz160 showing the variation in sediment growth between the two packages using sediment accumulation indices. The data are taken from sediment accumulation maps. Hz160-Hz150 values does not reach 1.0 on the fold crest since Asiman had thinner sediment over the crest at this time.

4.3.2 1D Sediment Accumulation Indices

Although the sediment accumulation indices on profiles across the fold can show the asymmetry and relative stratal growth between the intervals, examining the indices as a single value of each limb can be used to show the relative fold growth through time. The 1D index was calculated on the inflection point of the fold limbs for each interval. The Productive Series, including the Surakhany Formation evaporite, deep-water sediments of the Absheron and Akchagyl Formation and mass transport deposits of the Bakunian have been included. The horizons within the Productive Series were interpreted from the middle of the sequence to the Surakhany Evaporites.

Within the Productive Series, whilst sediment accumulation indices are low, above Hz50 on Asiman and Hz60 on Shafag, the indices are higher than 1, suggesting that there was fold growth and sediment thickening on both folds during deposition of the Productive Series (figure 4.8). The evaporite of the Surakhany Formation has an index value less than one on both limbs for both folds, indicating that there is limb thinning in this interval most likely because of the more ductile behaviour of the stratigraphy in this interval.

Within the lacustrine turbidites of the Post-Productive Series, the sediment accumulation indices vary between each limb on both fold structures (figure 4.8). The south limb of the Asiman fold structure has higher index values than the north limb in all intervals of the lacustrine turbidites, except for interval Hz150 – Hz140 (figure 4.8a). The largest disparity between the north and south limb values occurs within interval Hz110 – Hz100 where the north limb has a value of 1.16 and 1.46 for the south limb. From Hz140 – Hz130 through to Hz160 – Hz150 there is steady growth, with an increase of index values on both limbs. The interval with the highest sediment accumulation indices for both the north and south limbs occurs within interval Hz160 – Hz 150, with values of 1.48 and 1.39 for the south and north limbs respectively.

On the Shafag fold structure, the north limb has a higher sediment accumulation index value than the south limb between for the two lowest intervals, which is the opposite to Asiman (figure 4.8b). Between Hz120 and Hz 140, there is a notable increase in index values and the higher growth now switches to the south limb as opposed to the north limb in the preceding intervals. The index of 1.64 in this Hz140 – Hz120 interval is the highest value throughout the turbidite sequence, suggesting most

fold growth occurred at this time on the Shafag fold. Whilst the indices continue to be greater on the southern limb compared to the northern limb, both the index values as well as the total difference between the values on the limbs decreases from Hz140 to Hz160.

To compare the growth between the Shafag and Asiman folds, I compare the indices on the southern limb of both folds. This allows a comparison of how the stratal growth, and therefore fold growth, compares across the structures (figure 4.8c). Between Hz110 – Hz100 the Asiman south limb has a higher index value, 1.46, than the Shafag south limb, 1.24. During this interval, however, the Shafag north limb has higher values than the south limb, 1.41 (figure 4.8b), however this value is still lower than the southern limb value of 1.46 on Asiman. Moving up the section, the Shafag south limb displays a large increase in index value compared to Asiman from Hz120 to Hz150 (figure 4.8c). Asiman is growing more than Shafag during these times. Hz130 – Hz120 has an index value difference of 0.25, whilst Hz140 – Hz130 has the largest difference of 0.48. During these times, Shafag is growing significantly more than Asiman. The southern limb of Shafag has a higher value than Asiman in interval Hz150 – Hz140, however, this reverses to Asiman having a slightly higher value than Shafag for interval Hz160 – Hz150, albeit a very small difference, showing that Asiman was growing more in this interval than previous intervals.

The mass transport deposits cannot be directly compared to the lacustrine turbidite deposits since they are produced by a different depositional process, where beds are deposited instantaneously. However, fold growth appears to have been significantly higher in most recent times (figure 4.6), during deposition of the mass transport deposits, some of which onlap the fold crests, observed from Hz170 to Hz200 on Asiman (figure 4.4a) and Hz180 to Hz200 on Shafag (figure 4.4b). The deposits can be used to show the relative growth between the fold structures. Asiman has higher index values than Shafag for interval Hz180 – Hz170, with a difference of 1.87 between the southern limbs. In the subsequent interval, this relationship reverses and Shafag has higher indices when compared to Asiman, with a difference of 1.21 between the southern limbs. Within the shallowest interval Hz200 – Hz190, the highest indices are on the north limb of Asiman. The dominant fold growth alternates between the intervals within the mass transport deposit sequence. During Hz180 – Hz170, the Asiman fold is more

emergent, with more burial over Shafag, whereas in interval Hz190 - Hz180, Shafag is more emergent with more burial over Asiman.

To summarise, the 1D index allows comparison of the limb to crest thickness of each fold individually, which allows us to determine which limb was growing most through time on each fold structure. The growth is complex, with variations in growth on the southern and northern limbs of both folds through time showing that there was asymmetry to the growth. There was more growth on the Asiman south limb than the north limb in the two lowermost intervals, which is the reverse for Shafag. There is then more growth on the southern limb of both folds from Hz130 - Hz120 to Hz160 -Hz150, apart from within interval Hz150 – Hz140 on Asiman. Comparison of the indices on the southern limb shows that the highest increase in fold growth occurs on Shafag at Hz130 – Hz120. Mass transport deposits show more subtle variations of the limbs on each fold, however, when Shafag and Asiman are compared, it shows the dominant fold alternated. The indices show that the fold growth varies in space and time across and between both structures.

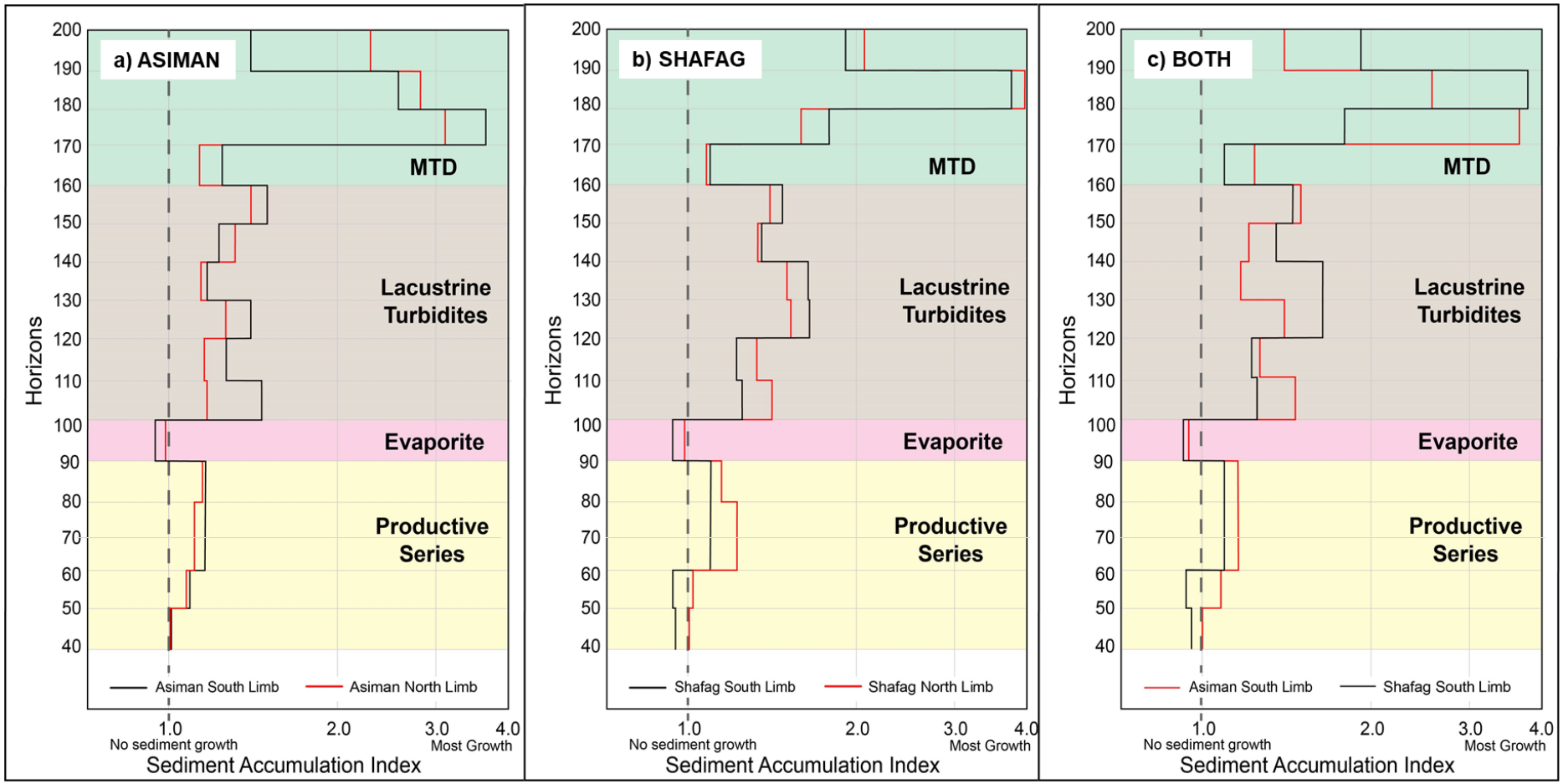


Figure 4.8:1D sediment accumulation indices for a) Asiman, b) Shafag and c) both southern limbs. Location of the limb thicknesses located on figure 4.4.

4.3.3 3D Sediment Accumulation Indices

Whilst the 1D and 2D indices can demonstrate the changes and alternations of growth on the limbs through time, 3D index maps can help with understanding the changes in space and time in more detail. By measuring the sediment thickness at 190 grid points from an isopach map, a three-dimensional plot of the sediment accumulation index can be made, as the example from Hz120 – Hz110 in figure 4.9b. Each value is divided by the thinnest sediment on the crest of either Shafag or Asiman and for Hz120 – Hz110 this is taken from the Asiman fold crest. The 3D map shows the relative growth across the entire Shafag – Asiman fold structure confirms that even at one interval the growth is complex with thickness variations along the limbs (figure 4.9b). Instead of manually measuring the isopach thicknesses on a grid from an isopach map, the sediment accumulation index map is calculated by dividing all the points on the isopach map (bin size of 25 m x 25 m) by the thinnest sediment value (figure 4.9c). This provides detailed sediment accumulation index maps that can be compared in space and also in time, by setting the colour bar to the same value for each map (figure 4.10). For the sediment accumulation index maps I focus on the detail of the Post-Productive Series, after deposition of the Surakhany evaporites.

Some key observations can be made by comparing the sediment accumulation index maps. Firstly, the alternating dominant fold crest through space and time can be seen clearly (figure 4.10). In the oldest interval Hz110 – Hz100, the Akchagyl interval, the fold crests have almost identical indices, showing that during these times, they displayed similar seabed topography. Moving up into Hz120 - Hz110, the Absheron Formation, the fold crests still have similar sediment accumulation indices, however they are lowest on the Asiman fold crest, suggesting that this was the dominant growing fold during this time. There is a dramatic change within interval Hz130 – Hz120, (figure 4.10), in line with the 1D indices (figure 4.8). The Shafag fold crest has values of 1.0, whereas the sediment is a lot thicker on the Asiman fold crest, with values of 1.4. This clearly displays the switch to Shafag becoming the dominant growing fold at this time. The Shafag fold also shows a change in shape, with the values of 1.0 covering a narrower, more round area than the intervals below. The Shafag fold stays dominant through intervals Hz140 – Hz130 and Hz150 – Hz140, however the index becomes lower over the

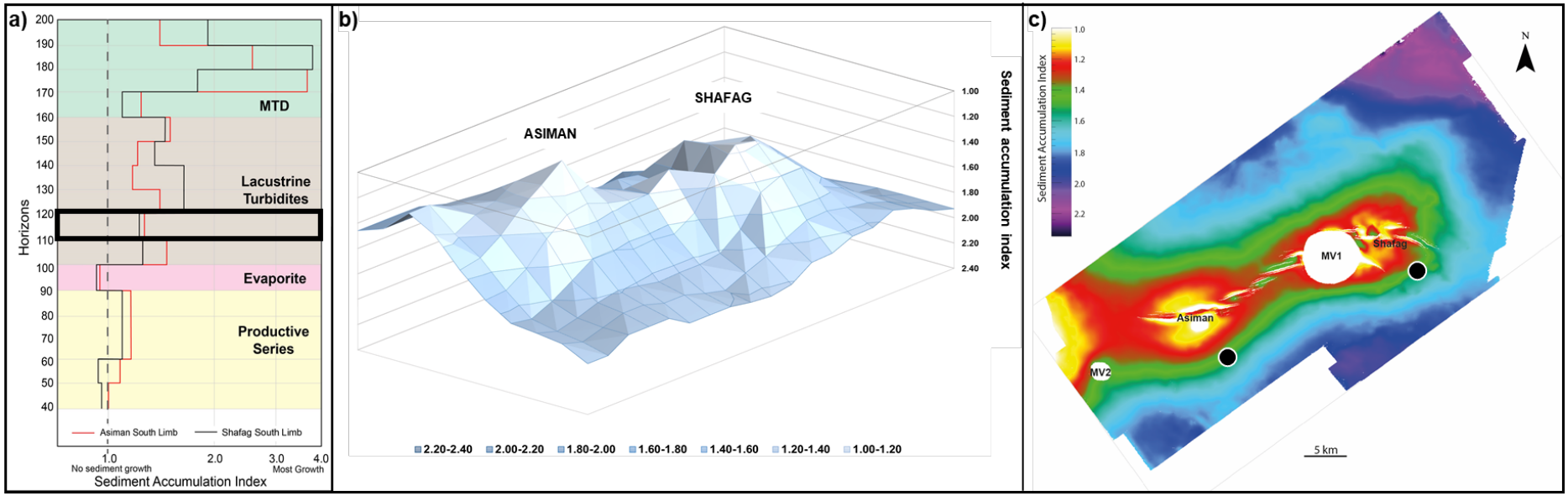


Figure 4.9: a) 1D sediment accumulation indices from the southern limbs of Asiman and Shafag. Hz 120 – Hz110 is highlighted in black. B) Sediment accumulation index map created using 190 data points measured across Hz120 – Hz110. C) Sediment accumulation index map calculated using every point from isopach map for Hz120 - Hz110. The two black dots are the locations from which the 1D indices were calculated in a)

Asiman crest than in interval Hz130 – Hz120, above the area of seismic wipe out in the fold core, which can be seen in the map of Hz130 – Hz120 (figure 4.10). The youngest interval of the lacustrine turbidites of the Absheron Formation, Hz160 – Hz150, displays another switch in the dominant fold growth, with the lowest sediment accumulation indices on the crest of Asiman rather than Shafag. The sediment accumulation index maps show how although the folds initially grew equally in the sequence, Asiman was then slightly dominant before Shafag became most dominant. At the end of the sequence Asiman becomes dominant once again.

The sediment accumulation index maps also highlight how the indices vary in-between the fold limbs and depocentres through space and time in a more detailed manner than the 1D index. Within interval Hz110 – Hz100, the 1D analysis showed that the Asiman north limb and the Shafag south limb have lower indices than their corresponding opposite limbs (figure 4.8). The northern limb of Asiman appears to be in connection with the large structure to the west outside of the dataset, which in turn causes variation in the indices (figure 4.10). The large western fold has an index value of less than 1.0 in all intervals, except for Hz110 – Hz100, because it is much larger than Shafag – Asiman. There are relatively low values to the southeast of Shafag in the lowermost intervals are due to stratal thinning that appears to trend northwest – southeast and can be seen throughout the intervals. Whilst the maps show similar maximum index values of approximately 2.0 – 2.2 on the flanks, interval Hz130 – Hz120 has significantly higher values on the flanks, up to 2.6 – 2.8 indicating that fold growth reached its maximum during this time. Active crestal normal faults also have the highest indices within interval Hz130 – Hz120, showing they are most active during this time. Throughout the intervals, a round depocenter between the southern limbs of Shafag and Asiman has the highest indices and highlights the asymmetry of the fold structure with most growth in the south. The highest indices within Hz160 – Hz150 are towards the east of the area, whereas the other intervals have highest values in the north-east of the area.

Another prominent feature throughout the sediment accumulation index maps are the high indices around the mud volcanoes, this will be explored in the next section.

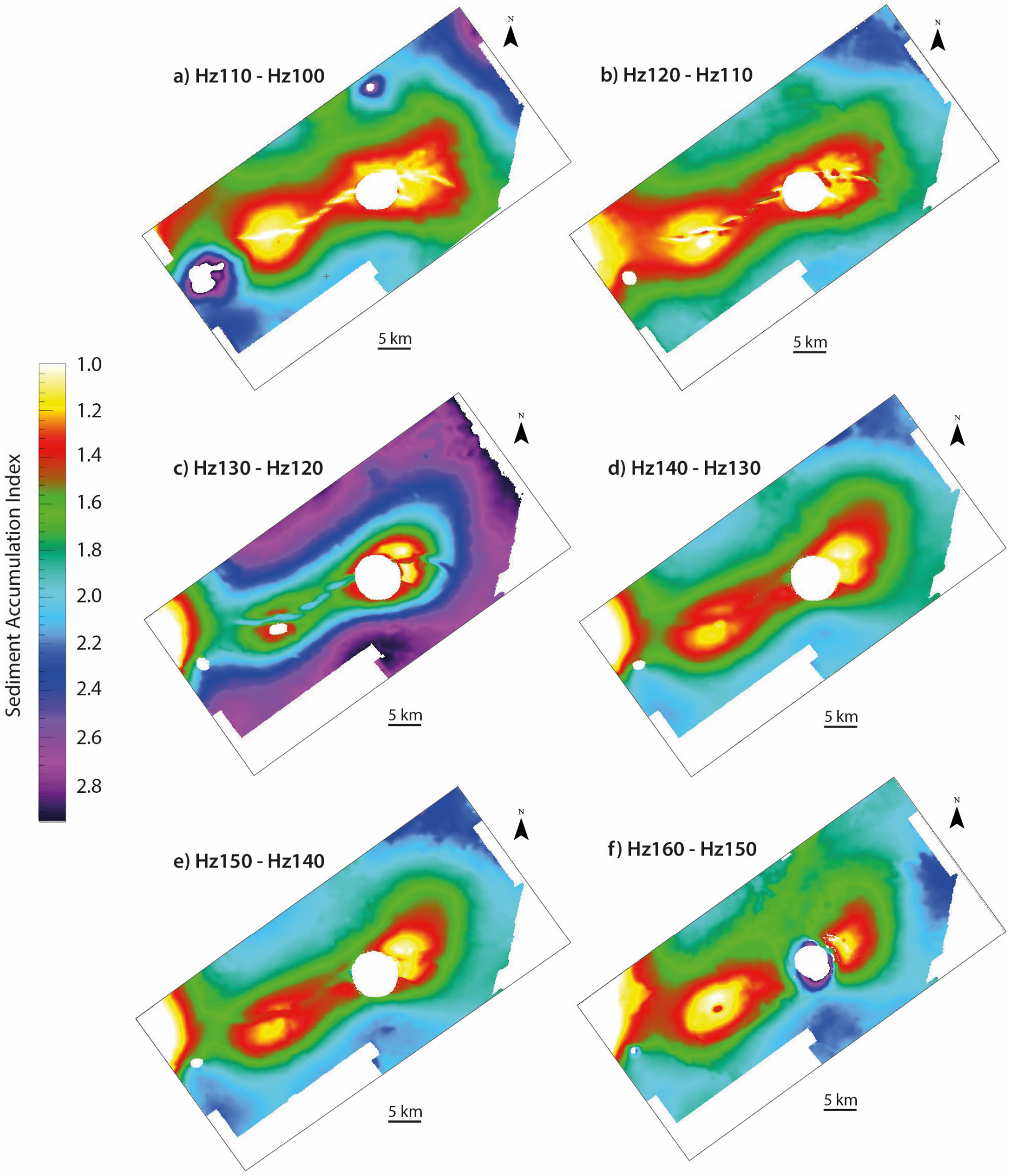


Figure 4.10: Sediment accumulation index maps for intervals between the top Absheron formation and top Surakhany Formation, Hz100 to Hz160. a) = oldest, f) = youngest. Each map is scaled to the same colour bar for comparison. The white circles are where mud volcanoes cause seismic wipe out in the data.

The 1D index analysis suggests that the lowest unit of the mass transport deposits, Hz170 – Hz160, showed a reduced growth when compared to the turbidite sequence (figure 4.8). However, the index map shows that the interval thickens towards the east, parallel to the fold axis, rather than perpendicular (figure 4.11). Whilst values over Asiman are 1.0, Shafag appears to have had less of an influence on the deposition of the interval.

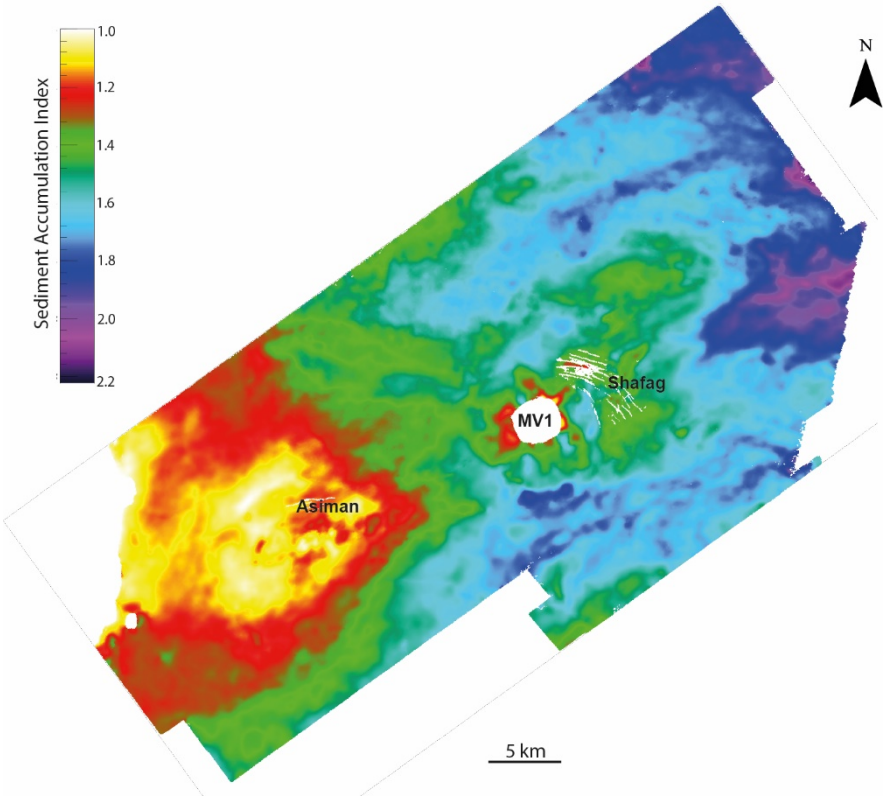


Figure 4.11: Sediment accumulation index map for Hz170 – Hz160, the oldest interval of the mass transport deposits.

The 1D index showed the mass transport deposits of intervals Hz180 – Hz170 and Hz190 - Hz180 to have significantly different distributions from Hz170 – Hz160. The sediment accumulation index map for Hz180 – Hz170 shows that the Asiman crest has an index of 1.0 and the Shafag crest has an index of 2.4, indicating that growth of Asiman was more prominent during this this interval (figure 4.12). The highest index values are once again in the east of the area. As also observed within the turbidite intervals, indices are higher on the southern limb of the folds.

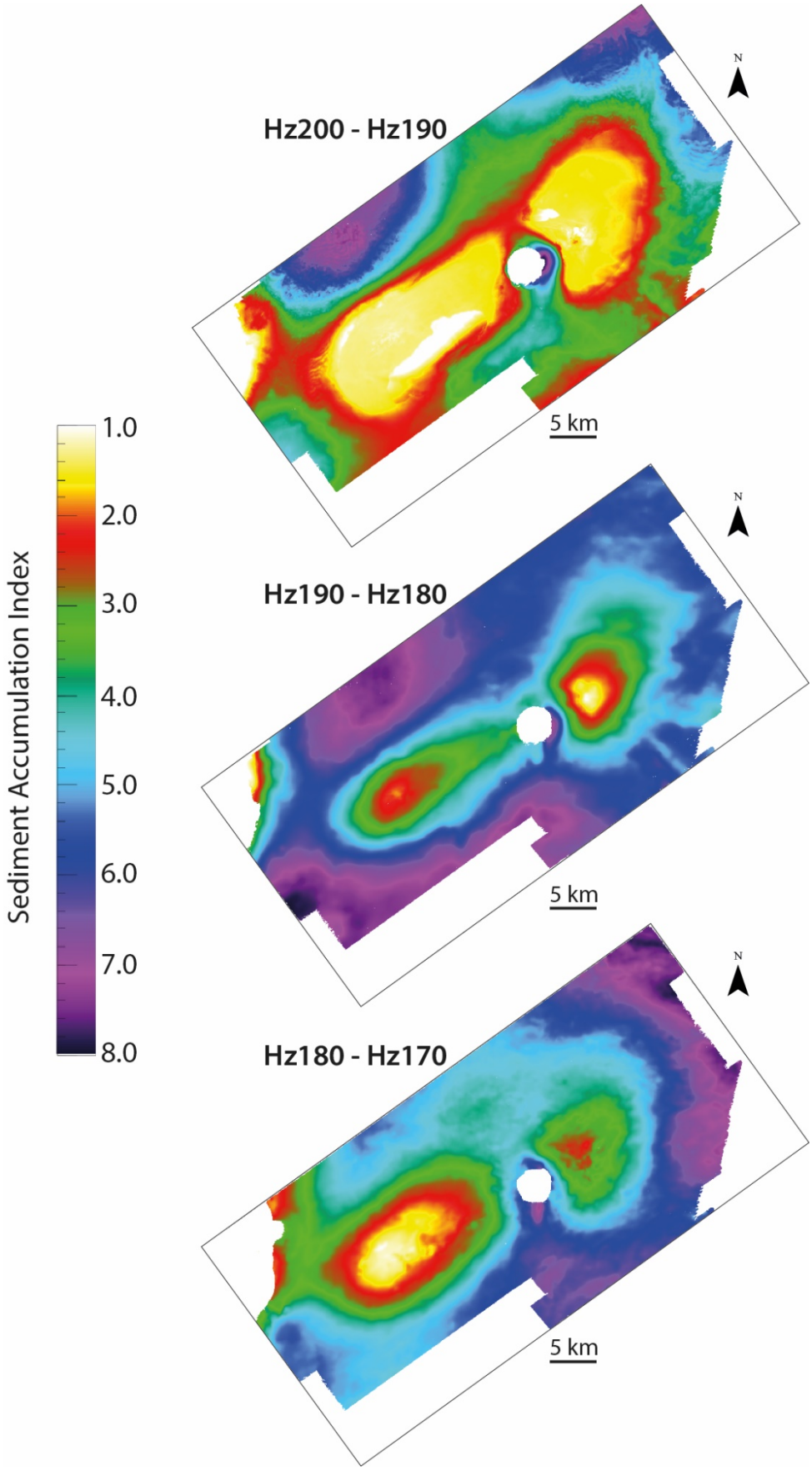


Figure 4.12: Sediment accumulation index maps for intervals between the Seabed and the Top Absheron Formation, Hz160 to Hz200. Each map is scaled to the same colour bar for comparison. The white circles are where mud volcanoes cause seismic wipe out in the dataset.

In contrast to the previous interval, interval Hz190 – Hz180 has the lowest indices on the Shafag crest compared to Asiman, with indices of 1.0 and 1.95 respectively (figure 4.12). The highest indices within the interval are located towards the south-west of Asiman and on the northern flank of the structure, opposite to the previous interval. The shallowest interval, Hz200 – Hz190, beneath the seabed, shows low values over a large area of both Shafag and Asiman (figure 4.12), due to onlap onto both structures (figure 4.4). Values decrease to below 1.0 along the southern limb of Asiman and a small area on the Shafag crest due to slumping of the seabed down the fold flank. Indices of 8.0 within the mass transport deposits, suggest that the fold growth was highest during these times, however these cannot be directly compared to the lacustrine turbidites since they had a different depositional system. The dominant fold structure alternates between Asiman and Shafag, as also observed within the turbidite sequences (figure 4.10).

4.3.4 Mud Volcanism

The sediment accumulation index maps show anomalies in sediment growth around the mud volcanoes. These are similar to salt withdrawal synclines that are common features seen in isopach maps around salt domes, where sediments locally accumulate within a narrow syncline (Trusheim, 1960). A total of three mud volcanoes are present within the dataset. High indices around MV2 and MV3 are limited to within Hz110 – Hz100, the Akchagyl Formation. MV2 is at the southwest end of the Asiman fold and MV3 is north of the Shafag fold (figure 4.10). The mud volcano to the north of Shafag, MV3, has high indices in a 3 km wide area around the mud volcano, forming a structure appearing similar to a salt withdrawal syncline. The mud volcano is extinct and sits on the evaporites of the Surakhany Formation, Hz100 (figure 4.13). Below MV3, within the Productive Series, ‘Christmas tree’-like geometries can be seen, indicating that there was active mud volcanism, with eruptions reaching the surface during deposition of the Productive Series (figure 4.13). No mud core is observed between the flows since the section does not intersect the mud volcano core. MV2, the mud volcano to the west of Asiman, has a similar geometry with a circular syncline rimming the volcanoes with very high (up to 2.8) sediment accumulation indices and a total diameter of 7 km (figure 4.14). Although there is no growth observed within subsequent intervals on the maps, volcanism was active through the Absheron turbidites. The feeder pipe is evident feeding the youngest volcano at Hz170 –

Hz160 and several episodes of mud eruption as seen by palaeo-mud cones (figure 4.14). The mud volcano between the two fold crests, MV1, has high sediment accumulation indices within a rim syncline or partial synclines, present from Hz160 - Hz150 to the seabed corroborated by growth packages on seismic data (figure 4.15).

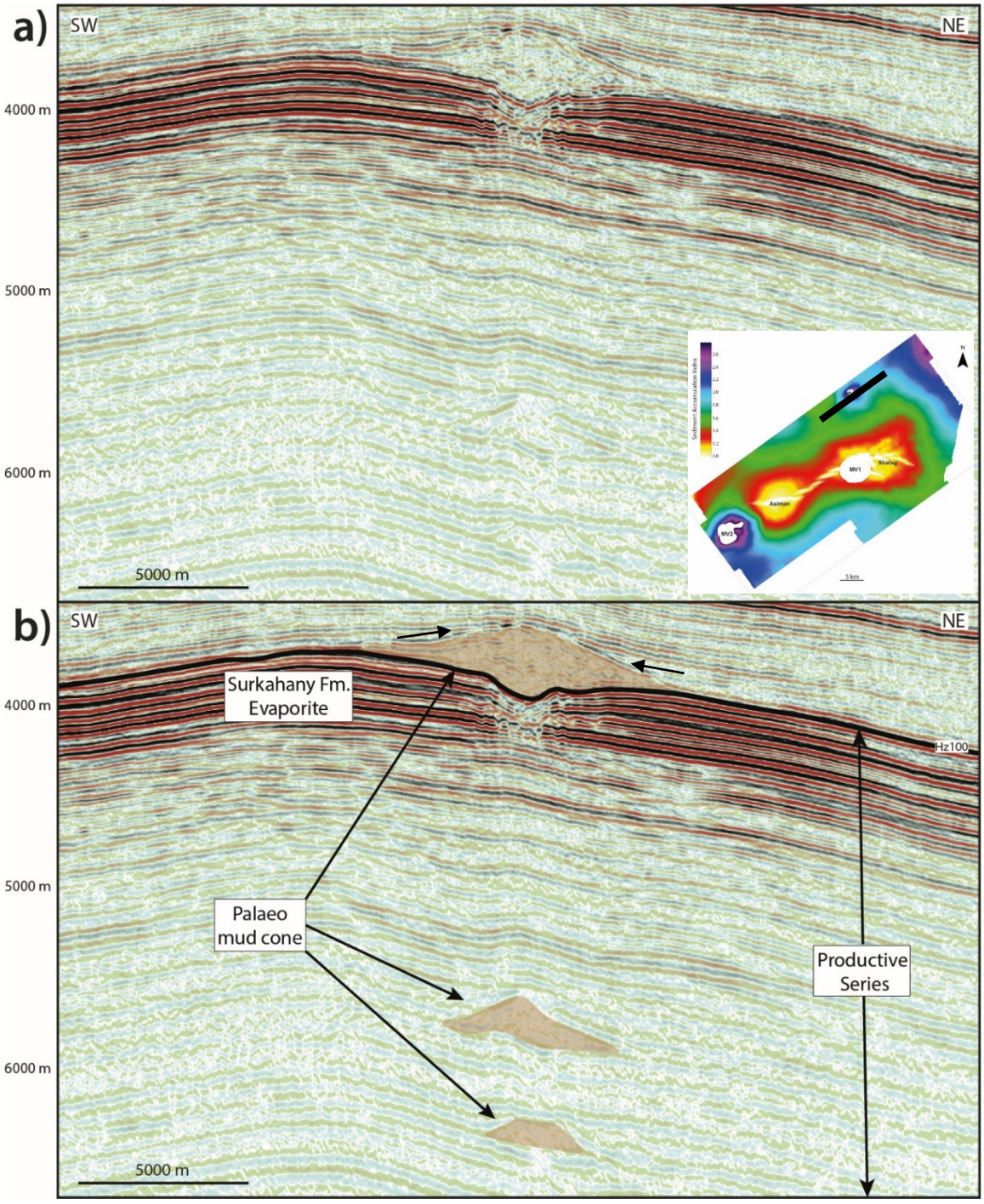


Figure 4.13: a) uninterpreted and b) interpreted seismic section of an extinct mud volcano in the north of the area, MV3. H/V = 1:3.

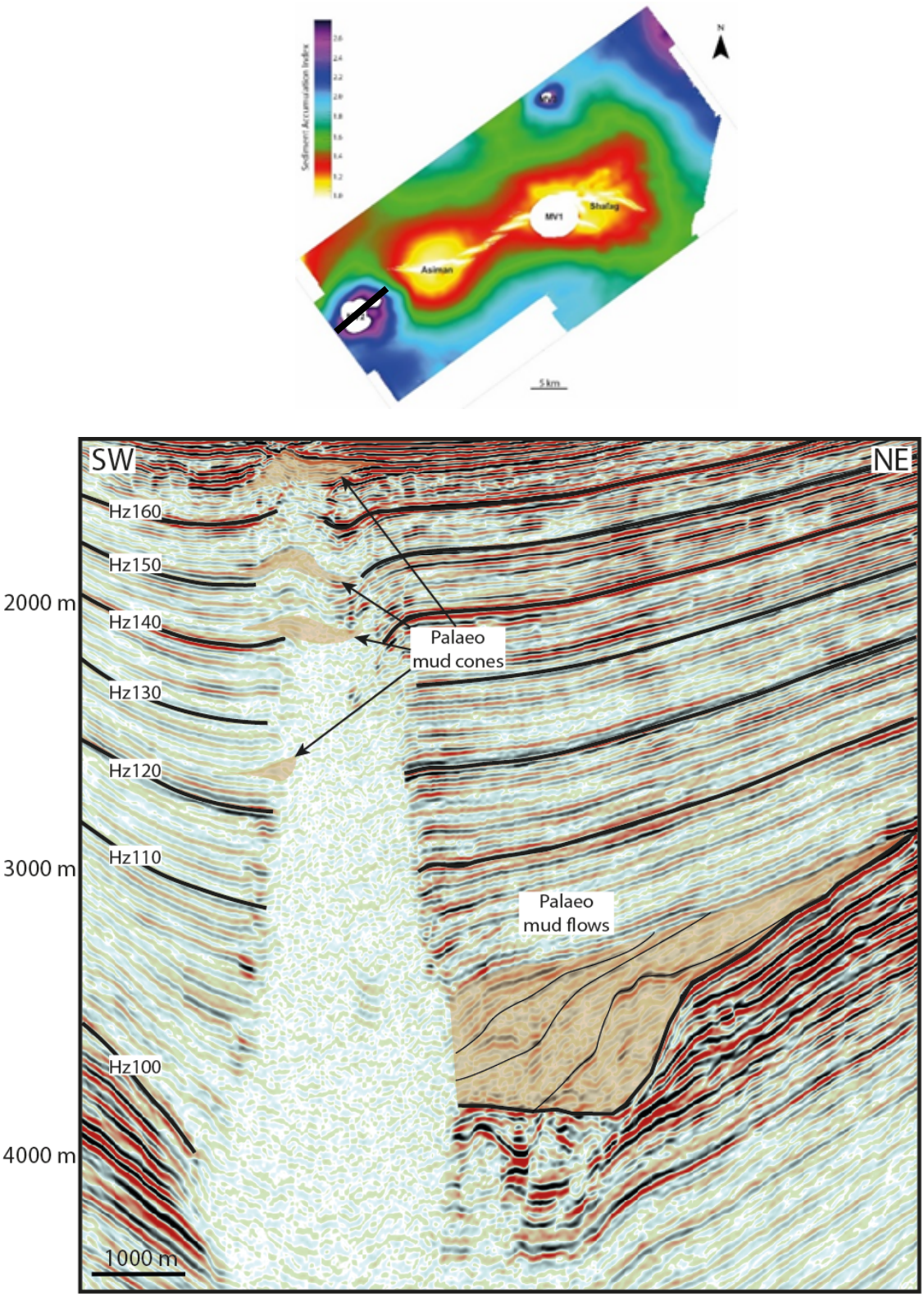


Figure 4.14: Palaeo mud cones of a mud volcano to the west of Asiman, showing mud volcano activity from Hz110 -Hz100 up to Hz170 – Hz160. H/V = 1:3.

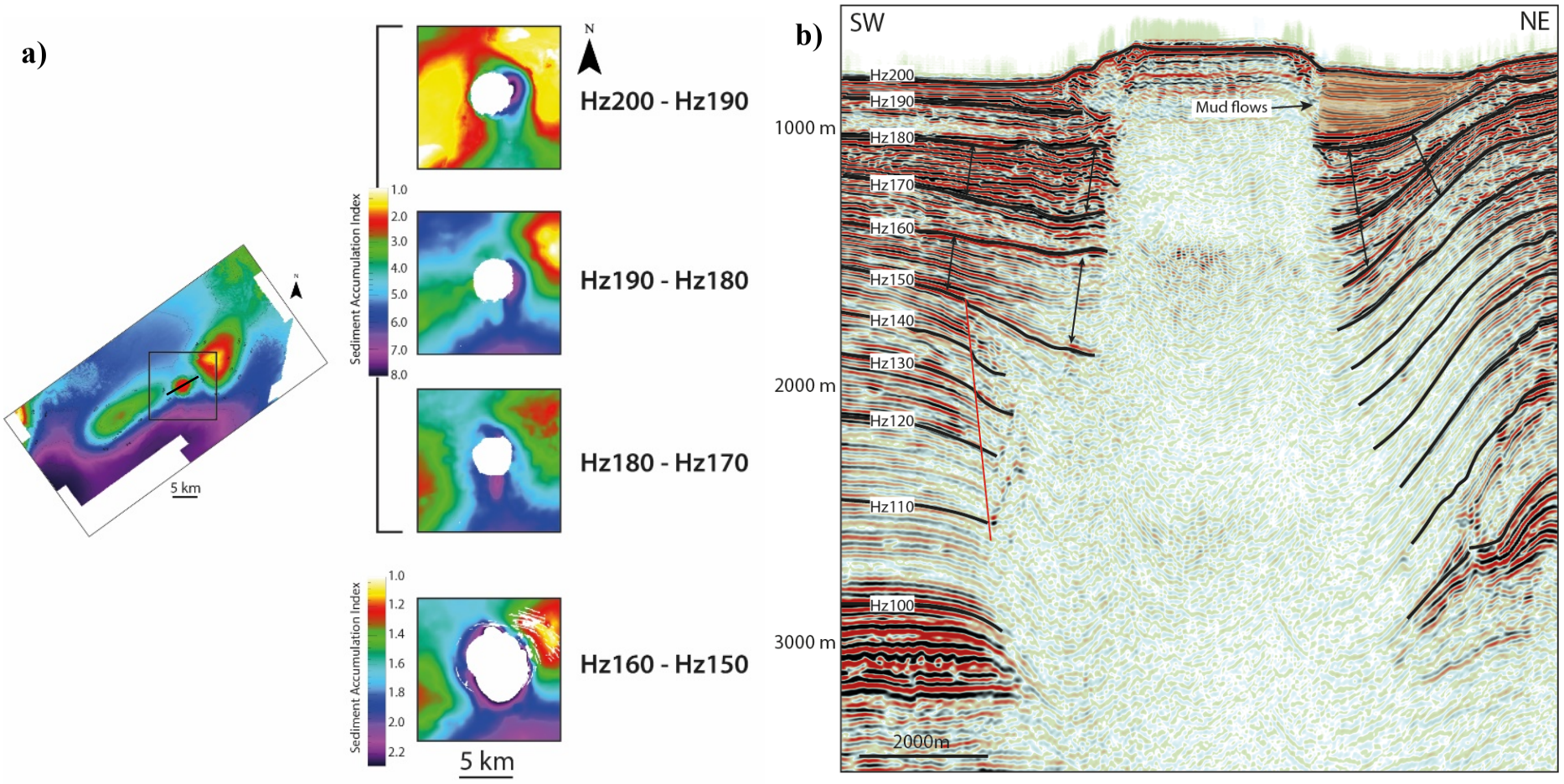


Figure 4.15: a) Sediment accumulation maps around the central mud volcano, MV1, which is active on the present-day seabed, showing sediment growth around the volcano. b) Seismic section across the central mud volcano showing the lack of seismic response in the feeder pipe and sediment growth around the pipe.

4.4 Discussion

The 1D and 3D SAI for the Post-Productive Series show that the distribution of sediment thickness varies frequently around the fold structures, indicating that the fold growth is complex. The sediment accumulation indices show that whilst there is minor fold growth during the Productive Series, the main folding phase initiated after deposition of the Surakhany Evaporites. Indices show that during this folding phase, pulses of growth occur on both folds throughout the Post-Productive Series. However, when analysed in more detail the folds show that growth varies both between the limbs on an individual fold as well as between both structures. Index values of 1.0 alternate between fold crests within the Post-Productive Series suggesting that the dominant fold influencing seabed topography is not consistent and changes through time.

1D sediment accumulation indices show the growth across the individual fold structure and can highlight periods of highest growth on the limbs of the structures through time. Sediment accumulation index maps highlight the 3D nature of the fold structures and how they interact through space and time by comparing the sediment thicknesses directly across the structures. The sediment accumulation index maps show that indices are not consistent throughout the intervals, in terms of both sediment thickness and the distribution of sediment along the flanks of the structures (figure 4.10). There is a significant increase in the sediment accumulation index in interval Hz130 – Hz120, with maximum index values of 2.8 on the fold flanks. This interval has the highest indices of the Absheron Formation, the most growth in the en-echelon crestal normal faults, as well significantly higher sediment accumulation indices over the fold crest of Asiman compared to Shafag. After this interval, the indices decrease and become consistent throughout the intervals, with a maximum index of approximately 2.0 - 2.2. The increase of index values within Hz130 – Hz120 and the subsequent decrease in following intervals indicate that, if the sedimentation rate is constant, the growth strata are not deposited over a consistently growing fold. Growth strata geometries are much more complex than those predicted by the simple kinematic models of fold growth (Erslev, 1991, Suppe et al., 1992, Hardy and Poblet, 1994, Hardy and Poblet, 1995, Poblet et al., 1997, Cristallini and Allmendinger, 2001, Salvini and Storti, 2002). The acceleration in fold growth within interval Hz130 - Hz120 could be due to the increase of the westward

motion of the basin relative to Iran, likely within the last 3 My (Axen et al., 2001, Allen et al., 2004, Ritz et al., 2006, Cifelli et al., 2015, Mattei et al., 2019, Walker et al., 2021), as discussed in Chapter 3. However, if the fold growth was purely controlled by far field tectonics, both folds would be expected to display similar sediment accumulation index and fold growth patterns, however, there is significantly less growth over the crest of Shafag in comparison to during this time. The shape of the fold crest also changes through time, with sediment accumulation indices of 1.0 over the fold crests becoming round and narrower, particularly the Shafag crest. This shape is not characteristic of typical detachment folds formed purely by tectonic shortening (Salvini and Storti, 2002). The palaeo-mud cones and patterns of growth strata surrounding the mud volcanoes demonstrate that mud has been mobile since at least the Productive Series, erupting nearly continuously through the entire Post-Productive Series up to the present day (figures 4.13, 4.14 and 4.15). This therefore leads to the hypothesis that the pattern of growth strata at Shafag-Asiman may be due to sediment loading of a deep mobile shale. The alternating dominant growing structure can be explained by shale withdrawal and sediment loading, with mobile shale moving into the core of one fold and then the other during a later interval. The increase in fold growth and significant change of geometry of Shafag during interval Hz130 – Hz120 can be explained by the inflation of the fold core with mobile shale at this time. The inflation of Shafag due to shale moving into the core can give an explanation as to why the fold growth is more than Asiman.

Compared to the Shafag and Asiman fold crests, the relative lower indices northwest and southeast of Shafag are due to a structure trending northwest – southeast causing thinning of the strata. These lower indices can be seen on regional isopach map for the Post-Productive Series (Green et al., 2009) (figure 4.16). The northern limb of Asiman is connected to a large fold to the west of the area, causing indices in the northwest to be lower than the south. A fold to the southeast of Shafag is visible from the regional isopach map, with thinning occurring between Shafag and this fold. Although these structures affect the distribution of sediment on the fold flanks, throughout Hz100 to Hz160 the southern flank has higher sediment accumulation values than the northern flank, making the fold structures asymmetrical.

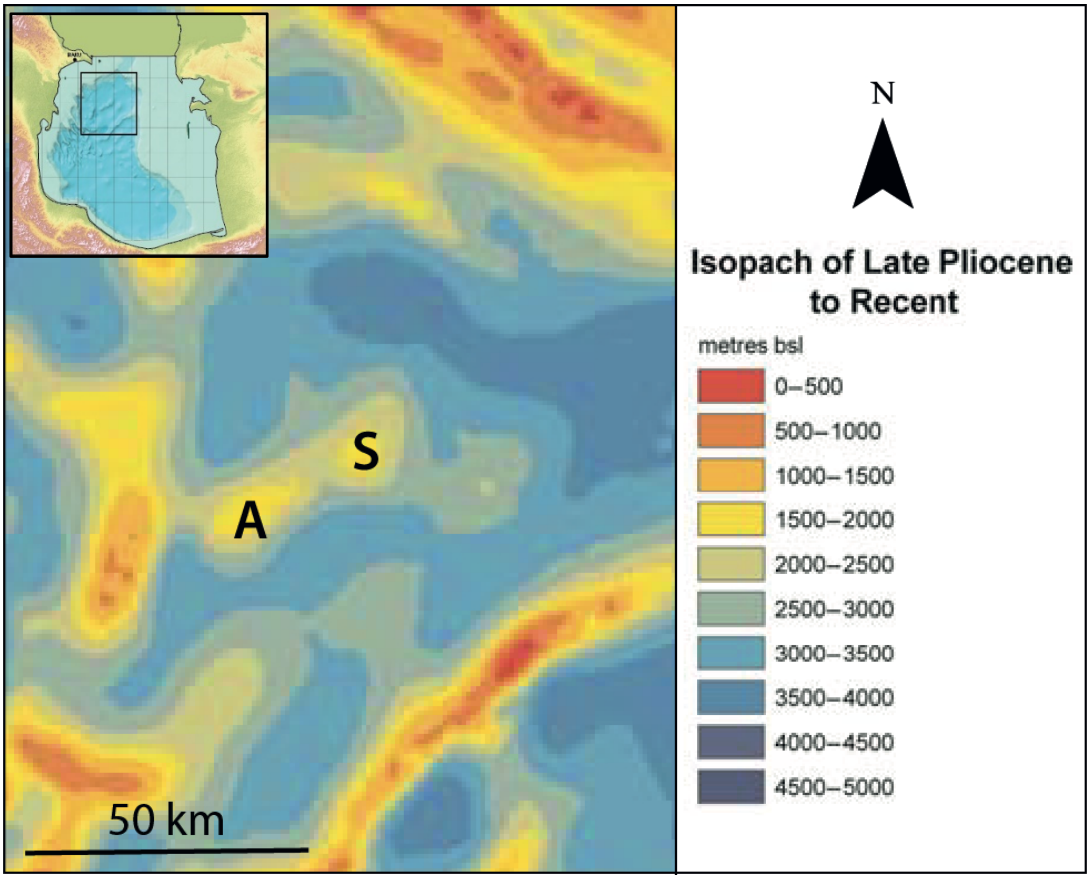


Figure 4.16: Isopach map of the Post-Productive Series from Green et al. (2009). Thinning of the strata can be seen in the yellow colours southeast of Shafag (S) and northwest of Asiman (A).

Moving up into the mass transport deposits, Hz160 to Hz200, the asymmetrical sediment distribution of the northern and southern flanks is not as clear (figure 4.12). The mass transport deposits are mostly sourced from outside of the area (Chapter 2) and infill the topography from one-fold to the other, with significant onlap onto the fold crests. They continue to display the alternating dominant fold growth during deposition, as observed in the intervals below. Although the distribution of the deposits within the Shafag-Asiman suggest that they are sourced from outside of the study area (Chapter 2), they may also be sourced from the crests of Shafag-Asiman themselves, as shown by present-day slumping occurring off the fold flanks (Chapter 2). Mass transport deposits are sourced from both growing fold structures and from the shelf throughout the basin (Richardson et al., 2011, Santos-Betancor et al., 2014). Although the deposits appear to e sourced from the north (Chapter 2), the direction of the deposits has also not been analysed in any detail. Therefore, although the folds were growing during deposition of the mass transport deposits, it is not possible to state whether this was higher or lower than during the lacustrine turbidite section based on the sediment accumulation indices. It can be concluded,

however, that the folds had an alternating dominant effect on the seabed topography as is also observed within the lacustrine turbidites.

As stated previously, mud volcanism in the area gives evidence for mobile shale movement. The mud volcano north of Shafag, MV3, shows evidence for palaeo-eruptions that occurred during deposition of the Productive Series. Although 1D indices indicate that the Productive Series was deposited before the onset of major structural growth, growth is visible from the sediment accumulation indices during deposition of the sequence. Whilst structural growth is documented to initiate in the latest Productive Series or Akchagyl times elsewhere in the basin (Devlin et al., 1999, Abdullayev, 2000, Santos-Betancor and Soto, 2015), the structural growth within the Productive Series at Shafag Asiman may have been enhanced by folding upon the mobile shale of the Maykop Formation, since it was mobile during these times, as evidenced by the palaeo-mud cones.

To test the hypothesis that sediment loading of the mobile shale influences the fold growth of Shafag – Asiman, I investigate the properties of the mobile shale beneath the fold structures and the controls and timing of mobile shale movement using numerical modelling shown in the subsequent chapter, Chapter 5.

4.5 Conclusions

Growth strata analysis using novel sediment accumulation indices show that fold growth of Shafag – Asiman initiated during deposition of the Productive Series, with the major phase of growth following deposition of the Surakhany Evaporites at the top of the Productive Series. Alternating dominant fold growth between Shafag and Asiman, both in space and time, as interpreted from growth strata are not typical of growth predicted by classic geometrical models. Another factor in the fold development must be influencing growth. Active mud volcanism was present during deposition of the Productive Series and continues to the present-day, giving evidence for mobile shale movement in the area through the development of the fold structures. Sediment loading of a mobile shale beneath Shafag-Asiman can explain the complex growth strata that is observed around the fold structures. This hypothesis is tested further within Chapter 5.

5. Numerical modelling the mechanical properties and influences of sediment load on a mobile shale cored fold structure.

This chapter is presented as a draft paper and therefore there is some repetition with other chapters.

5.1 Introduction

Mobile shale tectonics has been documented within 65 regions across the world, including the Niger Delta, the Gulf of Mexico, the Caribbean basin and the South Caspian Basin (Soto et al., 2021a). However, unlike salt tectonics, very few studies on the role of sediment loading on the deformation history within these regions have been published. Although both salt and mobile shale can produce thin-skinned deformation through extension, shortening and loading (Morley and Guerin, 1996), the intrinsic (material) properties of both mediums mean they act and respond differently depending on the local conditions (Jackson and Vendeville, 1994). Properties of salt remain relatively constant, but shale varies through time, depending on compaction and depth (Ewy et al., 2020), with movement dependent on the degree of overpressure within the pore fluids of the shale (Morley and Guerin, 1996). The effect of sediment load in salt tectonics has been demonstrated frequently (Waltham, 1997, Gemmer et al., 2004, Hudec and Jackson, 2007) and is well understood, however, deformation of mobile shale is relatively poorly understood. It is generally agreed that shale can behave as a visco-plastic solid (Dean et al., 2015, Albertz et al., 2010, Ings and Beaumont, 2010, Soto et al., 2021a) but can also behave as a suspension fluid as demonstrated by the wide-spread occurrence of mud volcanoes in shale provinces such as Trinidad, Nigeria and both on and offshore Azerbaijan (Barboza and Boettcher, 2000, Boettcher et al., 2000, Fowler et al., 2000, Graue, 2000, Hudec and Soto, 2021). Several large-scale numerical models have attempted to model mobile shale tectonics, for example the effect of delta propagation on mobile shales in the Niger Delta (Albertz et al., 2010, Ings and Beaumont, 2010, Dean et al., 2015) however to the best of our knowledge there have been no attempts to conduct numerical models to test whether sediment loading can contribute to growth of smaller-scale structures.

In this study I investigate the question of whether sediment loading of a thick shale detachment layer can affect detachment fold growth. I address the question of whether the loading of a weak visco-plastic shale can amplify the growth of a fold causing withdrawal of the shale on the flanks of the fold as shale flows into the core. The model is constructed to test this hypothesis for detachment folds forming in the South Caspian Basin. In particular, numerical models are based on the Shafag-Asiman structure which is well imaged on 3D seismic reflection data. The South Caspian Basin is a land-locked basin containing a 20 km thick sedimentary succession, one of the thickest successions of any basin on the planet (Allen et al., 2002), with the topmost 10 km of its sedimentary fill deposited within the last 6 Ma (Devlin et al., 1999). The rapid sedimentation rates generate abnormal conditions, such as low temperature gradients (Abrams and Narimanov, 1997) and overpressured sediments (Narimanov, 1993, Abrams and Narimanov, 1997). Growth strata on seismic data shows that the widespread folding in the South Caspian Basin commenced in latest Miocene to Pliocene times (Chapter 4). Syn-tectonic sediments of the Late-Miocene – Early Pliocene Productive Series and the Pliocene - recent Post-Productive Series were deposited upon the Oligo-Miocene Maykop Formation (Green et al., 2009), the visco-plastic shale detachment layer modelled in this chapter.

5.2 Methods

Numerical models were designed to analyse the impact of sediment loading on the formation of a shale cored detachment fold forming under conditions of tectonic shortening. The model set up was used to run sensitivity analysis to determine the relative impacts of different parameters on fold growth through time. These parameters are the material properties of the shale (viscosity and density), mud thickness, total applied shortening and overburden thickness/sedimentation rate. For the numerical models 2-D plane-strain finite-element models were designed and run using the Elfen numerical codes from Rockfield Global (Rockfield, 2010). The mechanical governing equation is a linear-momentum balance, and the details of the computation framework are given elsewhere (Crook et al., 2006, Thornton et al., 2014, Thigpen et al., 2019). The code is based on the Lagrangian method and employs adaptive remeshing of the finite element grid to account for large magnitude strains. Syn-kinematic sedimentation is simulated at 0.1 My increments equivalent to the pre-defined sedimentation rate,

allowing sediment to aggregate to a horizontal surface. The overburden and syn-kinematic sediments are modelled as poro-elastoplastic using a modified Cam Clay critical state model, described in detail in Crook et al. (2006) and Thigpen et al. (2019). In many numerical models of geological deformation rock strength is approximated using a Mohr-Coulomb constitutive property to simulate rock behaving elastically prior to failure. This material description is appropriate for rocks that are fully lithified but is not the most appropriate for young sediments deposited very rapidly as found in the South Caspian Basin, where the rocks can experience a significant portion of non-recoverable plastic deformation (Rance et al., 2013). The Modified Cam-Clay variant employed in the software (Soft Rock 3) has an evolving curved yield function governed by plastic volumetric strain via a piecewise linear/hardening law (Crook et al., 2006). A drained effective stress model is used which assumes that pore pressures remain hydrostatic. Although the stress path differs between a drained and undrained rheology, both responses tend to the critical state condition when they are sheared. In reality the shales will likely display a behaviour that is partially drained, between a drained and undrained response. Ideally, this would be studied in a fully coupled model where the pore pressure is explicitly evaluated, e.g. Obradors-Prats et al. (2017), however this is beyond the scope of this study.

Material properties used within the model are constrained, partially, by experimental data from the ACG field in the South Caspian Basin (Rance et al., 2013). A table of material properties are found in appendix A.

One of the complexities of numerical modelling of a mobile shale layer is determining material properties for the shale. As the viscosity of the Maykop in the South Caspian Basin is unknown at the time of deformation models are run with varying viscosity, to determine the most likely shale viscosity under the Shafag-Asiman structure, as well as to examine the effect of varying shale viscosity on fold growth during sediment loading through time.

Although previous studies have modelled the mobile shales as a visco-plastic Bingham material (Albertz et al., 2010, Ings and Beaumont, 2010, Dean, 2014), the visco-plastic mud layer in this study is modelled as a Herschel-Bulkley material with the consistency and flow index set to recover a Newtonian fluid description but with a very small yield stress. This gives a response that resembles a Bingham plastic and helps with model stabilisation. Soto et al. (2021a), report shear vane tests to show

that a shale at critical state is viscous and behaves as a Herschel-Bulkley material (Skempton, 1948). In this study, the Maykop shale layer is therefore modelled as a mobile visco-plastic material, at the critical state. There has been recent discussion in the literature that questions whether deeply buried shales can display viscous behaviour (Morley et al. 2017 and references therein e.g Day-Stirrat et al. 2010 and Morley et al. 2011) because above 80 °C (at ~ 2-3km burial depth) chemical compaction and cementation should lithify shale. However, under conditions where high fluid pressures build up in shales they can behave in a viscous way at greater depths (Soto et al. 2021a and references therein). One way of forming high pore fluid pressures in shales is by hydrocarbon generation (e.g Barker, 1990, Mazzini and Etiope, 2007)). Mud volcanoes in Azerbaijan contain >90% methane (Kopf, 2003, Bonini et al., 2013) whilst Feyzullayev and Lerche (2009) suggest that burial below 9 km takes the Maykop into the gas generation window. Basin modelling of the South Caspian Basin shows that the geothermal gradient in the South Caspian Basin in the Shafag-Asiman area is approximately 20^{o}C/km (bp 2021). The Maykop under Shafag-Asiman is at 9-10 km depth therefore reaches temperatures of 160^{o}C and above, deep into the gas generation window. Increased pore pressure due to gas generation would allow the critical state to be reached at a lower shear stress (Soto et al., 2021a), and evidence suggests that the Maykop shales are mobile in the Shafag-Asiman area (Chapter 4); and hence it is appropriate to model them with a visco-plastic rheology.

The presence of numerous mud volcanoes within the South Caspian Basin (Fowler et al., 2000, Yusifov and Rabinowitz, 2004) and this study (Chapter 4) demonstrates that over much of the basin there are places where there are significant overpressures. Timing of mud volcano activity in the SCB has been reported to have initiated after the onset of structural growth at 2 – 3.3 Ma (Fowler et al., 2000). This occurs just after an increase in sedimentation rate (Yusifov and Rabinowitz, 2004), which took place at approximately 4 Ma (Bagirov and Lerche, 1999). There is also an increase in mud volcano formation and activity at approximately 1.8 Ma (Yusifov and Rabinowitz, 2004). Bagirov and Lerche (1999) suggest that the increased sedimentation caused the hydrocarbon generation, accumulation of overpressure and migration of fluids that was necessary to initiate the growth of mud volcanoes. There are several mud volcanoes in the Shafag-Asiman area, one of which is present at the seabed, and two

others that are visible in the seismic data buried at various levels in the stratigraphy, testifying to the presence of fluid Maykop during the history of fold growth (Chapter 4).

Previous numerical modelling studies of shales have used a range of viscosities, ranging from 10^{12} Pa.s (Collier and White, 1990) up to 10^{18} Pa.s (Albertz et al., 2010, Ings and Beaumont, 2010). Viscosities used in salt modelling range from 10^{14} Pa.s to 10^{18} Pa.s, dependant on temperature, grain size and water content (Davison et al., 1996). Van Keken et al. (1993) suggests ranges of 10^{17} Pa.s to 10^{20} Pa.s as a function of grain size and temperature, with 10^{18} Pa.s most appropriate for fine grained salt. For the models in this chapter a viscosity range from 10^{17} Pa.s - 10^{22} Pa.s is applied, where at 10^{17} the mud starts to behave as a liquid and at 10^{22} Pa.s the mud behaves as a pseudo-elastic material.

The response observed within the visco-plastic layer depends on both the viscosity and density of the layer. These are both key parameters in the momentum balance equations, which is the fundamental control on the mud movement within the models. Previous modelling of salt shows that the density contrast between the overburden and the salt layer is vital in determining salt movement and diapirism (Waltham, 1997, Gemmer et al., 2004, Hudec and Jackson, 2007). This density contrast is most likely a key control on the movement of mud in shale tectonics too. Within the models presented here, density is controlled by the input of the layer porosity. Well data from the South Caspian Basin show that Maykop densities can decrease to 2000 kg/m^3 or even lower due to gas generation within the shale (Khalilov and Imanov, 1979, Khalilov and Imanov, 1980, Buryakovsky et al., 1982, Feyzullayev and Lerche, 2009, Soto et al., 2021b). A study by Marín-Moreno et al. (2013) investigating overpressure in the Black Sea calculates the porosity of the Maykop to be between 25% - 30%, with a density of 2200 kg/m^3 using inverse modelling and p-wave velocities. In their study the present-day Maykop is between 5-6 km deep. The Maykop under Shafag-Asiman is approximately 8.5-10 km deep at the present day. Marín-Moreno et al. (2013) suggest that the overpressure observed in the Black Sea is due to disequilibrium compaction whereas overpressure in the South Caspian Basin is likely to be enhanced by gas generation due to higher temperatures of the Maykop at the deeper burial depths than in the Black Sea (Feyzullayev and Lerche, 2009). As gas forms and fills the pore spaces within the shale, the overall density of the layer decreases. The density contrast between the overburden and the Maykop therefore becomes larger, causing the shale to become more mobile. The conclusion of this is that the

density of the Maykop under the Shafag-Asiman structure is expected to be lower than in the Marín-Moreno et al. (2013) Black Sea study. Therefore, models are run with an initial porosity of 25%, 30% and 35% for the Maykop and compare the models with the present day Shafag geometry. The results of the viscosity and porosity/density are then used to test model sensitivity to the other parameters.

By modelling a range of viscosities and densities for the Shafag fold it can be determined: 1) what impact different mud viscosities at different mud densities have on fold development during sediment loading and 2) what the most likely viscosity of the Maykop is under the Shafag-Asiman fold structure. It would be expected that the fold amplitude increases with lower viscosities compared to higher viscosities due to more mobile mud moving into the core of the fold as sediment loading on the fold flanks forces the mud into the growing fold core.

Tectonic loading is applied in two ways – (1) a horizontal compression applied as a lateral boundary condition and (2) an upward movement, where a pre-defined initial fold geometry of pre-kinematic strata is set (See arrows in figure 5.1). This is effectively the perturbation required for the fold to grow and replicates initiation over a basement structure, as documented in Chapter 3. The Shafag-Asiman fold forms above a structure in the basement beneath the Maykop shale, but the geometry cannot be confidently identified on the seismic data. Setting up the model with a pre-existing fault generates an asymmetry in the modelled fold, not seen in the real data. The original width of the model is 45 km, with a total of 10 km horizontal shortening to deform to the present-day width of 35 km, constrained by line-length balancing. In the base model (Experiment 1; table 5.1) the applied lateral compression and basal perturbation replicates the present-day shape of the Shafag fold. The model has an initialisation phase applying initial vertical and lateral stresses (loading of pre-kinematic overburden under gravity).

The geometry of the initial model set up is based on seismic data from the Shafag fold in the South Caspian Basin, with a simplified representation of the stratigraphy and lithology of the area. Figure 5.1 describes the initial model set up.

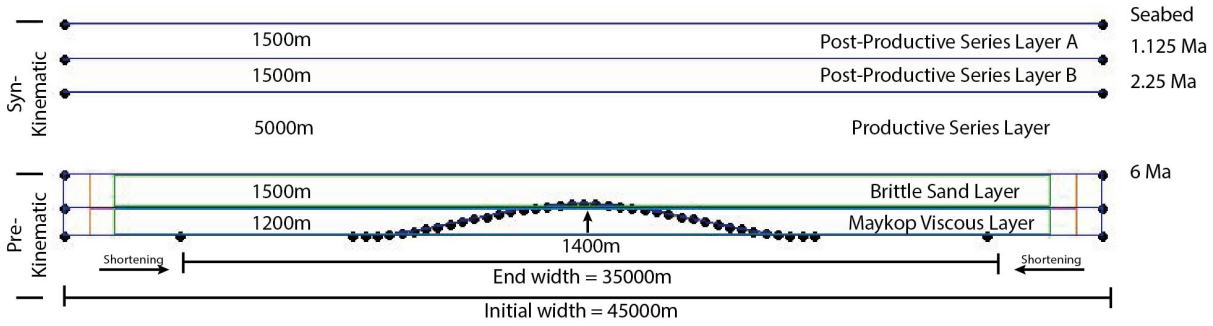


Figure 5.1: Simple model geometry used for sensitivity analysis with constant sedimentation rate based on values measured from seismic reflection data of the Shafag fold.

The sedimentation rate is made constant for the base model, to eliminate any potential sensitivities in the model to changes in sedimentation rate and a simplified lithological description of the Pliocene to Recent Caspian Sea sediments is used. The lower 1200m layer is a pre-kinematic visco-plastic layer modelled to replicate the shale detachment of the Maykop Formation. The lowermost 1500m layer in the model above the visco-plastic layer is defined as a pre-kinematic sandstone and represents post-Maykop and lowermost Productive Series deposited prior to onset of folding. This layer displays an elasto-plastic behaviour. The Productive Series, deposited from 6 - 2.25 Ma, is modelled as a syn-kinematic, 5000m thick unit consisting of sands. Within the South Caspian Basin the Upper Miocene to Pliocene Productive Series consists of sand-rich, fluvio-deltaic sands (Green et al., 2009). The top two units, the Post-Productive Series, are modelled as a syn-kinematic, 3 km thick sand package deposited from 2.25 Ma to the present day, representing the Akchagyl, Apsheron and Baku Formations. In the Shafag-Asiman area the Post-Productive Series consists of a mixed silt/sand succession deposited in a deep-water lacustrine environment.

Four experiments are set up to test the impact of the varying parameters on the extent to which sediment loading influences fold growth (table 5.1):

Table 5.1: Parameter values used in the model set up for each experiment.

Parameter	**Experiment 1a** **Base Case** **Viscosity + Density**	**Experiment 1b** **Shafag**	**Experiment 2** **Maykop thickness**	**Experiment 3** **Applied Shortening**	**Experiment 4** **Overburden thickness**
Initial Width (m)	45000	45000	45000	45000	45000
End Width (m)	35000	35000	35000	30000, 35000, 40000	35000
Perturbation height (m)	1400	1400	1400	2100, 1400, 700	1400
Pre-kinematic Sand thickness (m)	1500	1500	1500	1500	1500
Syn-kinematic Productive Series thickness (m)	5000	5200	5000	5000	5000
Syn-kinematic post-Productive series A thickness (m)	1500	1500	1500	1500	1000, 1500, 2000
Syn-kinematic post-Productive series B thickness (m)	1500	1300	1500	1500	1000, 1500, 2000

Syn-kinematic Productive Series sed rate (km/My)	1.333	1.575	1.333	1.333	0.1333
Syn-kinematic post-Productive series A sed rate (km/My)	1.333	0.790	1.333	1.333	0.888, 1.333, 1.777
Syn-kinematic post-Productive series B sed rate (km/My)	1.333	1.625	1.133	1.333	0.888, 1.333, 1.777
Maykop Thickness (m)	1200	1200	600, 1200, 1800	1200	1200
Maykop Viscosity (Pa S)	10^{17} - 10^{22}	10^{18}	10^{18}	10^{18}	10^{18}
Maykop Porosity (%)	35, 30, 25	30	30	30	30
Maykop Density (kg/m^3)	2252, 2169, 2085	2169	2169	2169	2169

Experiment 1a is the base case, used to explore the Maykop material properties of viscosity and density. Experiment 1b is used to compare the model to the real world Shafag data. Experiments 2 to 4 are based on the simple geometry of experiment 1a and test the sensitivity of the results to Maykop thickness, amount of tectonic shortening and variations in overburden thickness.

5.3 Results

5.3.1 Experiment 1a: Viscosity and Porosity/Density of Shale layer

In the initial model testing a lower limit of a viscosity of 10^{17} Pa.s was used, however the layer became too liquid and caused numerical instabilities and the results were therefore discarded. Figure 5.2 shows a comparison of the final model geometries for viscosities of the visco-plastic layer of 10^{18} Pa.s, 10^{19} Pa.s and 10^{20} Pa.s at porosities of 25%, 30% and 35%. Figure 5.2a shows the final model geometries for the three viscosities at 35% porosity. The model with 35% porosity and 10^{18} Pa.s viscosity shows significantly more axial fold growth and overburden thickening on the edge of the model than both 10^{19} Pa.s and 10^{20} Pa.s. The visco-plastic layer is also thinner at the model edge and thicker in the fold core. The greater axial fold growth with a viscosity of 10^{18} Pa.s creates greater seabed topography then in the models with viscosities of 10^{19} Pa.s and 10^{20} Pa.s. Figure 5.2b shows the final model geometries for the three viscosities at 30% visco-plastic layer porosity. They show similar geometries to the 35% porosity models, however the overburden thickening and visco-plastic layer thinning are less for the respective viscosities. The visco-plastic layer at 10^{18} Pa.s viscosity is thinner on the edge of the model than for both 10^{19} Pa.s and 10^{20} Pa.s, increasing on the limbs but not on the crest. The top of the visco-plastic layer in 10^{18} Pa.s is deeper than both 10^{19} Pa.s and 10^{20} Pa.s, even though the fold grows more through time for 10^{18} Pa.s. Figure 5.2c shows the final model geometries

for viscosities at 25% porosity where the effect on overburden thickness on the crest and model edge can still be seen to be greater in the 10^{18} Pa.s viscosity model, however the effect is minimal.

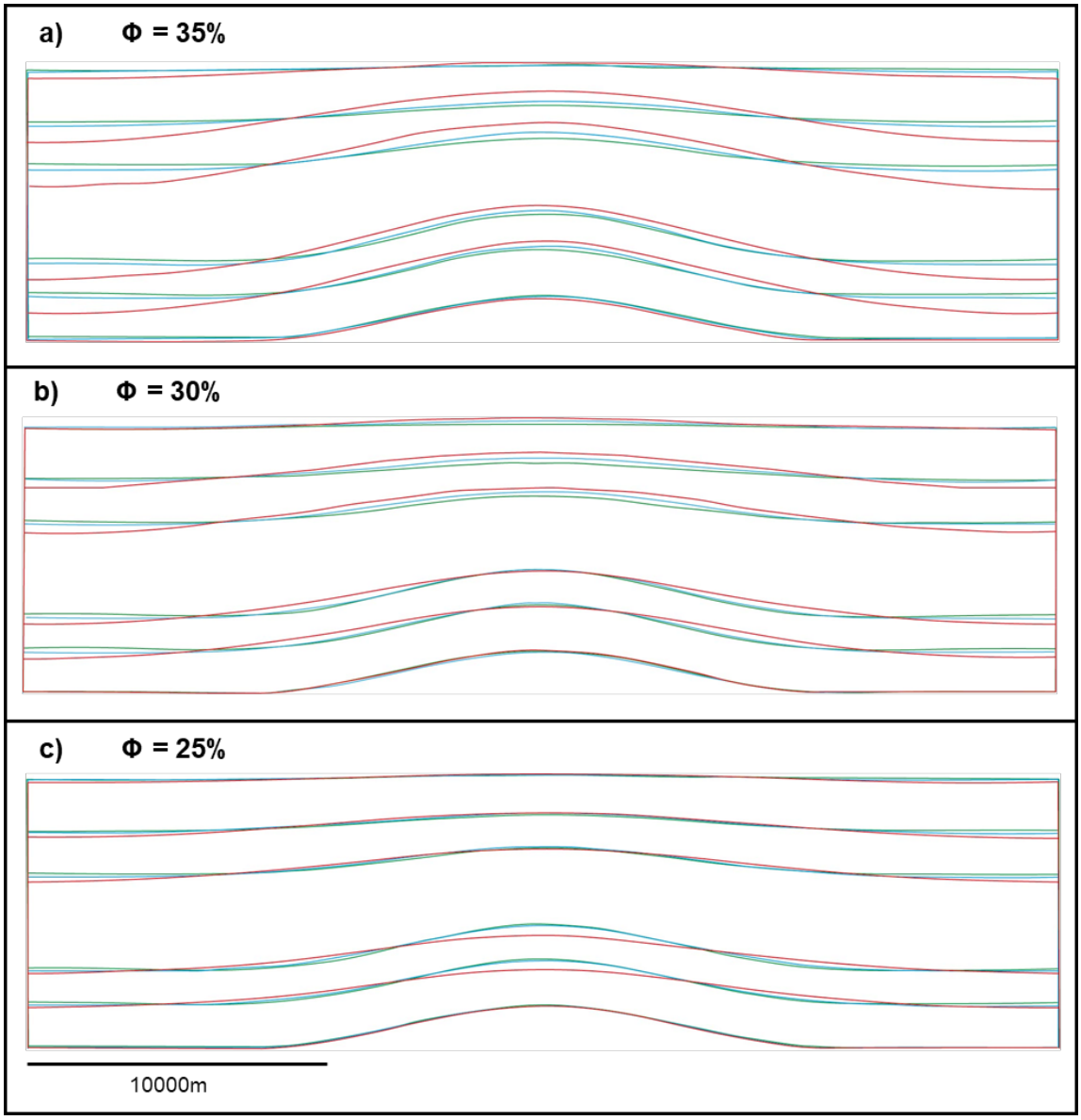


Figure 5.2: Fold geometries at end of model run in Experiment 1a for viscosities of 10^{18} (red), 10^{19} (blue) and 10^{20} (green) for (a) 35% (b) 30% and (c) 25% porosity.

Figure 5.3 shows a model through time, for a viscosity of 10^{18} and porosity of 30%. The colour contours indicate the displacement in x reached at the specified snapshot time. This shows how the particles within the visco-plastic layer move in comparison to the sand layers above. The initial model

at 0.1 My has two pre-kinematic layers, the visco-plastic layer and the pre-kinematic sandstone layer above. At 0.5 My syn-kinematic deposition starts during the initial shortening of the model.

During the entire model run the overburden layers show inward movement in x towards the centre of the model in response to the applied horizontal shortening (obvious by 2 My). The amount of shortening decreases upward within the syn-kinematic layers as the layers become younger, as expected. Within the overburden, the pre-kinematic sandstone layer above the visco-plastic shale layer records the largest amount of inward movement in x, in response to the applied tectonic load. In contrast, the underlying visco-plastic shale layer illustrates a more complex pattern. Firstly, the shale flows outward from the fold crest towards the model edges for up to approximately half the model width as it responds to the increase in slope from the fold crest to the limb at the base of the model, due to the upward component of displacement that uplifts the fold axis (visible from 2-5 My). This outward flow impedes how much the shale layer can shorten on the fold flanks. From 4 My, the distance that the shale flows outward from the fold crest starts to reduce significantly. Between 5 and 6 My, the outward flow is replaced by a dominant inward flow in the shale, and by 6 My no outward flow of shale is recorded. Off the fold flanks the total amount of inward shale movement has overtaken the tectonic shortening in the sandstone layer above, but towards the fold crest the inward shortening is still less than the total tectonic shortening in the overlying layer. By the end of the model run at 6.5 My inward flow in the shale layer has overtaken the total horizontal tectonic shortening over the entire model. Close to the model edges the inward particle displacement in the visco-plastic layer is significantly higher by approximately 2 km when compared to the deepest overburden layer, with a maximum inward displacement of 5278m in the centre of the visco-plastic layer.

The key transition between dominant outward versus inward flow in the shale appears to occur between 4 and 5 My. I infer that in this time interval the greater overburden load on the fold flanks compared to the crest, (due to the greater density contrast between the overburden and shale) starts to overcome the outward flow and drives the visco-plastic shale inwards towards the fold crest. This then generates positive feedback; as the shale flows towards the fold crest, there is more accommodation space generated off the fold flanks and greater thicknesses of syn-kinematic sediments can be deposited.

This in turn increases the overburden load with a resultant increase in rate at which visco-plastic shale is driven towards the fold axis.

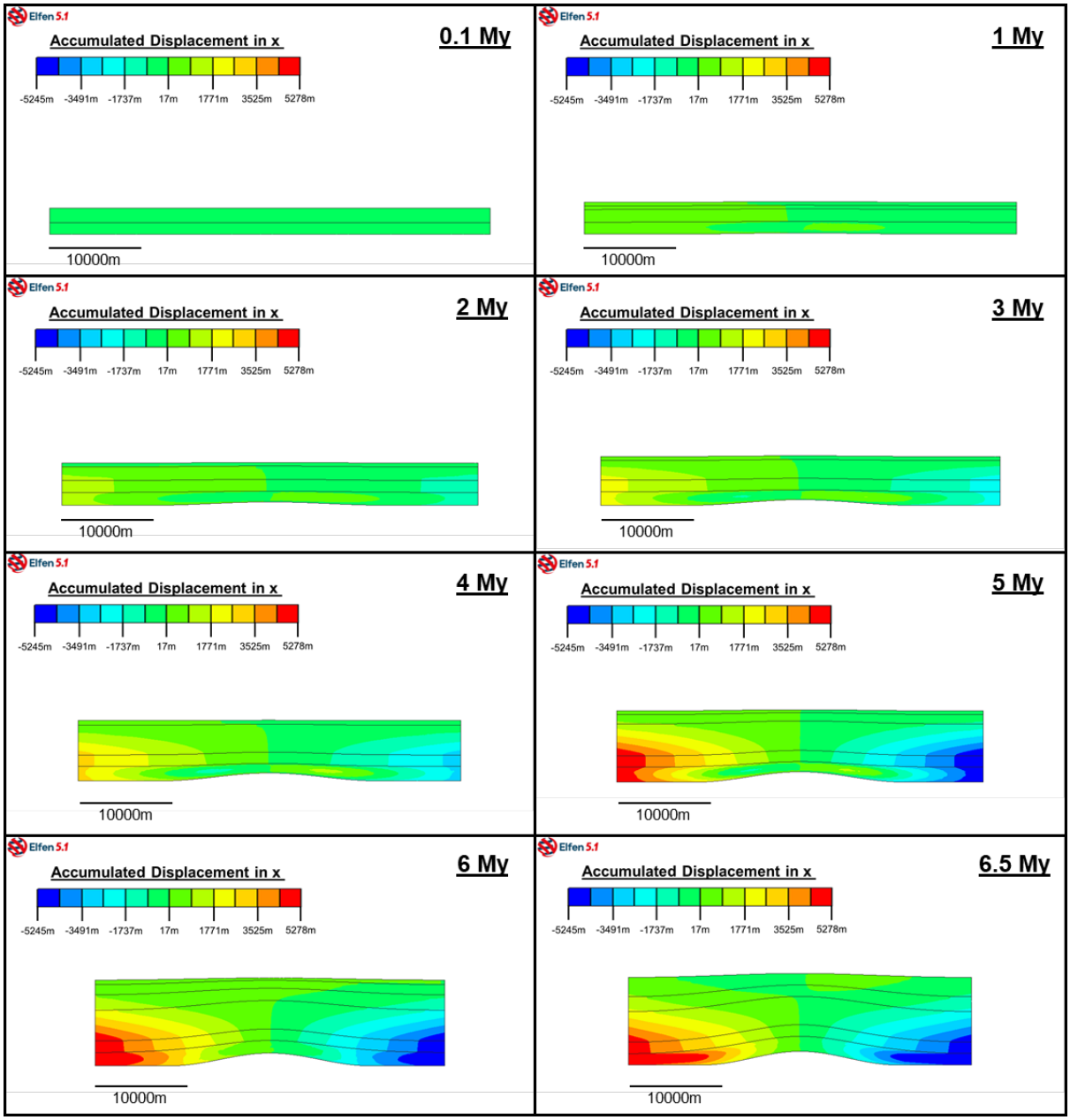


Figure 5.3: Contours showing accumulated displacement in x for a model with 30% visco-plastic layer porosity and 10^{18} Pa.s viscosity through time.

The contour maps show that the visco-plastic shale flows outwards and then inwards as more sediment is deposited on the fold flanks and the overburden load increases. However, although the contour maps are useful in providing snapshots of the model as it evolves through time, the details of the displacement can be difficult to observe. To explore the models in more detail the movement in the x direction is tracked for three starting positions within the visco-plastic layer through time (figures 5.4,

5.5 and 5.6). This allows the x-position of a node in the model to be followed through time, at 10,000 year intervals, and provides a more detailed insight into the model behaviour. The graphs can also be used to compare the full suite of density and viscosity models explored in experiment 1a. The positions tracked in the centre of the visco-plastic layer are at 4000m, 10000m and 16000m distance from the fold axis at the centre of the model. For comparison, the particle trajectory of the 16000m position within the pre-kinematic layer immediately above the shale layer is shown as an example of what the displacement in x would be for the same position in a layer deforming by purely tectonic shortening (figure 5.4 and 5.5).

Initially, the graph of 10^{18} Pa.s viscosity and 30% porosity is shown (figure 5.4) to describe in more detail the corresponding contour sections for the same model (figure 5.3).

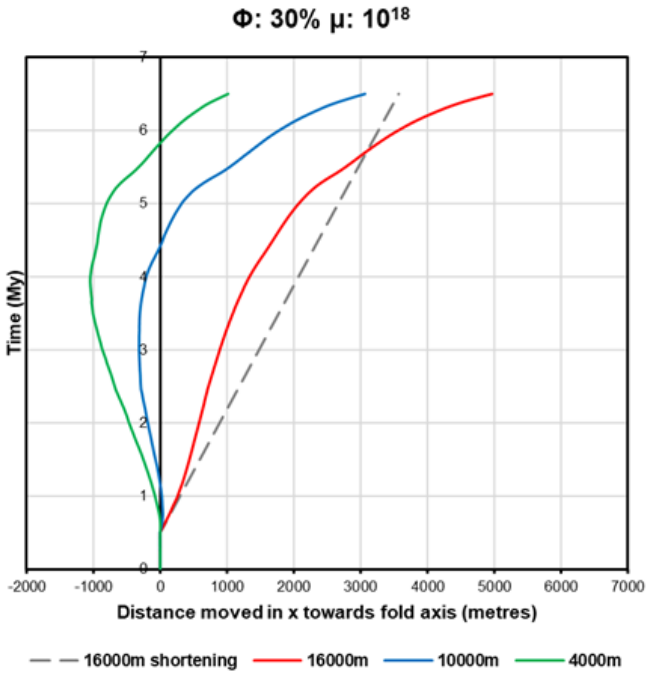


Figure 5.4: Distance of particle movement in x for the model of 30% porosity and 10^{18} Pa.s viscosity for the visco-plastic layer at three starting locations from the fold axis in the centre of the model, 16000m in red, 10000m in blue and 4000m in green. Applied tectonic shortening is shown at 16000m starting location by tracking within the elasto-plastic sand layer (grey dashed line).

The overlying pre-kinematic elasto-plastic layer shows a linear relationship between the movement in x and time whereas the visco-plastic layer behaves in a non-linear manner, with the amount of movement in x accelerating through time. The contour sections showed that particles first moved outwards and then inwards as more overburden was deposited (figure 5.3). By tracking the node at 10,000 yr intervals the time at which the outward flow switches inwards can be identified. For example, at the 4000m starting position, the node starts to move inwards at 4 My (figure 5.4). I infer

that this is the time at which there is enough vertical load from sediment deposited on the fold limb to override the effect of the basal uplift of the fold axis which caused the shale at these positions to initially move away from the fold crest. By 5.7 My, the 16000m position within the visco-plastic layer intersects the overlying layer trend. After this time, this position within the visco-plastic layer moves more towards the fold axis than the equivalent starting position within the overburden layer, but the rate of inward movement of the visco-plastic shale layer at this position started to accelerate earlier at ~4 My.

Varying the initial porosity of the visco-plastic layer at a viscosity of 10^{18} Pa.s does not affect the nonlinearity of the relationship between distance moved in x, versus time (figure 5.5). However, once the viscosity is increased to 10^{20} Pa.s the relationship becomes almost linear, regardless of the initial porosity; at geological timescales the shale is no longer behaving as a visco-plastic material, but appears to approximate the behaviour of an elasto-plastic material where one would expect a linear relationship between the lateral displacement in x and constant rate of applied shortening (figure 5.5).

Figure 5.6 shows the movement in x plotted for each position for the modelled viscosity range for each of the modelled porosities. These results show that for viscosities of 10^{18} and 10^{19} non-linear behaviour occurs in the shale; at higher viscosities, above 10^{20}, linear behaviour is seen and the shale is no longer visco-plastic, but appears to approximate a elasto-plastic behaviour, regardless of its porosity. It is inferred that the lateral displacement in the elasto-plastic shale layer records the response to the horizontal component of the tectonic shortening. The results also show that at shale porosities of 30% and 35%, the non-linear behaviour of the shale layer leads to more inward movement of shale towards the fold crest by the end of the model run when compared to the total horizontal displacement of 'elasto-plastic' shale. However, at a porosity of 25% the response is more complex.

At 10^{18} Pa.s viscosity for a porosity of 25% the relationship is non-linear, but the final inward movement of the shale does not exceed the final inward shortening recorded in the elasto-plastic layer above for the 4000 and 10000 positions and just exceeds it at the model margins. This may be for two reasons. The lower porosity, and therefore higher density, may cause the layer to become too stiff to be able to move inwards towards the fold axis at a fast enough rate, as there is not a great enough density differential between the overburden and the Maykop shale. The other reason may be due to the length of time for which the model runs and there may not be enough time to allow the denser visco-

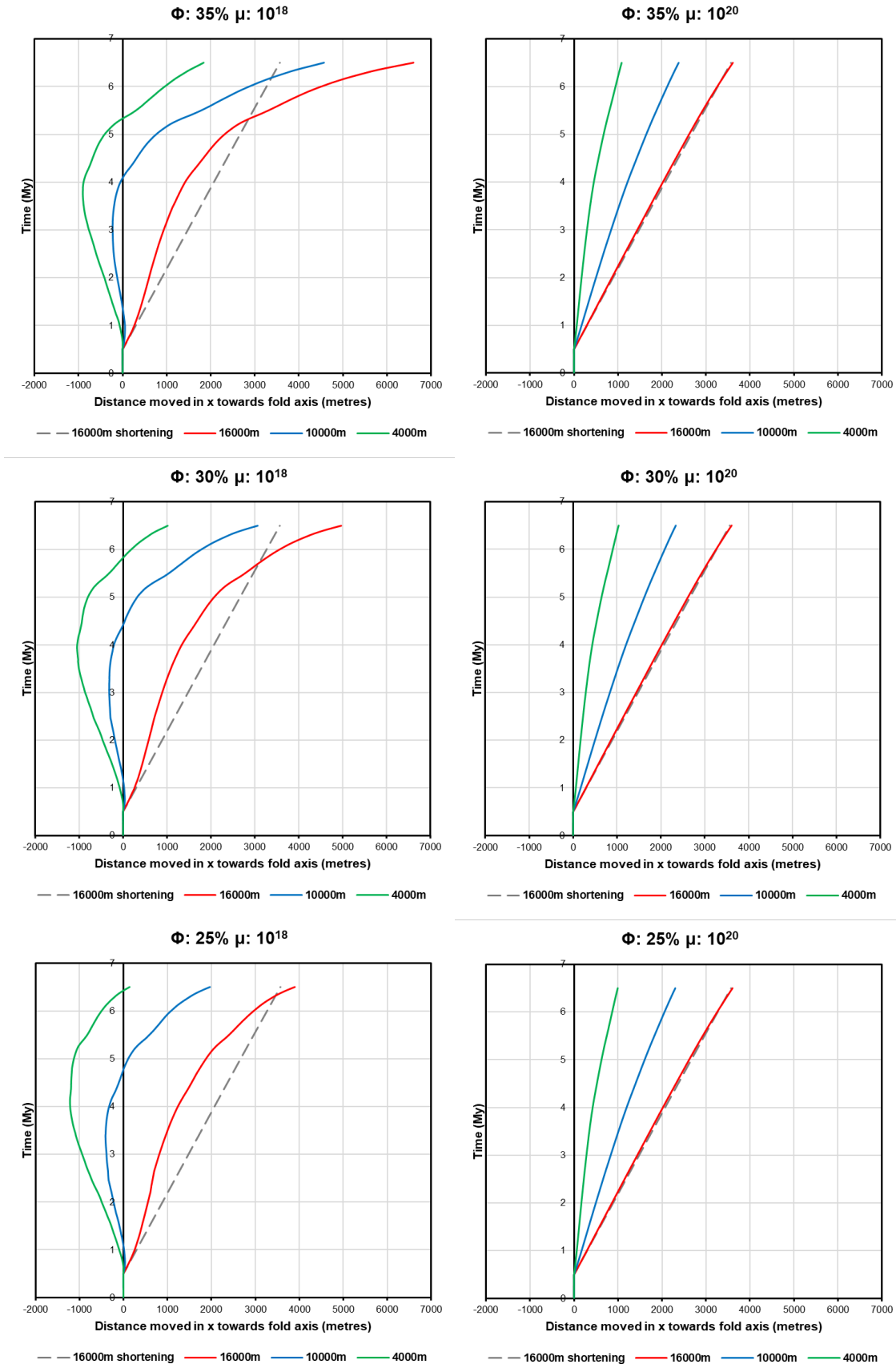


Figure 5.5: Distance of particle movement in x for models of 35%, 30% and 25% porosity of the visco-plastic layer at viscosities of 10^{18} and 10^{20} at three starting locations, from the fold axis in the centre of the model, 16000m in red, 10000m in blue and 4000m in green. Applied tectonic shortening is shown at 16000m location by tracking within the elasto-plastic sand layer, in grey.

plastic layer to flow towards the fold axis. A large density contrast in the highest porosity models (35%) results in the greatest rate of movement in x towards the fold axis (figure 5.5 and 5.6). The results presented in figures 5.3, 5.4, 5.5 and 5.6 show that while the final geometry of the fold can be seen to be dependent on both viscosity and porosity (density) of the visco-plastic layer, the behaviour is complex. The geometry of the fold and of the growth strata vary through time for different viscosity and density combinations. Ultimately, primarily the viscosity of the Maykop and then the magnitude of the density contrast between the overburden and the Maykop shale control the response. As more

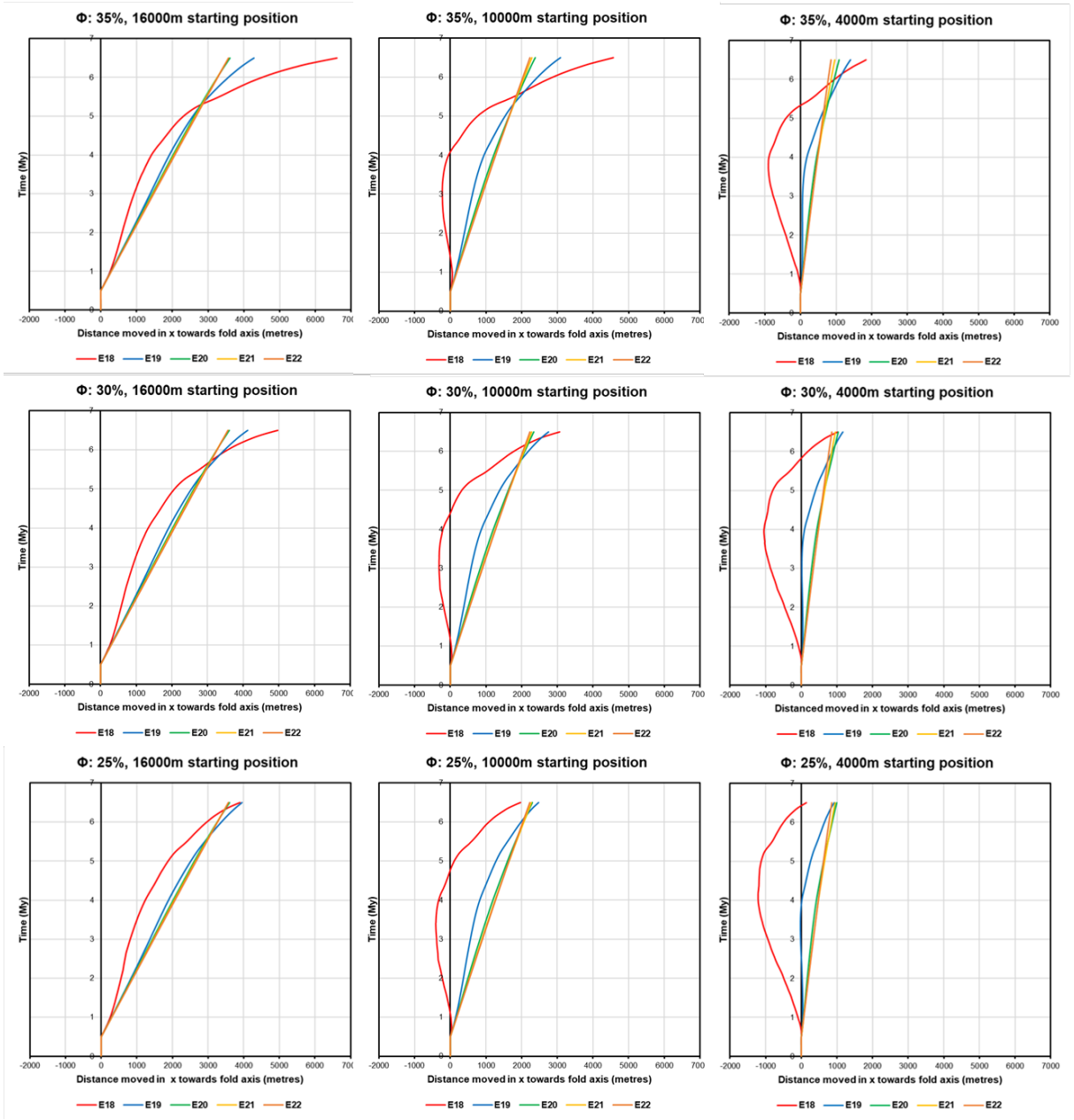


Figure 5.6: Particle distance moved in x through time within the visco-plastic layer for viscosities between 10^{18}-10^{22} at the 16000m, 10000m and 4000m starting position for visco-plastic layer porosities of 35%, 30% and 25%.

sediment is deposited, the particles in the visco-plastic layer move towards the fold axis at a faster rate from 4 Ma than the rate of applied tectonic shortening, for viscosities of 10^{18} and 10^{19} Pa.s viscosity, (Figure 5.5 and 5.6). There is thickening of sediment on the fold flanks and thinning of the sediment over the growing fold crest. This creates a thicker sediment package on the limb compared to the crest, creating a larger vertical load off the fold flanks within the visco-plastic layer, causing the particles to move towards the fold crest. This creates a feedback where the more shale that moves towards the crest, the greater the accommodation space on the edge of the model which creates an even greater pressure differential within the visco-plastic layer.

The density of the visco-plastic layer at 35%, 30% and 25% porosity is 2085 kg/m^{-3}, 2169 kg/m^{-3} and 2252 kg/m^{-3} respectively. The average overburden density reaches 2243 kg/m^{-3} at 4 My within all three models and 2391kg/m3 by the end of the model runs.

Sediment accumulation index

To compare the relative fold growth of the models and to enable the ability to compare model results with real-world data the ratio of the thickness of overburden on the edge of the fold to the thickness on of overburden on the fold crest is analysed. This ratio is defined as the sediment accumulation index (SAI) (figure 5.7) (see Chapter 4 for more discussion). It is calculated by dividing the thickness of the syn-kinematic overburden on the edge of the model by the thickness of the syn-

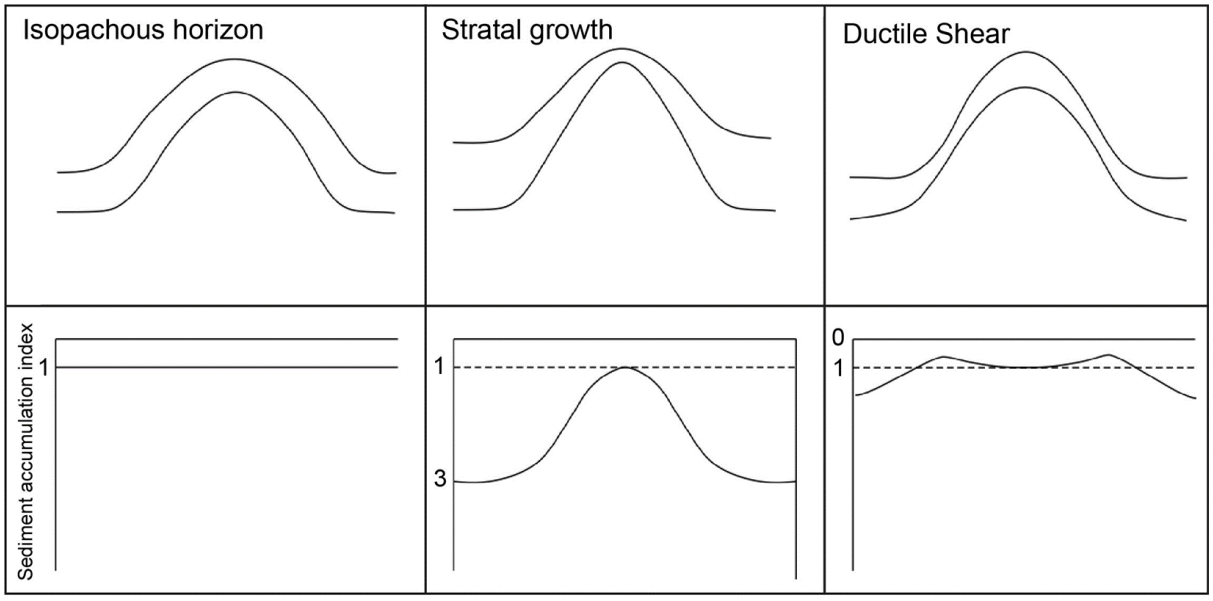


Figure 5.7: Sediment Accumulation Index (SAI) explanation. A larger index number means more thickening on the edge of the fold than over the crest.

kinematic overburden over the fold axis. A value of SAI = 1 shows no sediment growth, a value <1 shows increasing sediment growth and a value of >1 suggests ductile shear or limb thickening (figure 5.7).

The SAI is used to compare the final model geometry for each model. I have shown that increasing sediment loading on the edge of the model compared to the crest accelerates the movement of shale into the fold core and therefore a higher SAI should show a greater influence of fold growth due to sediment loading than just applied tectonic shortening. In figure 5.8 the SAI is plotted for the viscosity range of 10^{22}-10^{18} Pa.s for each of the three modelled porosities. The results show that as the viscosity decreases and porosity increases, the higher the SAI becomes, consistent with the interpretation that when the shale can move more easily into the fold core, more accommodation space on the fold edge is generated. At higher viscosities (10^{20} Pa.s and greater) and the lowest densities, where the Maykop detachment layer behaves as an elasto-plastic material, the SAI is very close to 1.3.

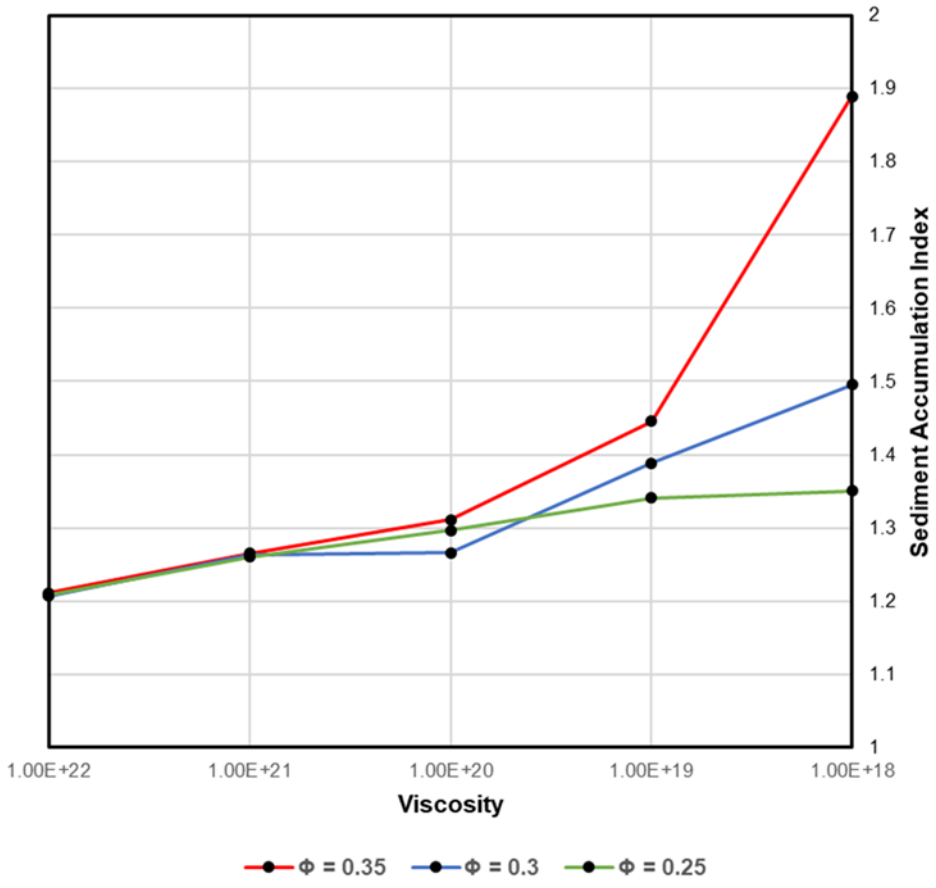


Figure 5.8: Sediment Accumulation Index (SAI) for viscosities of 10^{22}-10^{18} for 35% (red), 30% (blue) and 25% (green) porosity of the visco-plastic layer.

This suggests that for this suite of models, values of SAI above 1.3 indicate that fold growth has been amplified by sediment loading.

5.3.2 Experiment 1b: Shafag Model

In the second experiment, the initial simple model geometry is modified to match geometries and stratigraphy measured from seismic data across the Shafag culmination of the Shafag-Asiman fold. The objective for running this model is to compare the SAI values for the numerical models with those calculated from seismic profiles across the Shafag fold and thus provide a test for how well the numerical modelling results match real world data. A viscosity of 10^{18} Pa.s and porosity of 30% for the Maykop shale is used for this experiment. Although the 35% porosity models give the largest movement into the fold core, a density of 2085 kg/m^{-3} is likely to be unrealistically low for the Maykop shale layer, so 30% porosity is used instead. The difference with this model compared to the simple models run previously are the overburden thicknesses and sedimentation rates (table 5.1). The sedimentation rate for the seabed to 0.8 My is higher than in the simple model, 1625m/My compared to 1333m/My. The Shafag model has a lower sedimentation rate for the 0.8 My to 2.7 My at 790m/My compared to the 1333m/My in the simple model. The Productive Series has a sedimentation rate of 1575m/My in the Shafag model and is 1333m/My in the simple model. The total overburden volume for the Shafag model remains the same as in the simple model.

Figure 5.9 shows the final displacement in x for both the Shafag model and simple model at 6.5 My. The Shafag model visco-plastic layer has a maximum displacement of 6439m, whereas the simple model has a maximum displacement of 5278m, 1161m less than the Shafag model. The only difference between the two models is the sedimentation rate and this explains why the Shafag model shows more mud movement. The final layer, Post-Productive Series layer A, is deposited at 5.7 My in the Shafag model and at 5.375 My in the simple model. Therefore, by the time the layer is deposited in the Shafag model, the fold has developed for 0.325 My longer. This creates more seabed topography during deposition and therefore the final layer onlaps onto the fold crest more, which allows more sediment to be deposited in the depocenter on the edge of the model. More mud, therefore, moves into the fold core in the Shafag model than in the simple model. The SAI from the Shafag model geometry is 1.92 and for the simple model is 1.5.

The SAI calculated from Shafag seismic reflection data is 1.87, which is very close to the 1.92 value calculated for the Shafag numerical model. This close approximation between the real data and the numerical model suggests that model parameters of 10^{18} Pa.s viscosity and 30% porosity for the visco-plastic shale layer are reasonable values to use for this area of the South Caspian Basin, despite the fact that the numerical models use a simplified lithological description of the sedimentary succession in the area. Therefore, these values are used to test other parameter sensitivities in Experiments 2-4. These parameters are visco-plastic layer thickness, amount of total shortening and overburden thickness.

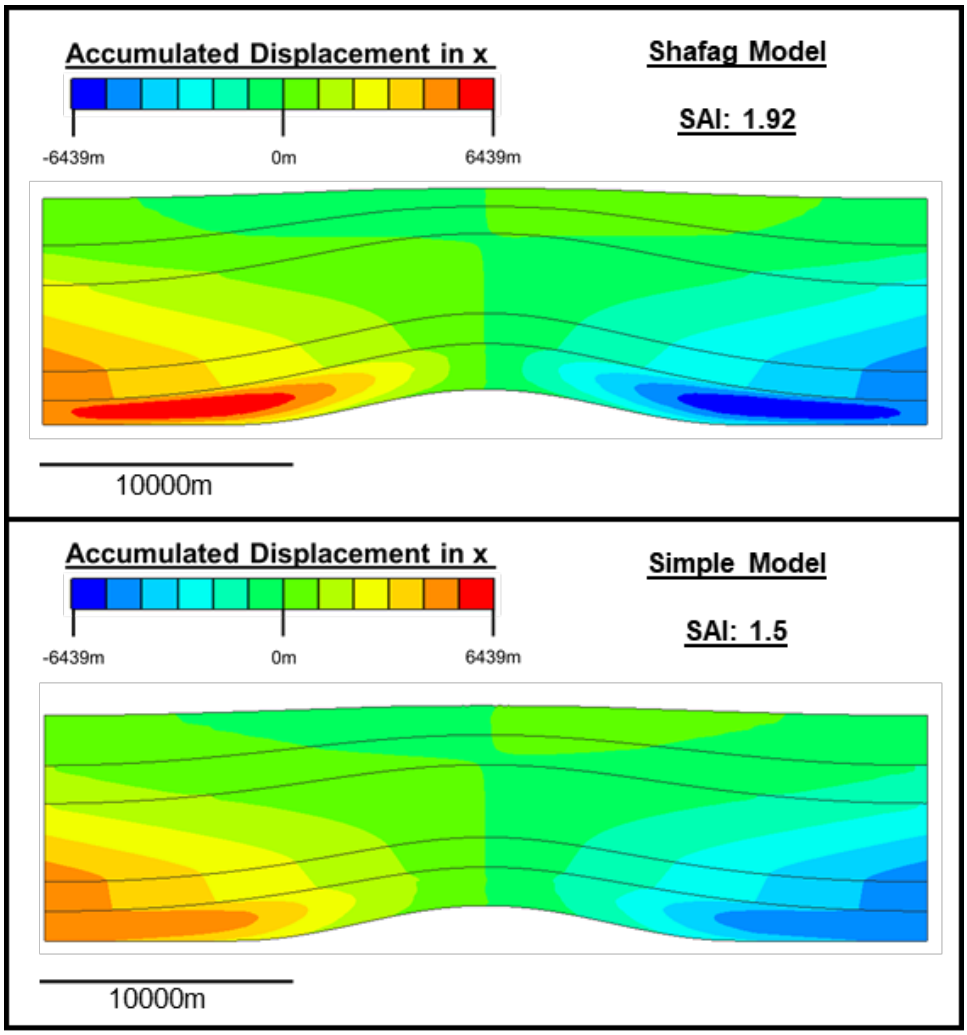


Figure 5.9: Displacement in x for the visco-plastic layer for models with the Shafag model geometry (variable sedimentation rate) and the simple model geometry (constant sedimentation rate).

5.3.3 Experiments of Sensitivity analysis

Three experiments were completed, Experiments 2, 3 and 4, based on the simple model parameters and properties of experiment 1a. Sensitivity parameters were altered for each experiment as described in table 5.1.

5.3.2.1 Experiment 2: Visco-plastic layer thickness

To test the effect of visco-plastic layer thickness on the final fold shape the simple model was run (Experiment 1a) with 1800m and 600m Maykop layer thickness (figure 5.10). The objective of this experiment was to test the effect of Maykop thickness on the models since there is uncertainty in total thickness of the layer within the South Caspian Basin. The experiment tests for real uncertainties in the Maykop thickness taken from seismic reflection data as well as generalising a result for thin and thick mobile shale layers. For the thicker Maykop, the limb to crest thickness of the top Maykop is less than in the original simple model. The top of the Maykop has a lower amplitude in the thicker layer model. This is due to the basal uplift deformation; the top of the Maykop gets affected less when the layer is thicker. So, despite there being a greater volume of visco-plastic shale, the lower amplitude at the top Maykop surface results in a lower overburden pressure differential between the fold crest and flank. Consequently, there is less flow of shale to the fold crest and less accommodation space generation on the flanks of the structure. This is reflected in the SAI of 1.31, less than the original model of 1.5.

In contrast, when the Maykop thickness is reduced by half there is more lateral mud movement into the fold core than the original model. Despite this, the SAI for the thinner layer thickness is 1.38, lower than the 1.5 of the original model. Although the shale travels a similar distance towards the fold crest, there is a lower volume of visco-plastic material in the thinner layer. As a result, there is less accommodation space for the overburden sediments off the fold flanks, with more deposition over the fold crest and therefore causing a lower SAI. Thus, variations in visco-plastic layer thickness can be seen to affect the fold shape and growth history; there is a subtle interplay between accommodation space for the overburden and amount of mud available to be driven towards the fold core.

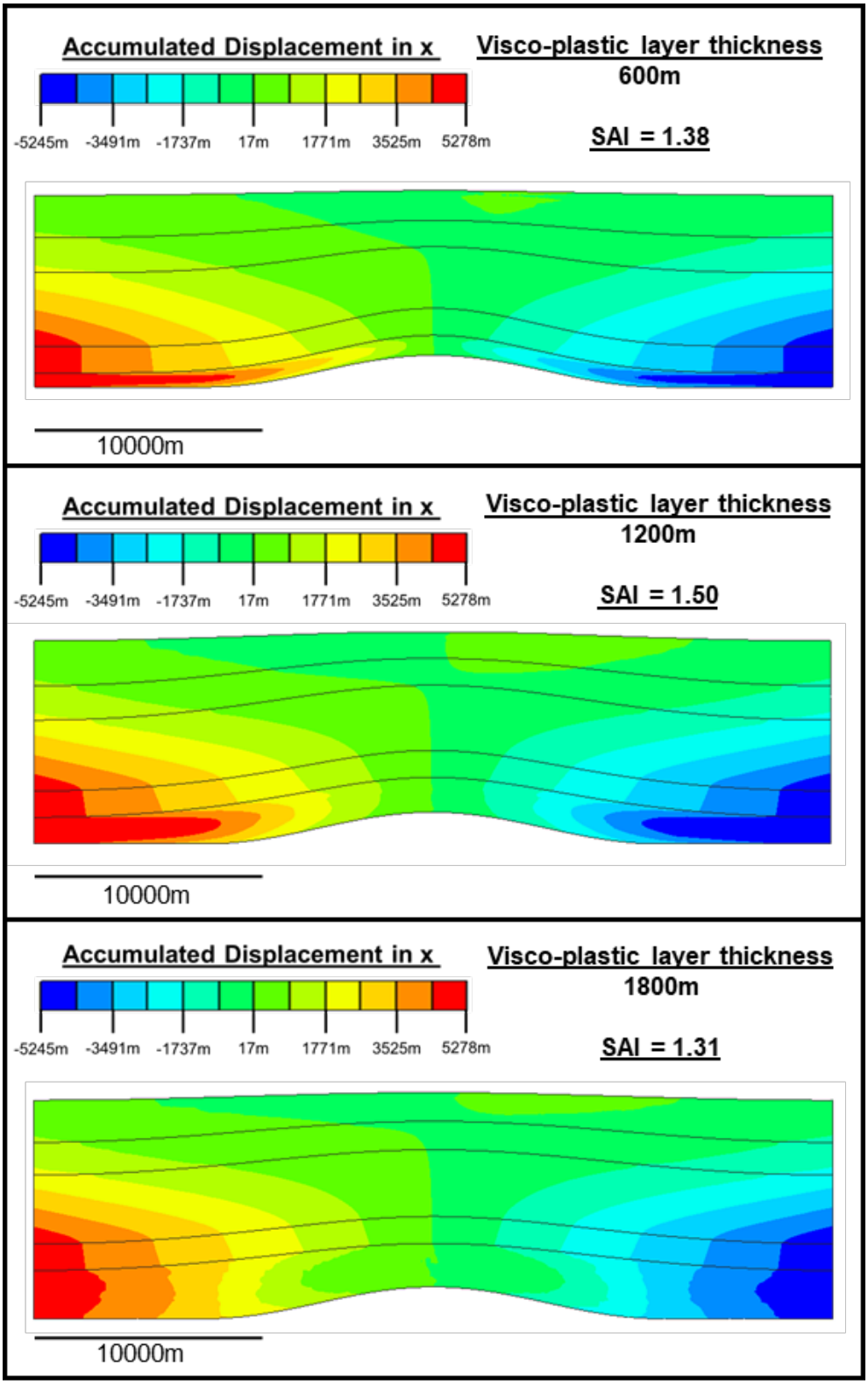


Figure 5.10: Displacement in x for the visco-plastic layer for models set with original initial visco-plastic layer thickness: 1200m, increased thickness: 1800m and decreased thickness: 600m.

5.3.2.2 Experiment 3: Variation in amount of Tectonic Shortening

To test the importance of the magnitude of tectonic shortening, an experiment was set up with increased and decreased amounts of applied shortening; all other parameters were unchanged from Experiment 1a. The models were run with increased and decreased amounts of applied shortening on the edge of model and height of the basal fold perturbation. In figure 5.11, h is the perturbation height and w is the total shortening applied to the edge of the model. In the case of increased shortening the maximum lateral displacement in x within the visco-plastic layer is 10000m, almost double that observed in the original base case model. The tectonic amplification of the fold allows for greater overburden thicknesses to be deposited off the fold flanks which in turn drives more shale into the fold core. The rate at which the fold grows is so great that there is not enough sediment to fully infill the base level topography which is reaches a maximum of 1100m off the fold flanks. The calculated SAI is very large reaching 4.85.

The decreased tectonic shortening model shows very little displacement in the visco-plastic layer (figure 5.11). However, there is 300m inward lateral movement within the visco-plastic layer relative to the pre-kinematic elasto-plastic layer above off the fold flanks. Interestingly, in the centre of the model there is movement away from the fold axis with visco-plastic shale moving down the fold flanks by up to 230m. This implies that the gradient in the Maykop by the upward movement in the basal fold is large enough to initiate outward flow, but that the lateral tectonic shortening is not enough to create the off-flank topography required for differential loading to trigger significant shale flow into the fold core. The resultant SAI value of 1.07 reflects this result.

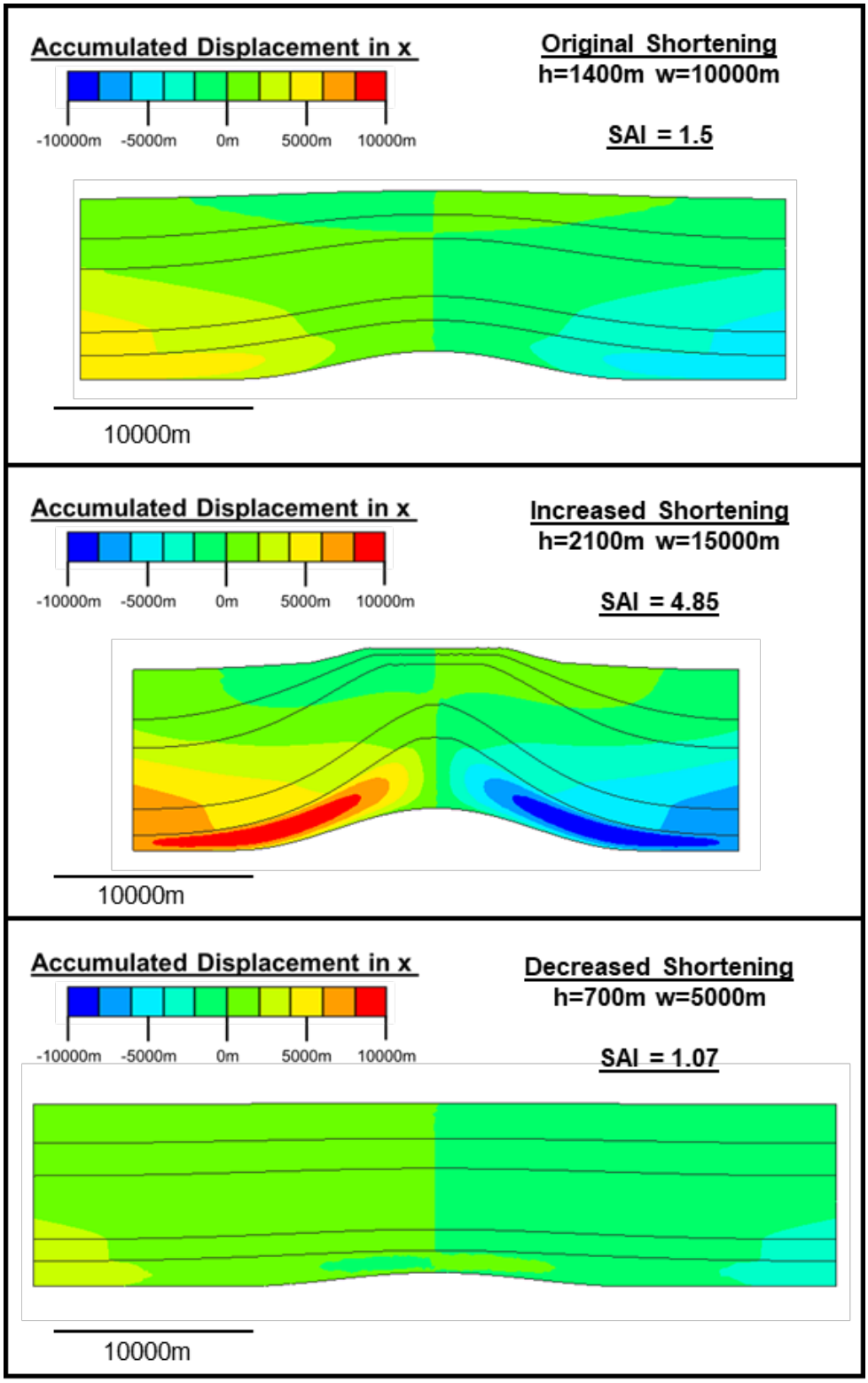


Figure 5.11: Displacement in x for the visco-plastic layer for models set with original applied tectonic shortening h=1400m w=5000m, increased applied tectonic shortening h=2100 w=7500, and decreased applied tectonic shortening h=700m w=2500m. h=perturbation height and w= shortening applied to both edges of the model.

5.3.2.3 Experiment 4: Sedimentation rate

To test the sensitivity of the models to sedimentation rate, models were run with increased and decreased Post-Productive Series thickness, the uppermost two layers, 4000m and 2000m respectively (figure 5.12). As per the previous sensitivity models, all other parameters in this experiment are the same as per Experiment 1a. Both model runs generate more inward movement of the visco-plastic shale than within the overlying overburden layer but the resultant fold geometry and in particular, growth strata layers are very different. The maximum displacement in x occurs in the thinner overburden model, with a maximum displacement of 5577m, this is 300m more than in the original and the increased overburden model. The seabed topography causes the sediment to fill the depocenters on the edge of the model first and then cover the fold crest. Therefore, with the lower sedimentation rate in this model, the sediment fills the edges but onlaps onto the fold limb, as there is not enough sediment deposited to cover the crest. A larger pressure differential is created within the visco-plastic layer between the fold flanks and the crest, as the overburden is thicker on the edge. This causes the greater displacement in x than we see in figure 5.12. This is reflected in the SAI, with a value of 1.95.

The increased thickness model has more sediment being deposited over the crest of the fold than in the original and decreased overburden thickness models. Therefore, there is a lower pressure differential between the limb and the crest than in both the original and decreased overburden thickness models. This causes the displacement in x within the visco-plastic layer to be lower than in the original model. This results in a relatively lower SAI of 1.33.

The result of this experiment is complex, where the response depends not just on the absolute sedimentation rate, but how sediment is distributed across the model. A high sedimentation rate will blanket the fold crest, with a resultant lower overburden pressure differential between the crest and the limbs and a hence a weaker feedback response. Conversely, a low sedimentation rate will fill the depocentres off the flanks of the fold and not blanket the crest and thus create a stronger feedback response. These results demonstrate the dynamic interaction between rate of structural growth and sedimentation rate.

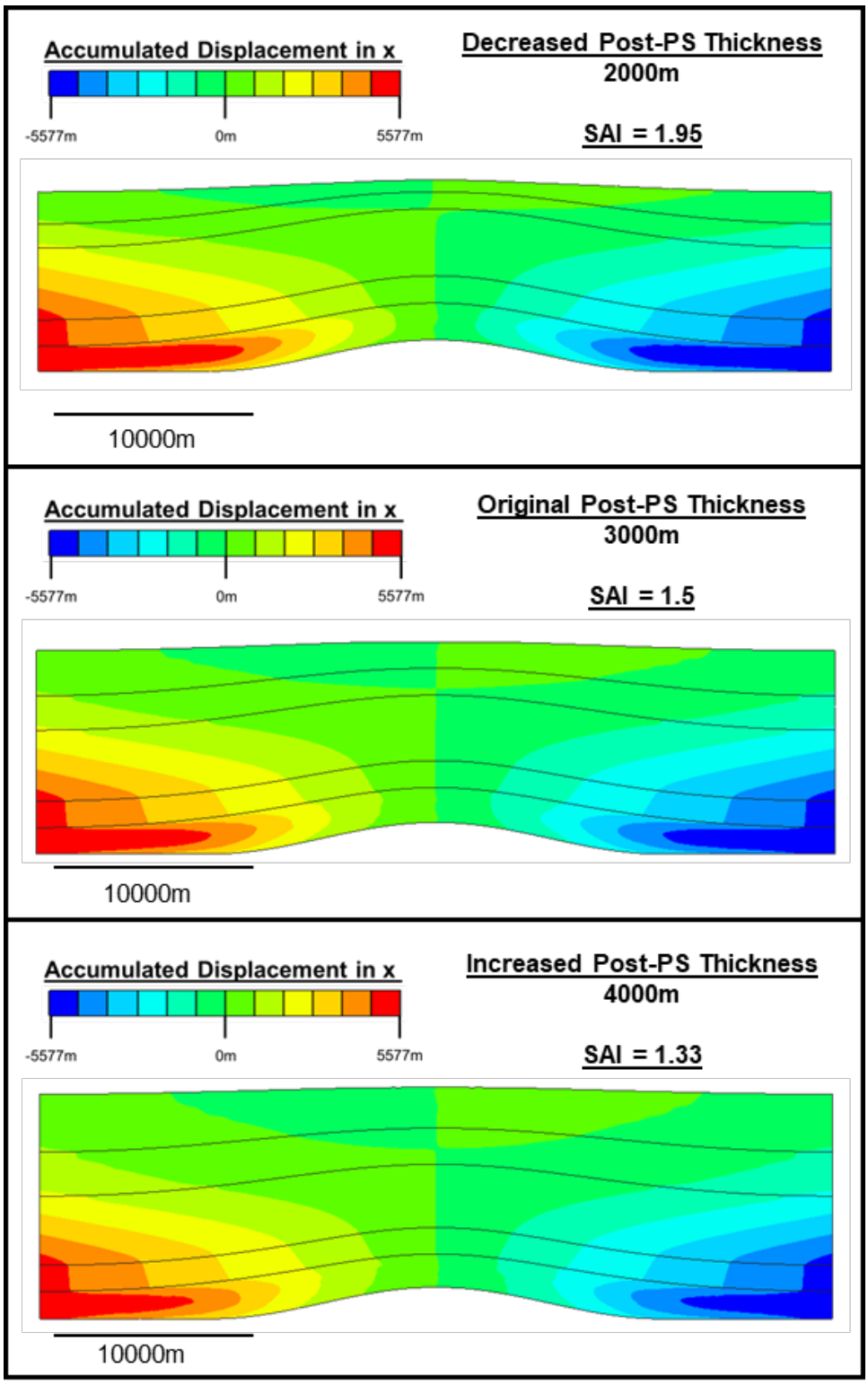


Figure 5.12: Displacement in x for the visco-plastic layer for models set with original overburden thickness 3000m, increased overburden thickness 4000m, and decreased overburden thickness 2000m.

5.4 Discussion

Under the conditions of the experiment setup, the results show that during tectonic shortening, visco-plastic shale movement into the fold core can amplify fold growth. The shale movement depends on both the shale layer material properties and the magnitude and distribution of overburden load. The initiation of mud movement into the fold core is dependent upon the viscosity of the mud, with fold amplification occurring at viscosities of 10^{18} Pa.s and 10^{19} Pa.s (Experiment 1a). The shale no longer behaves as a visco-plastic material at viscosities above 10^{19} Pa.s and is too fluid below 10^{18} Pa.s to allow for fold amplification to occur. Shale density (as described by varying the shale porosity), controls the magnitude of shale movement, with a lower density generating a larger difference in density between the visco-plastic shale and the overburden and hence more movement of shale from the flanks of the fold towards the core. It is interesting to note that in Experiment 1a the transition for the shale flow into the fold core occurring at a greater rate than the lateral movement due to the applied tectonic shortening occurs at ~ 4 My, from the start of the model for 35% and 30% shale porosities and at ~5 My for a porosity of 25%. At 4 My, the average overburden density is 2243 kg/m^3, compared to a density of the visco-plastic layer of 2085 kg/m^{-3}, 2169 kg/m^{-3} and 2252 kg/m^{-3} at porosities of 35%, 30% and 25% respectively. This suggests that the time at which the overburden is of an adequate thickness and the density becomes greater than the shale density, is when the non-linear feedback response starts.

Experiments 2, 3 and 4 were modelled to test the sensitivity of results from Experiment 1 to geological parameters that might be expected to exert a control. The results show that amplifying fold growth through sediment loading upon a visco-plastic shale is dependent upon the interplay between sedimentation rate and tectonic shortening. The interaction between both sensitivities determines the distribution of the overburden load across the fold. The results show that the overarching parameter to control the shale movement is the differential loading of the overburden, which depends on not only on absolute thickness, but how it is distributed across the fold. Experiments 2, 3 and 4 show that any parameter that allows for thinner overburden on the crest with respect to thicker overburden on the fold flanks will drive shale into the core of the fold, leading to amplification of the fold height. Although a thinner Maykop layer creates a greater amount of differential loading to occur (Experiment 2) the

volume of mud is lower and therefore with a longer model run time may weld out and limit the extent of mud movement and amplification of the fold core. All parameters tested show that they can have some control on mud movement into the fold core, however, tectonic shortening is required to initiate the feedback, which is most clearly demonstrated by Experiment 3. Applied shortening provides a fold perturbation to allow for differential loading of the crest and flanks to occur. A high amount of tectonic shortening allows for sediment to onlap onto the fold, regardless of sedimentation rate, shown in Experiment 3. Differential loading with a high sedimentation rate requires a high rate of tectonic shortening to allow for onlap, and therefore, differential loading to occur.

Are the results pertinent to the South Caspian Basin?

Although differential loading can occur in conditions with low sedimentation rate (Experiment 4), the effect of the loading also requires a low-density mud (Experiment 1a). A low-density mud is created by high pore pressures and overpressure, which in the Caspian is most likely created by hydrocarbon generation of gas within the shale layer (Feyzullayev and Lerche, 2009, Soto et al., 2021b). Although fluid generation through smectite-illite transition my increase pore-pressures (e.g. Bruce 1984, Fergusson 1985), gas generation creates the significant overpressure (e.g. Barker 1990, Osborne and Swarbrick 1997) within the Maykop Shale (Feyzullayev and Lerche, 2009). The South Caspian Basin is a cold basin with very high sedimentation rates, >1000m/My, and so the geothermal gradient is very low, 15-18^{o}C/km (Feyzullayev and Lerche, 2009). The Maykop Shale therefore enters the gas generation window very deep, with well data suggesting this occurs at the same time as pore pressure increase at approximately 5 km depth (Khalilov and Imanov, 1979, Khalilov and Imanov, 1980, Buryakovsky et al., 1982). Therefore, for other basins around the world to act in a similar manner to the South Caspian Basin they must enter the gas generation window. In the South Caspian this occurs due to deep fast burial as well as the shale layer occurring at depths of over 8 km. The results of our models are most likely applicable in areas of the world that have with these two features. However, Soto et al. (2021b) summarise shale densities of regions around the world and use well data from various basins, indicating that the South Caspian Basin has the lowest density shales of all the mobile shale basins for where there is data (Gulf of Mexico, Offshore Indonesia, Alboran Sea, Trinidad and South China Sea). Therefore, the shale properties may be different for these basins and create different fold

histories from those that have been modelled here, based on the Shafag-Asiman fold. Future modelling of folds within global regions of shale tectonics is important for understanding whether our model results can be applicable to other areas of the world.

Further analysis of other folds within the South Caspian Basin would reinforce the understanding of shale tectonics based on the results presented. The Maykop shale properties, such as thickness, likely change across the basin. Observing the geometry of folds where the Maykop properties vary compared to Shafag-Asiman will help to validate our model results, specifically the sensitivities such as Maykop thickness. Further modelling of the Shafag-Asiman fold will help improve the accuracy of the model results, specifically by using a coupled model where shale porosity and pore pressures are calculated through time. It is expected that the shale will initially act as a poro-elastoplastic solid until it becomes buried sufficiently enough to enter the gas generation window. Gas generation will create overpressure and reduce the mud density. An initially non-viscous shale would prevent the mud from initially flowing away from the fold axis during the first few million years. As hydrocarbons are produced, and more specifically gas, the mud density will decrease (Feyzullayev and Lerche, 2009, Soto et al., 2021b) and the mud will begin to flow into the fold core. The initial inhibition of the outward mud flow may allow the mud to flow further towards the fold axis than is shown in the models presented, depending on the timing of hydrocarbon generation. Buried, extinct mud volcanoes within the Shafag-Asiman fold structure indicate that liquid mud was present during deposition of the Productive Series (chapter 4), therefore shale movement was likely from at least this time.

The numerical models are set up so that the sediment deposition occurs as a uniform layer across the model, however in reality, the sediment deposition is asymmetrical. In the Shafag-Asiman area, the sediment is sourced from the east. This would cause asymmetry of the sediment loading, with more mud being forced into the fold core from the east. This could affect the fold shape through time due to changes of the timing of mud movement into the fold core.

5.5 Conclusions

The effect and magnitude of differential loading upon a visco-plastic shale layer is dependent upon 1) viscosity of the shale layer, 2) the density of the shale layer and 3) parameter sensitivities of the fold. The viscosity of the shale determines whether differential loading will cause fold amplification to take place with fold amplification occurring at viscosities of 10^{18} Pa.S and 10^{19} Pa.S. The density of the visco-plastic shale controls the magnitude of any resulting fold amplification, with a lower density causing greater fold amplification. The degree to which differential loading impacts visco-plastic shale movement is controlled by the distribution of sediment across the model, which is controlled by, but not limited to, the sensitivities tested in the experiments presented: visco-plastic shale thickness, overburden thickness and amount of applied tectonic shortening. Future studies could seek to replace the viscous assumption for the Maykop with a critical state model applied on the shales, on the premise that the shales should flow if sheared to the critical state. The model could be developed under a coupled modelling framework to incorporate pore pressures arising from rapid sediment loading and subsequent hydrocarbon generation. Density changes due to pore pressure increases used within future models could give an insight into whether the results from the experiments can be directly applied to surrounding folds in the South Caspian Basin as well as to further shale tectonic regions globally.

6. Deep-water lacustrine turbidite system of the South Caspian Basin and interaction with structures

This chapter has been written as the first draft for a paper and therefore there is some repetition with previous chapters.

6.1 Introduction

There is an increasing body of work documenting how deep-water channels interact with structures (Mayall and Stewart, 2000, Clark and Cartwright, 2009, Mayall et al., 2010, Clark and Cartwright, 2011, Jones et al., 2012, Jolly et al., 2016, Don et al., 2020, Pizzi et al., 2021, Mitchell et al., 2021a, Mitchell et al., 2021b, Howlett et al., 2021). By using a high-resolution 3D seismic reflection dataset, I investigate how deep-water lacustrine channels interact with a growing shale-cored anticline structure during the Plio-Pleistocene. The area of focus is the Shafag-Asiman fold structure within the deep-water South Caspian Basin (figure 6.1), in current water depths of approximately 600m-900m. The seismic data show that the predominantly silty muddy deep-water Pleistocene Absheron Formation contains a myriad of small sinuous channels approximately 100-300 m wide, and up to 50 m deep that traverse the entire dataset. Sedimentary features such as laterally migrating scroll bars allow the channel network to be mapped and described in detail.

The fold structure consists of two folds trending approximately NE-SW, Shafag and Asiman. The folds grow at varying rates from the start of the Absheron Formation to the present day (Chapter 4). A 4.5 km mud volcano can be observed on the seafloor, located between the two-fold axes (figure 6.1). At approximately 10 km deep a marine shale, and source rock for the area, the Maykop Formation is found. The shale is mobile, forming the shale diapirs and shale cored anticlines within the area (Devlin et al., 1999, Santos-Betancor and Soto, 2015). Above this is the Productive Series, a Pliocene fluvio-deltaic formation that was deposited as the basin became a land-locked lake. There was a significant base-level shift and the Paleo-Volga River migrated 700 km south and deposited fluvial sediments of the Productive Series from the north of the South Caspian Basin (Reynolds et al., 1998, Green et al., 2009). As the lake level decreased a thick evaporite was deposited in the centre of the basin (Chapter 2) (Green et al., 2009). At 2.7 Ma the basin became connected to the global ocean once more and a

marine shale was deposited, the Akchagyl Formation (Popov et al., 2006, Van Baak et al., 2019). Above this, the deep water lacustrine turbidites of the Absheron Formation were deposited between 2.13 Ma (Van Baak et al., 2019) or 1.8 Ma (Green et al 2009) to 0.85 Ma (Lazarev et al., 2019). It is these deep-water sediments and their interaction with the growing fold structures that I investigate in this chapter.

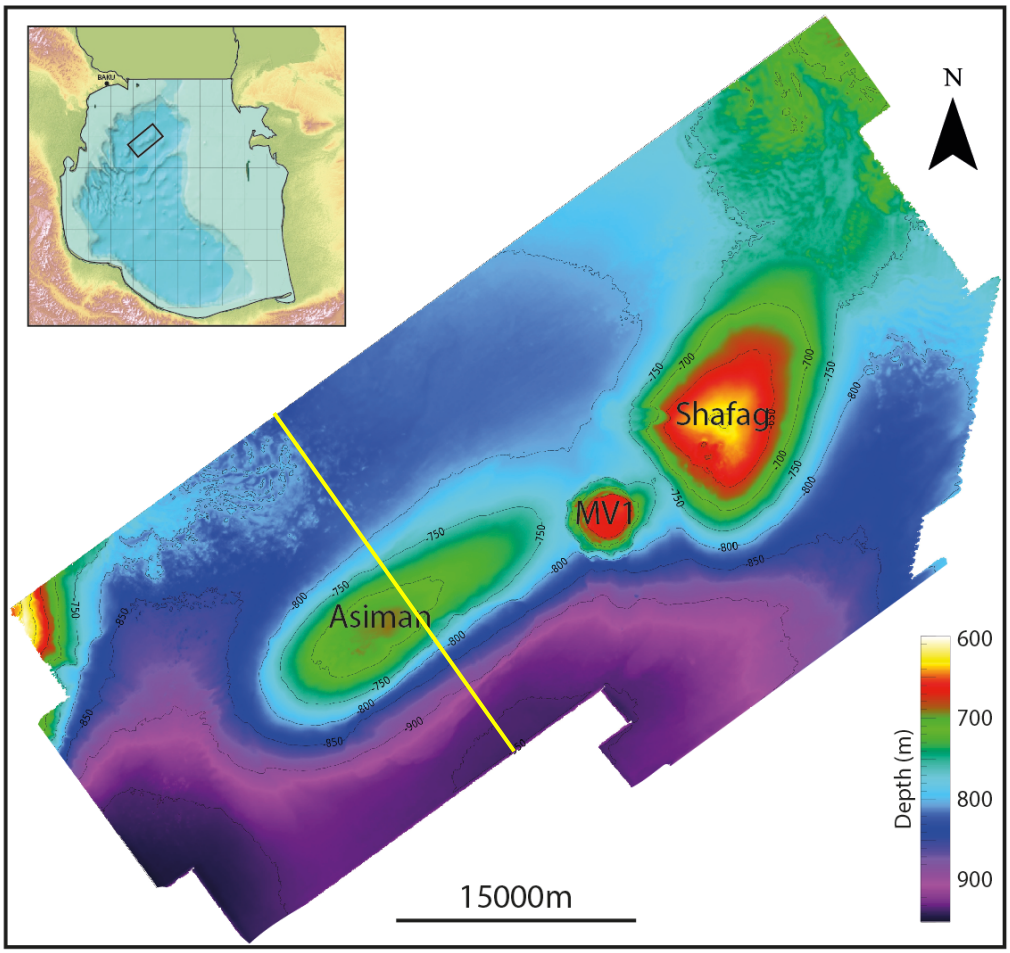


Figure 6.1: Present-day seabed bathymetry showing the Shafag-Asiman fold complex and associated mud volcano (MV1). Inset: location of the study area within the South Caspian Sea.

There are three river sources of sediment into the basin, the Paleo-Volga, Kura and Amu-Darya (figure 6.2). Seismic data in Abdullayev (2000) and Abreu and Nummedal (2007) shows large clinoforms building out from the Turkmenistan Shelf, passing into slope channel levee systems that are 15 km wide (figure 6.3). These are likely the updip component of the Absheron deep-water channel systems, suggesting that the main source area is from the Palaeo-Amu Darya River in the east.

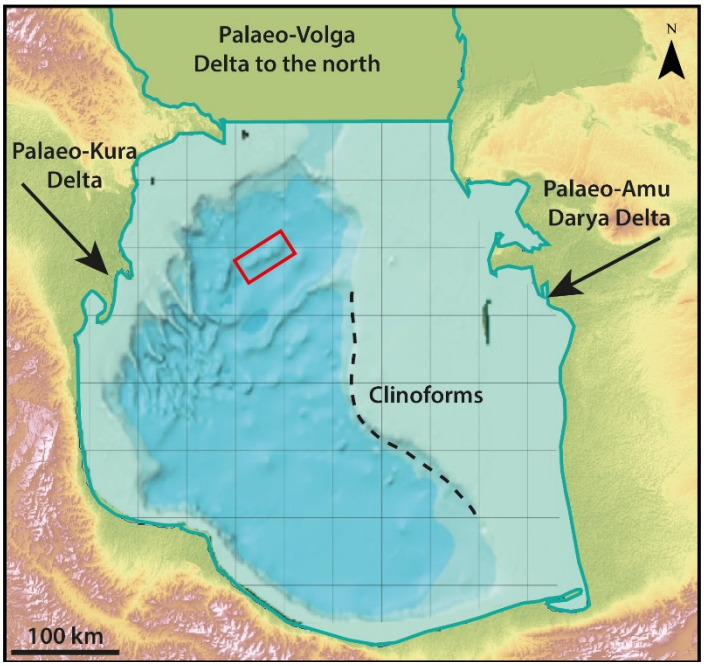


Figure 6.2: Bathymetry and topography map for the South Caspian Basin and surrounding areas showing the three river sources into the South Caspian Basin as well as the clinoforms prograding from the Turkmenistan Shelf as interpreted from 2D seismic data by Abdullayev (2000).

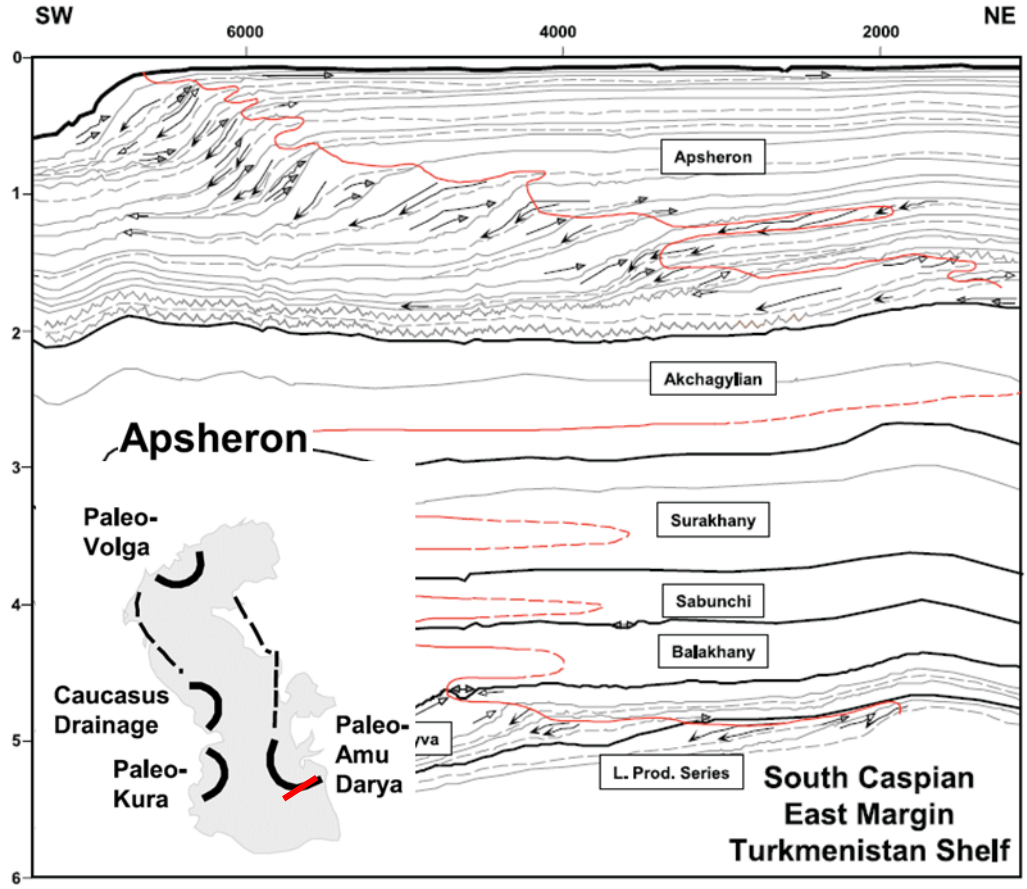


Figure 6.3: Line drawing of an interpreted seismic profile from the Eastern margin of the South Caspian Basin, showing progradation of the Palaeo-Amu Darya in the Absheron to Recent. Location is shown in red on the inset map. Offlap-break curve is shown in red (dashed line indicates the uncertainty in the location of the offlap break). Inset map shows the location of the river deltas during the Absheronian, with the Palaeo-Amu Darya further west than the present-day. Grey arrows show onlap. Black arrows show downlap and white arrows show truncation. From Abreu and Nummedal (2007).

Deep-water Lacustrine Systems and Marine Systems

Deep-water lacustrine systems differ from their marine counterparts mainly since lake systems are more sensitive to lake level and supply (Bohacs et al., 2000). Deposition within lakes is also more sensitive to changes in climate, with deposition in the Caspian during the Plio-Pleistocene exceptionally so (Forte and Cowgill, 2013). The interaction of accommodation space and sediment/water input is what fundamentally controls the deposition within a lake (Bohacs et al., 2000). The South Caspian Basin is tectonically complex with rapid rates of subsidence (Jackson et al., 2002, Allen et al., 2003) allowing the deposition of 1.7 km of the deep-water Absheron Formation in ~1 My. The present-day Caspian Sea is the largest lake in the world, five times larger than the second largest (Bohacs et al 2003). The tectonic complexity, sedimentation rates and size of the Caspian means that there are no modern analogues. There are two large intracratonic sag basins in China, the Songliao Basin and the Ordos Basin (Zhi-qiang et al., 2010, Zavala et al., 2022) that contain Cretaceous and Triassic deep-water lacustrine deposits respectively.

Models of channel architecture have previously been described as an order of systems, complexes, and elements (Sprague et al., 2005, Mayall et al., 2006, Porter et al., 2006, McHargue et al., 2011, Mayall and Kneller, 2021) (figure 6.4). A system is considered to be 1 – 3 km in width and 100 – 250m in depth. A complex can be anywhere from 500m to 1500m in width and 10's of metres thick. An element is often 50 to 100m in width and up to 20m in depth. The elements can have more detail such as smaller channel deposits, however this is unlikely to be interpreted from seismic data. Within this study I use the terms channel complex and channel element. A channel element is used to describe what appears as a singular channel on RMS amplitude maps whereas a complex contains more than one element and can display features such as scroll bars, lateral migration and aggradation.

This chapter aims to further our understanding of deep-water lacustrine systems and the interaction of channels with growing structures. Fold growth analysis (Chapter 4) demonstrates periods of higher and lower growth that varies both on the limbs and between the crests of the two fold structures. This provides a unique opportunity to examine how channel behaviour responds to times at when a fold crest created topography at the seabed with onlapping of sediments as opposed to periods when the structure was more subdued and was overlapped by the deep-water lacustrine sediments.

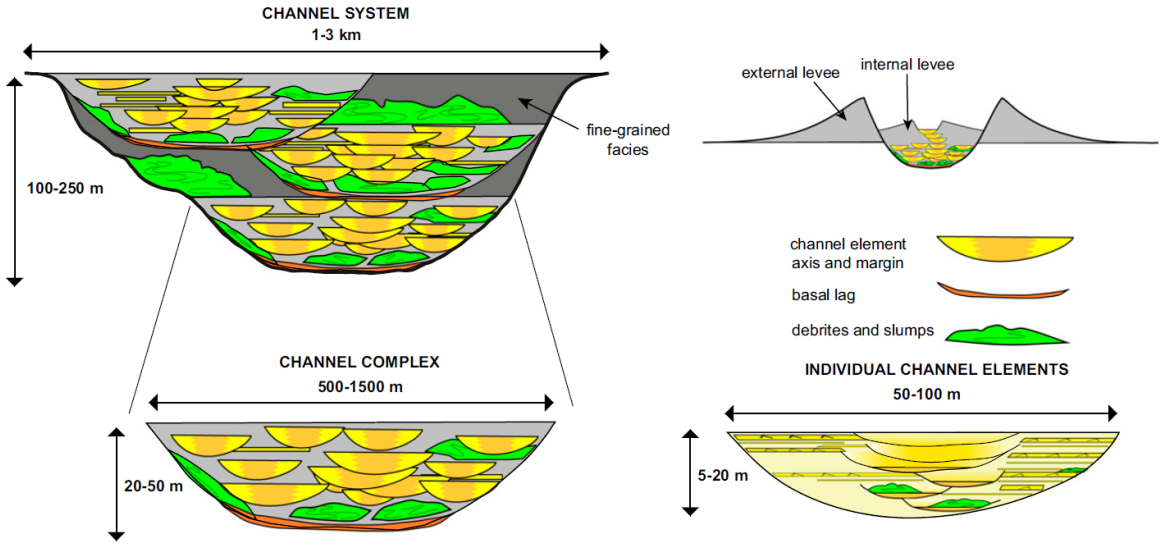


Figure 6.4: Model of channel architecture used when interpreting deep water marine depositional systems, highlighting the detail that occur in most channels. The model emphasizes three orders of channel systems, complexes and individual channel elements. In this study we use this terminology to describe the channel network. From Mayall and Kneller (2021)

6.2 Methodology

As discussed in Chapter 2, six horizons within the Absheron Formation were interpreted and have been described as Unit A – E, with Unit A the oldest unit and Unit E the youngest unit (figure 6.5). Isopach maps between the horizons were used to create a sediment accumulation index (SAI) map for five units as explained and discussed in Chapter 4. The sediment accumulation index maps are used as a proxy to show the relative fold growth through time. In this chapter I use the sediment accumulation index maps to show how the growth intervals relate to the distribution and characteristics of channels within the intervals and how they vary through time.

RMS amplitude maps were calculated in an isoproportional window of 50m around the interpreted horizons and these maps show good detail of channel images (figure 6.6). The channels are 100 - 300m wide and up to 50m deep and commonly appear as a small change in amplitude along a reflector in the seismic reflection data (figure 6.6). However, within the intervals the geometry of the reflectors varies

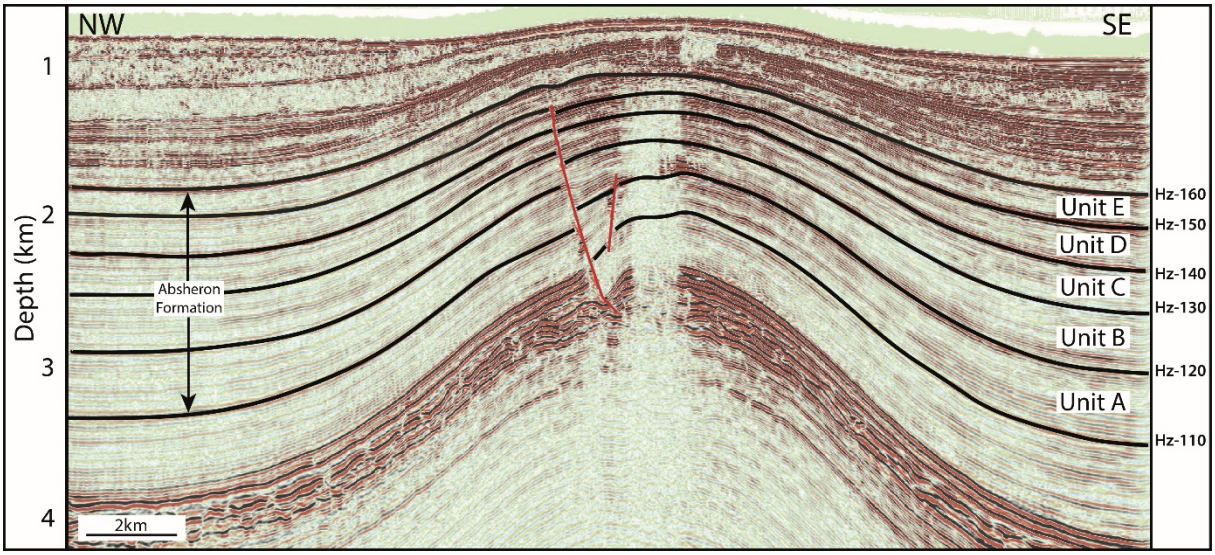


Figure 6.5: Section through Asiman fold axis with the six regional horizons, Hz160 – Hz110 interpreted for this study and units. Line location is labelled on figure 6.1.

and so complete maps with complete channels are often cut off. Using Paleoscan Software (Pauget et al., 2009) (Chapter 2) a geomodel is created to interpret every horizon within the Absheron succession. RMS amplitude maps of the horizons are then created to observe every channel, using a window of 50 m for each horizon as described in Chapter 2 (figure 6.7). A total of 259 channels are interpreted within the Absheron Formation around the Shafag-Asiman fold structure. Table 6.1 provides a summary of the intervals and indicates which intervals showed the highest relative fold growth rate as interpreted from the sediment accumulation index maps (Chapter 4). During Unit A (Hz120 – Hz110), Asiman was slightly more emergent than Shafag. During Unit B, C and D (Hz150 – Hz120), Shafag was more emergent with Asiman more overlapped. The earliest unit, Unit E (Hz160 – Hz150), showed the opposite, with Asiman having a lower sediment accumulation index value and therefore less overlap than Shafag (Chapter 4). The thickness values within table 6.1 were measured as the thickest values of each interval taken on the limb of the folds. The number of maps refers to the number of RMS maps calculated from Paleoscan from which the channels were interpreted.

Table 6.1: A summary of the units, highest relative fold growth of Asiman and Shafag, the thickness of each unit and the number of maps from which the channels were interpreted from within each unit.

Unit	Horizons	Highest Relative Growth		Thickness (m)	No. of maps	No. of channels
		Asiman	Shafag			
E	Hz160-Hz150	x		260	4	35
D	Hz150-Hz140		x	340	5	42
C	Hz140-Hz130		x	230	5	40
B	Hz130-Hz120		x	420	6	71
A	Hz120-Hz110	x		460	8	71

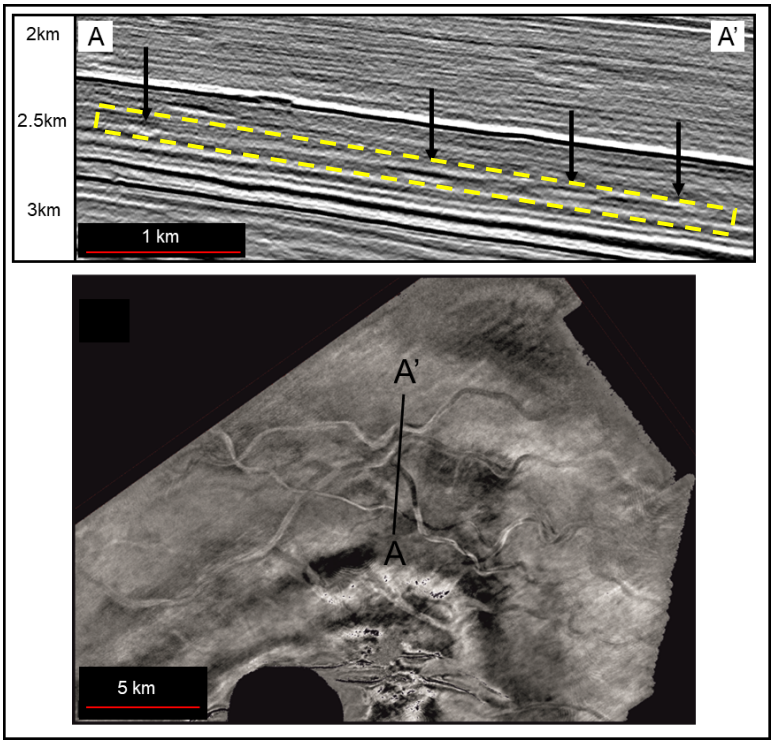


Figure 6.6. An RMS amplitude map calculated with a 50m window (yellow) from within Unit A and corresponding section showing the channels. The map shows the truncation of reflectors around the Shafag fold since the window from which the RMS amplitude was calculated is based on the horizon interpretation. Described in Chapter 2.

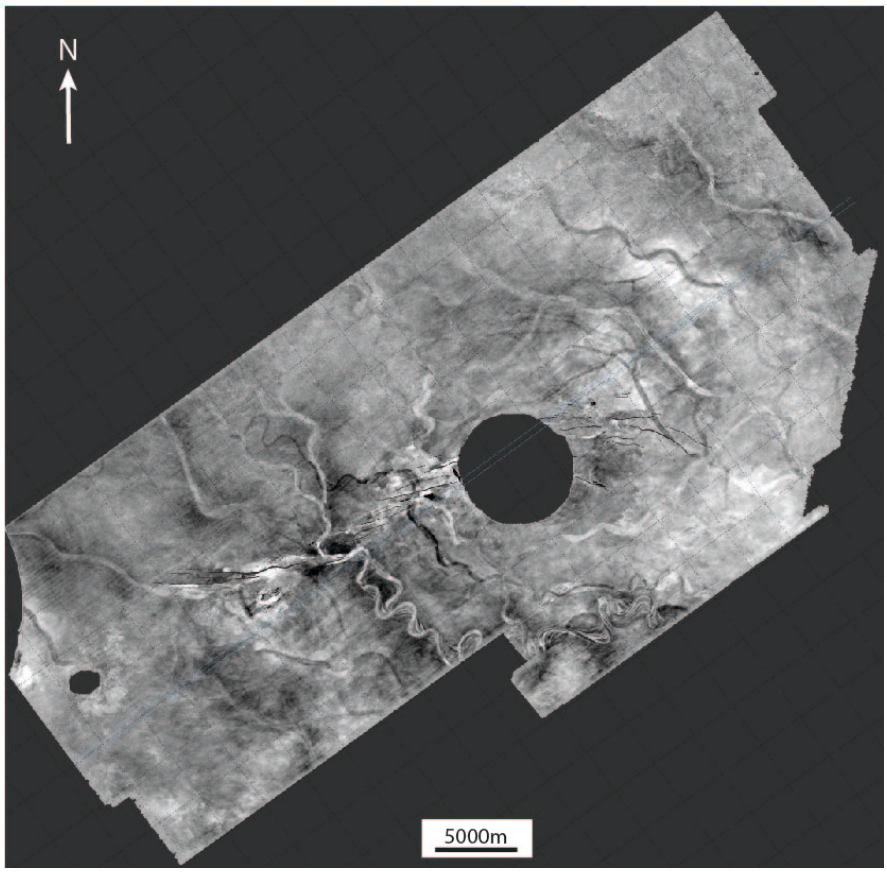


Figure 6.7: Example RMS amplitude map taken from a 50m window above and below a horizon within Unit B interpreted from a Palaeoscan geomodel. 28 RMS maps are used to interpret a total of 259 channels used in this study. The black circles are the mud volcanoes.

The channel direction can be determined from point bar scrolls that are beautifully imaged in the data. As a channel matures, the channel bend will migrate laterally and downstream giving the appearance of point bar scrolls moving downstream. The direction of the scrolls can be used to indicate flow direction. Scroll bars are observed which clearly indicate the flow direction with all scroll bars imaged giving a constant channel flow direction to the NW or W direction (figure 6.8). Rose diagrams are therefore plotted to show flow in a west/northwesterly direction.

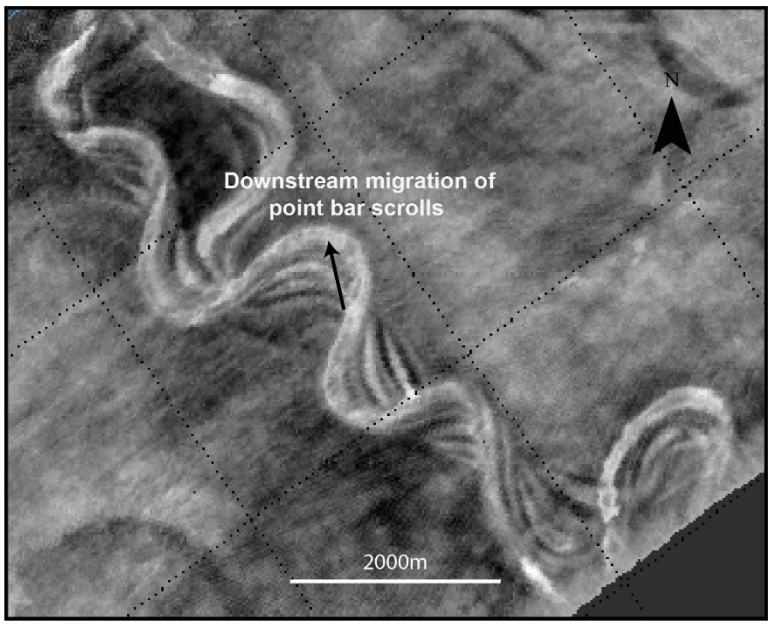


Figure 6.8: Point bar scrolls from Interval B showing a flow direction in a north westerly direction.

The channels were interpreted on each of the mapped intervals and mapped and measured in ArcGIS, as described in Chapter 2. Within ArcGIS, orientation, channel density and sinuosity were calculated within each interval. Sinuosity was calculated by dividing the length of a channel divided by a straight line through the end points of the channel. Channel densities were compared to sediment accumulation indices using violin plots. Channel architecture was also examined, and the results are interpreted and compared to sediment accumulation index maps to investigate the control of structural growth on channel geometries. For example, in Unit B, Shafag has a low sediment accumulation index when compared to Asiman, suggesting that there were fewer overlapping strata on Shafag than Asiman. It may be predicted that there will be a difference in the channel pathways and architecture in response to a change in seabed topography between the two structures.

6.3 Results

Here I present the results of the interpreted channels for each unit as described above. I describe the channel orientations, entry points, channel deflections, channel density, sinuosity and relation to structural growth by using the sediment accumulation index maps described in Chapter 4.

The orientations are measured for each channel within the stratigraphic sequence, units A-E. Orientations were measured as a straight line connecting the start and end point of channel within the data set. This was considered appropriate in order to determine the high-level changes in channel orientation. The data are presented as a composite map per unit which shows all channels mapped within that unit from the different horizons, and hence different depths within the interval. The data are colour coded by depth and the orientations per horizon are summarised in equal area rose diagrams, with a bin size of 10 degrees. The mean vector is calculated and plotted on rose diagrams with 95% confidence interval. The concentration parameter (κ) is also calculated and displayed.

Channel densities were calculated to investigate the relationship between the channels and the growing structures. If the channels are being deflected by an emergent structure it would be expected that there would be low densities of channels over that structure. The channel densities were calculated for each unit by calculating the length per unit area in 2 km x 2 km grids. To analyse the relationship of the channel density to the sediment accumulation index, the mean sediment accumulation index value was calculated using each square of the density grid as the boundary. The index value and density values were then plotted as a violin plot to see any correlation between the two values. The density maps were cropped to include either Shafag or Asiman so the density and index values could be compared between the folds. It would be expected that at low sediment accumulation index values the channel density will also be low. It may also be assumed that at high sediment accumulation values, in the depocentres, there may be increasingly higher channel densities.

6.3.1 Unit A (Hz120 – Hz110)

The data from the lowermost unit, unit A, between Hz120 and Hz110 are presented first. There are a total of 71 channels within this interval and when grouped together the main averaged channel orientation is a flow direction of 286° ± 8° (figure 6.9; table 6.2). However, when examined according to the horizons, a westerly flow direction dominates, with the second lowest horizon (orange in figure 6.9), having a predominantly NW flow direction (table 6.2). Whilst most channels enter the dataset from the east of the study area, within unit A there are some exceptions to this. Within the lowest horizon, purple, there are six channels, all entering the area from the northeast. There are a total of five channels that enter the study area from the southeast from throughout the base to the top of the interval. The fold crests of Asiman and Shafag highlighted in figure 6.9 are interpreted from the sediment accumulation index from the unit (Chapter 4). The orientation data averages out any deflections and changes in orientation along the channel length. However, there are six channels which show a change in orientation and deflect around Asiman whilst none deflect around Shafag, with channels clearly crossing the fold crest (figure 6.9). Some channels flow parallel to the Asiman fold axis and deflect along the southern limb, whilst NW flowing channels are commonly found in the Shafag area. These observations are best shown by the yellow, grey and blue horizons. Average channel sinuosities are relatively low at 1.14, however they increase slightly in the uppermost part of the unit, 1.18 for the green channels (table 6.2).

Table 6.2: Channel statistics and observations for each horizon interpreted within Unit A and the total for the unit.

Horizons	No. of channels	Mean vector direction (degrees)	95% confidence (degrees)	kappa	Average sinuosity	Deflections around fold crest
All channels	71	286	8	3.3	1.14	6 Asiman, 0 Shafag
	8	297	21	4.1	1.16	1 Asiman
	4	271	16	12.8	1.18	0
	12	281	17	4.2	1.13	1 Asiman
	11	276	12	8.6	1.12	1 Asiman
	8	278	13	8.6	1.11	1 Asiman
	8	280	22	3.7	1.17	1 Asiman
	14	316	18	3.3	1.12	1 Asiman
	6	255	45	1.64	1.16	0 Asiman

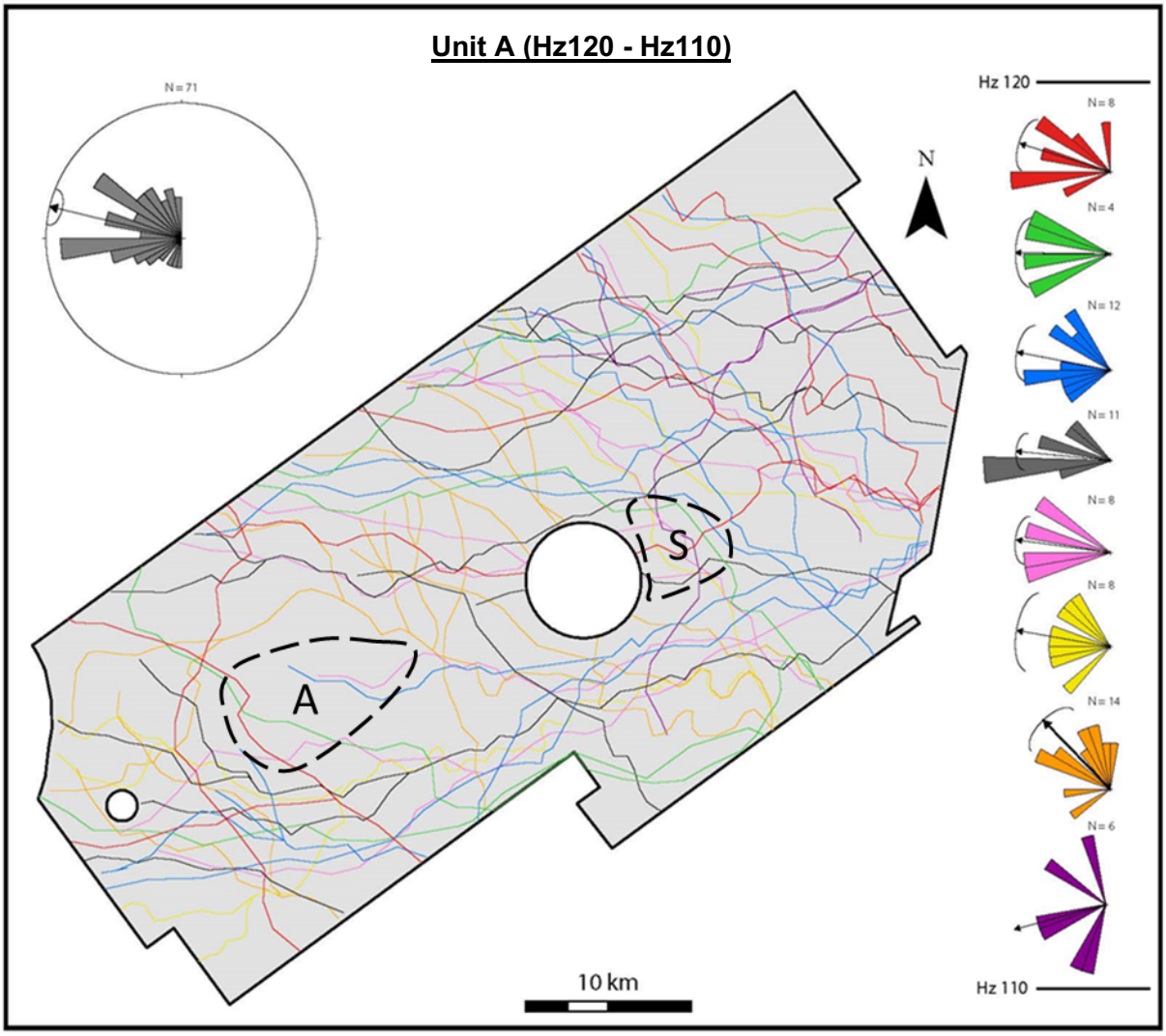


Figure 6.9: Map of channels interpreted within Unit A, colour coded for each horizon. N = 71. Channel orientations are plotted on equal area rose diagrams in 10° bin. The mean vector is shown as an arrow with 95% confidence interval. The outer circle is 30% of the data. Statistics are shown in table 6.2. The white circles on the map are areas of poor data quality due to mud volcanism. The locations of the Asiman (A) and Shafag (S) fold crests have been superimposed from the Unit A sediment accumulation index map.

Within Unit A, channel densities show that there is a clear relationship between channel location and structural growth (figure 6.10). The lowest channel densities occur over Asiman (figure 6.10c, d), where the sediment accumulation index is 1 (figure 6.10a, b). In contrast, the unit averaged sediment accumulation index is 1.1 over Shafag (figure 6.10a, b), indicating greater sediment overlap of the structure, and does not coincide with any channel density lows (figure 6.10c, e). The highest channel densities are along the eastern flank of the Shafag fold and on the southern limbs of both folds (figure 6.10c). The highest densities around the folds occur where there is a high sediment accumulation index, with the highest density values of 3.5 km/km^2 found where the sediment accumulation index is

1.4 or greater (figure 6.10 d, e). Low densities are also seen where the sediment accumulation index is high, suggesting that the channels may have been focussed in other areas with high sediment accumulation index values.

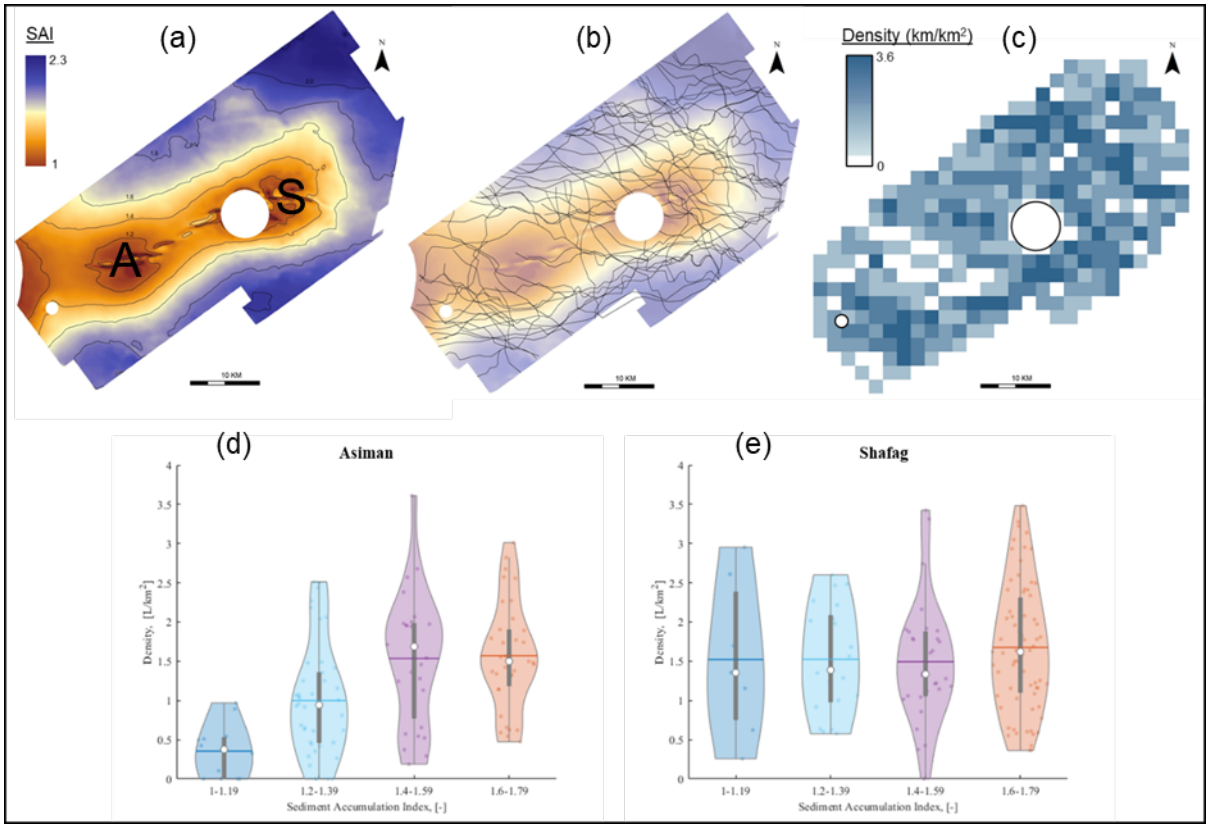


Figure 6.10: Maps produced for Unit A showing: a) sediment accumulation index (SAI). b) Sediment accumulation index overlain by the channel interpretations. c) Channel density calculated within 2 km x 2 km areas. Dark blue areas show a high concentration of channels, white areas show a low concentration of channels. Violin plots for d) Asiman and e) Shafag calculated by comparing the mean SAI with the channel density for the 2km x 2km shown in c). White circles on the maps are areas of poor data quality due to mud volcanism.

6.3.2 Unit B (Hz130 – Hz120)

Whilst Unit B contains the same number of channels as the previous unit, Unit A, the channel network shows clear differences (figure 6.11; table 6.3). When grouped together for the entire unit, the channels predominantly flow to the NW (mean orientation 301° ± 6°) (figure 6.11; table 6.3). However, when the individual layers are examined, more detail emerges. On the lowermost four horizons (orange, pink, grey and blue) the channels mostly flow towards the NW (table 6.3), moving upwards within the unit, there is a change in orientation at the green level, where channels predominantly flow westwards. The majority of the channels enter the dataset from east of the area, however, channels also enter from the SW, observed in all horizons except for at green times. In contrast to Unit A below, channels appear to avoid the Shafag fold crest and flow over the Asiman fold crest. There is one exception, in the lowermost horizon, orange, a channel flows around the western limb of Asiman, likely due to the growth of Asiman from unit A. The channels which avoid the Shafag fold crest are located within the top of the unit, with deflections occurring within grey, blue, green and red horizons. The channels in the green horizon can be seen to deflect around the flank of the Shafag fold, to the northeast of the fold crest. The channels do not appear to flow parallel to the Asiman fold structure, as they did in Unit A. The channels also become more sinuous within Unit B when compared to Unit A. The average sinuosity of all the channels within the unit is 1.21, with the grey horizon showing the horizon average channel sinuosity of 1.3.

Table 6.3: Channel statistics and observations for each horizon interpreted within Unit B and the total for the unit.

Horizons	No. of channels	Mean vector direction (degrees)	95% confidence (degrees)	kappa	Average sinuosity	Deflections around fold crest
All channels	71	301	6	4.9	1.21	6 Shafag
	17	303	15	3.9	1.15	2 Shafag
	7	275	10	17	1.24	1 Shafag
	12	291	12	7.4	1.2	1 Shafag
	16	299	8	12.8	1.3	2 Shafag
	9	307	9	17	1.23	0
	10	320	15	6.5	1.15	0

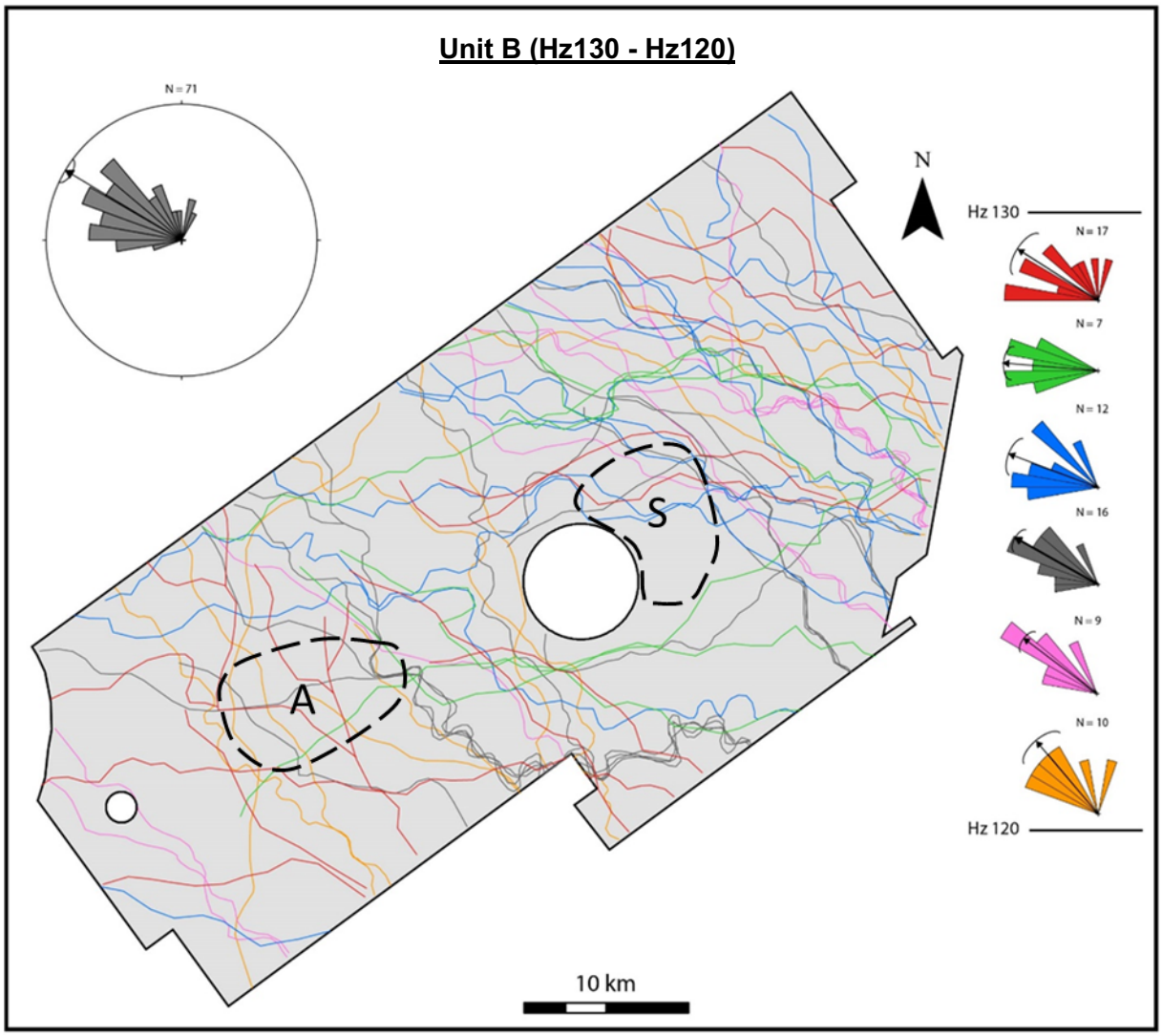


Figure 6.11: Map of channels interpreted within Unit B, colour coded for each horizon. N = 71. Channel orientations are plotted on equal area rose diagrams in 10° bin. The mean vector is shown as an arrow with 95% confidence interval. The outer circle is 30% of the data. Statistics are shown in table 6.3. The white circles on the map are areas of poor data quality due to mud volcanism. The locations of the Asiman (A) and Shafag (S) fold crests have been superimposed from the Unit B sediment accumulation index map.

Channel densities within Unit B once again highlight the relationship between the channel location and structural growth (figure 6.12). Whereas the lowest channel density occurred over Asiman in Unit A, in Unit B the lowest channel densities occur over the crest of Shafag (figure 6.12b, c) where the sediment accumulation index values are 1 (figure 6.12b, c, e). The sediment accumulation index over Asiman is 1.4 (figure 6.12a, b d), showing that there is more sediment overlapping Asiman. Channel densities are higher on the flanks of Shafag than Asiman (figure 6.12d, e). The highest channel densities occur off the eastern flank of Shafag, with channel densities of up to 5 km/km^2. A channel can be seen to follow along small normal faults on the Asiman fold crest (figure 6.12a), which have a

sediment accumulation index of 1.9, higher than the value of 1.4 on the fold crest (figure 6.12b). This is because sediment is trapped in the hanging wall of the normal fault as the fault grows. Channel densities are also high between the crests of the two folds, west of the mud volcano (figure 6.12b, c).

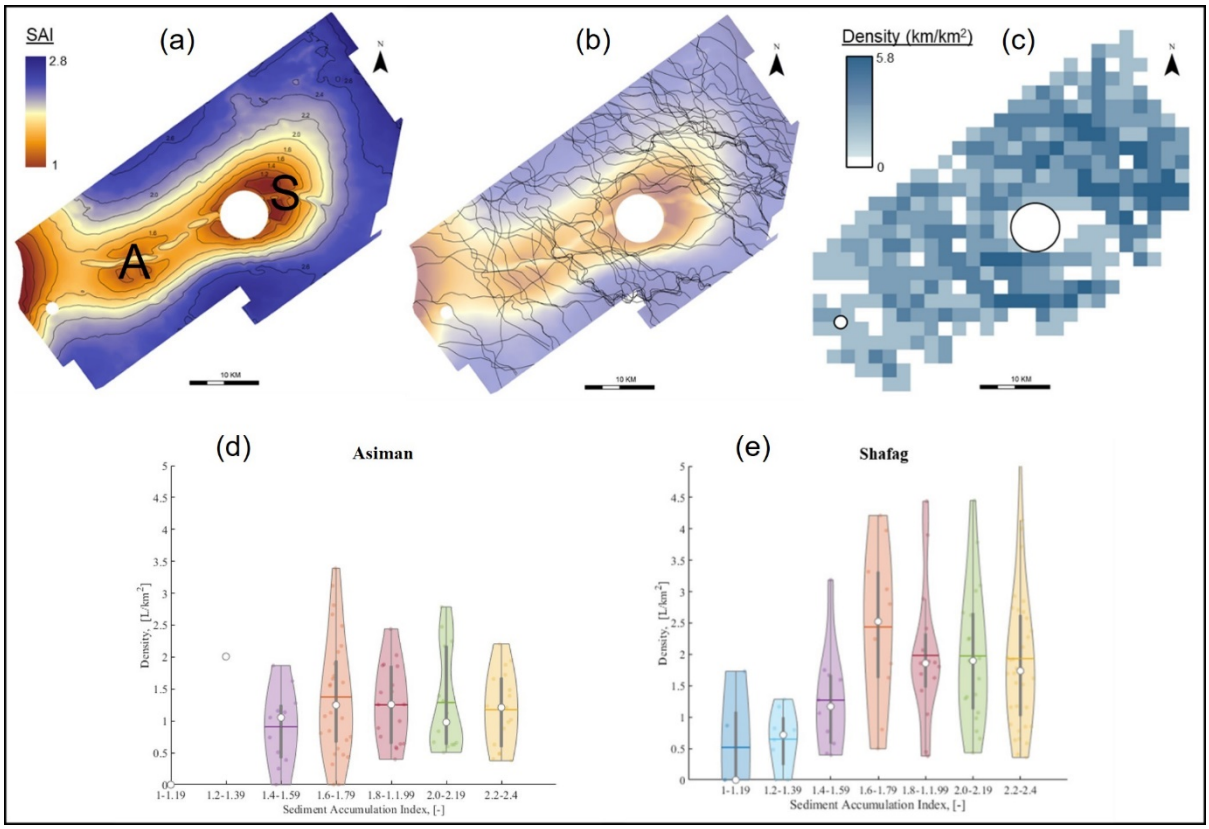


Figure 6.12: Maps produced for Unit B showing: a) sediment accumulation index (SAI). b) Sediment accumulation index overlain by the channel interpretations. c) Channel density calculated within 2 km x 2 km areas. Dark blue areas show a high concentration of channels, white areas show a low concentration of channels. Violin plots for d) Asiman and e) Shafag calculated by comparing the mean SAI with the channel density for the 2km x 2km shown in c). White circles on the maps are areas of poor data quality due to mud volcanism.

6.3.3 Unit C (Hz140 – Hz 130)

Unit C, Hz140 – Hz130, shows a very different distribution of channels when compared to Unit B below (figure 6.13). There are a total of 40 channels within the unit, showing a total mean flow direction of 292° ± 7°. Looking in more detail at the orientations within each horizon, all channels are oriented WNW, apart from channels at the green times, which on average are oriented 311° ± 14° NW (table 6.4). The entry point to the area varies frequently. For the lowest part of the interval (pink and grey channels), the channels enter the area from the east and southeast. Then at blue times, the channels enter from the south and at green times the channels enter from the southwest. The latest channels, red channels, show another change and enter from the east, south and southwest. Unlike within Unit B, channels do not appear to be significantly deflected around Shafag with only one channel, in the blue times, showing a potential deflection. There are two deflections around Asiman in the red and blue times. The red horizon shows some channels flowing over the crest of both Asiman and Shafag. The average channel sinuosity of the unit is 1.13, the lowest of the three units described thus far.

Table 6.4: Channel statistics and observations for each horizon interpreted within Unit C and the total for the unit.

Horizons	No. of channels	Mean vector direction (degrees)	95% confidence (degrees)	kappa	Average sinuosity	Deflections around fold crest
All channels	40	292	7	6.5	1.13	2 Asiman, 1 Shafag
	13	289	17	3.9	1.13	1 Asiman
	7	311	14	10.3	1.1	0
	8	292	10	17	1.18	1 Asiman, 1 Shafag
	8	287	11	12.8	1.13	0
	4	275	11	25.2	1.1	0

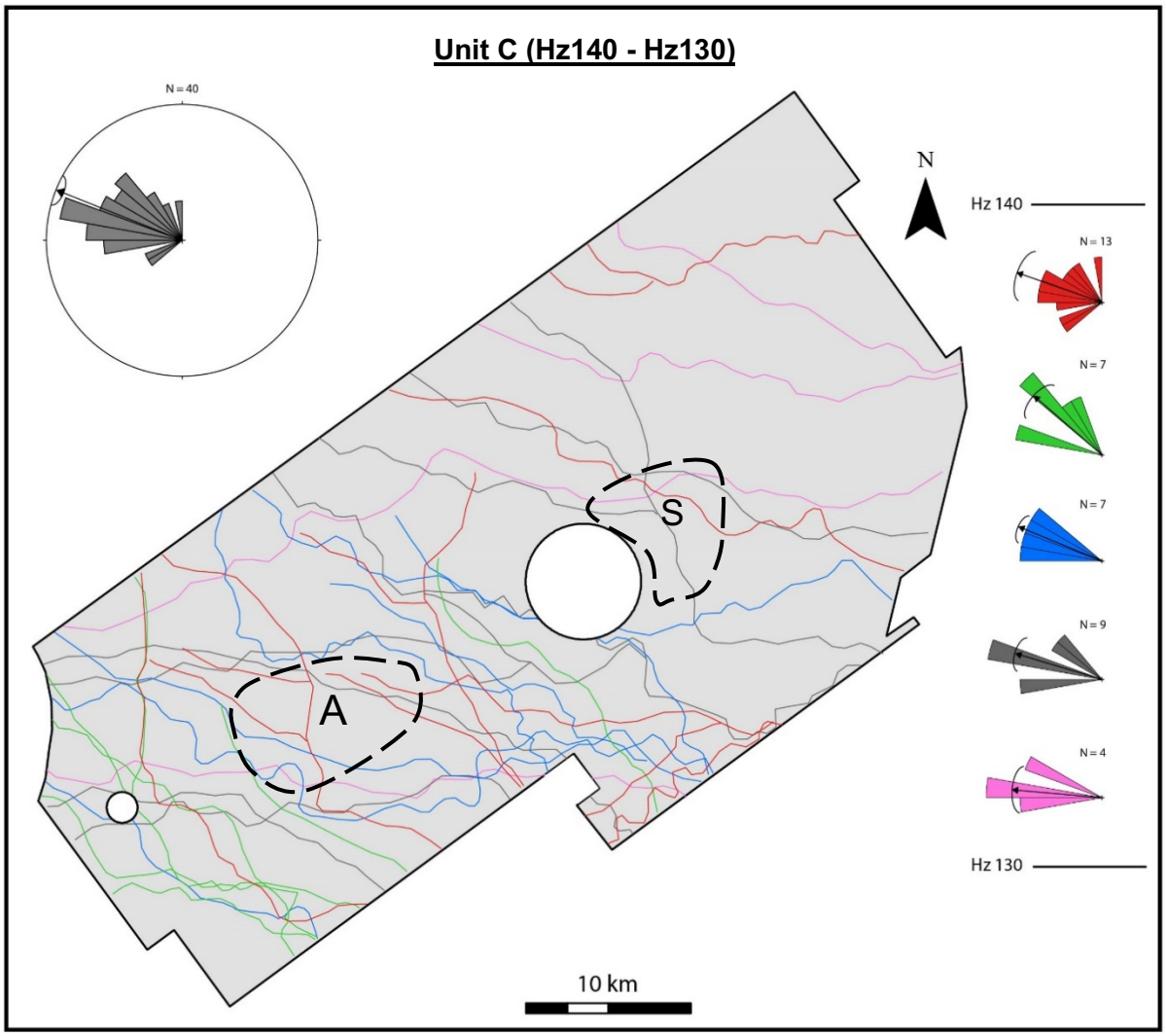


Figure 6.13: Map of channels interpreted within Unit C, colour coded for each horizon. N = 40. Channel orientations are plotted on equal area rose diagrams in 10° bin. The mean vector is shown as an arrow with 95% confidence interval. The outer circle is 30% of the data. Statistics are shown in table 6.4. The white circles on the map are areas of poor data quality due to mud volcanism. The locations of the Asiman (A) and Shafag (S) fold crests have been superimposed from the Unit C sediment accumulation index map.

The channel density map of Unit C does not show the clear relationship of channel density and structural growth as seen in the previous two units (figure 6.14). Channels entering the area from the east appear to cross over the crest of Shafag where the sediment accumulation index is 1 (figure 6.14a, b). Whilst the Asiman crest has a slightly higher sediment accumulation index, it appears that there are less channels crossing the fold crest (figure 6.14c). The highest channel densities are between the folds and to the west of Asiman, which is visible on the channel density maps (figure 6.14b, c). The channel densities northeast and east of Shafag are very low, in complete contrast to the previous two units. Whilst some of the highest channel densities corelate to the highest sediment accumulation index values (figure 6.14d, e), the highest densities, 3 km/km^2, are found on the flanks of Asiman, when the sediment accumulation index is between 1.4 and 1.6 (figure 6.14d)

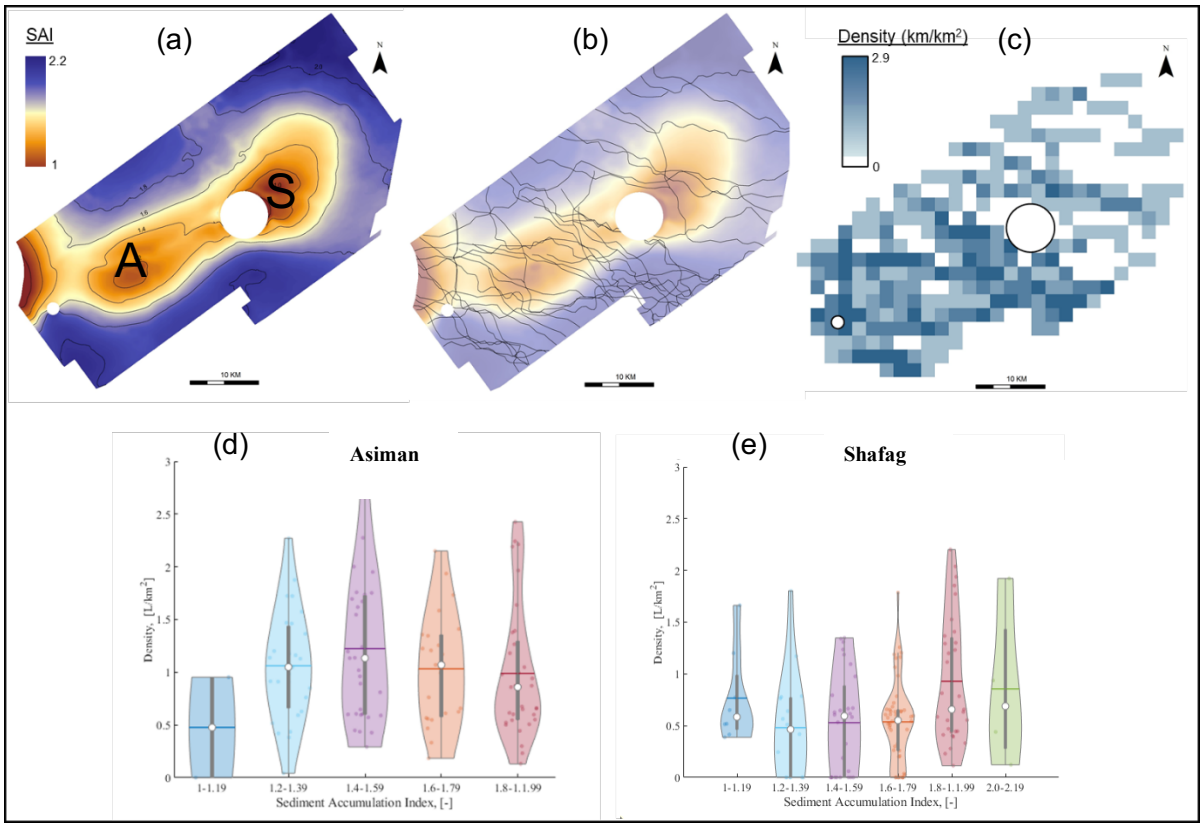


Figure 6.14: Maps produced for Unit C showing: a) sediment accumulation index (SAI). b) Sediment accumulation index overlain by the channel interpretations. c) Channel density calculated within 2 km x 2 km areas. Dark blue areas show a high concentration of channels, white areas show a low concentration of channels. Violin plots for d) Asiman and e) Shafag calculated by comparing the mean SAI with the channel density for the 2km x 2km shown in c). White circles on the maps are areas of poor data quality due to mud volcanism.

6.3.4 Unit D (Hz150 – Hz140)

In contrast to the previous units, Unit 4 shows significant differences in the channel network. Westerly and south-westerly flow dominates for the first time as opposed to strong predominance of north-westerly and northerly flow found in the preceding units. When grouped together for the entire unit, a total of 43 channels flow to the southwest, with a mean orientation of 253° ± 11°. However, when observed at the horizon scale, the channels show varying trends (figure 6.15). The earliest channels in the section have a flow direction towards the west-northwest, as shown by the pink and grey channels. The channels in the pink horizon have a mean vector of 282° ± 14° and the grey channels have an average orientation of 282° ± 13° (table 6.5). Moving up the unit, there is a second trend of channel orientations, shown by the blue and green channels. They show a flow direction towards the southwest, the blue channels have a mean orientation of 247° ± 19° and the green channels have a mean orientation of 213° ± 12°. The uppermost set of channels, during red times, shows a disperse range of channel orientations, with a mean orientation of 241° ± 24° and has two main orientation trends, south – southwest flowing channels on the northern flanks of the folds and a westerly flowing set of channels on the south-eastern flanks of the folds. The westward-trending grey and pink channels enter the area from the east and northeast, as do the blue channels. However, the green channels enter the area from the north as well as the northeast, which is not seen in any previous units. The red channels that flow towards the south – southwest also enter from the north, whereas the westerly-flowing set of channels enter from the east. The pink channels appear to get across the Shafag fold crest, as seen in the previous unit, Unit C. The grey and blue channels appear to be deflected around the Shafag fold axis. The blue, green and red channels appear flow parallel to the fold structures, particularly on the northern flanks of the folds. The green channels in the north also appear to deflect around the Asiman fold crest. The average sinuosity for all of the channels within the unit is 1.21, which is equivalent to Unit B and an increase on the sinuosity seen in Unit C. The average sinuosities are low in the westerly flowing pink and grey channels, 1.19 and 1.17 respectively, relative to the southwest trending blue and green channels, with average sinuosities of 1.28 and 1.23 respectively (table 6.5). There is a significant change in orientation, entry point and sinuosity at blue horizon times, suggesting there was a change in the channel system during channel this time.

Table 6.5: Channel statistics and observations for each horizon interpreted within Unit D and the total for the unit.

Horizons	No. of channels	Mean vector direction (degrees)	95% confidence (degrees)	kappa	Average sinuosity	Deflections around fold crest
All channels	43	253	11.4	2.87	1.21	2 Asiman, 4 Shafag
	10	242	24	2.75	1.17	0
	9	213	12	10.3	1.23	2 Asiman
	6	247	19	6.5	1.28	2 Shafag
	8	282	13	10.3	1.17	1 Shafag
	10	282	14	7.4	1.19	1 Shafag

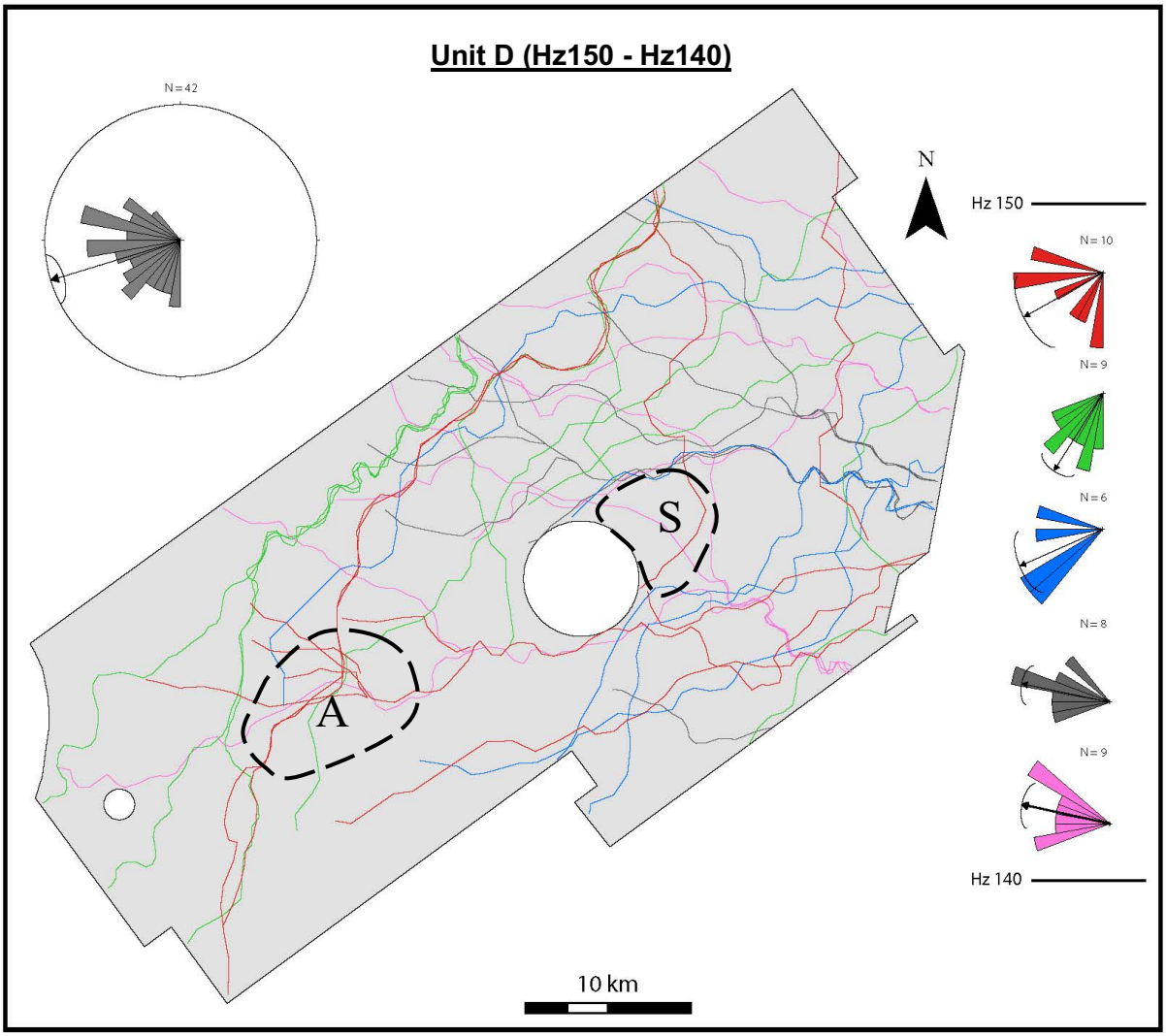


Figure 6.15: Map of channels interpreted within Unit D, colour coded for each horizon. N = 43. Channel orientations are plotted on equal area rose diagrams in 10° bin. The mean vector is shown as an arrow with 95% confidence interval. The outer circle is 30% of the data. Statistics are shown in table 6.5. The white circles on the map are areas of poor data quality due to mud volcanism. The locations of the Asiman (A) and Shafag (S) fold crests have been superimposed from the Unit D sediment accumulation index map.

Channel density maps further highlight the relationship between the channel network and the structural growth as well as a significant contrast in the channel network within Unit D in comparison to the previous units (figure 6.16). The Shafag fold crest has sediment accumulation index

values of 1 (figure 6.16a) and coincides with low density values (figure 6.16b, e), whereas the Asiman fold crest has minimum sediment accumulation index values of 1.15 (figure 6.16a) and shows more channels across the crest (figure 6.16b, c, d). However, the high density of channels on the Asiman fold crest is caused by normal faults that show increased sediment growth and focussing of the channels within the hanging wall (figure 6.16b). Channels flowing along the western margin of Asiman, coming from the north, flow towards an area of high sediment accumulation index, a depocentre, where index values are above 2 (figure 6.16b, d). The highest channel densities are to the northwest of Shafag, reaching densities up to 4 km/km^2, with the lowest channel densities to the south and east of Asiman, many areas with zero channels (figure 6.16c, e).

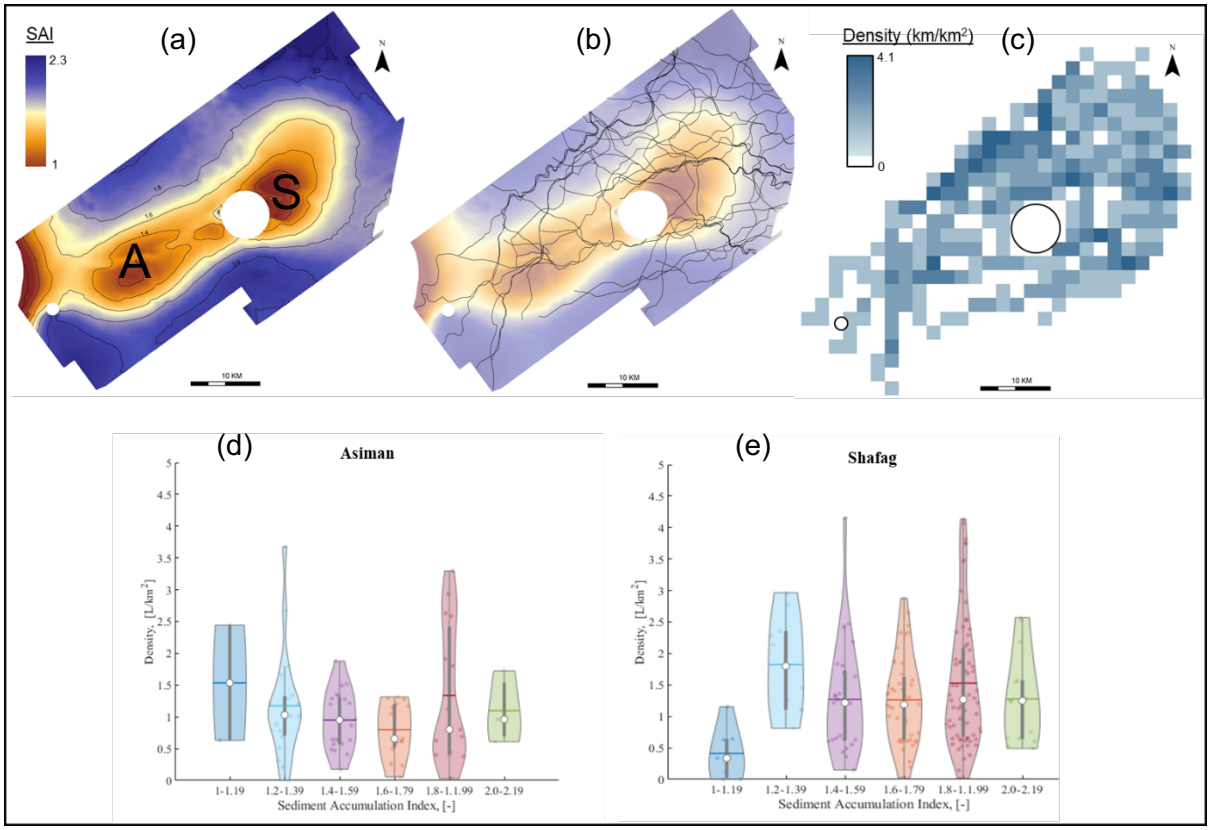


Figure 6.16: Maps produced for Unit D showing: a) sediment accumulation index (SAI). b) Sediment accumulation index overlain by the channel interpretations. c) Channel density calculated within 2 km x 2 km areas. Dark blue areas show a high concentration of channels, white areas show a low concentration of channels. Violin plots for d) Asiman and e) Shafag calculated by comparing the mean SAI with the channel density for the 2km x 2km shown in c). White circles on the maps are areas of poor data quality due to mud volcanism.

6.3.5 Unit E (Hz160 – Hz150)

The shallowest unit, Unit E, shows a significant difference in the channel network than within the underlying Unit D, but shows similar north/northwesterly flow to Units A, B and C. The unit contains 35 channels which grouped together show a mean orientation of 286° ± 12° (figure 6.17, table 6.6). However, by looking in more detail from the horizons, the channels to the northeast of Shafag flow northwest and on the southern flank of the folds, flow southwest. Channels within the lowermost grey horizon are located in the northeast of the area whereas the channels in the uppermost horizon, the red channels, are located in the southwest, near Asiman. Whilst there are only four channels in the grey channels, they show a consistent trend of northwest. However, moving up the unit the orientations become significantly more dispersed within the blue, green and red horizons. The entry point to the area is in the east of the area for all channels, with none flowing from the north as seen in Unit D. The blue, green and red channels appear to have focused entry points in the east and then disperse out within the area. Channels appear to focus around the central mud volcano and appear to flow parallel to the structures, specifically along the southern flank of Asiman. Whilst the average sinuosity of the full unit is 1.19, the grey channels have a very low sinuosity of 1.10 relative to the other horizons, with the green channels having the highest average sinuosity of 1.26 (table 6.6).

Table 6.6: Channel statistics and observations for each horizon interpreted within Unit E and the total for the unit.

Horizons	No. of channels	Mean vector direction (degrees)	95% confidence (degrees)	kappa	Average sinuosity	Deflections around fold crest
All channels	35	286	12	3	1.19	4 Asiman, 0 Shafag
	15	278	19	2.9	1.17	2 Asiman
	8	276	17	5.9	1.26	2 Asiman
	8	296	30	2.37	1.2	0
	4	319	6	100	1.1	0

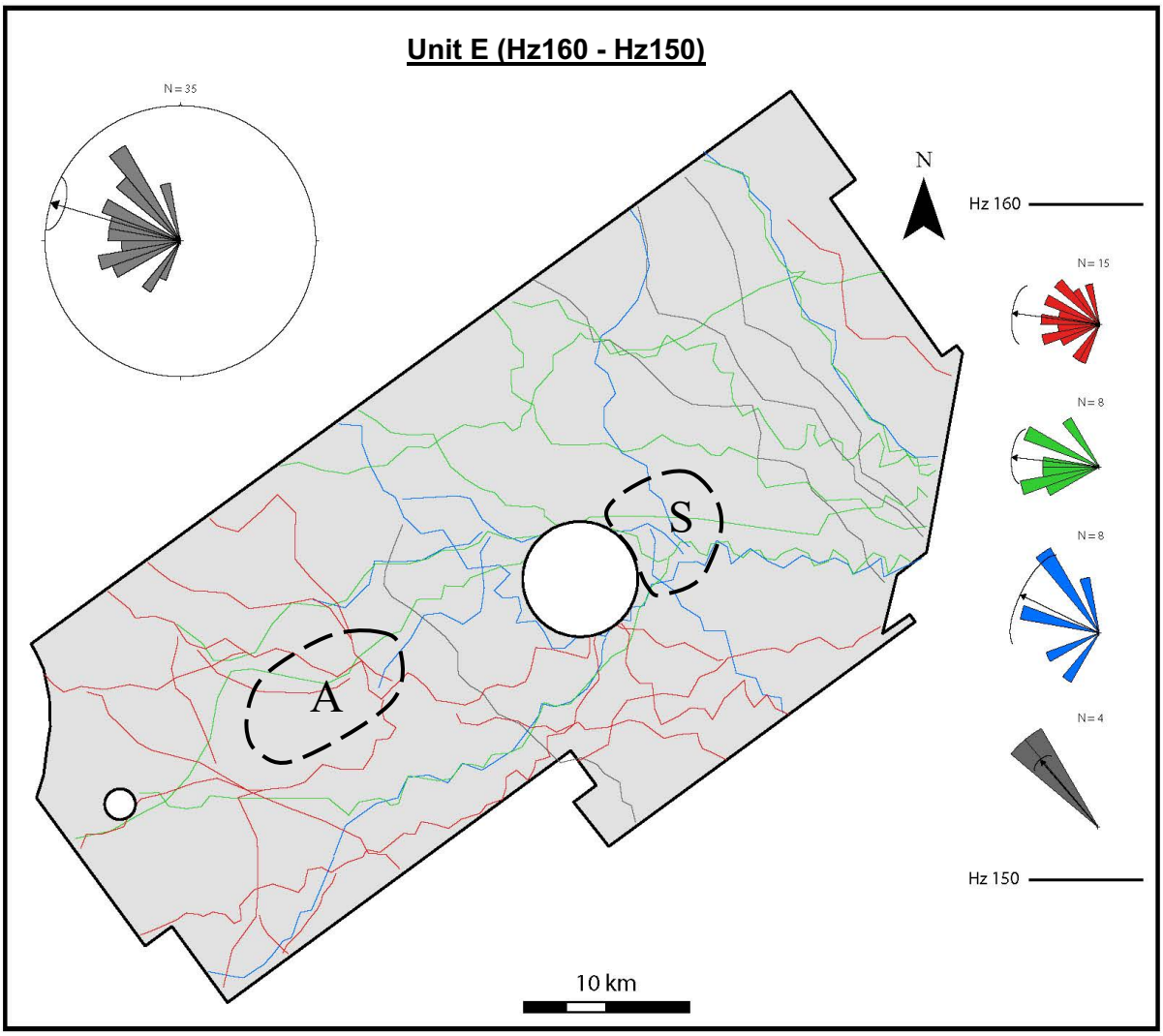


Figure 6.17: Map of channels interpreted within Unit E, colour coded for each horizon. N = 35. Channel orientations are plotted on equal area rose diagrams in 10° bin. The mean vector is shown as an arrow with 95% confidence interval. The outer circle is 30% of the data. Statistics are shown in table 6.6. The white circles on the map are areas of poor data quality due to mud volcanism. The locations of the Asiman (A) and Shafag (S) fold crests have been superimposed from the Unit E sediment accumulation index map.

Compared with the previous units, channel densities are relatively low and channels are more sparse (figure 6.18). The Shafag fold crest has a sediment accumulation index value of 1.05 – 1.3 (figure 6.18a) and channel densities can reach 1.17 km/km^2 (figure 6.18c, e). The Asiman fold crest, however, has a sediment accumulation index of 1 – 1.15 (figure 6.18a) with channel densities of 0 km/km^2 on the crest (figure 6.18c, d), showing that channels avoid the fold crest. Some channels flow over the fold crest of Asiman, but these are located where the normal faults on the crest were growing in previous

packages. Some of the highest channel densities are around the central mud volcano, where the sediment accumulation index is also highest, up to 2.4.

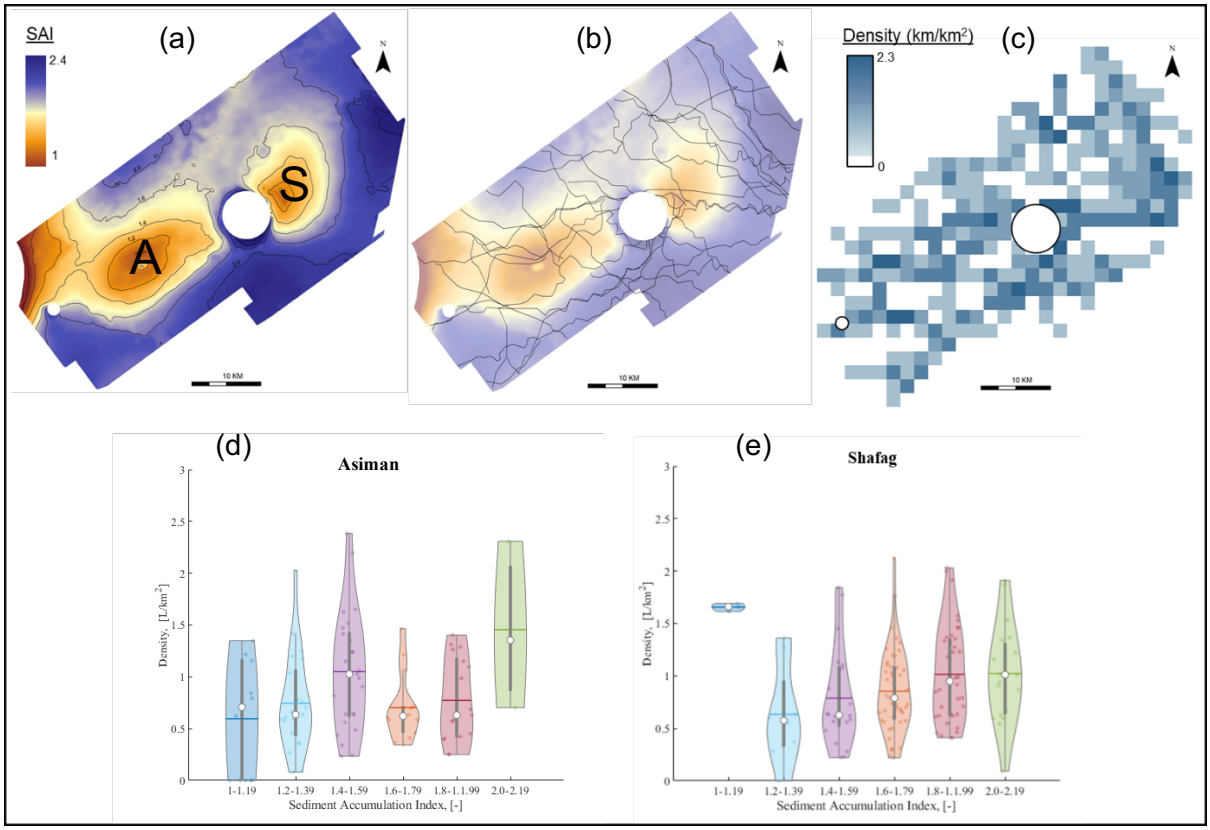


Figure 6.18: Maps produced for Unit E showing: a) sediment accumulation index (SAI). b) Sediment accumulation index overlain by the channel interpretations. c) Channel density calculated within 2 km x 2 km areas. Dark blue areas show a high concentration of channels, white areas show a low concentration of channels. Violin plots for d) Asiman and e) Shafag calculated by comparing the mean SAI with the channel density for the 2km x 2km shown in c). White circles on the maps are areas of poor data quality due to mud volcanism.

6.3.6 Channel Architecture

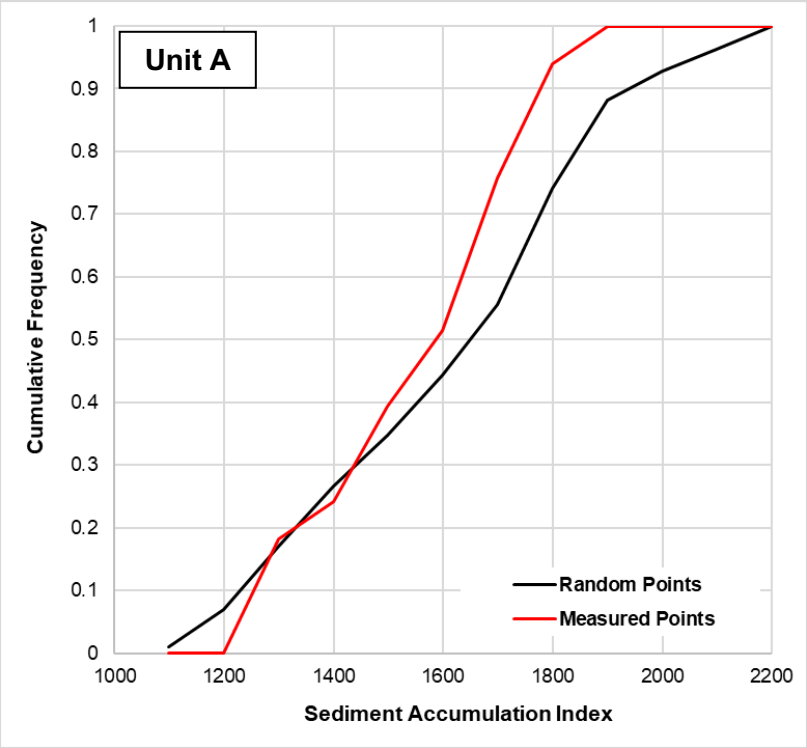
A more detailed analysis of changes in channel architecture can be used to indicate any changes in the depositional system at that time, either due to changes in sediment supply or seabed topography. The channel architecture used in this study is based on the terms channel element and channel complex, as discussed previously. The term channel element is used to describe an individual channel, that can be seen and interpreted from the RMS amplitude maps. The term channel complex is used to describe two or more elements which are related and appear to follow a similar flow path. The location on the map where a channel element or complex splits from a larger channel complex is defined as an avulsion point. 102 avulsion points were found within the five units of the Absheron Formation (Table 6.7).

Table 6.7: Total number of Avulsion points and number of avulsion points per horizon within each unit.

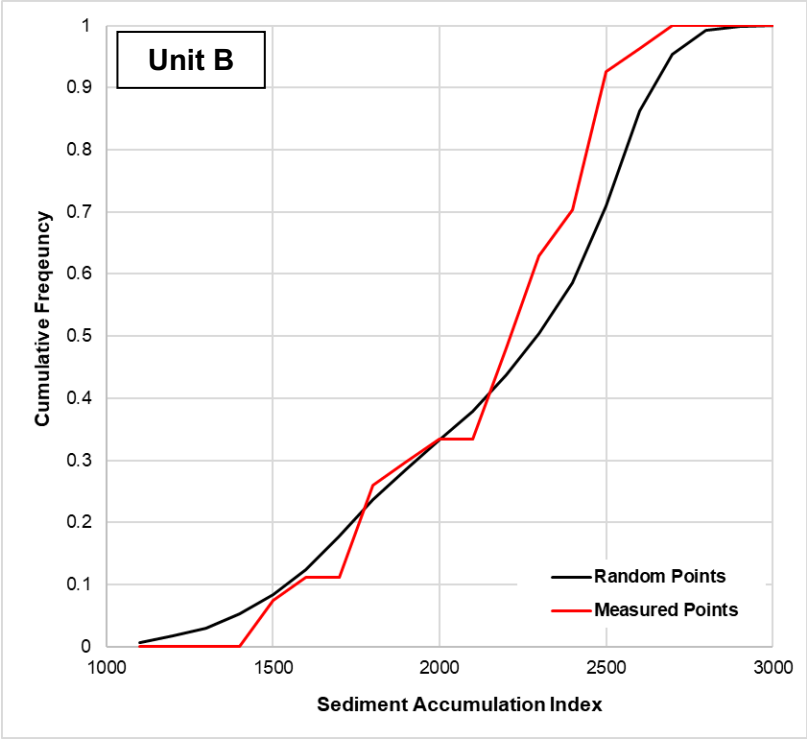
Unit	Total Avulsion points	Avulsion Points per horizon
E (Hz160 – Hz150)	11	6
		3
		2
		0
D (Hz150 – Hz140)	17	4
		3
		1
		3
		6
C (Hz140 – Hz130)	14	6
		3
		2
		2
		1
B (Hz130 – Hz120)	27	7
		1
		5
		9
		4
		1
A (Hz120 – Hz110)	33	3
		0
		6
		4
		4
		5
		8
		3

One might expect an avulsion point to occur when a channel encounters a change in slope gradient, for example, when it encounters a structure with seabed expression. A statistical analysis of the avulsion point distribution is completed to test this hypothesis and determine with the distribution of the avulsion points around the fold structures is random or not. To determine whether the avulsion points are influenced by the structure the avulsion points are compared with the sediment accumulation

index, which is used as a proxy for seabed topography for the units. For each avulsion point the value of the sediment accumulation index is recorded from the relevant sediment accumulation index map. Since the index is measured over a larger interval than the avulsion point, it is not a fully accurate approximation of the seabed at the time that the channels were active on the seabed. However, it is appropriate to use as a proxy since it gives an indication of the large-scale structure at the time. A Kolmogorov-Smirnov (K-S) test was undertaken to test the hypothesis that the sediment accumulation index values at each of the measured avulsion points is significantly different to the index values at random points. The random distribution is calculated by measuring the sediment accumulation index at 100,000 random points on the appropriate sediment accumulation index map. The K-S test is most useful with more data points. There are less than 20 avulsion points per unit in the uppermost three units and therefore the K-S test is conducted on the lowermost two units, Unit A and Unit B (figure 6.19). The normalised cumulative distribution function plots for sediment accumulation index for the measured avulsion points and random points returns D_{max} = 0.201 for Unit A and D_{max} = 0.218 for Unit B. At the 80% confidence level, D_{crit} = 0.187 for Unit A and D_{crit} = 0.207, within Unit B. D_{max} is greater than D_{crit} for both datasets and the null hypothesis that both distributions could have been drawn from the same probability distribution can be rejected. Confidence level higher than 80% cannot be used due to the small number of total data points. From the test it can be concluded that the avulsion points are not randomly located with respect to the sediment accumulation index and are likely controlled in some part by the growing structure. For an avulsion point to occur, there must have been something in the depositional system to cause it to occur. To determine what was occurring in the depositional system on a finer scale than the 100's m scale of the units the channel architecture of individual channel complexes and elements with avulsion points are investigated.



Dmax	0.201
α	0.8
Dcrit	0.187



Dmax	0.218
α	0.8
Dcrit	0.207

Figure 6.19: Normalised cumulative frequency of sediment accumulation index measured at each Avulsion point and 100k random points for Units A and B with K-S test statistics. At the 80% confidence level, Dmax > Dcrit so the null hypothesis is rejected suggesting that the distributions are not drawn from the same probability distribution.

Types of Avulsion Point

Two types of avulsion point are observed, with two terms defined for this dataset, point avulsion and lateral avulsion. Both types of avulsion only occur when channel complexes are developed. Lateral avulsion is defined where channel elements avulse from a channel complex at different points along the complex. Within Unit A, two avulsion points can be seen along a northwest flowing channel complex at locations 1 and 2 in figure 6.20. From the edge of the area up to location two, there are three channel elements which form the complex. The oldest channel flows to the northwest out of the area, the second channel element avulses off to the west at location one and the youngest element avulses off to the southwest at location two.

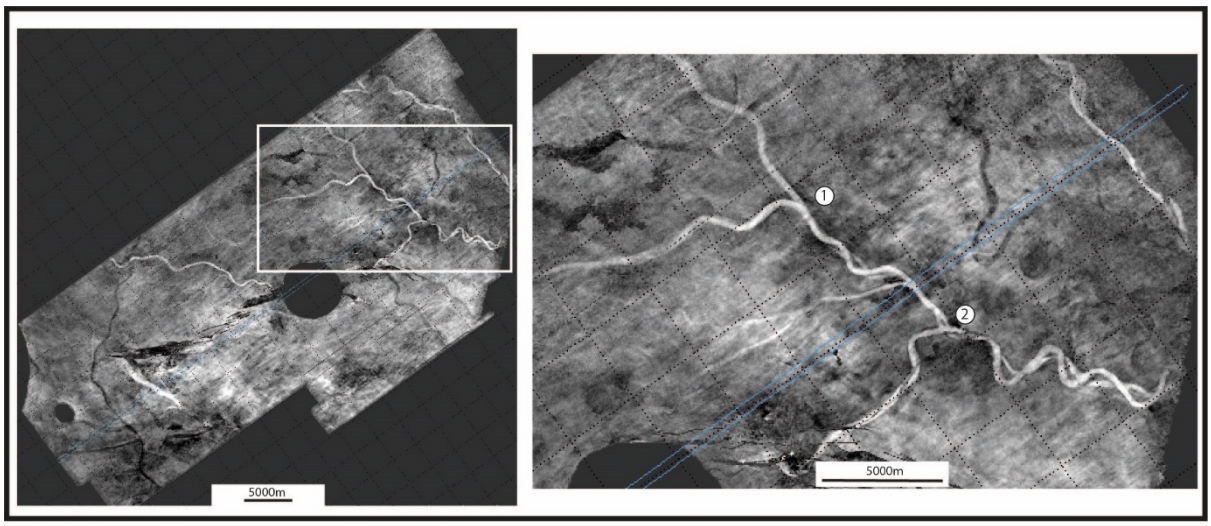


Figure 6.20 RMS map of a horizon within Unit A showing lateral avulsion points of a channel elements from a channel complex at locations 1 and 2.

Point avulsion is defined as an avulsion point where an aggrading and migrating channel complex splits into either a smaller channel complex or individual elements at the same location. Within Unit B (Hz130 – Hz120) a channel complex displays a detailed example of point avulsion (figure 6.21). A major channel complex consisting of five channel elements flows northwards from the southeast. The complex is laterally migrating and displays down-stream migration, shown by migrating point bar scrolls and the increasing sinuosity of the channel elements. Three observations can be made downstream along the channel complex. 1) south of the Asiman fold, five channel elements within a

channel complex laterally migrate, with vertical aggradation apparent towards the end of development (figure 6.21, line A). 2) A point avulsion then occurs (figure 6.21, red location 1) where the complex splits into two complexes, one with three elements and one with two (figure 6.21, line b). 3) A second point avulsion occurs, (figure 6.21, red location 2) and the channel complex splits into a complex of three elements and two single elements. The five elements can still be recognised and shift progressively to the west after deposition of the first channel. The channel complex flowing north splits into its three constitutive elements at lateral avulsion points (figure 6.21, line c). The elements become isolated, less sinuous and are no longer stacked and migrating. The second avulsion point (figure 6.21, location 2) occurs on the crest of the Asiman fold structure, between lines B and C on figure 6.21. The youngest, most sinuous channel element appears to be focussed along a growing extensional crestal fault (figure 6.21, channel 5).

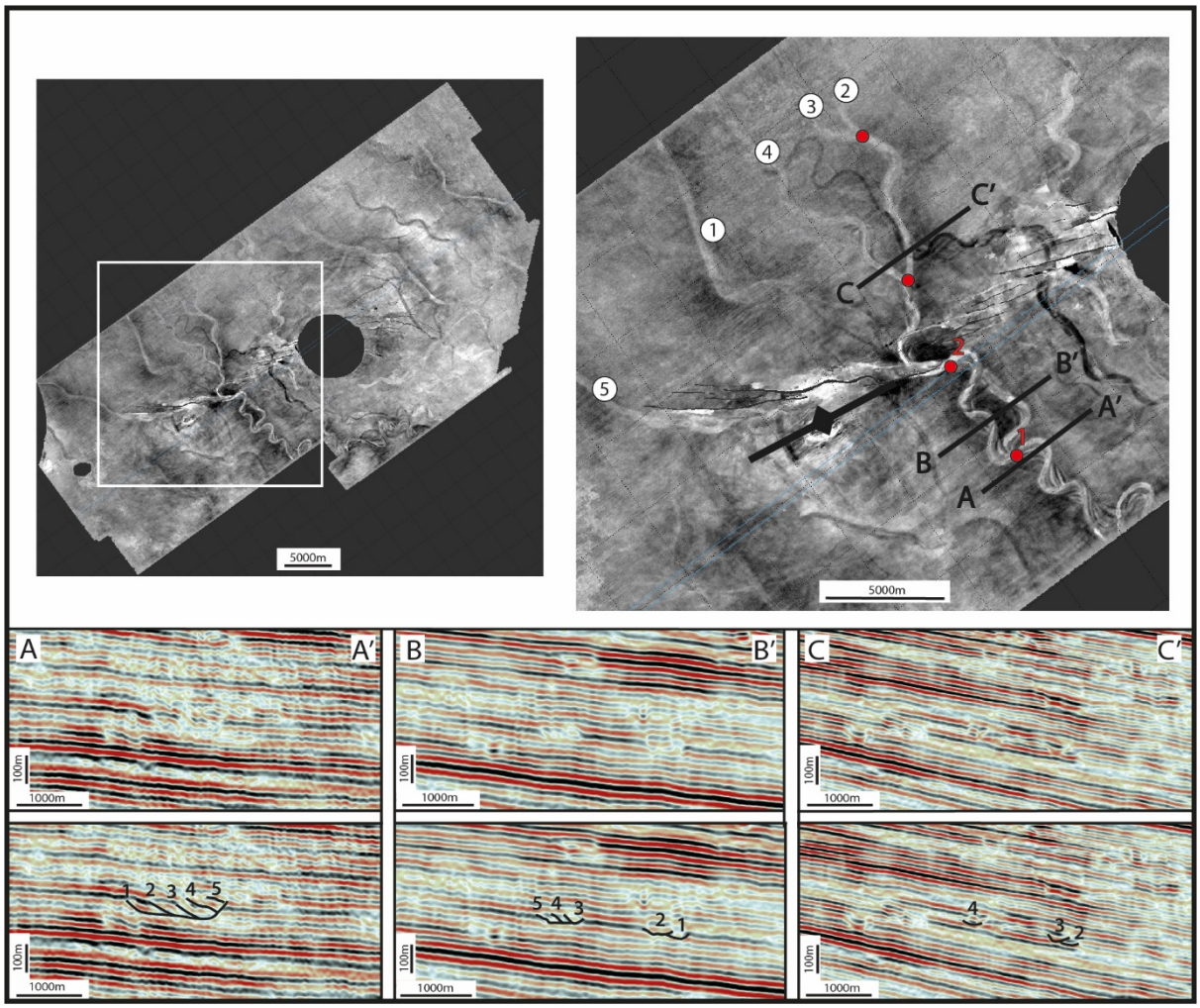


Figure 6.21: RMS map of a channel complex within Unit B showing point avulsions up-dip of the fold crest and lateral avulsions downdip of the fold crest. Avulsion points are highlighted in red. Labels 1 (oldest) – 5 (youngest) indicate the relative age of the channel elements. Uninterpreted and interpreted seismic sections for three sections A-A', B-B' and C-C' along the channel profile, showing a change from lateral migration and aggradation to isolated channel elements.

Within the centre of Unit B (Hz130 - Hz120), a similar point avulsion occurs along a channel complex, north-east of Shafag (figure 6.22). Again, a laterally stacked channel complex with four vertical aggrading channel elements, diverge and become isolated with a decrease in sinuosity. The larger complex splits into smaller complexes (figure 6.22, channel elements 3 and 4) and channel element (figure 6.22, channel elements 1 and 2). After the deposition of the first channel element, the isolated channel elements appear to rotate from a N orientation (figure 6.22, channel element 2) to a NW orientation for the latest channel element (figure 6.22, channel element 4). The isolated channel elements appear to rotate from a N orientation for the second earliest channel to a NW orientation for the latest channel of the channel element.

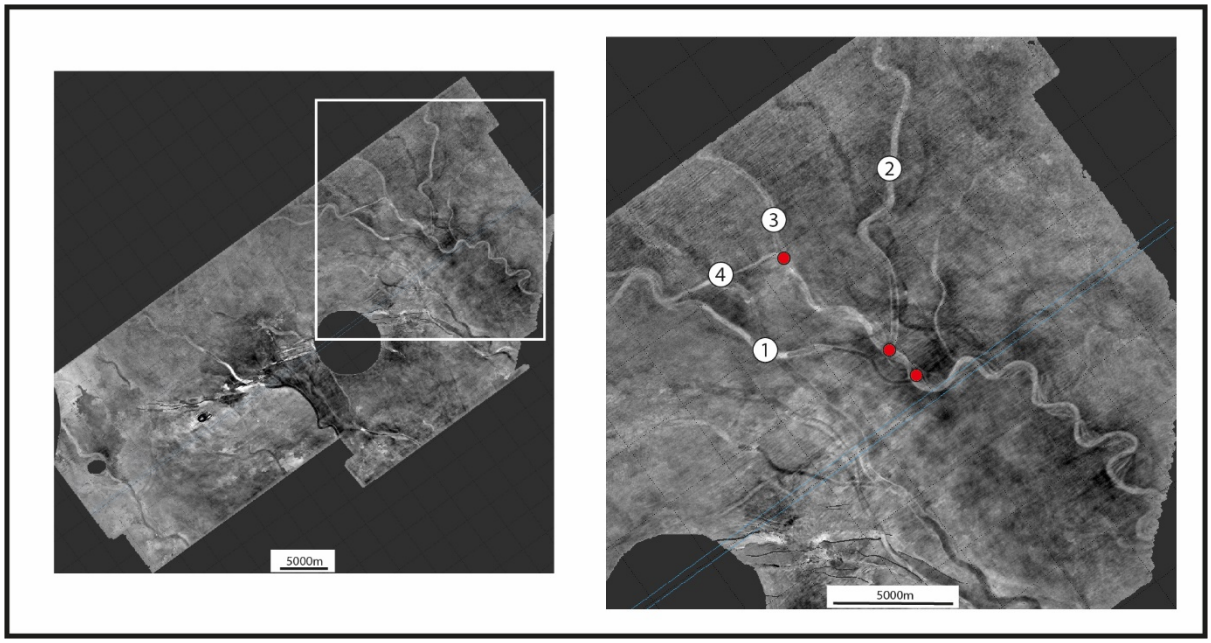


Figure 6.22: RMS map of a channel complex within Unit B showing point avulsions up-dip of the fold crest and lateral avulsions downdip of the fold crest. Avulsion points are highlighted in red. Labels 1 (oldest) – 4 (youngest) indicate the relative age of the channel elements.

Within the five units there are five examples of channel complexes that show this form of point avulsion. Two are found within Unit B (Hz130 – Hz120), which shows the highest SAI on the fold flanks. The other three systems are contained within Unit D (Hz150 - Hz140), which shows the second highest SAI on the fold flanks out of the five units.

The influence of structure on the avulsion of channel complexes and elements can shown by comparing the mapped channel complexes and elements and the unit equivalent sediment accumulation index map (figure 6.23 and 6.24). Complexes from Units B and D show that the point avulsions are located on the up-dip slope of the fold structure and lateral avulsions are located on the downslope of the structure. The channel complexes appear to follow sediment accumulation index contours, along a small structural high to the east of Shafag. The lateral avulsion of the channel elements from the channel complexes appears to be focussed towards a depocentre north of Asiman. Within both intervals, a channel element follows growing crestal normal faults. The faults show more growth within Unit B (Hz130 – Hz120), which is reflected by the greater focussing of a channel element along the faults.

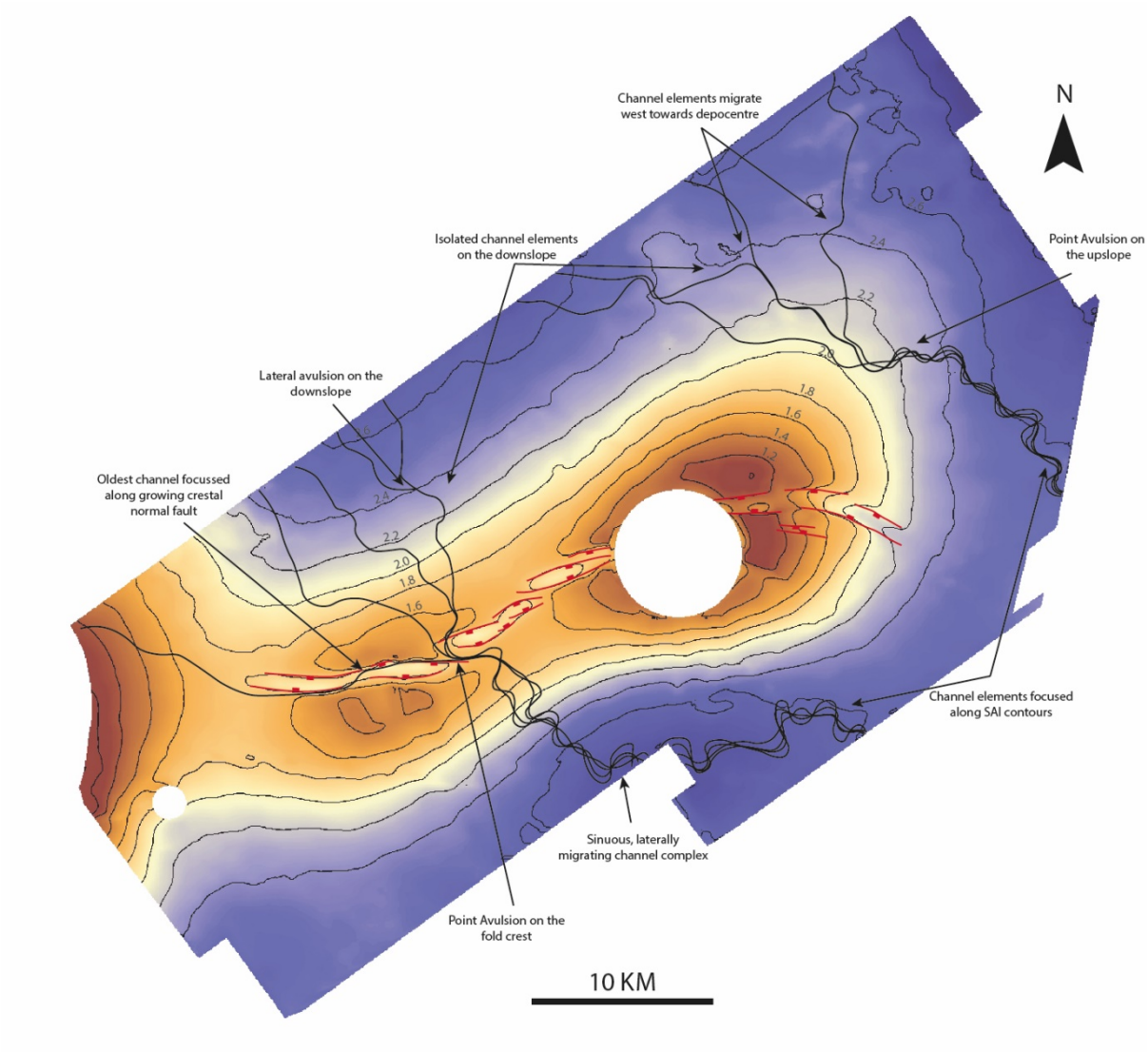


Figure 6.23: Channel complexes within Unit B overlain on to the unit equivalent sediment accumulation index map.

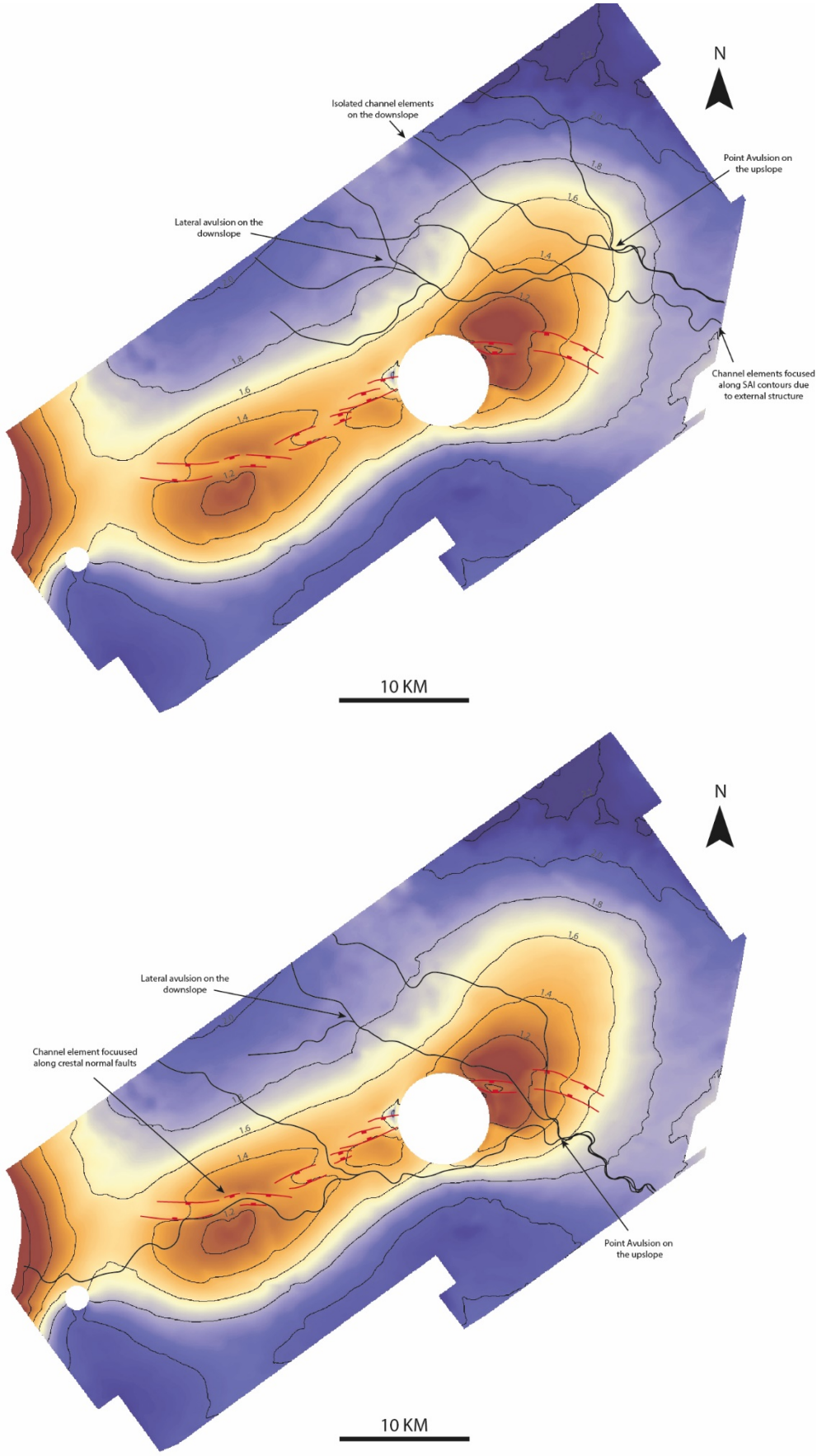


Figure 6.24: Channel complexes within Unit D overlain onto the unit equivalent sediment accumulation index map.

The point avulsions occur on the up-dip slope occur within Unit B and D, which are the two units that have the highest sediment accumulation index on the fold flanks out of the five units. Seismic sections show that within these intervals, there is significant onlap onto the Shafag fold (Figure 6.25a, b), specifically within horizons that contain numerous channel elements and channel complexes. Even though sediment is deposited over the fold crests on the scale of the sediment accumulation intervals, at the time the complexes are formed, the horizons onlap the Shafag fold and no sediment is deposited over the fold crest. There is less onlap over Asiman within the two units, D and B and fewer channel complexes develop (figure 6.25c). The point avulsion over Asiman within Unit B occurs due to interaction of the channel complex with the crestal normal faults (figure 6.23).

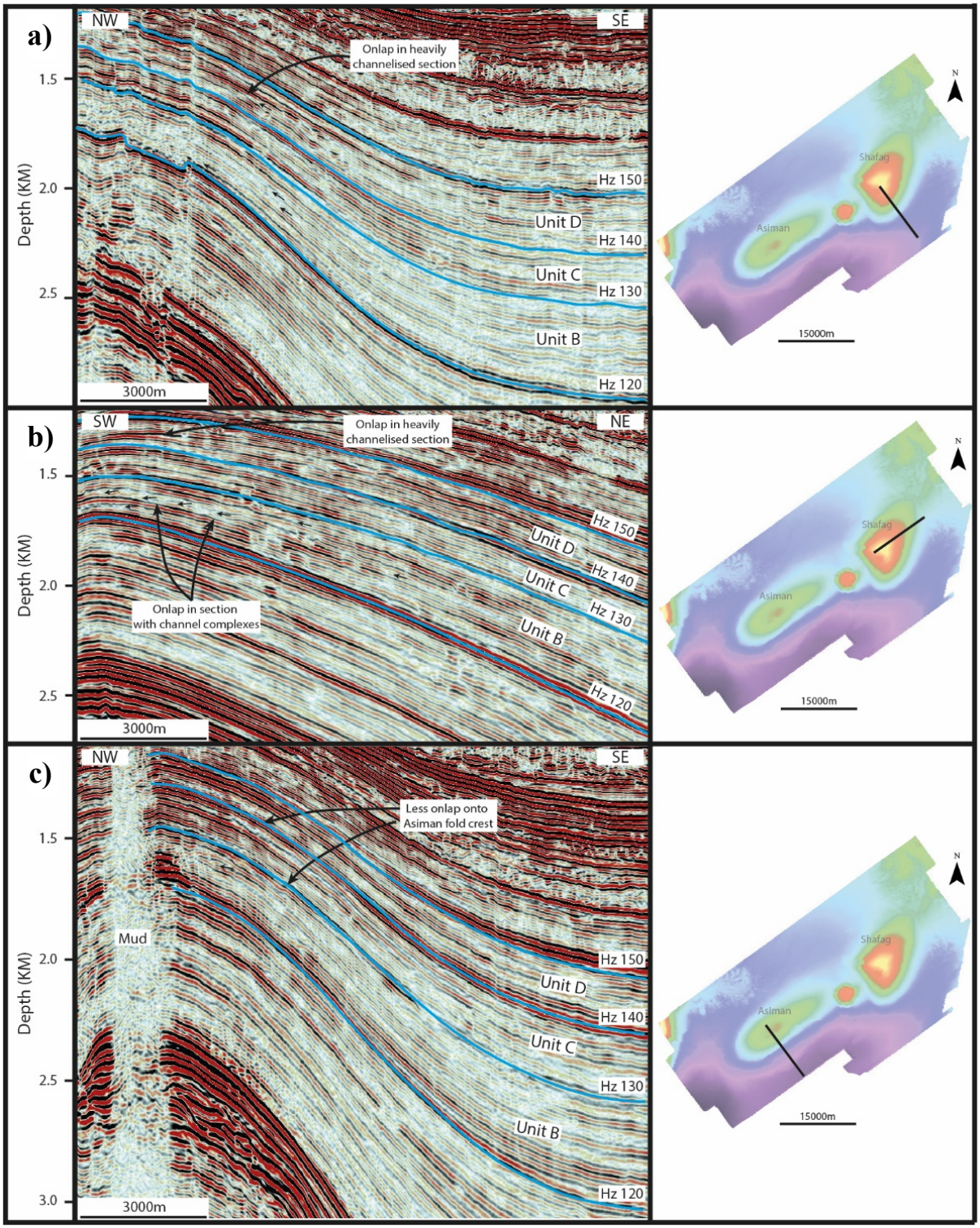


Figure 6.25: Sections showing onlap (black arrows) within units D and B across Shafag (a) and (b) and Asiman (c).

6.4 Discussion

The analysis of 259 channels within Units A-E of the Absheron Formation show how the channel network evolves and changes through time. Channel orientation, channel entry point to the area, deflection around structures and changes in sinuosity all vary between the units. The key observations from each unit are summarised in table 6.8.

Table 6.8: Summary of the main observations made of the channel network within each unit.

Unit	Mean Orientation (degrees)	Main Entry Points	High Channel Density Area	Fold with lowest channel density	Average Sinuosity
E (Hz160-Hz150)	286	E, S	S and N of Asiman, E of Shafag	Asiman crest	1.19
D (Hz150-Hz140)	253	N, NE, E	N of Asiman and Shafag. NE Shafag	Shafag crest	1.21
C (Hz140-Hz130)	292	SW, NE	Between fold crests and SE, SW of Asiman	Neither crest	1.13
B (Hz130-Hz120)	301	E, S, SW	NE of Shafag	Shafag crest	1.21
A (Hz120-Hz110)	286	E, NE, SE, SW	NE of Shafag S of Asiman	Asiman crest	1.14

I will now discuss what the potential impacts of structures within the area, structures external to the area, regional tectonics and climate are on the channel network through time. Whilst Units A, B, C and E flow west-northwest, significant changes in channel orientations can be seen within Unit D, where flow is in an average west-southwest direction. This is because channels in the upper part of Unit D flow into the area from the north and parallel to the folds.

6.4.1 Influence of Shafag-Asiman on the channel network

The measured channel characteristics vary across the structures between each unit. The results show that throughout the units, channels avoid areas of sediment accumulation index of less than 1.2. Sediment accumulation index values of <1.2 show that sediment is thinnest in these areas, which are coincident with the fold crests. A low sediment accumulation index coinciding with a low channel density suggests that at these times, the fold growth is greatest and creates seabed topography during that time interval. The seismic data also shows that more onlap occurs where there is a low sediment accumulation index, as would be expected. By using the sediment accumulation index and channel density it can be determined which fold is the dominant fold growing through time during the Absheronian. During Unit A, Asiman is the dominant fold, whereas. During Unit B and D, Shafag becomes the dominant fold, which then changes again during Unit E, where Asiman becomes the dominant. The sediment accumulation index for Unit C is lower over Shafag than Asiman, suggesting that Shafag should demonstrate seabed topography and therefore have less channels flowing over the crest. However, whilst there are times where the channels deflect around Shafag in Unit C (figure 6.13, blue channels), there are also times when channels flow over the Shafag crest (figure 6.13 pink, grey and red channels). Whilst the sediment accumulation index maps can show the general fold growth of each unit (Chapter 4), the channels can show a finer scale detail of the palaeo-seabed topography and how it can vary over a short timescale.

Whilst channels avoid the dominant growing fold crest, the channel network is also influenced by the structures on the flanks of the folds. The location of the channels relative to the folds influences characteristics such as the channel density, sinuosity and channel architecture. When the sediment accumulation index on the flanks of the folds within a unit is low, channel densities are disperse and not focussed along the structures, as seen in Unit C (section 6.3.3) and Unit E (section 6.3.5). The sediment accumulation index value is lower on the northern fold flanks than southern flanks within Unit E, which coincides with a low concentration of channels. However, on the southern flank of the folds the sediment accumulation index is higher and coincides with a greater concentration of channels. The areas where channels are most concentrated are located in areas with the highest sediment accumulation index in Units B and D. The areas with high sediment accumulation indices indicate areas of relatively

greater subsidence. This greater subsidence has focussed the channel elements and in some cases they form channel complexes where a series of elements utilize the same pathway. The confinement of the channels leads to the aggradation of the channel elements to form channel complexes. As a channel complex develops, the latest channel elements become more sinuous. Thus, the high average channel sinuosities which are observed within the units with the highest sediment accumulation index (Units B and D) are mostly due to the development of channel complexes.

The relationship between high and low sediment accumulation indices and channel sinuosity can be seen in several units. Low channel sinuosities occur within units A and C (table 6.8), where the sediment accumulation index around the flanks of the folds is low. A low structural growth causes lower channel sinuosities since channel complexes do not get developed. Although unit C has low average channel sinuosities, some of the channels during blue times deflect around the fold crests. This is also the level within the unit with the highest average sinuosity (table 6.4), suggesting that greater fold growth may have occurred, leading to greater channel sinuosities during this time. The link of high and low channel densities and sinuosities with high and low sediment accumulation indices is shown in Unit E. The sediment accumulation index map for the unit is asymmetrical, with a high index on the southern limbs of the folds and a low index on the northern limb of the folds. There is also a high index around the central mud volcano, where sediment thickens due to mud evacuation. On the southern limb of the folds high channel densities and high channel sinuosities coincides with the higher sediment accumulation index. On the north limb, the opposite is seen, with low densities and low sinuosities where the accumulation index is lower. Low density values are calculated in the areas with high sediment accumulation indices, however this is largely a function of the area that the densities were calculated within, since the 2 km by 2 km area was selected for optimal analysis over the fold crest.

Channel complexes form where elements flow down previous channel element pathways. The point at which the channel complex splits into smaller channel complexes and elements is defined as an avulsion point. Within the five units, channel complexes are mostly developed by a maximum of two or three channel elements which flow down a previous channel element pathway and do not commonly show lateral migration as seen in the complexes described in figures 6.21 – 6.24. These complexes create what is defined here as lateral avulsion and appear to occur on the down-dip side of the structure

as each element follows the development of the local seafloor gradient. This is commonly seen in Unit A, where channels avulse west (figure 6.20) on the north side of Shafag suggesting that there was seabed topography at that time causing the channels to flow westward. The sediment accumulation index map shows contours that also suggest a NW-SE trending high. This is significant as it shows that the Shafag-Asiman fold did not just develop as a simple NE-SW trending fold with synclines parallel to the fold axis and the seafloor was a lot more complex.

Point avulsions occur when a laterally migrating and aggrading channel complex splits into its constitutive elements and smaller complexes. The point avulsions occur on the up-dip side of the structure (figure 6.23 and 6.24), where each subsequent channel element must be following the changing local sea-floor gradient. The largest channel complexes, with up to five channel elements, are contained within Unit B, the unit with the highest fold growth and is the interval with the most point avulsions. This suggests there is a link between the channel complexes, point avulsions and highest fold growth. The channel complex containing five elements over Asiman has a laterally migrating section (figure 6.21, Line A) in the region with the highest sediment accumulation index. As the channel approaches the fold crest the lateral migration decreases and the aggradation increases (figure 6.21, Line B). More aggradation suggests more deposition (Kolla et al., 2007) and may be due to a greater focus of the channels between the growing fold axis. The point avulsion then occurs over Asiman and the complex splits into isolated elements (figure 6.21, Line C). The lateral sweep and aggradation suggest that there is more deposition than during times with straight isolated channel elements. The increased aggradation of the complexes may make the complexes more prone to avulsion. More deposition also links with the increase in sediment accumulation taken from the index maps. An increase in deposition could cause the increase in fold growth at these time intervals (Chapter 5). A model of the impact of structure on the channel network is displayed in figure 6.26.

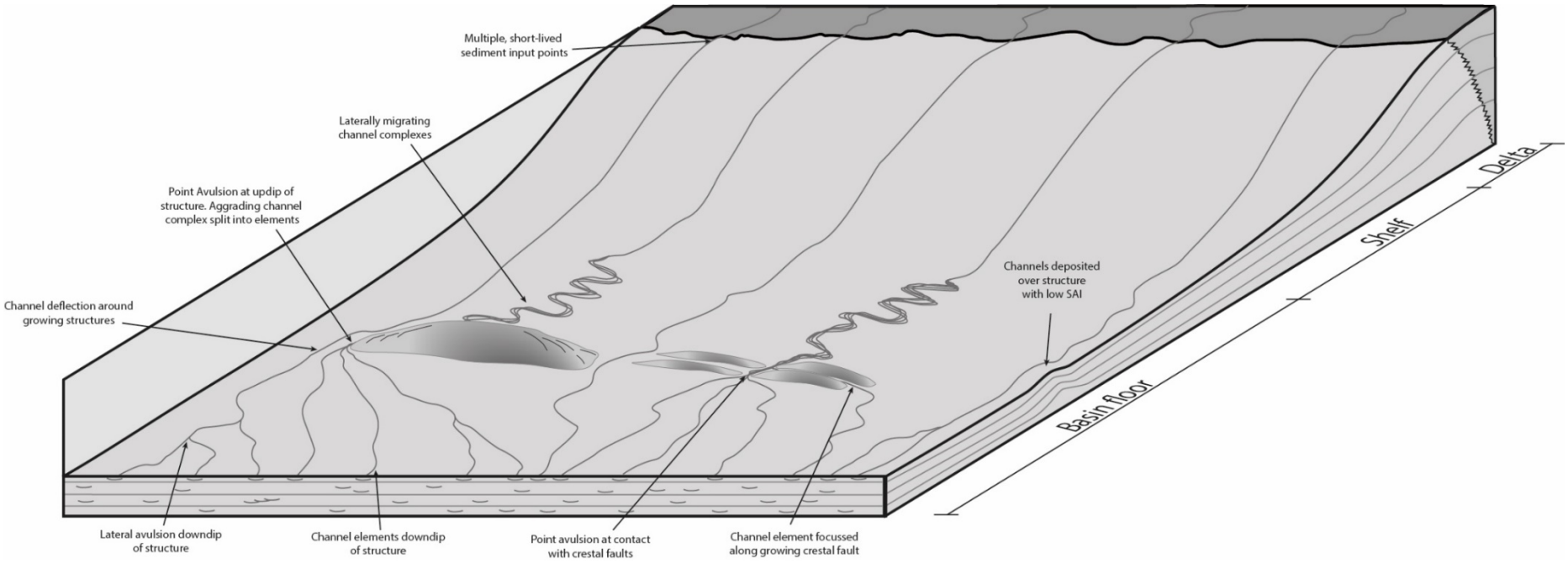


Figure 6.26: 3D depositional model of the deep water lacustrine turbidite system within the deep-water South Caspian Sea Basin.

6.4.2 Structures outside of the dataset

The South Caspian Basin has numerous anticlines growing during the Pleistocene, as demonstrated in chapter 3, which may influence the channel network distribution and architecture as has been shown at the Shafag-Asiman fold structure. Channel entry points and orientations vary between the units and are likely to be affected by seabed topography that lies outside of the study area. The seismic data used in this study area is a small area of the wider deep-water South Caspian Basin and is surrounded by other growing folds. There is a small fold on the present-day seabed, directly to the south-east of Shafag (figure 6.27), the edge of which likely causes the higher sediment accumulation index values observed to the southeast of Shafag (Chapter 4). This structure appears to influence the location of some of the channel complexes (figure 6.23 and 6.24). Within the Shafag – Asiman dataset channel complexes split into smaller complexes and individual channel elements due to the interaction with structure, either on the up-dip of the structure, point avulsions, or down-dip of the structure, lateral avulsions. The splitting of the complexes due to changes in seabed topography outside of the area may be why the area is dominated by elements rather than channel complexes, especially towards the top of the section, above unit B.

It also appears to influence the entry point to the study area. Within Unit E, the entry point has a 'blind spot' adjacent to this external fold, where no channels enter the area. Below Unit D, the channel entry points are more extensive along the south-eastern edge of the dataset, entering from the southwest. The fold likely affected the channel entry to the study area as it grew through time. The sediment accumulation index maps show that there is a decrease in index value between Shafag and the external fold throughout all the units, indicating a minor structural high was likely present throughout all units. This structural high likely caused channels to be diverted into the SW of the area early in the Absheron, as sediment accumulation index maps appear to show that the trend of a SE-NW high was more prominent towards the base of the Absheron and top of Productive Series (chapter 4, Hz110 - Hz100). Regional isopach maps from Green et al. (2009) show deposition of the deep-water sediments thin onto these adjacent folds.

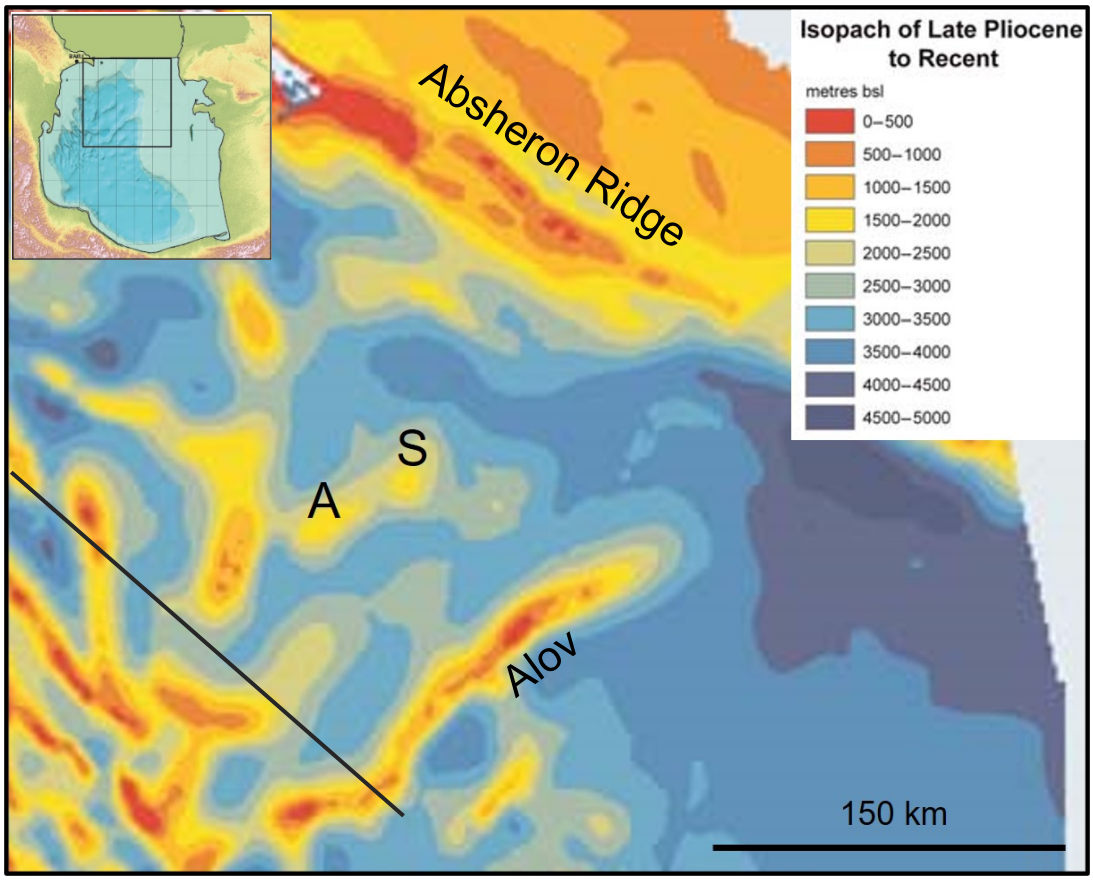


Figure 6.27: Isopach map of the Late Pliocene to recent sediments modified from Green et al., (2009). The Asiman and Shafag structures are labelled A and S respectively. The location of the seismic line from figure 6.28 is shown by the black line.

During the youngest intervals, Unit A, B and C, channels often entered the area from the southwest. Within Units D and E, the channel entry points are clustered around the east. This may be due to seabed topography caused by the large fold structure to the south of the study area, known as Alov (figure 6.27). The fold is over 100 km long and regional seismic reflection data show that during the Pleistocene there is significant onlap onto the fold (figure 6.28). The structure could have caused channels to divert away from the Shafag-Asiman area, preventing the channels entering the area from the southwest (figure 6.29). Abdullayev (2000) suggests that the Alov fold causes axial parallel channel systems to develop to the southeast of the structure. To the northeast of Shafag-Asiman there are no fold structures which could divert channels supplied from the southeast to enter the area from the north

and northwest as seen in Unit D. There must have been a temporary supply from the northeast. Figure 6.29 shows the possible channel source and flow paths into the area.

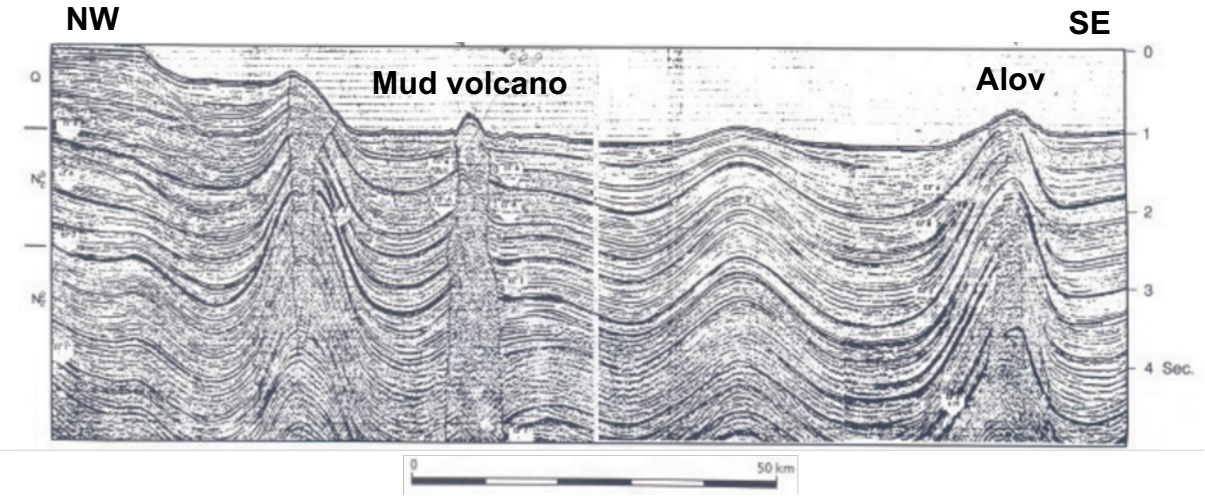


Figure 6.28: Regional 2D seismic line across the centre of the South Caspian Basin showing fold structures and mud volcanoes. The 'Alov' structure is labelled. The strata show significant thinning onto the structure From Narimanov (1997). Location on figure 6.25.

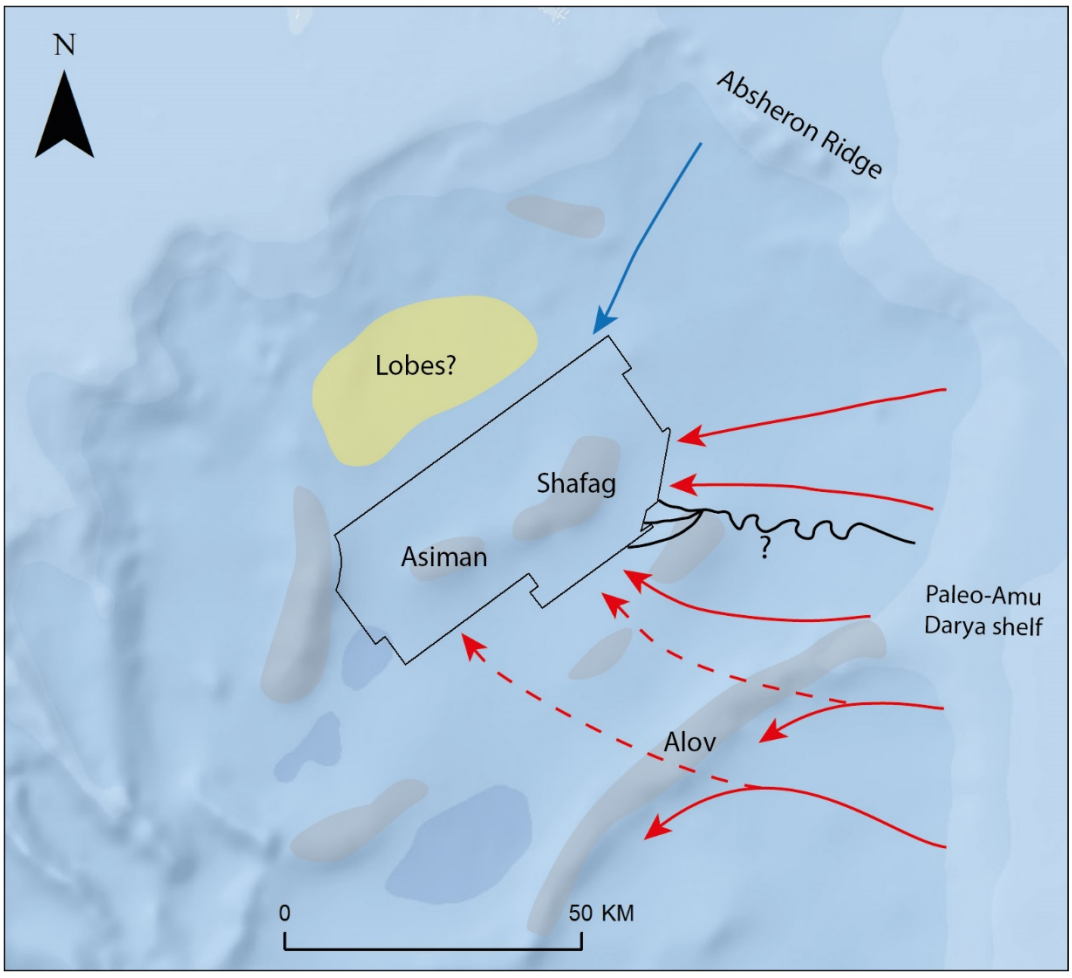


Figure 6.29: Regional bathymetry map of the deep-water South Caspian Sea Basin around the Shafag - Asiman data set (black box). Fold structures on the present-day seabed are shown in grey. Red arrows show possible channel sources from the Paleo Amu-Darya. Dashed lines show channels entering Shafag – Asiman before the Alov structure blocked the flow path. The blue arrow shows the likely source area for the SW trending channels within Unit D. The black channel shows a possible channel complex splitting into channel elements on a structure outside of the dataset.

6.4.3 Tectonic controls

The orientation and entry point change observed within Unit D could be due tectonic events at this time. Shortening occurs throughout the Absheronian (Allen et al., 2003, Abdullayev et al., 2012), with tectonic reorganisation causing a change in the principal stress orientations within the basin, as the basin moves northwest relative to Eurasia and southwest relative to Iran (Priestley et al., 1994, Jackson et al., 2002). Subduction along the Absheron Ridge, to the northeast of Shafag-Asiman within the South Caspian (figure 6.29), was ongoing during the Pleistocene with earthquakes occurring under the ridge (Jackson et al., 2002, Allen et al., 2003). Slope instability due to earthquakes could have caused turbidites to be sourced from the Absheron Ridge to the north of the study area from where the channels are sourced. This could explain why the channels return to being sourced from the east towards the top Unit D interval as well as during Unit E above, since the change in source is not a long-term event. A significant tectonic event could have been due to the subduction and rotation of the basin. The onset of the presently active tectonics is debated, with Ritz et al. (2006), Ritz (2009), Cifelli et al. (2015), Mattei et al. (2019), suggesting that the westward component of movement, causing clockwise rotation of the basin during the Pleistocene, after the original start of subduction in the Pliocene (Jackson et al., 2002, Allen et al., 2002). I have shown that the Shafag fold axis rotates through time, from E-W to NE-SW through the Absheronian (Chapter 3), likely coincident with the rotation of the basin during the Pleistocene. The Unit D channel orientation changes occur after the fold axis rotation and cessation of growth on the en-echelon normal faults, suggesting that by this time the basin had undergone significant tectonic reorganisation. The tectonic reorganisation may have caused a change in the source area from the east to northeast, possibly due to a redirection of the Amu Darya River as the Kopeh Dagh mountains developed to the east.

6.4.4 Climatic controls

Changes within lacustrine depositional systems are controlled by tectonics and climate due to the sensitivity of the system to accommodation space and sediment/water supply (Bohacs et al., 2000), with the Caspian very sensitive to climate in the Plio-Pleistocene (Forte and Cowgill, 2013). The

transition from the Akchagyl transgression to the Absheronian coincided with an intensification of northern hemisphere glaciation (Knies et al., 2009, Laberg et al., 2010, Forte and Cowgill, 2013). The Amu Darya River is sourced from the significantly glaciated mountains of the Pamir Mountains in Tajikistan (UNECE, 2011). Changes in climate will therefore have a significant effect on the sediment source and water input of the Palaeo Amu-Darya into the South Caspian Basin.

Orbital forcing has been postulated to control cyclostratigraphy of deposition South Caspian Basin on a scale of 400ky cycles (Abreu and Nummedal, 2007). The authors show seismic sections on the Turkmenistan shelf in the east of the South Caspian Sea with prograding packages containing 18 seismically defined intervals from the base of the Absheron Formation to the present day (Abreu and Nummedal, 2007), suggesting that lake level fluctuations occur at time scales of 100 ky. These timescales are in line with the 100 ky Milankovitch cycles of eccentricity. Since climate appears to affect the base-level and depositional system of the South Caspian Basin, the entry point variations observed throughout the five units analysed could be influenced by orbital forcing affecting the source area. The five units are deposited over approximately 1.2 My. High frequency changes on the coloured horizon scale or within the horizons may be due to fine scale orbital forcing timescales such as 41 ky obliquity cycles or 23 ky precession cycles. Climate changes on this scale may subsequently cause sediment supply changes into the basin.

The Absheron Formation is deposited over approximately 1.2 million years. The thickness of the formation is approximately 1700m in the thickest part of the area. By using a constant sedimentation rate of 170m per 100,000 years it can be estimated that the channel changes within Unit D occurred approximately 1 million years ago. At this time, there was a significant change in both the climate and the tectonic configuration of the South Caspian. The change in depositional system could have been affected by climate because at this time the climate system had a significant change, called the Mid-Pleistocene Transition (Berger and Jansen, 1994, Head et al., 2008, Maslin and Brierley, 2015). At the Mid-Pleistocene Transition (1.25Ma - 0.75Ma), the climate cycles changed from varying at a 41ky timescale before the transition, to a 100 ky climate cycle after the transition (Shackleton and Opdyke, 1977, Clark et al., 2006), in which glacial and interglacial periods become longer and more intense (Clark et al. 2006 and references therein). The change in channel orientations that are observed in Unit

D may have coincided with the initiation of a prolonged glacial or interglacial event, with an increase or decrease in base level, sediment supply and source area from the shelf all possible due to a significant shift in climate. This may also explain why there is no significant change in entry point and source area observed within intervals below Unit D, before the Mid-Pleistocene Transition times, where glacial cycles were less pronounced.

6.4.5 Comparison with Marine Systems

The analysis of 259 channels within the deep-water turbidites of the Absheron Formation at Shafag-Asiman show that channels approximately 100-300m wide predominantly pass through the area as single channel elements, with some complexes present. Changes to channel entry points occur at the scale of 10,000s of years. The density of channels and timescale of changes are significantly different from most marine systems (Sprague et al., 2005, Porter et al., 2006, McHargue et al., 2011, Mayall and Kneller, 2021). It is known that the processes of deep-water lacustrine turbidite deposition are different to marine deposition since lakes are more sensitive to changes in accommodation and climate than marine systems (Bohacs et al. 2000 and references therein). This is the main reason for the high channel densities and fine scale changes in channel geometries within the Shafag – Asiman area, which is not observed within marine systems. The depositional system can be affected by a change in sediment supply, a change in lake water level or structures. As discussed above, the variation in channel entry points could be due to either a change in source area from the shelf or by seabed topography external to the study area. The Shafag-Asiman fold structure sits within the middle of a depression, surrounded to the N, E and W by a shelf with three rivers historically terminating in the basin. This varies from marine environments, in which there is often a single shelf area with a much larger open abyssal plain environment. I interpret there to be no long-term single point supply to the area and this is likely what causes the depositional system to be dominated by elements with complexes, rather than a hierarchy of elements stacking into complexes which then stack into systems as is observed in many deep marine environments (Mayall and Kneller, 2021) (Figure 6.30).

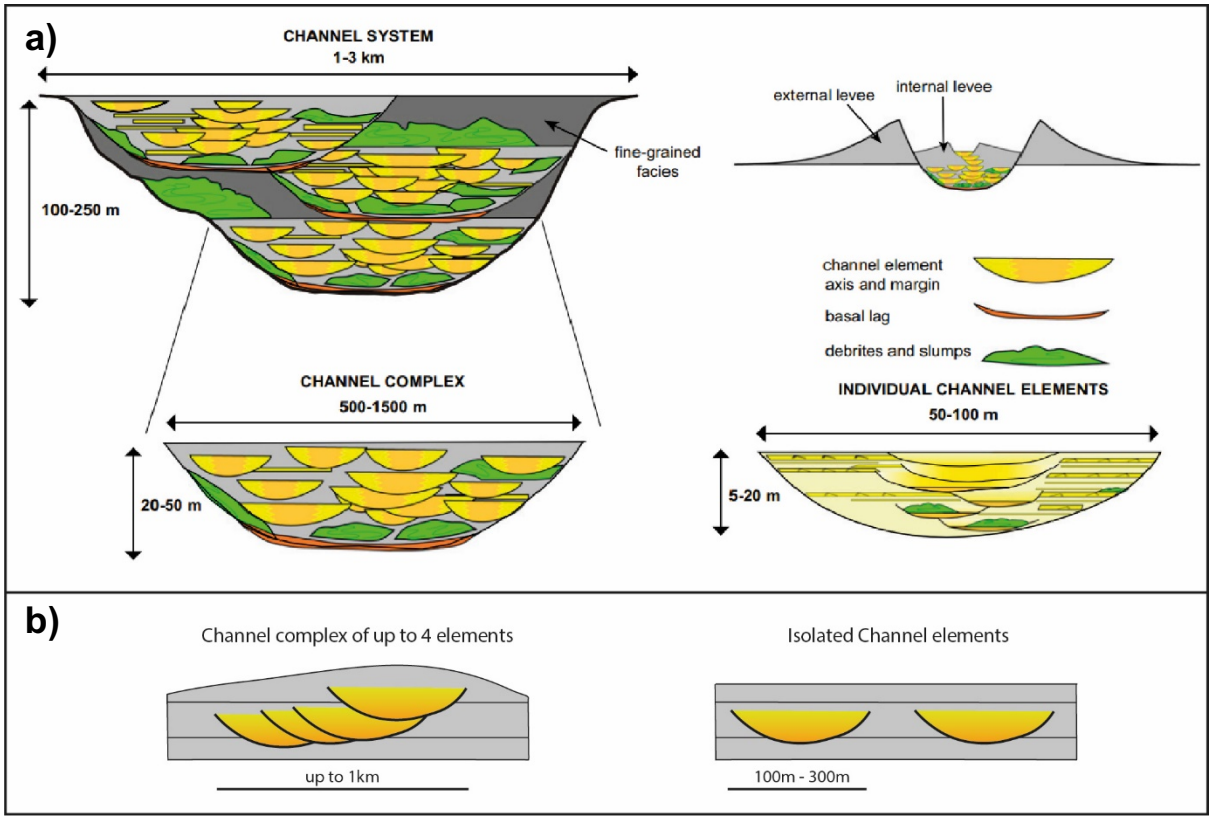


Figure 6.30: Comparison of deep water turbidite systems between (a) marine from Mayall and Kneller (2021) and b) Shafag-Asiman.

6.4.6 Comparison with Lacustrine Systems

The Caspian Sea is the largest lake in the world (Bohacs et al., 2003) in a unique and complex tectonic setting. Although there are many deep lakes in the world, e.g Lake Baikal (Flower et al., 1995), East African Rift Lakes (Zhang and Scholz, 2015) none are within as tectonically complex basins as the South Caspian and mostly sit within rift basins (Xian et al., 2018). Rift basins are usually more elongate than the SCB and with deep water sediments having less distance to travel, and grabens/half grabens causing slumps/slides due to seabed topography (Zhang and Scholz, 2015, Xian et al., 2018). Within active continental rift basins, axial drainage parallel to the fault zone occurs as well as vertical stacking of turbidite lobes on the footwall scarp (Gawthorpe and Leeder, 2000) (figure 6.31). Basins more similar to the South Caspian are the large ancient Chinese basins, the Songliao Basin (Zhi-qiang et al., 2010) and the Ordos Basin (Zavala et al., 2022).

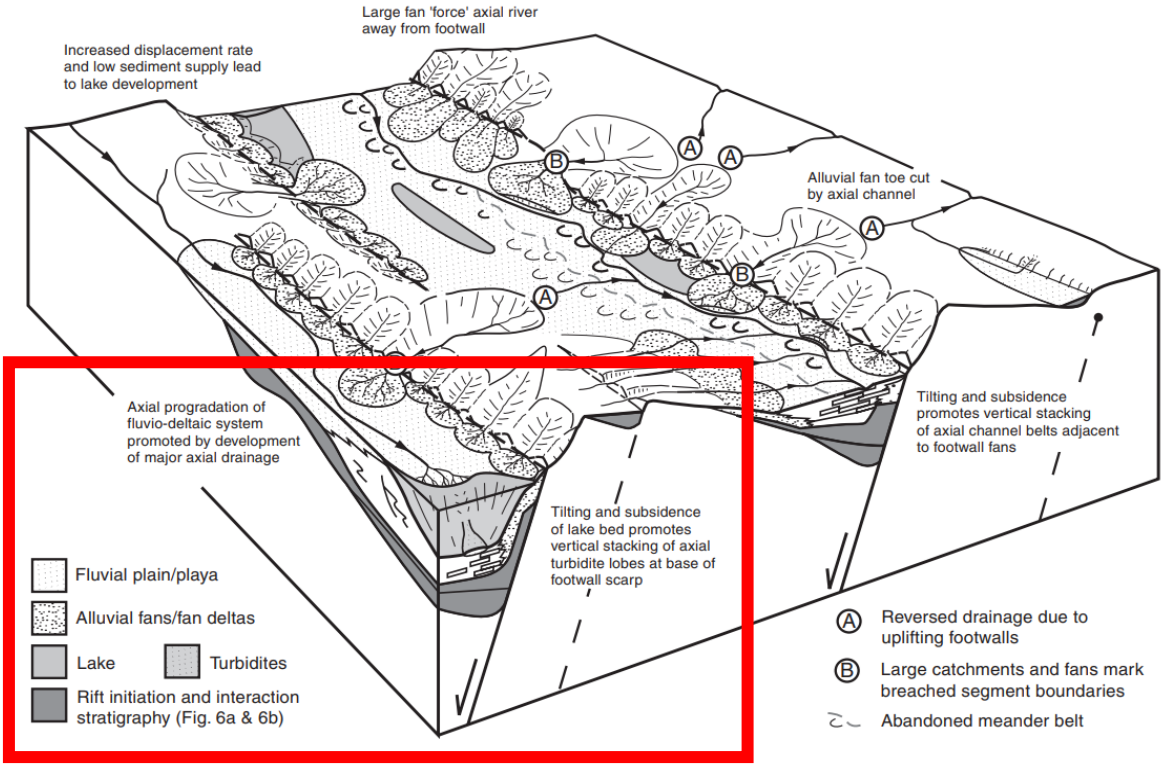


Figure 6.31: Active continental rift depositional system from Gawthorpe and Leeder (2000). Footwall scarp lacustrine turbidites are highlighted by the red box.

Lacustrine basins are classified in three ways, overfilled, balanced-filled and underfilled, depending on the lake level and the spill point (Carroll and Bohacs, 1999). It is important to understand the basin type for comparison with other lacustrine basins as this influences the depositional system (Bohacs et al., 2000). The current day Caspian Sea is documented as underfilled (Zavala et al., 2022) and has been the same since the Pleistocene (Abdullayev 2000). An underfilled basin often classed as evaporative, and is therefore often brackish, which includes the Caspian Sea (Matishov et al., 2018, Zavala et al., 2022). An underfilled lake occurs when accommodation space is greater than the supply of water and sediment into the lake (Bohacs et al., 2000), causing an enclosed lake. Although the Caspian Sea is documented as underfilled, this is not consistent with the deep-water nature of the basin during deposition of the Absheron Formation. The South Caspian Basin is over-filled since the overall Caspian Sea contains three separate basins, the North, Middle and South Caspian Basins. The South Caspian is overfilled, spilling into the Middle Caspian and contains progrades on the Turkmenistan Shelf (Abdullayev, 2000, Abreu and Nummedal, 2007), indicative of an over-filled basin (figure 6.32).

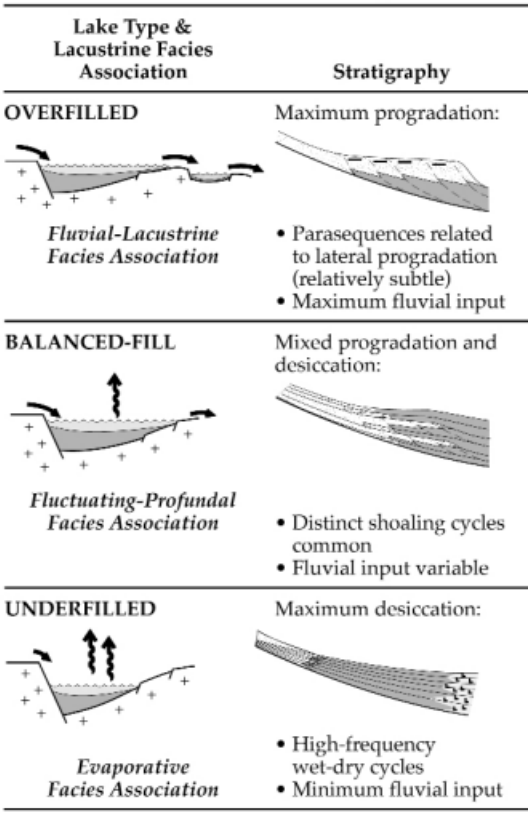


Figure 6.32: Lake types from Bohacs et. al. (2000). The deep water turbidites of the South Caspian Basin are deposited in an overfilled lake.

Many studies suggest that hyperpycnal flows form in deep water lakes (Mulder and Syvitski, 1995, Plink-Björklund and Steel, 2004, Zavala et al., 2006). High density flows with high sediment load from river input into a relatively low-density freshwater lake allows sediment to be transported long distances (Mulder and Syvitski, 1995). It is likely that the flows depositing the Absheron Formation were hyperpycnal flows, rather than sediment input from slope failures. The large distance travelled of the channels as well as the rapidly fluctuating orientations and sediment input points suggest direct riverine input controlled by flood events, as is the case with hyperpycnal deposits (Mulder and Syvitski, 1995). The also tend to deposit fine-grained deposits (Mulder et al., 2003) which is why large lobe complexes may not be present within the Shafag - Asiman area.

Cretaceous lacustrine turbidites were deposited in the Songliao Basin, China in a large post-rift depression that resembled the size of the Caspian Sea (Zhi-qiang et al., 2010). The depositional slope was shallow and resembled continental margin marine slope, rather than the steep slopes seen in rifted lacustrine basin (Zhi-qiang et al., 2010). The type of flow required to create the turbidites is disputed, with Zhi-qiang et al. (2010) suggesting that the deposits are similar to marine turbidite deposits and Pan

et al. (2020) suggesting that the deposits are caused by hyperpycnal flows. Deepwater lacustrine channels can be seen in seismic data which appear to be of a similar size and geometry to the channels within the Shafag-Asiman area (figure 6.33). They show distal fans that are not present in the Shafag – Asiman area, suggesting that distal fans may be located to the north of Shafag - Asiman. The Zhi-qiang et al. (2010) and Pan et al. (2020) studies also show the channel network to be element dominated, similar to the Shafag – Asiman area. The source area for the channels from the delta front to the north appears to show channel elements all the way up to the shelf edge, sourced from numerous areas. This can't be observed with the Shafag – Asiman dataset, however, it can be predicted that this is the same situation in the South Caspian Basin (figure 6.29).

The Triassic Yancheng Formation of the Ordos Basin, China was deposited in deep water lake that underwent rapid subsidence as the basin was closed off from the Paleo-Tethys due to the Indonesian orogeny (Yang et al., 2017, Zavala et al., 2022). The tectonic situation appears to be similar to that seen in the South Caspian Basin, with the Yanchang Formation showing a transition from fluvial deltaic deposits to deep-water lacustrine deposits (Zhao et al., 2015). The formation shows the nature of the input into the basin, showing a series of small channels feeding the deeper water and an absence of focussed channels and canyons.

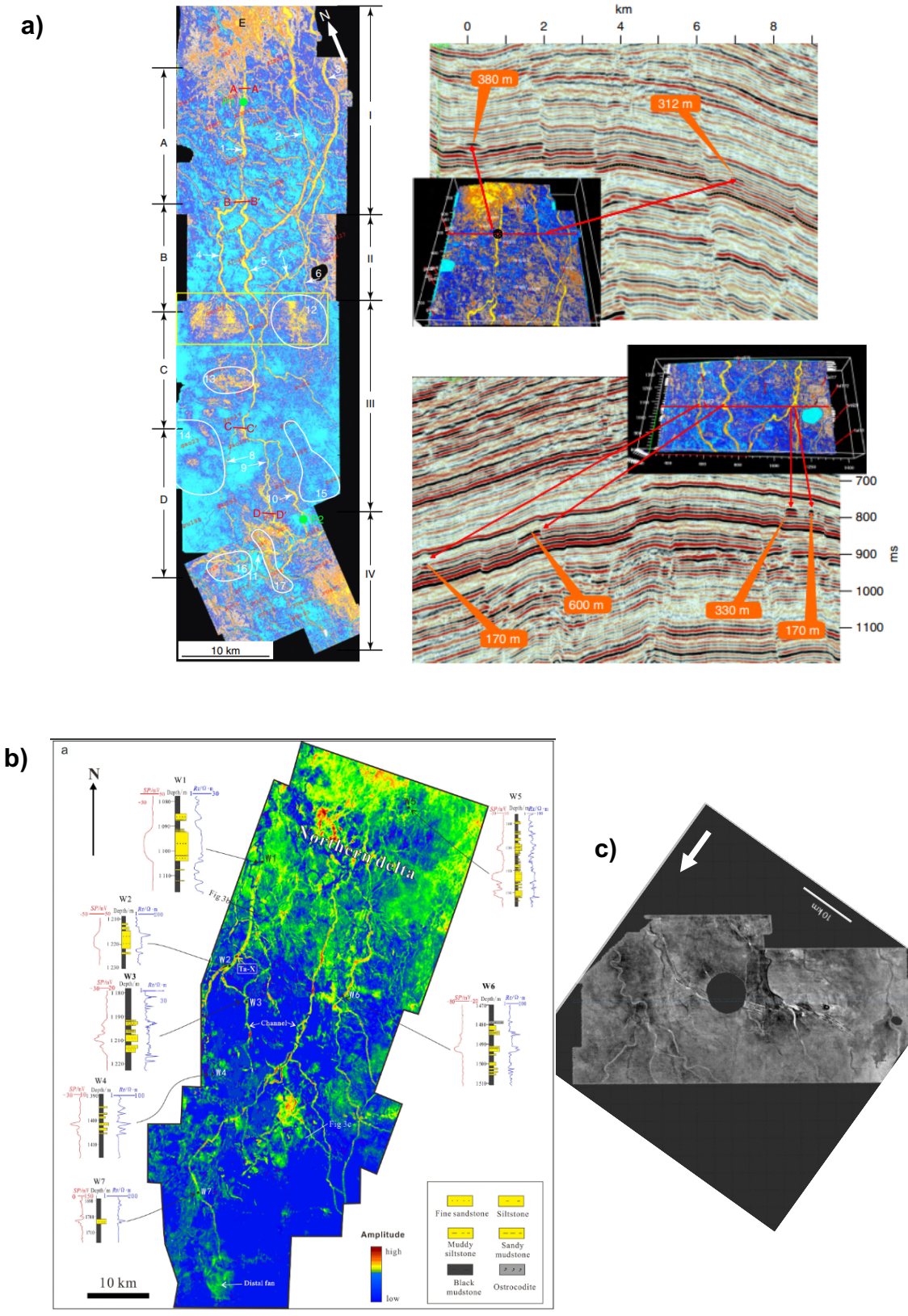


Figure 6.33: Seismic images a) and b) from the Songliao Basin, China showing deep-water turbidites and lobes in a similar depositional setting to the South Caspian Basin. From a) Zhi-Qiang (2010) and b) Pan (2020). c) RMS amplitude map taken from unit B of this study scaled to match the map in b).

6.5 Conclusions

The Pleistocene deep-water lacustrine channel network within the Shafag – Asiman area is controlled by seabed topography created during fold growth. Whilst the general orientation of the deep-water channels is controlled by changes in regional input but in the study area, the distribution of channels and the avulsion points are controlled by sea-floor topography created by the growing structures. Low channel densities occur on the crest of the dominant growing fold structure which changes through time, consistent with results interpreted from sediment accumulation indices. Areas of greater subsidence focus the channel elements into complexes, increasing total channel density and sinuosity. Although most channels are sourced from the Paleo-Amu Darya to the southeast and flow northwest – west, a brief switch in source direction occurs leading to south-westerly flow sourced from the northwest. Variation in entry point to the area are primarily caused by structures outside of the dataset however the switch to a north westerly source is caused by active tectonics or climate. The channel network analysed in this study shows that lacustrine deep-water channel systems have distinctive architectures which are different to marine deep-water systems, the channel network is dominated by isolated elements rather than channel complexes or larger systems.

7. Discussion

In this thesis I have explored the development of the Shafag – Asiman fold structure within the South Caspian Basin, both in terms of regional and local development, using novel sediment growth analysis and numerical modelling. I have then described the deep-water lacustrine turbidite channel network using exquisitely detailed amplitude maps imaged over the Shafag – Asiman fold structure and investigated the network interaction with the growing fold structures. In this chapter, I synthesise the novel findings of the thesis (section 7.1) and then investigate overarching themes that can be drawn from the discoveries presented (section 7.2, 7.3 and 7.4). Lastly, I suggest ideas for future work that could expand upon the research and findings presented in this thesis (section 7.5).

7.1 Summary of novel findings

I used high quality 3D seismic data to investigate the development of the Shafag – Asiman fold structure in the regional context of the South Caspian Basin. In Chapter 3, unusual fold growth patterns interpreted from detailed isopach maps records an anti-clockwise rotation of the Shafag – Asiman fold axis, captured in stages during the fold growth in the Pleistocene. The torqued axial plane of the fold structure was generated under transpressive dextral shear upon a thick weak shale detachment underlying the structures, which is required to facilitate the axial rotation. I integrated work completed by McCaffrey and Jolly (2007) to put the development of the Shafag-Asiman fold structure into the context of the regional tectonics of the South Caspian Basin. The Central Caspian region in which the Shafag-Asiman structure is located departs from the regions on the perimeter of the basin, by displaying no distinct orientation trend. Structures in the north of the region interpreted to be formed by constrictional deformation, in concordance with the transpressive dextral shear of the Shafag-Asiman structure, is caused by the relative southwest and northwest movement of the South Caspian Basin with respect to Iran and Eurasia respectively. Whilst the far field tectonics influences the fold growth, the location of the Shafag-Asiman fold structure is controlled by a deep basement fault.

In Chapter 4 I analysed the fold growth of the Shafag - Asiman structure using growth strata, applying the novel technique of sediment accumulation indices. By comparing the sediment distribution

across both fold structures, I demonstrated that the Shafag - Asiman fold structures vary in structural growth both spatially and through time. Whilst growth occurred during the Pliocene Productive Series, the major pulse of fold growth occurred during the Pleistocene deposition of the Absheronian turbidites. The dominant fold through the beginning of the Pleistocene is the Asiman structure. This then switched to the Shafag fold structure, which grew most through deposition of the Absheron Formation. However, in the uppermost interval, the Asiman structure appears dominant again. Channel analysis in Chapter 6 confirms the observations from the sediment accumulation indices in Chapter 4. Channels avoided areas of low sediment accumulation index (<1.2) on the crests of the fold structures, emphasising the alternating periods of influence on the seabed topography. The channel analysis also confirmed that the Shafag fold axis created seabed topography in a more east - west orientation early in the fold growth compared to the present-day fold structure, confirming the observations made in Chapter 3. Growth strata show that the fold structures are asymmetrical, with most sediment accumulation on the southern flanks, and that growth does not conform with classic geometrical models and buckle folding, suggesting there must be another important factor in the fold development.

The alternating growth of the Shafag – Asiman fold structures and contemporaneous mud volcano activity analysed within Chapters 4 and 6, offered evidence for the influence of sediment loading of a mobile shale during the development of the fold structures. In Chapter 5, I tested this hypothesis using 2D numerical modelling. I applied a model geometry based on a simplified adaptation of the Shafag fold geometry to test varying viscosity and porosity (for modelling density) parameters for the mobile shale. The results suggested that a viscosity value of 10^{18} Pa.s and a density value of 2169 kg/m^3 for the mobile shale produced the best match to a geologically realistic fold geometry. These values were input to a model that matched the geometry and sedimentation rate observed on the Shafag structure. Comparing sediment accumulation indices from the model with the Shafag seismic data validated the viscosity and density results. I also demonstrated how the distribution of sediment load across the fold is the dominant control on the growth of the structure. This is determined by the interaction of structural growth and sediment input.

In Chapter 6, analysis of the deep-water lacustrine channel network showed how the growing Shafag – Asiman structure controlled not only the channel distribution, but also channel characteristics

such as sinuosity and channel architecture. I demonstrated how highly sinuous, laterally migrating channel complexes occur up-dip of the fold structures during intervals with the highest fold growth. Straight, isolated channel elements occur down-dip of the fold structures, flowing into depocentres. The channel system is an element dominated system, that is comprised of individual channel elements up to 300 m in width. This contrasts with marine systems which form a hierarchy of channel elements, complexes and kilometre scale systems supplied from a single input point. I showed how the sediment supply to the Shafag – Asiman area is dominated by southeastern input from the Turkmenistan Shelf. However large-scale folds within the basin cause the channel entry point to change over time. A change in the location of sediment supply to the basin from the southeast to northeast occurs for a brief period, likely controlled by tectonic events or change in climate, which influenced the channel architecture.

I will now investigate cross-cutting themes that have arisen from the research chapters. Firstly, I discuss the influence and timing of sediment loading on the Shafag-Asiman fold growth and how this can be applied to other structures with the South Caspian Basin as well as basins globally. I then discuss numerical modelling of the fold structure and how models can be evolved based on the work presented within this thesis. Lastly, I will discuss the application of sediment accumulation indices for structural development and whether they can be used to predict deep-water sedimentary systems.

7.2 Influence of sediment loading on fold development

I have shown from regional analysis (Chapter 3) that fold location is controlled by deep basement faults and far-field tectonics. Further analysis of the Shafag-Asiman fold structure within the centre of the South Caspian Basin showed that fold growth is influenced by sediment loading of a mobile shale substrate (Chapter 5). Sediment accumulation indices show how the fold growth is not constant and highly complex where the fold structures do not display growth strata that is typical from simple kinematic models (Suppe et al., 1992, Hardy and Poblet, 1994, Hardy and Poblet, 1995, Poblet et al., 1997, Allmendinger, 1998, Cristallini and Allmendinger, 2001, Salvini and Storti, 2002). Whilst more evolved geomechanical modelling techniques that include finite element and discrete element modelling show that detachment fold growth is more complex than the simple kinematic models (Hardy and Finch, 2005, Guzofski et al., 2009, Vidal-Royo et al., 2012). Guzofski et al. (2009) model a fold in

the South Caspian Basin using 3D finite element models and demonstrate that the modelled fold also grows in a complex way, presenting results with both limb rotation and kink band migration. In this research I observe highly variable fold patterns both spatially and temporally. Initial fold geometries within the Post-Productive Series are broad with Shafag and Asiman appearing connected with symmetrical growth patterns. Through time, sediment thickening patterns indicate that the folds develop in a way that is not typical purely by shortening (Salvini and Storti, 2002) (Chapter 4) whilst also revealing the anti-clockwise rotation of the Shafag fold axis through time (Chapter 3). 2D numerical modelling demonstrates that mobile shale can cause increased growth of the fold crest due to inflation of the fold core (Chapter 5). The alternating dominant growth of the structures is highlighted by the relationship between channel density and the sediment accumulation indices (Chapter 6), proving that the growth and influence on the seabed topography alternates between the folds. I interpret the alternating fold growth of Shafag and Asiman to be due to the greater influence of mobile shale, with mud moving into the fold core and accelerating the fold growth.

Whilst sediment loading of the mobile shale may have a significant impact on the growth history of the fold structures, far field tectonics and basement structures control the fold location. In Chapter 3, I discuss how the fold orientations in the northern part of the deep-water South Caspian Basin, may be formed due to constrictional deformation, based on deformation models by Ghosh et al. (1995), as the effects of the two active plate movements of the South Caspian Basin relative to Iran and Eurasia act on the basin (Jackson et al., 2002, Copley and Jackson, 2006, Walker et al., 2021). The northeast – southwest trend of the Shafag - Asiman structure is perpendicular to the direction of the northwest – southeast shortening caused by the basin relative to Eurasia. Sediment accumulation indices reveal thinning over a northwest – southeast structure, either side of Shafag (Chapter 4) which is growing during the Pleistocene. Channels also show rotation towards the west on the northern limbs of the structures, due to seabed topography caused by the structure (Chapter 6). This structure may grow in response to the northeast - southwest shortening caused by the relative movement of the Iranian plate to the South Caspian, coincident with the dextral shear inferred from the fold axis rotation.

The interaction of Shafag – Asiman with the more subtle northwest – southeast trending structure causes round depocenters to form on the northern flank of Asiman and the southern flank of

Shafag (Chapter 4). Channel analysis (Chapter 6) shows the northwest – southeast trending fold focusses channels into the depocentres. At the top of the turbidite sequence, the Asiman fold structure becomes more dominant on the seabed than Shafag (Chapter 4 and 6; Unit E, Hz160 - Hz150). In the interval below this, the depocentre on the northern flank of Asiman contains a high density of channels and aggrading channel complexes (Chapter 4 and 6; Unit D, Hz150 – Hz140), which may indicate more deposition. More sediment load on the fold flank may subsequently force more shale into the Asiman fold core and cause the increased growth in the layer above (Chapter 5). This is plausible given that, in chapter 5, I have showed how the distribution of sediment across the fold can accelerate the rate of fold growth.

Timing of mobile shale movement under the Shafag-Asiman fold structure

After concluding that mobile shale influences Shafag-Asiman fold growth, the question arises as to how the mobile shale and sediment loading affects the fold growth through time. 2D numerical modelling in Chapter 5 demonstrated how the Oligo-Miocene Maykop Formation can act as a mobile shale and influence fold growth through sediment loading, under the assumption that the shale had reached the critical point during fold formation (Soto et al., 2021a), likely due to hydrocarbon generation. The model results show how the visco-plastic Maykop shale can cause a tighter fold crest with a steeper fold limb forming than if the shale was elasto-plastic and did not inflate the fold crest. Therefore, when the shale begins to move into the fold core under the influence of the sediment load, there may be a change in the fold geometries compared to if the fold was controlled purely by shortening and basement structures (Salvini and Storti, 2002). Sediment accumulation indices presented in Chapter 4 show that the Shafag – Asiman fold crests had a change in fold geometry during the Hz130 – Hz120 interval, with the fold crests becoming tighter, similar to numerical modelling results when the mobile shale inflates the fold core. En-echelon crestal normal faults along the fold crests have the most syn-kinematic deposition within the Hz130 – Hz120 interval (Chapter 3 and 4), concurrent with the greatest amount of anti-clockwise rotation of the fold axis, which requires mobile shale in the fold core to act as a free surface (Chapter 3). The growth rate of the Shafag fold crest significantly increases during interval Hz130 – Hz120 and is the interval within the Absheron Formation with the highest growth rate (Chapter 4).

Numerical modelling results in Chapter 5 show that mud begins to move into the fold crest between 2.5 Ma – 1.5 Ma, coinciding with deposition of the early intervals of the Absheron Formation, which started approximately 2.13 Ma (Lazarev et al., 2019, Lazarev et al., 2021, Vasiliev et al., 2022) – 1.8 Ma (Green et al., 2009). Assuming a constant sedimentation rate through the Absheronian, deposition of the Hz130 – Hz120 interval occurred approximately 1.8 Ma – 1.5 Ma, coinciding with the timing of mud movement into the fold core taken from the numerical modelling results (Chapter 5). Therefore, I propose that the changes observed within the Hz130 – Hz120 are due to the initiation of mobile shale moving into the Shafag fold core during this time.

The timing may also coincide with a pulse of active tectonic activity due to the relative westward movement of the South Caspian with respect to Iran, which occurs since approximately 5 Ma - 2 Ma (Axen et al., 2001, Allen et al., 2004, Cifelli et al., 2015, Walker et al., 2021), since modelling results show that an increase in shortening can accelerate the rate in which mobile shale can flow into the shale core (Chapter 5). The timing documented for the westward motion of the basin relative to Iran are based on fault data from within mountain belts surrounding the basin, therefore the shortening effects of the relative westward plate motion may be delayed in the centre of the basin where Shafag – Asiman is situated and is therefore observed later than in the mountain belts.

Application to other South Caspian Basin folds

A question that now arises is how applicable are the results from Shafag – Asiman to the wider South Caspian Basin? The results that I have presented suggest certain conditions are required for sediment loading to influence the fold growth. Numerical modelling results presented in Chapter 5 show how the influence of sediment loading on the fold growth is dependent on the interaction between sediment input and shortening and the distribution of sediment over the fold structure. Structures towards the edge of the basin, in the Talysh and ACG areas as well as the Alov domain in the south are more likely to be affected by shortening than within the central part of the basin (Chapter 3). Numerical models run with greater shortening rates relative to sedimentation rate show final fold geometries that resemble a symmetrical box fold with a flat crest, as more mobile shale is forced into the fold core. This resembles the geometry of the fold structure described by Santos-Betancor and Soto (2015) in the

Talysh domain, in the west of the basin (figure 7.1). The authors suggest that mobile shale inflates the fold core and increases the fold growth. The sedimentation rate of the Post-Productive Series within the numerical model is higher than over the Talysh fold, causing the greater sediment thickness within the model result. However, this highlights the importance of the ratio of shortening to sedimentation rate on the fold growth as seen from the model results and can have a significant effect on the real-life geometry of folds.

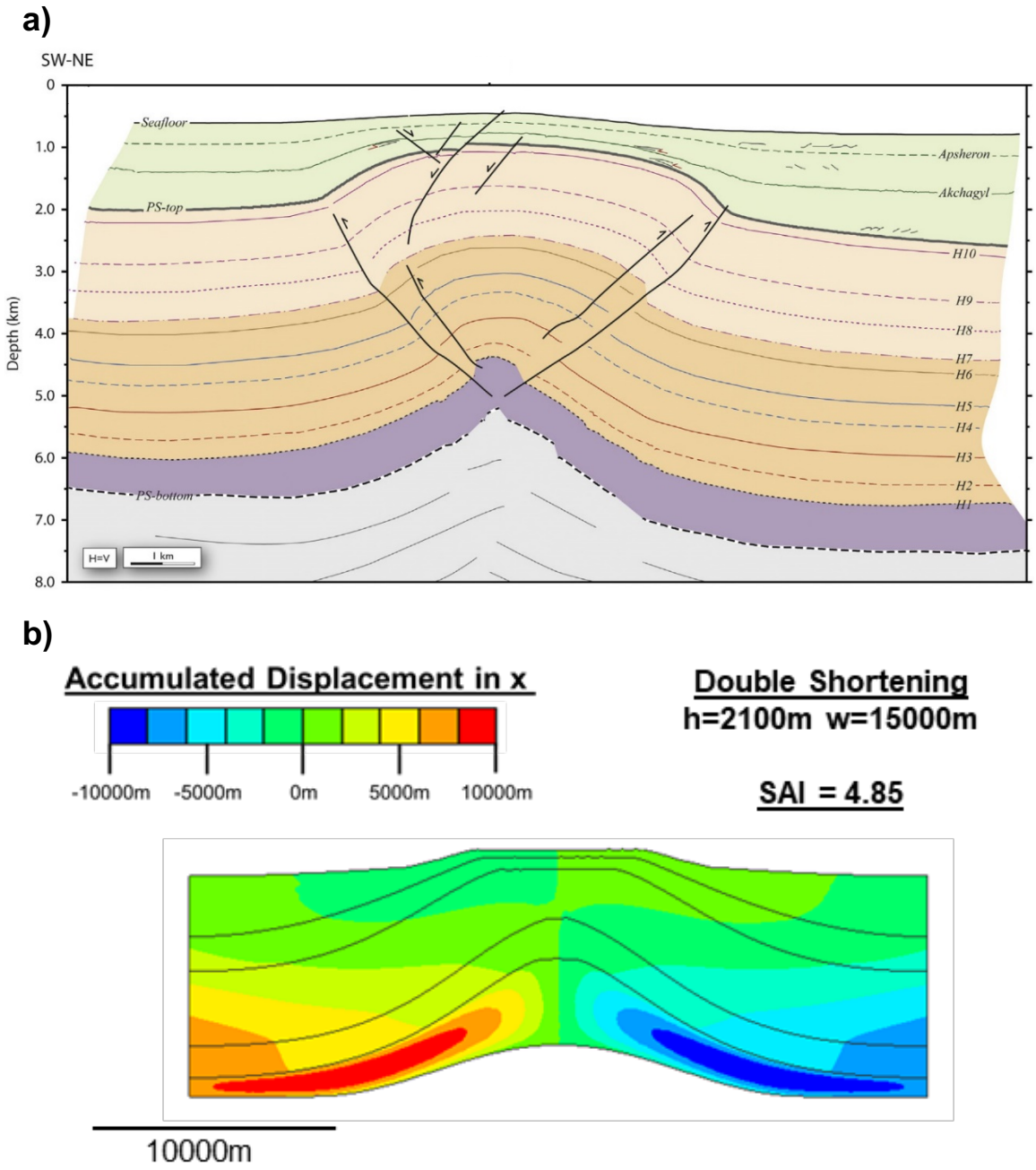


Figure 7.1: a) interpretation of a seismic section of a fold structure in the west of the South Caspian Basin from Santos-Betancor and Soto (2015) and comparison with b) numerical model with double shortening from chapter 5 showing similar fold geometries.

Whist the location within the basin has a significant impact on the magnitude of shortening on the structures, the location of a fold structure within the basin also impacts the thickness and distribution of sediment on a structure. The Absheron Formation shows significant overlap onto Shafag – Asiman, whereas in the folds within the Talysh, ACG and Alov areas, the stratigraphy over the structures is thinner and there is more onlap onto the fold crests. The Shafag – Asiman structure receives more sediment as it is the centre of the basin and, as I have shown in Chapter 6, receives sediment from the southeast. Folds in the west of the basin may receive sediment deposited from the Palaeo-Kura River in the west, which may alter the distribution of sediment across the folds.

The varying influences on fold growth within the basin can affect the timing of mud movement into the fold core (Chapter 5). The timing, therefore, is likely to be different for each fold in the basin. In salt tectonics, the salt accelerates into the fold core when buoyancy effects take place, this occurs when the seabed gradients are greater than 1/5 of the salt layer gradient (Waltham, 1997). Buoyancy also affects mobile shale (Brown, 1990) may be even more significant than salt (Hudec and Soto, 2021) since densities of the mobile shale can be lower than that of salt, which stay fairly constant at 2200 kg/m^3, as it is incompressible (Hudec and Jackson, 2007). Increased shortening rates lead to a steeper gradient on the flank of the mobile shale layer than the seabed allowing for buoyancy effects to accelerate shale into the fold core, which causes the large fold growth in the double shortened model. Lower shortening rates, as seen at Shafag-Asiman, causes the movement of shale into the fold core to be too slow to allow buoyancy effects to take place. Santos-Betancor and Soto (2015) and Sánchez-Borrego et al., (2016) suggest that in the fold in the west of the basin, mobile shale inflated the core of the fold during the Pliocene, in the Productive Series. The effects of the tectonic shortening are greater for this fold than the Shafag – Asiman fold in the centre of the basin, and possibly forced the shale into the fold core at an earlier time than the Shafag-Asiman structures. Folds on the western and eastern edges of the basin, which are more affected by shortening than in the centre of the basin, are likely to have mobile shale inflating the fold core at an earlier time to Shafag – Asiman, assuming that the Maykop Shale is mobile at each fold structure.

Application to folds globally

A seismic section trending northeast – southwest across the South Caspian Basin (Bertello et al.) gives a total shortening of 14%. This is relatively low compared to other fold belts with a mobile shale detachment, for example, Niger Delta up to 26% (Pizzi et al., 2020) and NW Borneo 17% (Morley, 2009). Fold belts such as the Pyrenees and Zagros show shortening of 20% or more (Muñoz, 1992, Beaumont et al., 2000, McQuarrie, 2004). Shortening within the South Caspian Basin appears to be relatively low when compared to other fold belts in the world, as shown by the fold wavelengths observed within various salt and shale tectonic basins (Morley et al., 2011) (figure 7.2). The fold wavelengths of the South Caspian Basin have a wider range and mean of fold wavelengths than any other folds in deep water fold thrust belts (figure 7.2).

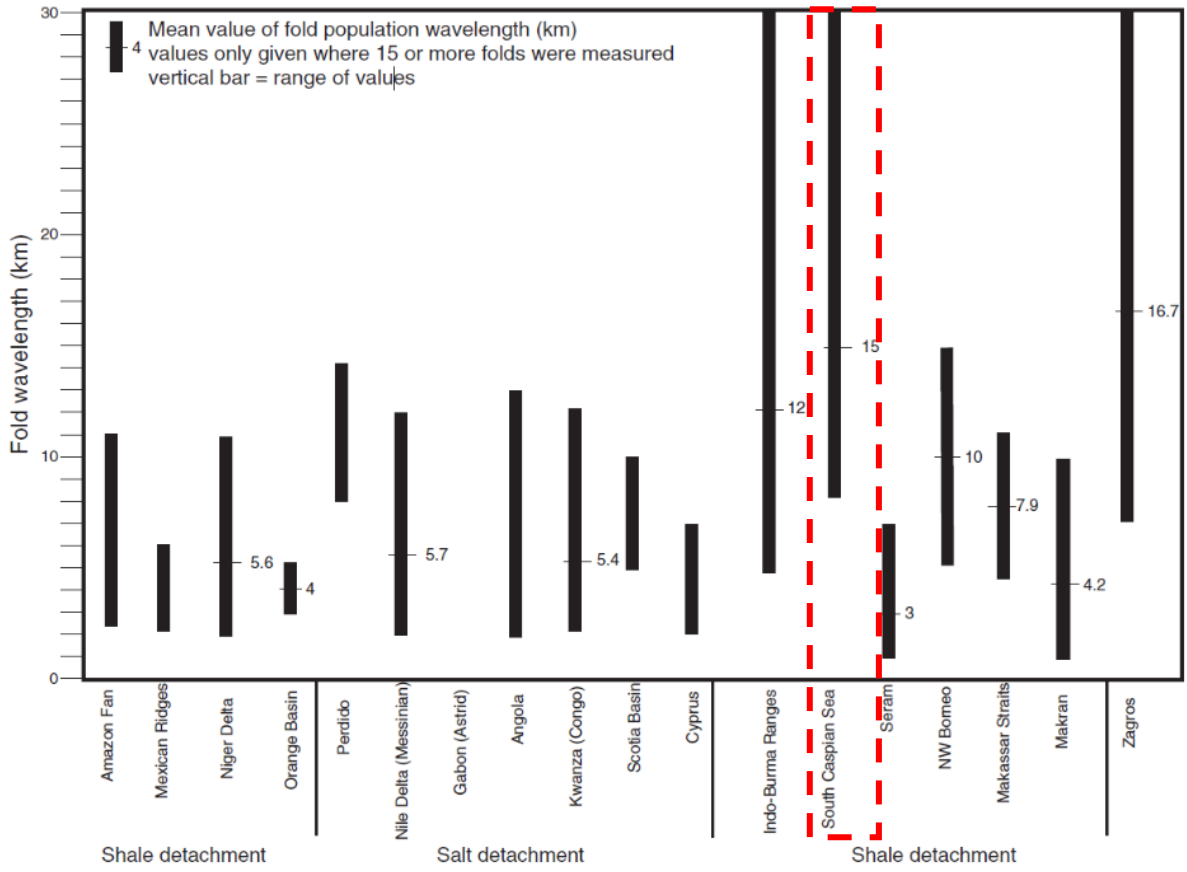


Figure 7.2: Fold wavelengths found within deep-water fold and thrust belts, including both salt and shale detachments. The Zagros Mountains are for comparison with an orogenic fold and thrust belt. The South Caspian Sea Basin is highlighted in red and contains the largest mean fold wavelenth of all fold belts included..From Morley et al. (2011).

Although the range of fold wavelengths of the Mexican Ridges fold belt in the west of the Gulf of Mexico are small in comparison to the South Caspian Basin (figure 7.2), the total shortening is documented to be similar to the measurement of shortening for the South Caspian Basin, up to 15% (Yarbuh and Contreras, 2017). The Mexican Ridges fold belt contains a thick sediment package and although not as thick as in the South Caspian Basin, the section still reaches 5 km thick. The stratigraphic thickness is high relative to the fold wavelength compared to other fold belts (figure 7.3). Therefore, sediment loading of the mobile shale during fold growth may be similar to that interpreted at Shafag-Asiman. Fold and thrust belts with lower stratigraphic thickness compared to fold wave lengths within fold belts with higher percentage shortening may show fold development similar to the numerical models of high shortening and folds on the perimeter of the South Caspian Basin.

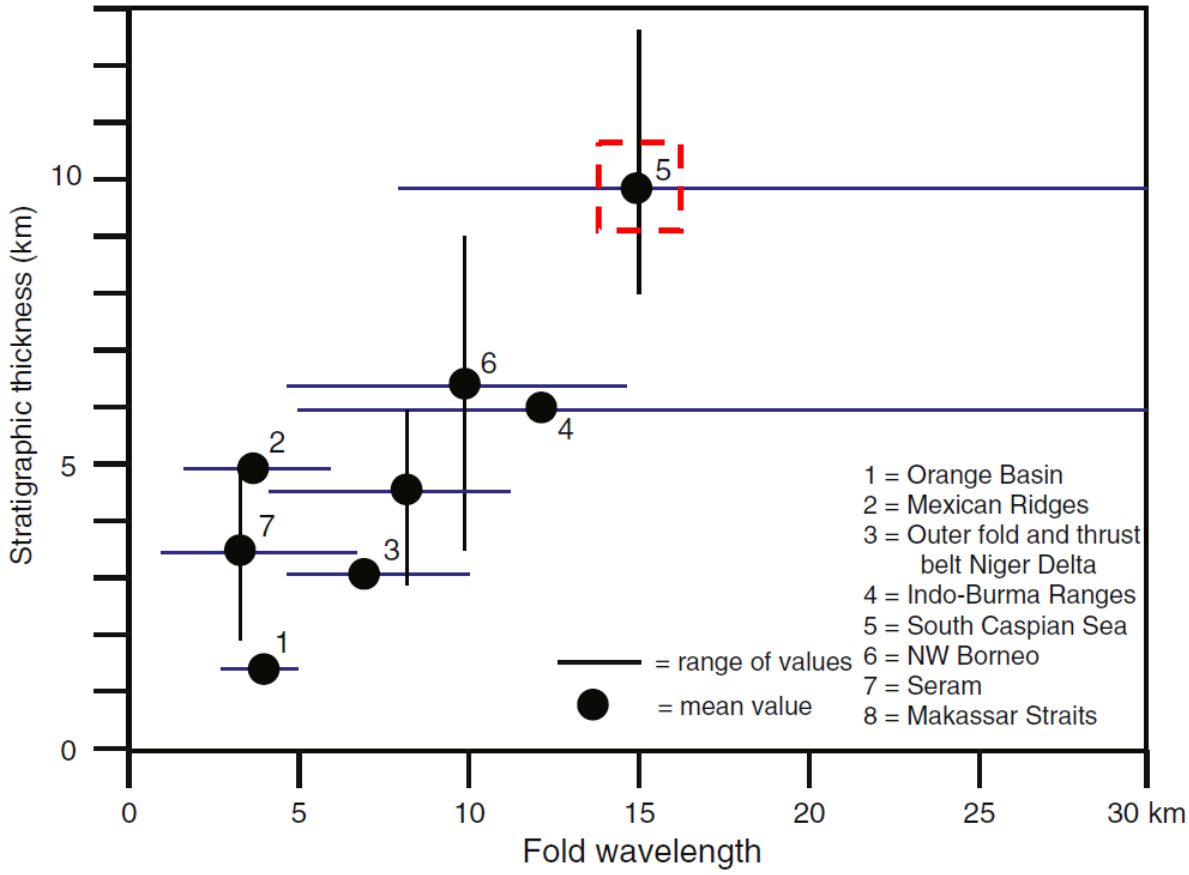


Figure 7.3: Fold wavelength vs. stratigraphic thickness for a range of deep-water fold and thrust belts. The South Caspian Basin is highlighted in red and shows both the highest fold wavelengths and stratigraphic thickness. From Morley et al. (2011).

I have discussed how the timing of mud movement into the fold core of the Shafag – Asiman fold structure occurs within the Absheron Formation, indicated by a change in fold geometry, increased

fold growth and dextral shear and rotation of the fold structure. By analysing the fold structures within the basin in the same way as I have described in this thesis, it may be possible to observe the timing of the movement of shale into the fold core of other structures within the basin and fold belts with a shale detachment. Creating isopach maps and using sediment accumulation index maps can show a change in fold geometry as well as any potential fault growth on the crests of the structures coinciding with acceleration of fold growth and inflation of the fold core.

7.3 Evolving numerical models of fold growth in the South Caspian Basin and beyond

Two-dimensional numerical modelling results reveal that inflation of the fold core due to mobile shale causes the acceleration of fold growth (Chapter 5). Feedback is created in which there is an acceleration of the mobile shale into the fold core, increasing shale withdrawal on the limbs and subsequently increasing the amount of sediment load on the limbs, which in turn forces additional mud into the fold core. Within the numerical models, feedback causes fold growth to accelerate through time. A comparison of sediment accumulation indices within the Post-Productive Series shows the potential acceleration of fold growth, however, whilst the mass transport deposits have highs sediment accumulation indices, they cannot be directly compared to the lacustrine turbidites since they are deposited differently to the turbidites and have not been studied in any detail. However, during the deposition of the turbidite sequence, the sediment accumulation indices did not indicate an acceleration in fold growth throughout the deposition of the sequence. The highest rate of fold growth during the interval is interpreted to be during interval Hz130 – Hz120, within the lower part of the turbidite sequence. The indices then decrease through the younger intervals. The numerical models were set up to provide a simple view of the impact of sediment loading on a mobile shale substrate during fold growth. The model is created as a two-dimensional symmetrical fold with the mobile shale modelled as a visco-plastic layer, with no change in viscosity or density through time. In reality, the movement of the mobile shale beneath the Shafag and Asiman fold structure will vary through time, even after the

critical point is reached and the shale becomes mobile, due to the complex three-dimensional nature of the structures.

The two-dimensional numerical models have plane-strain, where shale only moves towards and away from the fold core in one plane, in reality the shale will move in and out of the plane, evidenced by the dominant growing structure changes through time (Chapter 4). The movement of shale in and out of the plane of the two-dimensional section of a mud-cored fold in the South Caspian Basin is also suggested by Santos-Betancor and Soto (2015). This implies that the mobile shale may not constantly accelerate into the fold core, as the results of the modelling imply. Another potential influence on the shale properties through time is the release of overpressure and decrease in shale volume through the eruption of mud volcanoes. Within the Shafag-Asiman structure there is one large mud volcano between the fold crests, which has evidence for activity during the mid Absheron to the present-day (Chapter 4). There are also two buried mud volcanoes, one which was extruded during Productive Series times and one during the Absheron (Chapter 4). The eruption of mud volcanoes may release the overpressure within the mobile shale and subsequently cause fluctuations in the density and viscosity of the shale, which in turn may lead to punctuated fold growth. The evacuation of mud also creates depocentres for sediment deposition, which will alter the distribution of sediment over the fold and therefore alter the sediment loading of the mobile shale.

Shortening within the numerical models was input as one horizontally applied stress, with a constant shortening rate through time. The development of the Shafag-Asiman fold structure is formed under a more complex tectonic configuration than has been applied within the numerical models. As discussed within Chapter 3, Shafag-Asiman is formed under the influence of two active plate motions during the Pleistocene, which causes dextral shear of the structures. Two simultaneous directions of applied shortening provide a much more complex and dynamic shortening history than is applied within the numerical models. Modelling results show that increasing or decreasing the shortening rate can have a significant impact on fold growth and the volume of mud moving into the fold core. With two directions of applied horizontal shortening, it is possible that the direction and magnitude of maximum horizontal shortening is punctuated. This may be what causes the fold growth to increase or decreases

between intervals, however, this is difficult to conclude without further modelling of the complex nature of shortening within the South Caspian Basin.

The turbidite channels within the Absheron Formation are supplied to the Shafag-Asiman fold structures from the southeast (Chapter 6). The modelled syn-kinematic sediment is input as a symmetrical blanketing of sediment over the fold structure, rather than modelled as a more realistic asymmetrical input with sediment flux entering from one side. The thickest package of sediment is on the southern limb of Shafag (Chapter 4). A higher concentration of channels occurs on the southern flanks of the folds through most of the section (Chapter 6), including channel complexes displaying aggradation. Aggradation implies an increase in sediment deposition (Kolla et al., 2007). Therefore, more channel complexes on the southern limbs of the folds likely indicates more sediment deposition of the southern limbs of the folds, increasing the effect of sediment loading and shale movement into the fold core. Whilst the mass transport deposits of the Bakunian have not been studied in detail, sediment accumulation indices show that they infill the fold flanks, with thickness on the flanks varying significantly between the intervals (Chapter 4). The variable distribution of the deposits will create a difference in the overburden thickness across the fold structure, causing a significant impact on fold amplification as inferred from modelling results (Chapter 5).

The numerical modelling results achieved the initial aims of understanding the influence of sediment loading on fold growth of Shafag – Asiman and to understand the properties of the mobile shale layer. The models were based on a simple model geometry and did not incorporate the complexities of the Shafag – Asiman fold discussed above. The modelling results could be enhanced by more accurately matching the realistic conditions under which the fold grew. A three-dimensional model set up would allow for results that match the Shafag-Asiman fold structure more accurately. The two active tectonic regimes could be incorporated into a three-dimensional model and introduce the strike-slip aspect on the fold growth. The mobile shale could also move in and out of the plane, unlike the two-dimensional model and potentially highlight the alternating dominant growth between the two structures. Asymmetrical sedimentation could be applied within a three-dimensional model, incorporating the change of sediment input directions that have been presented in the channel analysis (Chapter 6) and the mass transport deposits (Chapter 4). The three-dimensional model should also

include hydrocarbon generation and overpressure allowing for a more realistic development of the mobile shale through time. The results of the two-dimensional models are based on a visco-plastic shale layer that does not change or evolve through time. In reality, the properties of the shale layer will change through fold development, with pore pressures increasing with increasing overburden deposition as well as hydrocarbon generation. Within the models, the Maykop shale is modelled as a visco-plastic material from that start, however, the shale likely became mobile at a later time than this, with evidence of mud volcanism during the middle of the Pliocene Productive Series (Chapter 4). The overpressure may also be reduced by the evacuation of mud in the form of mud volcanoes, stopping the shale from flowing by reducing strength (Soto et al., 2021a). The large mud volcano developed on the seabed may not be sourced from the Maykop shale, however, and may be sourced from the Surakhany Formation, as shown by the thinning of the formation within the seismic data (Chapter 4). This is also observed on a large mud volcano in the northeast of the basin (Blouin et al., 2019). The two extinct mud volcanoes at Shafag – Asiman may have reduced the pressure within the Maykop shale as this was likely the source for the mud volcanoes. Implementing mud volcanism into three-dimensional models may aid the understanding of how the properties of the Maykop shale changes and evolves through time.

7.4 The application of sediment accumulation indices on structural development and turbidite architecture

In this thesis, I have used the novel technique of sediment accumulation indices to analyse the fold growth and relationship with lacustrine turbidite channels. The relative fold growth between the Shafag and Asiman fold structures (Chapter 4) is supported by the channel density (Chapter 6), showing that the relative fold growth shown by the sediment accumulation indices is valid. The method may be applied to other folds within the South Caspian Basin, to determine the fold growth history within the

Pleistocene to recent times, where high sedimentation rate relative to fold growth rate creates overlap of the sediments onto the fold crest.

The seismic dataset used in this thesis beautifully displays the lacustrine turbidite channels, allowing me to interpret the channel network and channel architecture fully. I compare the channel network to the sediment accumulation indices with results indicating a correlation between the two, shown by the channel density as well as sinuosity and avulsion points (chapter 6). I have shown that sinuous, channel complexes are located in areas where the sediment accumulation indices are highest, in both space and time. The complexes are located within intervals that have the highest fold growth and preferentially form in the depocentres, where indices are highest. The complexes aggrade, increasing deposition relative to single channel elements. More deposition into the depocentres may create feedback whereby mobile shale evacuation into the fold core allows for larger depocentres, more deposition of aggrading channel complexes and subsequently more mobile shale withdrawal and inflation of the fold crest. These concepts can be proposed due to the high-quality images of the channels. For datasets with a lower resolution than the seismic dataset used in this research, sediment accumulation indices may provide a way to estimate the likely channel network and architecture for folds structures actively growing in an environment with high sedimentation rates. Within the Shafag – Asiman dataset, I see that the highest channel sinuosities, channel densities and the most channel complexes occur where the sediment accumulation indices are relatively high. By creating isopach maps and subsequent sediment accumulation index maps across a fold structure, the areas with higher channel density and channel complexes may be inferred.

The use of sediment accumulation indices is most appropriate on folds similar to Shafag – Asiman, low amplitude detachment folds with overlapping sediments. Appropriate folds to be examined are located within the centre of the South Caspian Basin, where significant overlap of the Absheron Formation occurs. Examples of this within the basin are on the Absheron (figure 7.4a) and Shah Deniz (figure 7.4b) fold structures, both in the deep-water basin to the north of Shafag – Asiman. These fold structures are appropriate to test whether the same link between sediment accumulation and channel

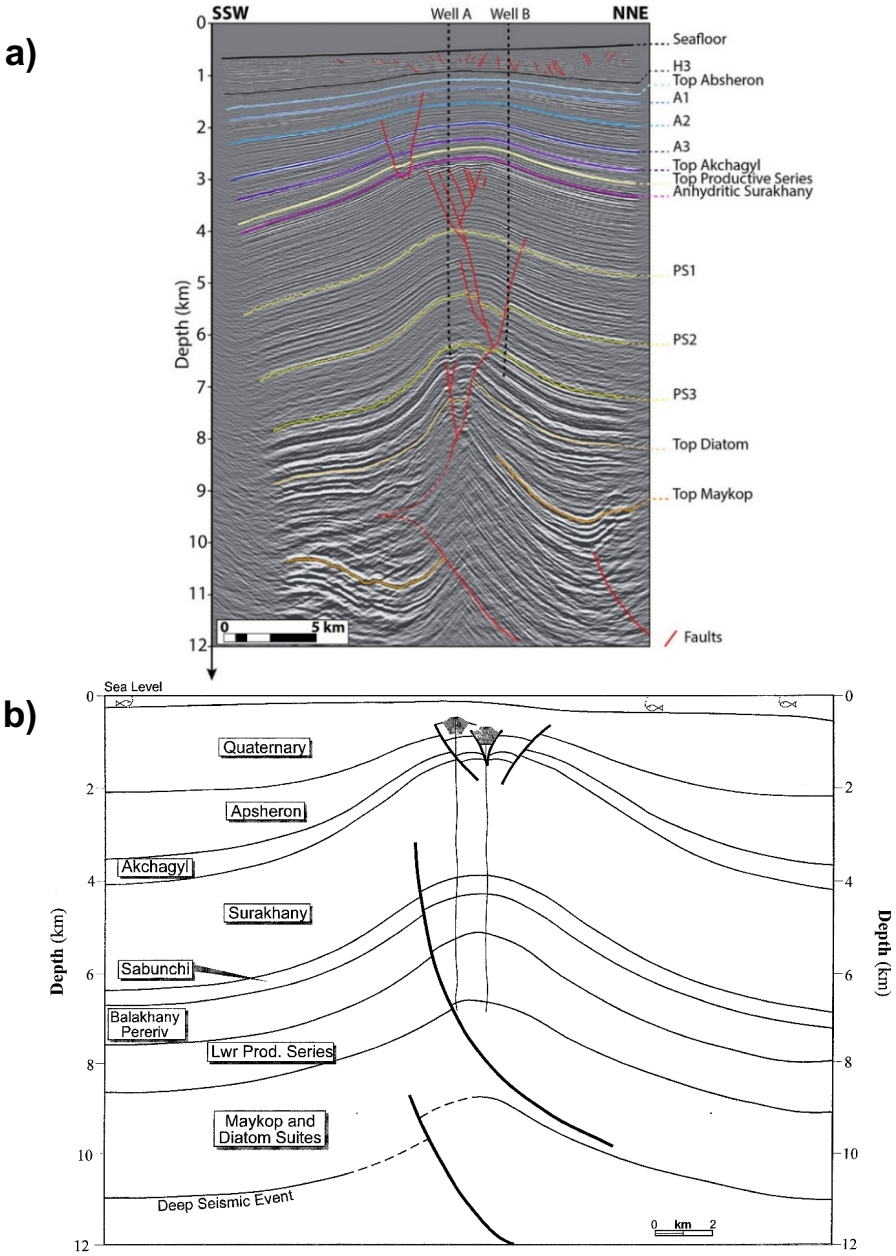


Figure 7.4: a) Seismic section through the Absheron fold from Blouin et al. (2019) and b) an interpretation of a seismic section through the Shah Deniz fold from Fowler et al. (2000). Both structures are in the deepwater part of the South Caspian Basin, to the north of the Shafag-Asiman fold structure and have similar overlapping strata of the Absheron and are therefore ideal structures to implement and replicate the methods used within this thesis.

characteristics occurs, since 3D seismic data has been shot over the structures previously and they both have thick turbidite sections of the Absheron Formation.

Sediment accumulation indices and subsequent channel characteristic analysis can be applied to folds other than Shafag-Asiman in the South Caspian Basin since they are developed within the same stratigraphic and tectonic framework. The question arises as to whether the method can be applied to

other basins in the world. Detachment folds with low amplitudes and overlapping syn-kinematic strata are observed in seismic data in numerous basins around the world (Contreras, 2010). The detachment level of the low amplitude structures can either be salt such as in Santos and Campos Basin, offshore Brazil (Demercian et al., 1993) or, as within the South Caspian Basin, mobile shale such as the Mexican Ridges fold belt in the western Gulf of Mexico (Yarbuh and Contreras, 2017). In both the Santos Basin and Mexican Ridges fold belt, the low amplitude folds are symmetrical and overlapped by turbidite deposits (figure 7.5). Both fold belts are located within deep-water marine environments, rather than a lacustrine setting as within the South Caspian Basin. Although I have suggested that deep-water marine and lacustrine turbidite environments differ (Chapter 6), sediment accumulation indices measured in the syn-kinematic strata may still indicate relative fold growth rates and the relationship with channel characteristics.

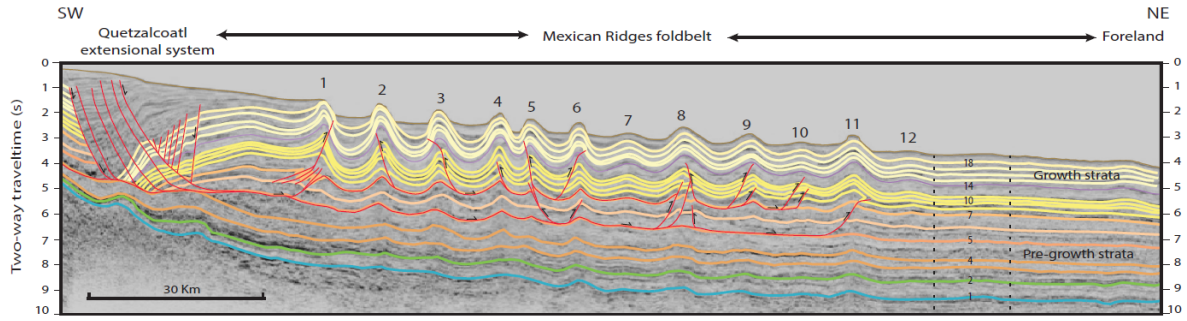


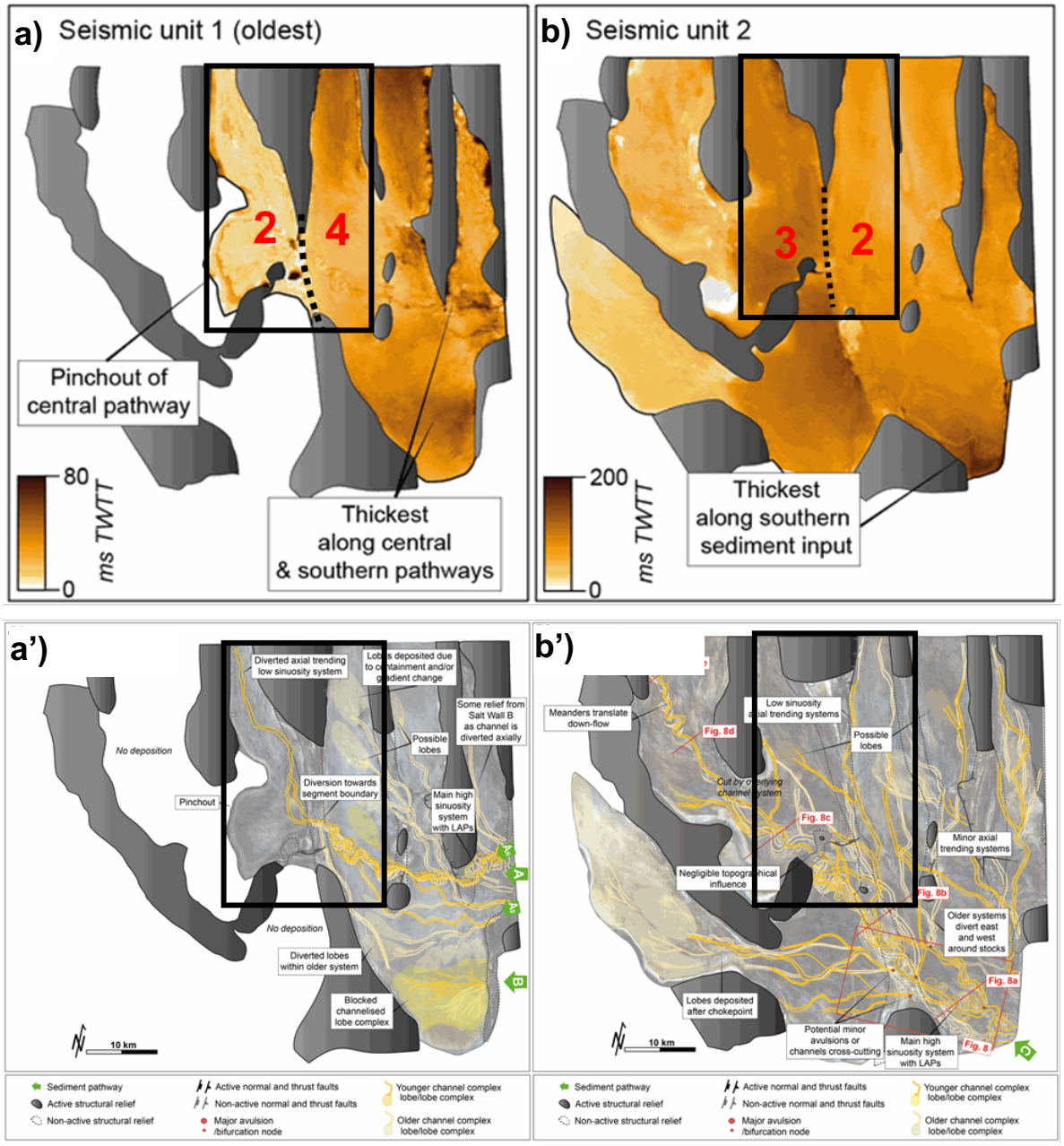
Figure 7.5: Seismic section through the Mexican Ridges fold belt showing overlapping growth strata across the fold belt. Fold structures on the north-eastern extent of the belt appear to look similar to the Shafag-Asiman fold structure, however, the fold wavelengths are narrower in the Mexican Ridges fold belt. From Yarbuh and Contreras (2017).

Whilst salt and mobile shale have different intrinsic properties and will have different structural deformation responses, growing salt or mobile shale cored anticlines will both cause seabed topography that will control deep-water channel paths (Mayall and Stewart, 2000, Clark and Cartwright, 2009, Mayall et al., 2010, Clark and Cartwright, 2011, Jones et al., 2012, Jolly et al., 2016, Don et al., 2020, Pizzi et al., 2021, Mitchell et al., 2021a, Mitchell et al., 2021b). An example of this is from the Kwanza Basin in offshore Angola (Howlett et al., 2021).

Howlett et al. (2021) interpret a high-density channel network, with many channels deflected around salt walls. However, the dataset includes salt cored anticlines of which turbidites overlap. The authors suggest that an increase in sediment accumulation causes small scale diversions, less than 5 km,

around structures as well as causing avulsion along structural highs, similar to the observations that I have made within the Shafag – Asiman dataset. The dataset interpreted by Howlett et al. (2021), is on a much larger scale than the Shafag – Asiman dataset used within this thesis, covering 3,500 km^2 compared to 1,660 km^2. However, by investigating the relationship between sediment thickness and channel architecture over a salt cored fold crest, I can compare the sediment accumulation indices and channel interpretations with my results at Shafag – Asiman. I have approximated sediment accumulation indices based on isochron maps from four units above a salt cored anticline from within the interpretations of Howlett et al. (2021) (figure 7.6). The indices show that seafloor topography due to the growing salt core was highest in the oldest unit and lowest in the oldest unit, agreeing with the authors interpretations. The most evolved and sinuous channel complexes occur where the sediment accumulation index is highest, in seismic unit 1. The channels become less sinuous on the down-dip flank, similar to my observations at Shafag – Asiman. Again, within unit 2, the complexes are most evolved in the area with the highest sediment accumulation index, on the eastern flank. By unit 3, the seabed topography is relatively lower and the sediment accumulation indices in this interval are lower than the previous two units (figure 7.6). The channel complexes are more sinuous and more evolved on the flank with the highest sediment accumulation indices (figure 7.6), than on the flank with the lower index, where the channels become straight and deposit lobes. As the salt core becomes inactive, the indices become 4.0, as shown in unit 4, since the area becomes a depocenter for a different growing structure to the west, and large channel complexes are present. The observations from the work of Howlett et al. (2021) are consistent with the observations that I have made on the Shafag – Asiman area, showing that the link between sediment accumulation indices, structural growth and channel architecture may be applicable in other areas of syn-kinematic turbidite deposition.

In both the work within thesis and the work of Howlett et al. (2021), there are no age data for the intervals. Age data allow for normalisation of isopach maps and the creation of sediment accumulation rate maps (Doughty-Jones, 2014, Pizzi, 2019). Sediment accumulation rate maps can be used to compare intervals qualitatively. Sediment accumulation index maps allows for a semi-qualitative comparison in space and time when there are no age data available. Indices can also be used to evaluate relative growth strata patterns from isopachs between mapped surfaces that have assigned



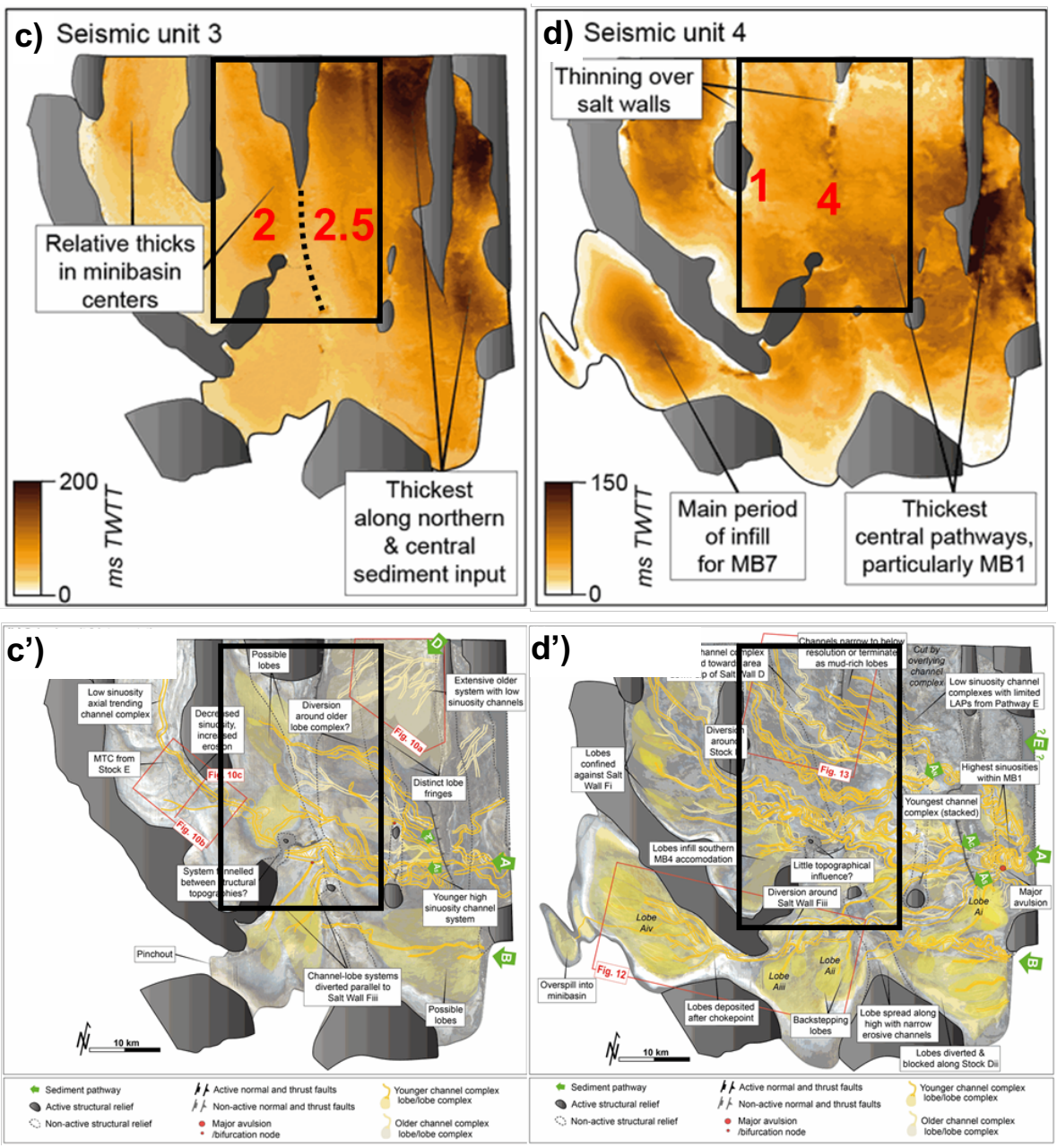


Figure 7.6: Isochron maps (a, b c and d) and corresponding channel interpretations (a', b', c' and d') for seismic intervals 1 (a and a'), 2 (b and b'), 3 (c and c') and 4 (d and d') from Howlett et al. (2021). A growing salt cored topographic high is highlighted in a black box. I have calculated sediment accumulation indices from the isochron maps based on the thin value on the crest of the salt cored structure. Indices are shown in red. The sediment accumulation indices show the relative growth of the structure as well as showing that high indices coincide with highly sinuous channel complexes and lower indices coincide with low sinuosity complexes, similar to what I have observed at Shafag-Asiman.

ages. Within the Absheron turbidite succession overlapping the Shafag – Asiman fold structure, a sediment accumulation index of <1.2 on the crest suggests there was seabed topography at the time. This value could be used to show seabed topography during the development of other folds.

7.5 Future Work

The interpretations and themes discussed within this thesis have introduced ideas and concepts that can be evolved and progressed further. Below I describe ways in which they could be developed further.

Future numerical modelling of mobile shales

As discussed in section 7.3, numerical modelling of the Shafag – Asiman fold structure should be developed into a three-dimensional model incorporating:

- Two active shortening directions to create dextral shear.
- A critical state model applied to the visco-plastic shale layer whereby shales would flow once sheared to the critical state
- A coupled model in which pore pressures increase during increased shortening, rapid sediment loading and subsequent hydrocarbon generation.
- An asymmetrical sediment input direction.

Just as I compared two-dimensional modelling results with two-dimensional sediment accumulation indices, three-dimensional model results could be supported by comparison to sediment accumulation index maps. Results such as timing of dextral en-echelon normal fault growth, alternating dominant growth of the fold crests and potential mud volcano formation could be compared with index maps. Results from three-dimensional models would allow for more accurate timing of shale inflation of the fold core than is given by the two-dimensional modelling results.

I have proposed that at the Shafag – Asiman fold structure a mobile shale viscosity of 10^{18} Pa.s and a density of 2169 kg/m^3 (based on a porosity of 30%) provides the most realistic result for the mobile shale underlying the fold. Modelling of other fold structures in the basin using these material properties would be an interesting future study, to observe whether the properties produce realistic fold growth histories and geometries. A catalogue of fold geometries could be produced using varying amounts of shortening and sedimentation rate to predict fold growth histories as well as the potential properties of the mobile shale below a fold in the basin. Analysis could then be extended beyond the

South Caspian to determine whether the shale properties are applicable to other basins, potentially starting with the Mexican ridges fold belt for reasons discussed above.

Mass transport deposits over the Shafag-Asiman fold structures are imaged in high-quality within the seismic data. Whilst analysis was out of the scope of this thesis, determining the direction and origin of each mass transport deposit would aid with modelling. Understanding the source direction would allow for the deposits to be input into the models from the direction they are sourced from.

Further use of sediment accumulation indices

I have introduced sediment accumulation indices for use in understanding fold growth through time as well as the relationship with the channel network at Shafag - Asiman. This method should be applied to other folds in the South Caspian Basin using 3D seismic datasets to determine timing of fold growth and potential inflation of the fold core with mobile shale. Fold rotation and crestal fault activity should also be analysed using isopach and sediment accumulation index maps within the Post-Productive Series on other folds in the basin to compare with the observations that I have made at Shafag – Asiman.

The relationship between the channel network and the sediment accumulation indices should be analysed to determine whether channels avoid structures with low sediment accumulation indices, for example at Shafag – Asiman channels avoid structures where indices are less than 1.2. The channel network should also be analysed to determine whether the relationships of channel density, channel sinuosity and avulsion points have the same relationship as at Shafag – Asiman. If the same relationships are observed, this can also be extended to other basins, with the channel network within the salt influenced Kwanza Basin interpreted by Howlett et al. (2021) appearing to display similar relationships to my interpretations at Shafag – Asiman. Fold belts such as the mobile shale influenced Mexican ridges fold belt would also be good to analyse to determine whether the methods and principles can be used in actively growing fold belts around the world.

Lacustrine channel network within the South Caspian Basin

I have meticulously interpreted the Pleistocene deep-water turbidite channel network of the Shafag-Asiman area, in the deepest part of the South Caspian Basin. Whilst I have been able to infer the potential influence of structures outside of the dataset, the area is only a small area of the turbidite system. The next step would be to analyse seismic data away from Shafag – Asiman and to interpret how structures effect the turbidites both up-dip and down-dip of the system. Up-dip towards the source on the Turkmenistan Shelf in the east, observations of the sediment sources on the Turkmenistan shelf will help to confirm whether there are multiple input locations, rather than an established deep canyon system often found in marine systems. Interpreting the channel network over other structures in the same level of detail as I have completed in this thesis will aid fold growth analysis and comparison with Shafag – Asiman to determine whether other folds grew similarly in space and time. This will also help to confirm whether the channel network is element dominated from the source region or whether channel complexes avulse into channel elements due to seabed topography caused by growing structures. Down-dip, to the north of the study area, it would be interesting to see any evidence for lobes or channel termination, since there are no mappable lobes within the Shafag – Asiman area.

8. Conclusions

With the use of high-quality 3D seismic refection data, I have analysed the fold growth history of the Shafag – Asiman fold structure in the central South Caspian Basin and the interaction of lacustrine turbidite channels with the structures. Based on the research presented within this thesis I conclude that:

1. **The Shafag – Asiman fold structure developed in response to transpressive dextral shear due two contemporaneous NNW-SSE and NE-SW active plate motions, demonstrated by torquing of the axial plane during growth in the Pleistocene.**
    - During deposition of the Pleistocene Absheron Formation, the Shafag - Asiman fold axis rotated anti-clockwise. The Shafag fold axis rotated 60° and the Asiman axis rotated 10°. Fold axis rotation coincides with growth into en-echelon crestal normal faults displaying a sigmoidal pattern and horsetail splay indicative of dextral shear. The deep-lying (<10 km deep) Maykop shale acts as free surface, allowing fold axis rotation to take place.
    - The location, original orientation, and initial growth of the Shafag – Asiman fold structure in is controlled by shortening of deep basement faults.
    - Constrictional deformation may be the cause of 'egg-box' like structures and influence varying fold trends in the deep-water central part of the South Caspian Basin and Shafag-Asiman region. Growth strata and channel analysis show evidence for NW – SE trending fold structures on the northern and southern flanks of Shafag, trending obliquely to the Shafag – Asiman fold structure, giving evidence for constrictional deformation.
    - Transpressive dextral shear and constrictional deformation in the deep-water central South Caspian Basin is caused by the relative SW and NW motion of the basin with respect to the Iranian and Eurasian plates respectively.

2. **Shafag – Asiman fold growth during the Plio-Pleistocene has been influenced by shortening and sediment loading of a mobile shale substrate.**
    - Growth strata analysis using sediment accumulation indices in combination with the comprehensive interpretation of the turbidite channel network demonstrates the complex

growth history of the Shafag – Asiman fold structure, with the folds showing alternating growth dominance through time.

- The Maykop shale has been mobile since deposition within the Pliocene Productive Series through to the present-day, demonstrated by palaeo-mud volcanism.
- Finite element modelling of the Shafag fold structure suggests the fold formed by shortening and sediment loading of a visco-plastic layer equivalent to the Maykop shale with viscosity of 10^{18} Pa.s and porosity of 30%.
- Sediment loading is highly sensitive to the distribution of sediment across the limbs and crest of the fold structures, controlled by shortening and sedimentation rate.

3. **An acceleration in fold growth due to mobile shale inflation of the Shafag fold core initiated approximately 2 Ma – 1.5 Ma.**
    - Finite element modelling shows the inward movement of the visco-plastic shale layer occurs at approximately 2.5 Ma – 1.5 Ma on the Shafag fold structure.
    - An acceleration in fold growth occurs within the Pleistocene Absheron Formation, after 2.1 Ma, as shown by growth strata analysis.
    - The acceleration in fold growth is coincident with the timing of numerically modelled shale inflation of the fold core.
    - In areas with a greater influence of shortening than at Shafag-Asiman, such as fold structures within areas on the perimeter of the basin, the timing of the shale movement will likely occur at an earlier time.

4. **Novel sediment accumulation indices can be used to investigate channel interactions with growing structures.**
    - A sediment accumulation index <1.2 over the crests of the Shafag – Asiman fold structures indicates that the fold crest created seabed topography with channels avoiding these areas.

- Relatively higher sediment accumulation indices on the flanks of the Shafag – Asiman fold structure coincide with sinuous channels that form complexes. Relatively lower indices, but greater than 1.2, coincide with straighter isolated channel elements. Channel complex point avulsion occurs on the up-dip side of structures whereas lateral avulsion occurs on the down dip side of the structures.
- Sediment accumulation indices can be used where age data is not available or on a finer scale than aged surfaces to predict channel architecture. The use of indices is faster than comprehensively mapping the channel network or can be used where data is not of high enough quality to map channels in detail.
- The method can be applied to turbidite channel networks deposited over other fold structures within the deep-water South Caspian Basin as well as over growing structures within fold belts cored by both salt and mobile shale detachments.

5. **Lacustrine turbidites in the deep-water part of the South Caspian Basin were sourced from the Palaeo - Amu Darya to the east.**
    - Downstream channel migration visible from highly detailed ‘scroll bars’ of channel complexes indicate that deep-water lacustrine turbidite channels are sourced to the Shafag-Asiman fold structures from the southeast, from the Palaeo-Amu Darya River.
    - Large growing fold structures outside of the Shafag – Asiman study area influence the entry point of the channels to the Shafag-Asiman fold structures. Channels initially enter the study area from the southwest, south and east. During the growth of the fold structures through the Pleistocene, turbidite channels enter from the east and southeast as they are diverted away from the study area by large structures to the south.
    - A brief change in source direction occurs towards the end of turbidite deposition, where channels enter the area from the northeast.

6. **Deep-water lacustrine turbidite systems are element dominated with limited large-scale hierarchy. They contrast with deep-water marine systems where larger channel complexes and channel systems are dominant.**
    - Channels with widths of 100m - 300m dominate the channel network of the deep-water turbidite network imaged over Shafag – Asiman, forming isolated channel elements and channel complexes with a maximum of five channel elements. There are no large-scale channel systems as commonly found in marine systems.
    - The turbidite channel network is similar to channel networks seen in the lacustrine Songliao Basin in China. Within the Songliao Basin, no large-scale canyon supplies the turbidite network.

References

ABDULLAYEV, E. & LEROY, S. A. 2016. Provenance of clay minerals in the sediments from the Pliocene Productive Series, western South Caspian Basin. *Marine and Petroleum Geology,* 73**,** 517-527.

ABDULLAYEV, N., KADIROV, F. & GULIYEV, I. 2017. Subsidence history and basin-fill evolution in the South Caspian Basin from geophysical mapping, flexural backstripping, forward lithospheric modelling and gravity modelling. *Geological Society, London, Special Publications,* 427**,** 175-196.

ABDULLAYEV, N. R. 2000. Seismic stratigraphy of the Upper Pliocene and Quaternary deposits in the South Caspian Basin. *Journal of Petroleum Science and Engineering,* 28**,** 207-226.

ABDULLAYEV, N. R., RILEY, G. W. & BOWMAN, A. P. 2012. Regional controls on lacustrine sandstone reservoirs: the Pliocene of the South Caspian Basin. *In:* BAGANZ, O. W., BARTOV, Y., BOHACS, K. & NUMMEDAL, D. (eds.) *Lacustrine Sandstone Reservoirs and Hydrocarbon Systems AAPG Memoir 95.*

ABDULLAYEV, N. R., WEBER, J., VAN BAAK, C. G., ALIYEVA, E., LESLIE, C., RILEY, G. W., O'SULLIVAN, P. & KISLITSIYN, R. 2018. Detrital zircon and apatite constraints on depositional ages, sedimentation rates and provenance: Pliocene Productive Series, South Caspian Basin, Azerbaijan. *Basin Research,* 30**,** 835-862.

ABRAHAO, D. & WARME, J. E. 1990. Lacustrine and Associated Deposits in a Rifted Continental Margin--Lower Cretaceous Lagoa Feia Formation, Campos Basin, Offshore Brazil: Chapter 18. *Lacustrine basin Exploration: Case studies and Modern Analogues.*

ABRAMS, M. A. & NARIMANOV, A. A. 1997. Geochemical evaluation of hydrocarbons and their potential sources in the western South Caspian depression, Republic of Azerbaijan. *Marine and Petroleum Geology,* 14**,** 451-468.

ABREU, V. & NUMMEDAL, D. 2007. Miocene to Quaternary sequence stratigraphy of the South and Central Caspian basins. *Oil and GAs of the Greater Caspina area: AAPG Studies in Geology 55.*

ALBERTZ, M., BEAUMONT, C. & INGS, S. J. 2010. Geodynamic modeling of sedimentation-induced overpressure, gravitational spreading, and deformation of passive margin mobile shale basins. *In:* WOOD, L. J. (ed.) *Shale Tectonics: AAPG memoir 93.*

ALIEV, A. 1960. Geology and Hydrocarbons of the Kura-Araks Region. *Baku, Azerbaijan State Publisher of Hydrocarbon Literature***,** 361.

ALLEN, M., JACKSON, J. & WALKER, R. 2004. Late Cenozoic reorganization of the Arabia-Eurasia collision and the comparison of short-term and long-term deformation rates. *Tectonics,* 23.

ALLEN, M. B., JONES, S., ISMAIL-ZADEH, A., SIMMONS, M. & ANDERSON, L. 2002. Onset of subduction as the cause of rapid Pliocene-Quaternary subsidence in the South Caspian basin. *Geology,* 30**,** 775-778.

ALLEN, M. B., VINCENT, S. J., ALSOP, G. I., ISMAIL-ZADEH, A. & FLECKER, R. 2003. Late Cenozoic deformation in the South Caspian region: effects of a rigid basement block within a collision zone. *Tectonophysics,* 366**,** 223-239.

ALLMENDINGER, R. W. 1998. Inverse and forward numerical modeling of trishear fault-propagation folds. *Tectonics,* 17**,** 640-656.

ALLMENDINGER, R. W., CARDOZO, N. & FISHER, D. M. 2011. *Structural geology algorithms: Vectors and tensors*, Cambridge University Press.

ALSOP, G. I., MARCO, S., LEVI, T. & WEINBERGER, R. 2017. Fold and thrust systems in Mass Transport Deposits. *Journal of Structural Geology,* 94**,** 98-115.

AMUNDSEN, L. & LANDRØ, M. 2014. Broadband Seismic Technology and Beyond: Part VII: CGG's BroadSeis—A Change of Thinking.

ANADÓN, P., CABRERA, L., JULIA, R. & MARZO, M. 1991. Sequential arrangement and asymmetrical fill in the Miocene Rubielos de Mora Basin (northeast Spain). *Lacustrine facies analysis***,** 257-275.

AXEN, G. J., LAM, P. S., GROVE, M., STOCKLI, D. F. & HASSANZADEH, J. 2001. Exhumation of the west-central Alborz Mountains, Iran, Caspian subsidence, and collision-related tectonics. *Geology,* 29**,** 559-562.

BAGANZ, O. W., BARTOV, Y., BOHACS, K. M. & NUMMEDAL, D. 2012a. *Lacustrine Sandstone Reservoirs and Hydrocarbon Systems: AAPG Memoir 95*, AAPG.

BAGANZ, O. W. T., BAGIROV, E., MICHAEL, G. E. & SHULTZ, A. 2012b. Productive series play of the Paleo-Volga Delta, South Caspian Basin: Exploration history, sedimentation, and petroleum system. *In:* BAGANZ, O. W., BARTOV, Y., BOHACS, K. & NUMMEDAL, D. (eds.) *Lacustrine sandstone reservoirs and hydrocarbon systems: AAPG Memoir 95.* AAPG Special Volumes.

BAGIROV, E. & LERCHE, I. 1999. *Impact of natural hazards on oil and gas extraction: the South Caspian basin*, Springer Science & Business Media.

BAHORICH, M. S. & FARMER, S. L. 1995. 3-D seismic discontinuity for faults and stratigraphic features: The coherence cube. *SEG Technical Program Expanded Abstracts 1995.* Society of Exploration Geophysicists.

BAHORICH, M. S. & FARMER, S. L. 1996. Method of seismic signal processing and exploration. Google Patents.

BARBOZA, S. A. & BOETTCHER, S. S. 2000. Major and trace element constraints on fluid origin, Offshore Eastern Trinidad.

BARKER, C. 1990. Calculated volume and pressure changes during the thermal cracking of oil to gas in reservoirs (1). *AAPG bulletin,* 74**,** 1254-1261.

BARNES, A. E. 2016. *Handbook of poststack seismic attributes*, Society of Exploration Geophysicists.

BARRON, E. J. 1990. Climate and Lacustrine Petroleum Source Prediction: Chapter 1. *In:* KATZ, B. J. (ed.) *Lacustrine Basin Exploration: Case Studies and Modern Analogs, AAPG Memoir 50.*

BEAUMONT, C., MUÑOZ, J. A., HAMILTON, J. & FULLSACK, P. 2000. Factors controlling the Alpine evolution of the central Pyrenees inferred from a comparison of observations and geodynamical models. *Journal of Geophysical Research: Solid Earth,* 105**,** 8121-8145.

BECHTOLD, B. 2016. *Violin Plots for MatLab, Github Project* [Online]. Available: https://github.com/bastibe/Violinplot-Matlab [Accessed].

BERBERIAN, M. 1983. The southern Caspian: a compressional depression floored by a trapped, modified oceanic crust. *Canadian Journal of Earth Sciences,* 20**,** 163-183.

BERBERIAN, M. & KING, G. C. P. 1981. Towards a paleogeography and tectonic evolution of Iran. *Canadian journal of earth sciences,* 18**,** 210-265.

BERGER, W. H. & JANSEN, E. 1994. Mid-Pleistocene climate shift-the Nansen connection. *Washington DC American Geophysical Union Geophysical Monograph Series,* 85**,** 295-311.

BERTELLO, F., COOPER, C., CASTELLANO, P. & RONCHITELLI, G. P. Improved characterization of a complex structure in the Azerbaijan offshore revealed by 3D Pre-Stack Depth Migration and Depth Continuity Cube applications. 2001. OnePetro.

BLOUIN, A., IMBERT, P., SULTAN, N. & CALLOT, J. P. 2019. Evolution model for the Absheron Mud Volcano: from in situ observations to numerical modeling. *Journal of Geophysical Research: Earth Surface,* 124**,** 766-794.

BOETTCHER, S., JACKSON, J., NEAL, J. & QUINN, M. 2000. Lithosphere-scale cross-section and tectonic synthesis, offshore eastern Trinidad: Geological Society of Trinidad and Tobago 2000 Society of Petroleum Engineers Conference Proceedings.

BOHACS, K. M., CARROLL, A. R. & NEAL, J. E. 2003. Lessons from large lake systems-Thresholds, nonlinearity, and strange attractors. *In:* CHAN, M. A. & ARCHER, A. W. (eds.) *Extreme depositional environments: mega end members in geologic time.* Geological Society of America.

BOHACS, K. M., CARROLL, A. R., NEAL, J. E. & MANKIEWICZ, P. J. 2000. Lake-basin type, source potential, and hydrocarbon character: an integrated sequence-stratigraphic-geochemical framework. *Lake basins through space and time: AAPG Studies in Geology,* 46**,** 3-34.

BONINI, M., TASSI, F., FEYZULLAYEV, A. A., ALIYEV, C. S., CAPECCHIACCI, F. & MINISSALE, A. 2013. Deep gases discharged from mud volcanoes of Azerbaijan: New geochemical evidence. *Marine and Petroleum Geology,* 43**,** 450-463.

BRANDES, C. & TANNER, D. C. 2014. Fault-related folding: A review of kinematic models and their application. *Earth-Science Reviews,* 138**,** 352-370.

BROWN, K. M. 1990. The nature and hydrogeologic significance of mud diapirs and diatremes for accretionary systems. *Journal of Geophysical Research: Solid Earth,* 95**,** 8969-8982.

BRUCE, C. H. 1984. Smectite dehydration--its relation to structural development and hydrocarbon accumulation in northern Gulf of Mexico basin. *AAPG Bulletin,* 68**,** 673-683.

BRUNET, M.-F., KOROTAEV, M. V., ERSHOV, A. V. & NIKISHIN, A. M. 2003. The South Caspian Basin: a review of its evolution from subsidence modelling. *Sedimentary Geology,* 156**,** 119-148.

BURBANK, D. W. & VERGÉS, J. 1994. Reconstruction of topography and related depositional systems during active thrusting. *Journal of Geophysical Research: Solid Earth,* 99**,** 20281-20297.

BURYAKOVSKY, L., DZHAFAROV, I. & DZHEVANSHIR, R. 1982. Prediction of Petrophysical Properties of Oil and Gas Reservoirs and Seals. Moscow: Nedra Publishing House.

CARDOZO, N. & ALLMENDINGER, R. W. 2013. Spherical projections with OSXStereonet. *Computers & Geosciences,* 51**,** 193-205.

CARROLL, A. R. & BOHACS, K. M. 1999. Stratigraphic classification of ancient lakes: Balancing tectonic and climatic controls. *Geology,* 27**,** 99-102.

CARTWRIGHT, J., BOUROULLEC, R., JAMES, D. & JOHNSON, H. 1998. Polycyclic motion history of some Gulf Coast growth faults from high-resolution displacement analysis. *Geology,* 26**,** 819-822.

CASTLE, J. W. 1990. Sedimentation in Eocene Lake Uinta (Lower Green River Formation), Northeastern Uinta Basin, Utah: Chapter 15. *In:* KATZ, B. J. (ed.) *Lacustrine Basin Exploration: Case Studies and Modern Analogs AAPG memoir 50.*

CHILDS, C., NICOL, A., WALSH, J. J. & WATTERSON, J. 2003. The growth and propagation of synsedimentary faults. *Journal of Structural Geology,* 25**,** 633-648.

CIFELLI, F., BALLATO, P., ALIMOHAMMADIAN, H., SABOURI, J. & MATTEI, M. 2015. Tectonic magnetic lineation and oroclinal bending of the Alborz range: Implications on the Iran-Southern Caspian geodynamics. *Tectonics,* 34**,** 116-132.

CLARK, I. R. & CARTWRIGHT, J. A. 2009. Interactions between submarine channel systems and deformation in deepwater fold belts: Examples from the Levant Basin, Eastern Mediterranean sea. *Marine and Petroleum Geology,* 26**,** 1465-1482.

CLARK, I. R. & CARTWRIGHT, J. A. 2011. Key controls on submarine channel development in structurally active settings. *Marine and Petroleum Geology,* 28**,** 1333-1349.

CLARK, P. U., ARCHER, D., POLLARD, D., BLUM, J. D., RIAL, J. A., BROVKIN, V., MIX, A. C., PISIAS, N. G. & ROY, M. 2006. The middle Pleistocene transition: characteristics, mechanisms, and implications for long-term changes in atmospheric pCO2. *Quaternary Science Reviews,* 25**,** 3150-3184.

COHEN, H., HARDY, S., ALSOP, G., BLUNDELL, D. & DAVISON, I. 1996. Numerical modelling of stratal architectures resulting from differential loading of a mobile substrate. *In:* G, A., D, B. & I, D. (eds.) *Salt Tectonics.* Geol. Soc. Lond. Special Publ.

COLLIER, J. & WHITE, R. 1990. Mud diapirism within Indus fan sediments: Murray Ridge, Gulf of Oman. *Geophysical Journal International,* 101**,** 345-353.

CONTRERAS, J. 2010. A model for low amplitude detachment folding and syntectonic stratigraphy based on the conservation of mass equation. *Journal of Structural Geology,* 32**,** 566-579.

COPLEY, A. & JACKSON, J. 2006. Active tectonics of the Turkish-Iranian plateau. *Tectonics,* 25.

CRISTALLINI, E. O. & ALLMENDINGER, R. W. 2001. Pseudo 3-D modeling of trishear fault-propagation folding. *Journal of Structural Geology,* 23**,** 1883-1899.

CROOK, A., OWEN, D., WILLSON, S. & YU, J. 2006. Benchmarks for the evolution of shear localisation with large relative sliding in frictional materials. *Computer methods in applied mechanics*

engineering, 195**,** 4991-5010.

DAHLSTROM, C. D. A. 1969. The upper detachment in concentric folding. *Bulletin of Canadian Petroleum Geology,* 17**,** 326-346.

DAHLSTROM, C. D. A. 1990. Geometric constraints derived from the law of conservation of volume and applied to evolutionary models for detachment folding: geologic notes. *AAPG bulletin,* 74**,** 336-344.

DAVISON, I., BOSENCE, D., ALSOP, G. I. & AL-AAWAH, M. H. J. G. S., LONDON, SPECIAL PUBLICATIONS 1996. Deformation and sedimentation around active Miocene salt diapirs on the Tihama Plain, northwest Yemen. 100**,** 23-39.

DAY-STIRRAT, R., MCDONNELL, A. & WOOD, L. 2010. Diagenetic and seismic concerns associated with interpretation of deeply buried mobile shales. *In:* WOOD, L. J. (ed.) *Shale Tectonics AAPG Memoir 93.*

DEAN, S. 2014. *Tectonic and gravitational fold and thrust belts: Insights from discrete element simulations and Galicia ocean-continent transition zone: New seismic reflection constraints.* Doctoral Dissertation, Rice University.

DEAN, S., MORGAN, J. & BRANDENBURG, J. 2015. Influence of mobile shale on thrust faults: Insights from discrete element simulationsInfluence of Mobile Shale on Thrust Faults. *AAPG Bulletin,* 99**,** 403-432.

DECELLES, P. G., GRAY, M. B., RIDGWAY, K. D., COLE, R. B., SRIVASTAVA, P., PEQUERA, N. & PIVNIK, D. A. 1991. Kinematic history of a foreland uplift from Paleocene synorogenic conglomerate, Beartooth Range, Wyoming and Montana. *Geological Society of America Bulletin,* 103**,** 1458-1475.

DEMERCIAN, S., SZATMARI, P. & COBBOLD, P. R. 1993. Style and pattern of salt diapirs due to thin-skinned gravitational gliding, Campos and Santos basins, offshore Brazil. *Tectonophysics,* 228**,** 393-433.

DESHENG, L. & MING, L. 1990. Hydrocarbon Accumulation in Meso-Cenozoic Lacustrine Remnant Petroliferous Depressions and Basins, Southeastern China: Chapter 20. *In:* KATZ, B. J. (ed.) *Lacustrine Basin Exploration: Case Studies and Modern Analogs, AAPG Memoir 50.*

DEVILLE, E., BATTANI, A., GRIBOULARD, R., GUERLAIS, S., HERBIN, J., HOUZAY, J., MULLER, C. & PRINZHOFER, A. 2003. The origin and processes of mud volcanism: new insights from Trinidad. *Geological Society, London, Special Publications,* 216**,** 475-490.

DEVLIN, W., COGSWELL, J., GASKINS, G., ISAKSEN, G., PITCHER, D., PULS, D., STANLEY, K. & WALL, G. 1999. South Caspian basin: young, cool, and full of promise. *GSA today,* 9**,** 1-9.

DEWEY, J., HEMPTON, M., KIDD, W., SAROGLU, F. & ŞENGÖR, A. 1986. Shortening of continental lithosphere: the neotectonics of Eastern Anatolia—a young collision zone. *Geological Society, London, Special Publications,* 19**,** 1-36.

DIX, C. H. 1955. Seismic velocities from surface measurements. *Geophysics,* 20**,** 68-86.

DON, J., SHAW, J. H., PLESCH, A., BRIDGWATER, D. D. & LUFADEJU, G. 2020. Characterizing the growth of structures in three dimensions using patterns of deep-water fan and channel systems. *AAPG Bulletin,* 104**,** 177-203.

DOUGHTY-JONES, G. 2014. *The influence of fold and salt-wall growth on deepwater sedimentary systems in an active salt mini-basin, offshore Angola.* Imperial College London.

EGAN, S. S., MOSAR, J., BRUNET, M.-F. & KANGARLI, T. 2009. Subsidence and uplift mechanisms within the South Caspian Basin: insights from the onshore and offshore Azerbaijan region. *Geological Society, London, Special Publications,* 312**,** 219-240.

ENGDAHL, E. R., VAN DER HILST, R. & BULAND, R. 1998. Global teleseismic earthquake relocation with improved travel times and procedures for depth determination. *Bulletin of the Seismological Society of America,* 88**,** 722-743.

EPARD, J.-L. & GROSHONG JR, R. 1995. Kinematic model of detachment folding including limb rotation, fixed hinges and layer-parallel strain. *Tectonophysics,* 247**,** 85-103.

EPARD, J.-L. & GROSHONG JR, R. H. 1993. Excess area and depth to detachment. *AAPG bulletin,* 77**,** 1291-1302.

ERSLEV, E. A. 1991. Trishear fault-propagation folding. *Geology,* 19**,** 617-620.

EVANS, R. J., DAVIES, R. J. & STEWART, S. A. 2007. Internal structure and eruptive history of a kilometre scale mud volcano system, South Caspian Sea. *Basin Research,* 19**,** 153-163.

EWY, R., DIRKZWAGER, J. & BOVBERG, C. 2020. Claystone porosity and mechanical behavior vs. geologic burial stress. *Marine and Petroleum Geology,* 121**,** 104563.

FERGUSSON, L. J. 1985. The mineralogy, geochemistry and origin of Lower Tertiary smectite-mudstones, East Coast deformed belt, New Zealand.

FEYZULLAYEV, A. & LERCHE, I. 2009. Occurrence and nature of overpressure in the sedimentary section of the South Caspian Basin, Azerbaijan. *Energy, Exploration and Exploitation,* 27**,** 345-366.

FLOWER, R. J., MACKAY, A. W., ROSE, N. L., BOYLE, J. L., DEARING, J. A., APPLEBY, P. G., KUZMINA, A. E. & GRANINA, L. Z. 1995. Sedimentary records of recent environmental change in Lake Baikal, Siberia. *The Holocene,* 5**,** 323-327.

FORD, M., WILLIAMS, E. A., ARTONI, A., VERGÉS, J. & HARDY, S. 1997. Progressive evolution of a fault-related fold pair from growth strata geometries, Sant Llorenç de Morunys, SE Pyrenees. *Journal of structural Geology,* 19**,** 413-441.

FORTE, A. M. & COWGILL, E. 2013. Late Cenozoic base-level variations of the Caspian Sea: a review of its history and proposed driving mechanisms. *Palaeogeography, Palaeoclimatology, Palaeoecology,* 386**,** 392-407.

FOWLER, S., MILDENHALL, J., ZALOVA, S., RILEY, G., ELSLEY, G., DESPLANQUES, A. & GULIYEV, F. 2000. Mud volcanoes and structural development on Shah Deniz. *Journal of Petroleum Science and Engineering,* 28**,** 189-206.

GAWTHORPE, R. L. & LEEDER, M. R. 2000. Tectono-sedimentary evolution of active extensional basins. *Basin Research,* 12**,** 195-218.

GEMMER, L., INGS, S. J., MEDVEDEV, S. & BEAUMONT, C. 2004. Salt tectonics driven by differential sediment loading: Stability analysis and finite-element experiments. *Basin Research,* 16**,** 199-218.

GERSZTENKORN, A. & MARFURT, K. J. 1999. Eigenstructure-based coherence computations as an aid to 3-D structural and stratigraphic mapping. *Geophysics,* 64**,** 1468-1479.

GHOSH, S., KHAN, D. & SENGUPTA, S. 1995. Interfering folds in constrictional deformation. *Journal of Structural Geology,* 17**,** 1361-1373.

GINSBURG, G. & SOLOVIEV, V. 1994. Mud volcano gas hydrates in the Caspian Sea. *Bulletin of the Geological Society of Denmark,* 41**,** 95-100.

GRAHAM, R. & PEPPER, A. Observations on structures associated with Mud Diapirism and their role in petroleum charging and trapping. AAPG International Conference and Exhibition, Cape Town, South Africa, 2008.

GRAUE, K. 2000. Mud volcanoes in deepwater Nigeria. *Marine and Petroleum Geology,* 17**,** 959-974.

GREEN, T., ABDULLAYEV, N., HOSSACK, J., RILEY, G. & ROBERTS, A. M. 2009. Sedimentation and subsidence in the south Caspian Basin, Azerbaijan. *Geological Society, London, Special Publications,* 312**,** 241-260.

GUEST, B., GUEST, A. & AXEN, G. 2007. Late Tertiary tectonic evolution of northern Iran: A case for simple crustal folding. *Global and Planetary Change,* 58**,** 435-453.

GUZOFSKI, C. A., MUELLER, J. P., SHAW, J. H., MURON, P., MEDWEDEFF, D. A., BILOTTI, F. & RIVERO, C. 2009. Insights into the mechanisms of fault-related folding provided by volumetric structural restorations using spatially varying mechanical constraints. *AAPG bulletin,* 93**,** 479-502.

HALE, D. 2009. Structure-oriented smoothing and semblance. *CWP report,* 635**,** 261-270.

HARDING, T. P. 1973. Newport-Inglewood trend, California—An example of wrenching style of deformation. *AAPG Bulletin,* 57**,** 97-116.

HARDY, S. & FINCH, E. 2005. Discrete-element modelling of detachment folding. *Basin Research,* 17**,** 507-520.

HARDY, S. & FORD, M. 1997. Numerical modeling of trishear fault propagation folding. *Tectonics,* 16**,** 841-854.

HARDY, S. & POBLET, J. 1994. Geometric and numerical model of progressive limb rotation in detachment folds. *Geology,* 22**,** 371-374.

HARDY, S. & POBLET, J. 1995. The velocity description of deformation. Paper 2: sediment geometries associated with fault-bend and fault-propagation folds. *Marine and Petroleum Geology,* 12**,** 165-176.

HARLAND, W. 1971. Tectonic transpression in caledonian Spitsbergen. *Geological Magazine,* 108**,** 27-41.

HEAD, M. J., PILLANS, B. & FARQUHAR, S. A. 2008. The Early-Middle Pleistocene Transition: characterisation and proposed guide for the defining boundary. *Episodes***,** 255-259.

HEMPTON, M. R. 1987. Constraints on Arabian plate motion and extensional history of the Red Sea. *Tectonics,* 6**,** 687-705.

HINDS, D., ALIYEVA, E., ALLEN, M., DAVIES, C., KROONENBERG, S., SIMMONS, M. & VINCENT, S. 2004. Sedimentation in a discharge dominated fluvial-lacustrine system: the Neogene Productive Series of the South Caspian Basin, Azerbaijan. *Marine and Petroleum Geology,* 21**,** 613-638.

HOLLINGSWORTH, J., JACKSON, J., WALKER, R. & NAZARI, H. 2008. Extrusion tectonics and subduction in the eastern South Caspian region since 10 Ma. *Geology,* 36**,** 763-766.

HORSFIELD, B., CURRY, D., BOHACS, K., LITTKE, R., RULLKÖTTER, J., SCHENK, H., RADKE, M., SCHAEFER, R., CARROLL, A. & ISAKSEN, G. 1994. Organic geochemistry of freshwater and alkaline lacustrine sediments in the Green River Formation of the Washakie Basin, Wyoming, USA. *Organic Geochemistry,* 22**,** 415-440.

HOWLETT, D. M., GAWTHORPE, R. L., GE, Z., ROTEVATN, A. & JACKSON, C. A. L. 2021. Turbidites, topography and tectonics: Evolution of submarine channel-lobe systems in the salt-influenced Kwanza Basin, offshore Angola. *Basin Research,* 33**,** 1076-1110.

HOYLE, T. M., LEROY, S. A. G., LÓPEZ-MERINO, L., VAN BAAK, C. G. C., MARTÍNEZ CORTIZAS, A., RICHARDS, K. & AGHAYEVA, V. 2021. Biological turnovers in response to marine incursion into the Caspian Sea at the Plio-Pleistocene transition. *Global and Planetary Change,* 206**,** 103623.

HUC, A., LE FOURNIER, J., VANDENBROUCKE, M. & BESSEREAU, G. 1990. Northern Lake Tanganyika--An Example of Organic Sedimentation in an Anoxic Rift Lake: Chapter 10. *In:* KATZ, B. J. (ed.) *Lacustrine Basin Exploration: Case Studies and Modern Analogs, AAPG Memoir 50.*

HUDEC, M. R. & JACKSON, M. P. 2007. Terra infirma: Understanding salt tectonics. *Earth-Science Reviews,* 82**,** 1-28.

HUDEC, M. R. & SOTO, J. I. 2021. Piercement mechanisms for mobile shales. *Basin Research,* 33**,** 2862-2882.

HUDSON, S. M., JOHNSON, C. L., EFENDIYEVA, M. A., ROWE, H. D., FEYZULLAYEV, A. A. & ALIYEV, C. S. 2008. Stratigraphy and geochemical characterization of the Oligocene–

Miocene Maikop series: Implications for the paleogeography of Eastern Azerbaijan. *Tectonophysics,* 451**,** 40-55.

IMBUS, S. W., ENGEL, M. H. & ELMORE, R. D. 1990. Organic Geochemistry and Sedimentology of Middle Proterozoic Nonesuch Formation--Hydrocarbon Source Rock Assessment of a Lacustrine Rift Deposit: Chapter 12. *In:* KATZ, B. J. (ed.) *Lacustrine Basin Exploration: Case Studies and Modern Analogs, AAPG memoir 50.*

INAN, S., YALÇIN, M. N., GULIEV, I. S., KULIEV, K. & FEIZULLAYEV, A. A. 1997. Deep petroleum occurrences in the Lower Kura Depression, South Caspian Basin, Azerbaijan: an organic geochemical and basin modeling study. *Marine and Petroleum Geology,* 14**,** 731-762.

INGS, S. J. & BEAUMONT, C. 2010. Continental margin shale tectonics: Preliminary results from coupled fluid-mechanical models of large-scale delta instability. *Journal of the Geological Society,* 167**,** 571-582.

JACKSON, J., PRIESTLEY, K., ALLEN, M. & BERBERIAN, M. 2002. Active tectonics of the south Caspian basin. *Geophysical Journal International,* 148**,** 214-245.

JACKSON, M. 1990. *Salt diapirs of the Great Kavir, central Iran*, Geological Society of America.

JACKSON, M. & VENDEVILLE, B. 1994. Regional extension as a geologic trigger for diapirism. *Geological society of America bulletin,* 106**,** 57-73.

JACKSON, M. P. A. & TALBOT, C. J. 1986. External shapes, strain rates, and dynamics of salt structures. *GSA Bulletin,* 97**,** 305-323.

JAMISON, W. R. 1987. Geometric analysis of fold development in overthrust terranes. *Journal of Structural Geology,* 9**,** 207-219.

JANOCKO, M., NEMEC, W., HENRIKSEN, S. & WARCHOŁ, M. 2013. The diversity of deep-water sinuous channel belts and slope valley-fill complexes. *Marine and Petroleum Geology,* 41**,** 7-34.

JOLLY, B. A., LONERGAN, L. & WHITTAKER, A. C. 2016. Growth history of fault-related folds and interaction with seabed channels in the toe-thrust region of the deep-water Niger delta. *Marine and Petroleum Geology,* 70**,** 58-76.

JONES, G., MAYALL, M. & LONERGAN, L. 2012. Contrasting depositional styles on a slope system and their control by salt tectonics: through-going channels, ponded fans, and mass transport complexes. *In:* N, R., P, W., M, C. D. A. S., S, H., E, M., MAYALL, M., R, F., T, D. A., A, S., CAMPION, K., T, H., R, S. & F, S. (eds.) *New Understanding of the Petroleum Systems of Continental Margins of the World.*

JONES, R. & SIMMONS, M. 1996. A review of the stratigraphy of Eastern Paratethys (Oligocene-Holocene). *Bulletin-Natural History Museum Geology Series,* 52**,** 25-50.

JONES, R. & SIMMONS, M. 1998. A review of the stratigraphy of Eastern Paratethys (Oligocene-Holocene), with particular emphasis on the Black Sea. *In:* A, R. (ed.) *Regional and Petroleum Geology of the Black Sea and Surrounding Region, AAPG memoir 68.*

JORISSEN, E. L., ABELS, H. A., WESSELINGH, F. P., LAZAREV, S., AGHAYEVA, V. & KRIJGSMAN, W. 2020. Amplitude, frequency and drivers of Caspian Sea lake-level variations during the Early Pleistocene and their impact on a protected wave-dominated coastline. *Sedimentology,* 67**,** 649-676.

KADIROV, F., LERCHE, I., GULIEV, I., KADYROV, A., MUKHTAROV, A. & FEYZULLAYEV, A. Gravity model of mud volcanoes. Abstracts, AAPG Annual Meeting, Salt Lake City, Utah, USA, 2003.

KADIROV, F. A. & GADIROV, A. H. 2014. A gravity model of the deep structure of South Caspian Basin along submeridional profile Alborz–Absheron Sill. *Global and Planetary Change,* 114**,** 66-74.

KATZ, B. J. 1990a. Controls on distribution of lacustrine source rocks through time and space: Chapter 4. *In:* KATZ, B. J. (ed.) *Lacustrine Basin Exploration: Case Studies and Modern Analogs, AAPG memoir 50.*

KATZ, B. J. 1990b. *Lacustrine basin exploration Case Studies Modern Analogs*.

KATZ, B. J. 1995. Factors controlling the development of lacustrine petroleum source rocks-an update. *In:* HUC, A. & KATZ, B. J. (eds.) *Paleogeography, Paleoclimate, and Source Rocks.*

KERIMOV, V. Y., KHALILOV, E. & MEKHTIYEV, N. Y. 1992. Paleogeographic conditions of formation of the South Caspian depression during the Pliocene in relation to its oil-gas potential. *Petroleum Geology: A digest of Russian literature on Petroleum Geology.*

KHAIN, V., GADJIEV, A. & KENGERLI, T. Tectonic origin of the Apsheron Threshold in the Caspian Sea. Doklady Earth Sciences, 2007. Springer Science & Business Media, 552.

KHAIN, V., SOKOLOV, B., KLESHCHEV, K. & SHEIN, V. 1991. Tectonic and geodynamic setting of oil and gas basins of the Soviet Union (1). *AAPG bulletin,* 75**,** 313-325.

KHALILOV, E., MEKHTIYEV, S. F. & KHAIN, V. Y. 1987. Some geophysical data confirming the collisional origin of the Greater Caucasus. *Geotectonics,* 21**,** 132-136.

KHALILOV, N. Y. & IMANOV, A. 1979. Effect of anomalous high-pressures of beds on drilling indicators. *NEFTYANOE KHOZYAISTVO***,** 9-13.

KHALILOV, N. Y. & IMANOV, A. 1980. Predicting overpressures in exploratory drilling. *Oil and Gas Geology,* 5**,** 41-45.

KNAPP, C. C., KNAPP, J. H. & CONNOR, J. A. 2004. Crustal-scale structure of the South Caspian Basin revealed by deep seismic reflection profiling. *Marine and Petroleum Geology,* 21**,** 1073-1081.

KNIES, J., MATTHIESSEN, J., VOGT, C., LABERG, J. S., HJELSTUEN, B. O., SMELROR, M., LARSEN, E., ANDREASSEN, K., EIDVIN, T. & VORREN, T. O. 2009. The Plio-Pleistocene glaciation of the Barents Sea–Svalbard region: a new model based on revised chronostratigraphy. *Quaternary Science Reviews,* 28**,** 812-829.

KOLLA, V., POSAMENTIER, H. W. & WOOD, L. J. 2007. Deep-water and fluvial sinuous channels—Characteristics, similarities and dissimilarities, and modes of formation. *Marine and Petroleum Geology,* 24**,** 388-405.

KOPF, A., DEYHLE, A., LAVRUSHIN, V. Y., POLYAK, B. G., GIESKES, J. M., BUACHIDZE, G. I., WALLMANN, K. & EISENHAUER, A. 2003. Isotopic evidence (He, B, C) for deep fluid and mud mobilization from mud volcanoes in the Caucasus continental collision zone. *International Journal of Earth Sciences,* 92**,** 407-425.

KOPF, A. J. 2002. Significance of mud volcanism. *Reviews of Geophysics,* 40**,** 2-1-2-52.

KOPF, A. J. 2003. Global methane emission through mud volcanoes and its past and present impact on the Earth's climate. *International Journal of Earth Sciences,* 92**,** 806-816.

KRIJGSMAN, W., TESAKOV, A., YANINA, T., LAZAREV, S., DANUKALOVA, G., VAN BAAK, C. G. C., AGUSTÍ, J., ALÇIÇEK, M. C., ALIYEVA, E., BISTA, D., BRUCH, A., BÜYÜKMERIÇ, Y., BUKHSIANIDZE, M., FLECKER, R., FROLOV, P., HOYLE, T. M., JORISSEN, E. L., KIRSCHER, U., KORICHE, S. A., KROONENBERG, S. B., LORDKIPANIDZE, D., OMS, O., RAUSCH, L., SINGARAYER, J., STOICA, M., VAN DE VELDE, S., TITOV, V. V. & WESSELINGH, F. P. 2019. Quaternary time scales for the Pontocaspian domain: Interbasinal connectivity and faunal evolution. *Earth-Science Reviews,* 188**,** 1-40.

LABERG, J. S., ANDREASSEN, K., KNIES, J., VORREN, T. O. & WINSBORROW, M. 2010. Late Pliocene–Pleistocene development of the Barents Sea ice sheet. *Geology,* 38**,** 107-110.

LAMBIASE, J. J. 1990. A model for tectonic control of lacustrine stratigraphic sequences in continental Rift Basins: Chapter 16. *In:* KATZ, B. J. (ed.) *Lacustrine Basin Exploration: Case Studies and Modern Analogs, AAPG memoir 50.*

LAZAREV, S., JORISSEN, E. L., VAN DE VELDE, S., RAUSCH, L., STOICA, M., WESSELINGH, F. P., VAN BAAK, C. G., YANINA, T. A., ALIYEVA, E. & KRIJGSMAN, W. 2019. Magneto-biostratigraphic age constraints on the palaeoenvironmental evolution of the South Caspian basin during the Early-Middle Pleistocene (Kura basin, Azerbaijan). *Quaternary Science Reviews,* 222**,** 105895.

LAZAREV, S., KUIPER, K. F., OMS, O., BUKHSIANIDZE, M., VASILYAN, D., JORISSEN, E. L., BOUWMEESTER, M. J., AGHAYEVA, V., VAN AMERONGEN, A. J., AGUSTÍ, J., LORDKIPANIDZE, D. & KRIJGSMAN, W. 2021. Five-fold expansion of the Caspian Sea in the late Pliocene: New and revised magnetostratigraphic and 40Ar/39Ar age constraints on the Akchagylian Stage. *Global and Planetary Change,* 206**,** 103624.

LIRO, L. M. & PARDUS, Y. C. 1990. Seismic Facies Analysis of Fluvial-Deltaic Lacustrine Systems--Upper Fort Union Formation (Paleocene), Wind River Basin, Wyoming: Chapter 14. *In:*

KATZ, B. J. (ed.) *Lacustrine Basin Exploration: Case Studies and Modern Analogs, AAPG memoir 50.*

LIU, E., WANG, H., PAN, S., QIN, C., JIANG, P., CHEN, S., YAN, D., LÜ, X. & JING, Z. 2021. Architecture and depositional processes of sublacustrine fan systems in structurally active settings: An example from Weixinan Depression, northern South China Sea. *Marine Petroleum Geology,* 134**,** 105380.

LORENZ, V. 1975. Formation of phreatomagmatic maar–diatreme volcanoes and its relevance to kimberlite diatremes. *Physics and Chemistry of the Earth.* Elsevier.

MANGINO, S. & PRIESTLEY, K. 1994. Seismic Studies of the Caspian Basin and Surrounding Regions. CAMBRIDGE UNIV (UNITED KINGDOM) DEPT OF EARTH SCIENCES.

MARFURT, K. J., KIRLIN, R. L., FARMER, S. L. & BAHORICH, M. S. 1998. 3-D seismic attributes using a semblance-based coherency algorithm. *Geophysics,* 63**,** 1150-1165.

MARÍN-MORENO, H., MINSHULL, T. A. & EDWARDS, R. A. 2013. Inverse modelling and seismic data constraints on overpressure generation by disequilibrium compaction and aquathermal pressuring: application to the Eastern Black Sea Basin. *Geophysical Journal International,* 194**,** 814-833.

MARÍN-MORENO, H., MINSHULL, T. A. & EDWARDS, R. A. 2013. A disequilibrium compaction model constrained by seismic data and application to overpressure generation in the Eastern Black Sea Basin. *Basin Research,* 25**,** 331-347.

MASLIN, M. A. & BRIERLEY, C. M. 2015. The role of orbital forcing in the Early Middle Pleistocene Transition. *Quaternary International,* 389**,** 47-55.

MATISHOV, D. G., YAITSKAYA, N. A. & BERDNIKOV, S. V. 2018. Temperature and salinity variations in Caspian Sea waters in the 20th century. *Oceanology,* 58**,** 786-795.

MATTEI, M., CIFELLI, F., VISCONTI, A. L., NOZAEM, R., WINKLER, A. & SAGNOTTI, L. Oroclinal bending in Northern Iran: new constraints on the age of South Caspian subduction and extrusion tectonics. Geophysical Research Abstracts, 2019.

MAYALL, M., JONES, E. & CASEY, M. 2006. Turbidite channel reservoirs—Key elements in facies prediction and effective development. *Marine and Petroleum Geology,* 23**,** 821-841.

MAYALL, M. & KNELLER, B. 2021. Seismic interpretation workflows for deep-water systems: A practical guide for the subsurface. *AAPG Bulletin,* 105**,** 2127-2157.

MAYALL, M., LONERGAN, L., BOWMAN, A., JAMES, S., MILLS, K., PRIMMER, T., POPE, D., ROGERS, L. & SKEENE, R. 2010. The response of turbidite slope channels to growth-induced seabed topography. *AAPG bulletin,* 94**,** 1011-1030.

MAYALL, M. & STEWART, I. 2000. The architecture of turbidite slope channels.

MAZZINI, A. & ETIOPE, G. 2017. Mud volcanism: An updated review. *Earth-Science Reviews,* 168**,** 81-112.

MCCAFFREY, K. & JOLLY, R. Basement Inheritance Controls on Fold Evolution in the South Caspian Sea. AAPG European Region Conference, 2007 Athens, Greece.

MCHARGUE, T., PYRCZ, M. J., SULLIVAN, M. D., CLARK, J., FILDANI, A., ROMANS, B., COVAULT, J., LEVY, M., POSAMENTIER, H. & DRINKWATER, N. 2011. Architecture of turbidite channel systems on the continental slope: patterns and predictions. *Marine and Petroleum Geology,* 28**,** 728-743.

MCHARGUE, T. R. 1990. Stratigraphic Development of Proto-South Atlantic Rifting in Cabinda, Angola--A Petroliferous Lake Basin: Chapter 19. *In:* KATZ, B. J. (ed.) *Lacustrine Basin Exploration: Case Studies and Modern Analogs, AAPG memoir 50.*

MCQUARRIE, N. 2004. Crustal scale geometry of the Zagros fold–thrust belt, Iran. *Journal of structural Geology,* 26**,** 519-535.

MELLO, M. & MAXWELL, J. 1990. Organic geochemical and biological marker characterization of source rocks and oils derived from lacustrine environments in the brazilian continental margin: Chapter 5. *In:* KATZ, B. J. (ed.) *Lacustrine Basin Exploration: Case Studies and Modern Analogs, AAPG memoir 50.*

MITCHELL, W. H., WHITTAKER, A. C., MAYALL, M. & LONERGAN, L. 2021a. New models for submarine channel deposits on structurally complex slopes: Examples from the Niger delta system. *Marine and Petroleum Geology,* 129**,** 105040.

MITCHELL, W. H., WHITTAKER, A. C., MAYALL, M., LONERGAN, L. & PIZZI, M. 2021b. Quantifying the relationship between structural deformation and the morphology of submarine channels on the Niger Delta continental slope. *Basin Research,* 33**,** 186-209.

MOODY, J. D. & HILL, M. J. 1956. Wrench-fault tectonics. *Geological Society of America Bulletin,* 67**,** 1207-1246.

MORLEY, C. & GUERIN, G. 1996. Comparison of gravity-driven deformation styles and behavior associated with mobile shales and salt. *Tectonics,* 15**,** 1154-1170.

MORLEY, C., KING, R., HILLIS, R., TINGAY, M. & BACKE, G. 2011. Deepwater fold and thrust belt classification, tectonics, structure and hydrocarbon prospectivity: A review. *Earth-Science Reviews,* 104**,** 41-91.

MORLEY, C., VON HAGKE, C., HANSBERRY, R., COLLINS, A., KANITPANYACHAROEN, W. & KING, R. 2017. Review of major shale-dominated detachment and thrust characteristics in the diagenetic zone: Part I, meso-and macro-scopic scale. *Earth-Science Reviews,* 173**,** 168-228.

MORLEY, C., VON HAGKE, C., HANSBERRY, R., COLLINS, A., KANITPANYACHAROEN, W. & KING, R. 2018. Review of major shale-dominated detachment and thrust characteristics in the diagenetic zone: Part II, rock mechanics and microscopic scale. *Earth-Science Reviews,* 176**,** 19-50.

MORLEY, C. K. 2009. Growth of folds in a deep-water setting. *Geosphere,* 5**,** 59-89.

MORTON, A., ALLEN, M., SIMMONS, M., SPATHOPOULOS, F., STILL, J., HINDS, D., ISMAIL-ZADEH, A. & KROONENBERG, S. 2003. Provenance patterns in a neotectonic basin: Pliocene and Quaternary sediment supply to the South Caspian. *Basin research,* 15**,** 321-337.

MULDER, T. & SYVITSKI, J. P. M. 1995. Turbidity currents generated at river mouths during exceptional discharges to the world oceans. *The Journal of Geology,* 103**,** 285-299.

MULDER, T., SYVITSKI, J. P. M., MIGEON, S., FAUGÈRES, J.-C. & SAVOYE, B. 2003. Marine hyperpycnal flows: initiation, behavior and related deposits. A review. *Marine and Petroleum Geology,* 20**,** 861-882.

MUÑOZ, J. A. 1992. Evolution of a continental collision belt: ECORS-Pyrenees crustal balanced cross-section. *Thrust tectonics.* Springer.

MUTTI, E., TINTERRI, R., BENEVELLI, G., DI BIASE, D. & CAVANNA, G. 2003. Deltaic, mixed and turbidite sedimentation of ancient foreland basins. *Marine Petroleum Geology,* 20**,** 733-755.

NADIROV, R., BAGIROV, E., TAGIYEV, M. & LERCHE, I. 1997. Flexural plate subsidence, sedimentation rates, and structural development of the super-deep South Caspian Basin. *Marine and Petroleum Geology,* 14**,** 383-400.

NARIMANOV, A. 1993. The petroleum systems of the South Caspian Basin. *Basin Modeling Advances and Applications. Norwegian Petroleum Society, Special Publications,* 3**,** 599-608.

NARIMANOV, N., BABAYEV, N., GAHRAMANOV, G. & JAVAD-ZADEH, Z. 2019. Cenozoic stage of development of local structures of the Lower Kura Depression and Baku Archipelago related to their oil and gas prospectivity. *Geological Journal,* 54**,** 2419-2430.

NUMMEDAL, D., CLIFTON, H. E. & WILLIAMS, E. 2012. Late Miocene and Early Pliocene High-Frequency Lake Level Cycles in Lacustrine Hydrocarbon Reservoir Strata, South Caspian Basin: Insights for Subseismic-scale Lithofacies Variations. *Lacustrine Sandstone Reservoirs and Hydrocarbon Systems.* AAPG Memoir.

OBRADORS-PRATS, J., ROUAINIA, M., APLIN, A. C. & CROOK, A. J. L. 2017. Assessing the implications of tectonic compaction on pore pressure using a coupled geomechanical approach. *Marine and Petroleum Geology,* 79**,** 31-43.

OSBORNE, M. J. & SWARBRICK, R. E. 1997. Mechanisms for generating overpressure in sedimentary basins: A reevaluation. *AAPG bulletin,* 81**,** 1023-1041.

PAN, S., LIU, H., XU, D., WEI, P., QU, Y., GUAN, X., LIU, C. & ZHANG, S. 2020. Sublacustrine gravity-induced deposits: The diversity of external geometries and origins. *Sedimentary Geology,* 407**,** 105738.

PAUGET, F., LACAZE, S. & VALDING, T. 2009. A global approach in seismic interpretation based on cost function minimization. *SEG Technical Program Expanded Abstracts 2009.* Society of Exploration Geophysicists.

PEIZHEN, Z., MOLNAR, P. & DOWNS, W. R. 2001. Increased sedimentation rates and grain sizes 2–4 Myr ago due to the influence of climate change on erosion rates. *Nature,* 410**,** 891-897.

PÉREZ-BELZUZ, F., ALONSO, B. & ERCILLA, G. 1997. History of mud diapirism and trigger mechanisms in the Western Alboran Sea. *Tectonophysics,* 282**,** 399-422.

PIZZI, M. 2019. *Quantification of tectonic controls on the distribution and architecture of deep-water facies during the growth of the toe-thrusts region of the Niger Delta.* Imperial College London.

PIZZI, M., LONERGAN, L., WHITTAKER, A. C. & MAYALL, M. 2020. Growth of a thrust fault array in space and time: An example from the deep-water Niger delta. *Journal of Structural Geology,* 137**,** 104088.

PIZZI, M., WHITTAKER, A. C., LONERGAN, L., MAYALL, M. & MITCHELL, W. H. 2021. New statistical quantification of the impact of active deformation on the distribution of submarine channels. *Geology,* 49**,** 926-930.

PLANKE, S., SVENSEN, H., HOVLAND, M., BANKS, D. & JAMTVEIT, B. 2003. Mud and fluid migration in active mud volcanoes in Azerbaijan. *Geo-Marine Letters,* 23**,** 258-268.

PLINK-BJÖRKLUND, P. & STEEL, R. J. 2004. Initiation of turbidity currents: outcrop evidence for Eocene hyperpycnal flow turbidites. *Sedimentary Geology,* 165**,** 29-52.

POBLET, J. & MCCLAY, K. 1996. Geometry and kinematics of single-layer detachment folds. *AAPG bulletin,* 80**,** 1085-1109.

POBLET, J., MCCLAY, K., STORTI, F. & MUÑOZ, J. A. 1997. Geometries of syntectonic sediments associated with single-layer detachment folds. *Journal of Structural Geology,* 19**,** 369-381.

POLLARD, D. D. & SEGALL, P. Theoretical displacements and stresses near fractures in rock: with applications to faults, joints, veins, dikes, and solution surfaces. Fracture mechanics of rock, 1987. 277-347.

POPOV, S. V., SHCHERBA, I. G., ILYINA, L. B., NEVESSKAYA, L. A., PARAMONOVA, N. P., KHONDKARIAN, S. O. & MAGYAR, I. 2006. Late Miocene to Pliocene palaeogeography of the Paratethys and its relation to the Mediterranean. *Palaeogeography, Palaeoclimatology, Palaeoecology,* 238**,** 91-106.

PORTER, M., SPRAGUE, A., SULLIVAN, M., JENNETTE, D., BEAUBOUEF, R., GARFIELD, T., ROSSEN, C., SICKAFOOSE, D., JENSEN, G. & FRIEDMANN, S. 2006. Stratigraphic organization and predictability of mixed coarse-and fine-grained lithofacies successions in a lower Miocene deep-water slope-channel system, Angola Block 15. *In:* P, H. & L, W. (eds.) *Giant hydrocarbon reservoirs of the world: From Rocks to reservoir characterization and modeling: AAPG Memoir 88/SEPM Special Publication.*

POSAMENTIER, H. W. & KOLLA, V. 2003. Seismic geomorphology and stratigraphy of depositional elements in deep-water settings. *Journal of sedimentary research,* 73**,** 367-388.

PRIESTLEY, K., BAKER, C. & JACKSON, J. 1994. Implications of earthquake focal mechanism data for the active tectonics of the South Caspian Basin and surrounding regions. *Geophysical Journal International,* 118**,** 111-141.

RANCE, J., PROFIT, M., DEE, S. & ROBERTS, D. Predicting the paleo evolution of overpressured geological structures. 47th US Rock Mechanics/Geomechanics Symposium, 2013. OnePetro.

RANDEN, T., MONSEN, E., SIGNER, C., ABRAHAMSEN, A., HANSEN, J. O., SÆTER, T. & SCHLAF, J. 2000. Three-dimensional texture attributes for seismic data analysis. *SEG Technical Program Expanded Abstracts 2000.* Society of Exploration Geophysicists.

REILINGER, R., MCCLUSKY, S., VERNANT, P., LAWRENCE, S., ERGINTAV, S., CAKMAK, R., OZENER, H., KADIROV, F., GULIEV, I. & STEPANYAN, R. 2006. GPS constraints on continental deformation in the Africa-Arabia-Eurasia continental collision zone and implications for the dynamics of plate interactions. *Journal of Geophysical Research: Solid Earth,* 111.

RENAUT, R. W. & LAST, W. M. 1994. *Salt lake sedimentology and geochemistry: introduction and historical perspective*.

REYNOLDS, A. D., SIMMONS, M. D., BOWMAN, M. B., HENTON, J., BRAYSHAW, A. C., ALI-ZADE, A. A., GULIYEV, I. S., SULEYMANOVA, S. F., ATEAVA, E. Z. & MAMEDOVA, D. N. 1998. Implications of outcrop geology for reservoirs in the Neogene Productive Series: Apsheron Peninsula, Azerbaijan. *AAPG bulletin,* 82**,** 25-49.

REZANOV, I. & CHAMO, S. 1969. Reasons for absence of a'granitic'layer in basins of the South Caspian and Black Sea type. *Canadian Journal of Earth Sciences,* 6**,** 671-678.

RICHARDSON, S. E., DAVIES, R. J., ALLEN, M. B. & GRANT, S. F. 2011. Structure and evolution of mass transport deposits in the South Caspian Basin, Azerbaijan. *Basin Research,* 23**,** 702-719.

RITZ, J.-F. 2009. Extrusion tectonics and subduction in the eastern South Caspian region since 10 Ma: COMMENT. *Geology,* 37**,** e191-e191.

RITZ, J.-F., NAZARI, H., GHASSEMI, A., SALAMATI, R., SHAFEI, A., SOLAYMANI, S. & VERNANT, P. 2006. Active transtension inside central Alborz: A new insight into northern Iran–southern Caspian geodynamics. *Geology,* 34**,** 477-480.

ROBERT, A. M., LETOUZEY, J., KAVOOSI, M. A., SHERKATI, S., MÜLLER, C., VERGÉS, J. & AGHABABAEI, A. 2014. Structural evolution of the Kopeh Dagh fold-and-thrust belt (NE Iran) and interactions with the South Caspian Sea Basin and Amu Darya Basin. *Marine and Petroleum Geology,* 57**,** 68-87.

ROBINSON, N., FORD, A., HOWIE, J., MANLEY, D., RIVIERE, M., STEWART, S. & THOMAS, R. 2005. 4D time-lapse monitoring of Chirag Field. *The Leading Edge,* 24**,** 928-932.

ROCKFIELD 2010. ELFEN forward modeling user manual. Rockfield Software Ltd Swansea, UK.

ROWAN, M. G., PEEL, F. J. & VENDEVILLE, B. C. 2004. Gravity-driven fold belts on passive margins. *AAPG Memoir,* 82.

SALVINI, F. & STORTI, F. 2002. Three-dimensional architecture of growth strata associated to fault-bend, fault-propagation, and décollement anticlines in non-erosional environments. *Sedimentary Geology,* 146**,** 57-73.

SÁNCHEZ-BORREGO, I., SOTO, J. I., RUEDA, M. & BETANCOR, I. S. 2016. Nonparametric estimation to reconstruct the deformation history of an active fold in the Caspian Basin. *Mathematical Geosciences,* 48**,** 985-1011.

SANDERSON, D. J. & MARCHINI, W. 1984. Transpression. *Journal of Structural Geology,* 6**,** 449-458.

SANTOS-BETANCOR, I. & SOTO, J. 2015. 3D geometry of a shale-cored anticline in the western South Caspian Basin (offshore Azerbaijan). *Marine and Petroleum Geology,* 67**,** 829-851.

SANTOS-BETANCOR, I., SOTO, J. I., LONERGAN, L. & MACELLARI, C. 2014. Gravity-Instabilities Processes and Mass-Transport Complexes During Folding: The Case of a Shale-Cored Anticline in the Western South Caspian Basin. *Mathematics of Planet Earth.* Springer.

SCHOLZ, C. A. 1995. Deltas of the Lake Malawi Rift, East Africa: Seismic Expression and Exploration Implications 1. *AAPG Bulletin,* 79**,** 1679-1697.

SCLATER, J. G. & CHRISTIE, P. A. F. 1980. Continental stretching: An explanation of the post-mid-Cretaceous subsidence of the central North Sea basin. *Journal of Geophysical Research: Solid Earth,* 85**,** 3711-3739.

ŞENGÖR, A. 1990. A new model for the late Palaeozoic—Mesozoic tectonic evolution of Iran and implications for Oman. *Geological Society, London, Special Publications,* 49**,** 797-831.

SHABANIAN, E., BELLIER, O., SIAME, L., ARNAUD, N., ABBASSI, M. R. & COCHEMÉ, J.-J. 2009. New tectonic configuration in NE Iran: Active strike-slip faulting between the Kopeh Dagh and Binalud mountains. *Tectonics,* 28.

SHACKLETON, N. J. & OPDYKE, N. D. 1977. Oxygen isotope and palaeomagnetic evidence for early Northern Hemisphere glaciation. *Nature,* 270**,** 216-219.

SHIKALIBEILY, E. S. & GRIGORIANTS, B. 1980. Principal features of the crustal structure of the South-Caspian Basin and the conditions of its formation. *Tectonophysics,* 69**,** 113-121.

SKEMPTON, A. 1948. Vane tests in the alluvial plain of the River Forth near Grangemouth. *Geotechnique,* 1**,** 111-124.

SMITH-ROUCH, L. S. 2006. Oligocene–Miocene Maykop/diatom total petroleum system of the South Caspian Basin Province, Azerbaijan, Iran, and Turkmenistan. *US Geological Survey Bulletin,* 2201**,** 1-27.

SOTO, J., HEIDARI, M. & HUDEC, M. 2021a. Proposal for a Mechanical Model of Mobile Shales. *Scientific Reports,* 11**,** 1-11.

SOTO, J., HUDEC, M., MONDOL, N. & HEIDARI, M. 2021b. Shale transformations and physical properties—Implications for seismic expression of mobile shales. *Earth-Science Reviews,* 220**,** 103746.

SPRAGUE, A., GARFIELD, T., GOULDING, F., BEAUBOUEF, R., SULLIVAN, M., ROSSEN, C., CAMPION, K., SICKAFOOSE, D., ABREU, V. & SCHELLPEPER, M. 2005. Integrated slope channel depositional models: the key to successful prediction of reservoir presence and quality in offshore West Africa. *Veracruz, Mexico, Colegio de Ingenenieros Petroleros de México***,** 1-13.

STEININGER, F. F. & RÖGL, F. 1984. Paleogeography and palinspastic reconstruction of the Neogene of the Mediterranean and Paratethys. *Geological Society, London, Special Publications,* 17**,** 659-668.

STEWART, S. A. & DAVIES, R. J. 2006. Structure and emplacement of mud volcano systems in the South Caspian Basin. *AAPG bulletin,* 90**,** 771-786.

SUPPE, J., CHOU, G. T. & HOOK, S. C. 1992. Rates of folding and faulting determined from growth strata. *In:* K, M. (ed.) *Thrust tectonics.* Springer.

SUPPE, J., SÀBAT, F., MUNOZ, J. A., POBLET, J., ROCA, E. & VERGÉS, J. 1997. Bed-by-bed fold growth by kink-band migration: Sant Llorenç de Morunys, eastern Pyrenees. *Journal of Structural Geology,* 19**,** 443-461.

SYLVESTER, K., WALDREN, D., BAGIROV, B. & ALASKAROV, E. 2012. Balakhany IX and X integrated studies shallow-water Gunashli Field, Caspian Sea. *In:* BAGANZ, O. W., BARTOV, Y., BOHACS, K. & NUMMEDAL, D. (eds.) *Lacustrine sandstone reservoirs and hydrocarbon systems: AAPG Memoir 95.*

THIGPEN, J. R., ROBERTS, D., SNOW, J. K., WALKER, C. D. & BERE, A. 2019. Integrating kinematic restoration and forward finite element simulations to constrain the evolution of salt diapirism and overburden deformation in evaporite basins. *Journal of Structural Geology,* 118**,** 68-86.

THORNTON, D., CROOK, A. & ENGINEERING, R. 2014. Predictive modeling of the evolution of fault structure: 3-D modeling and coupled geomechanical/flow simulation. *Rock Mechanics,* 47**,** 1533-1549.

THORSEN, C. E. 1963. Age of growth faulting in southeast Louisiana. *Gulf Coast Association of Geological Societies Transactions,* 13**,** 103 - 110.

TRUSHEIM, F. 1960. Mechanism of salt migration in northern Germany. *AAPG Bulletin,* 44**,** 1519-1540.

UNECE 2011. Drainage basin of the Aral Sea and other transboundary waters in Central Asia. . *Second assessment of transboundary rivers, lakes and groundwaters.* New York and Geneva: United Nations Economic Comission for Europe (UNECE).

VAN BAAK, C. G. C., GROTHE, A., RICHARDS, K., STOICA, M., ALIYEVA, E., DAVIES, G. R., KUIPER, K. F. & KRIJGSMAN, W. 2019. Flooding of the Caspian Sea at the intensification of Northern Hemisphere Glaciations. *Global and Planetary Change,* 174**,** 153-163.

VAN KEKEN, P., SPIERS, C., VAN DEN BERG, A. & MUYZERT, E. 1993. The effective viscosity of rocksalt: implementation of steady-state creep laws in numerical models of salt diapirism. *Tectonophysics,* 225**,** 457-476.

VAN RENSBERGEN, P., MORLEY, C., ANG, D., HOAN, T. & LAM, N. 1999. Structural evolution of shale diapirs from reactive rise to mud volcanism: 3D seismic data from the Baram delta, offshore Brunei Darussalam. *Journal of the Geological Society,* 156**,** 633-650.

VASILIEV, I., VAN DER MEER, M. T. J., STOICA, M., KRIJGSMAN, W., REICHART, G.-J., LAZAREV, S., BUTISEACĂ, G. A., NIEDERMEYER, E. M., ALIYEVA, E., VAN BAAK, C. G. C. & MULCH, A. 2022. Biomarkers reveal two paramount Pliocene-Pleistocene connectivity events in the Caspian Sea Basin. *Palaeogeography, Palaeoclimatology, Palaeoecology,* 587**,** 110802.

VERNANT, P., NILFOROUSHAN, F., HATZFELD, D., ABBASSI, M., VIGNY, C., MASSON, F., NANKALI, H., MARTINOD, J., ASHTIANI, A. & BAYER, R. 2004. Present-day crustal deformation and plate kinematics in the Middle East constrained by GPS measurements in Iran and northern Oman. *Geophysical Journal International,* 157**,** 381-398.

VIDAL-ROYO, O., CARDOZO, N., MUÑOZ, J. A., HARDY, S. & MAERTEN, L. 2012. Multiple mechanisms driving detachment folding as deduced from 3D reconstruction and geomechanical restoration: The Pico del Aguila anticline (External Sierras, Southern Pyrenees). *Basin Research,* 24**,** 295-313.

WALKER, R. T., BEZMENOV, Y., BEGENJEV, G., CAROLIN, S., DODDS, N., GRUETZNER, C., JACKSON, J., MIRZIN, R., MOUSAVI, Z. & RHODES, E. 2021. Slip-Rate on the Main Köpetdag (Kopeh Dagh) Strike-Slip Fault, Turkmenistan, and the Active Tectonics of the South Caspian. *Tectonics,* 40**,** e2021TC006846.

WALTHAM, D. 1997. Why does salt start to move? *Tectonophysics,* 282**,** 117-128.

WARSITZKA, M., KLEY, J. & KUKOWSKI, N. 2013. Salt diapirism driven by differential loading—Some insights from analogue modelling. *Tectonophysics,* 591**,** 83-97.

WILCOX, R. E., HARDING, T. T. & SEELY, D. 1981. Basic wrench tectonics. *AAPG Bulletin,* 57**,** 74-96.

WOOD, L. J. 2011. *Shale Tectonics: AAPG Memoir 93*, AAPG.

WU, S., BALLY, A. W., MOHRIAK, W. & TALWANI, M. 2000. Slope tectonics-comparisons and contrasts of structural styles of salt and shale tectonics of the northern Gulf of Mexico with shale tectonics of offshore Nigeria in Gulf of Guinea. *Geophysical Monograph-American Geophysical Union,* 115**,** 151-172.

XIAN, B. Z., WANG, J. H., LIU, J. P., DONG, Y. L., GONG, C. L. & LU, Z. Y. 2018. Delta-fed turbidites in a lacustrine rift basin: the Eocene Dongying depression, Bohai Bay Basin, East China. *Australian Journal of Earth Sciences,* 65**,** 135-151.

YANG, R., JIN, Z., VAN LOON, A. J., HAN, Z. & FAN, A. 2017. Climatic and tectonic controls of lacustrine hyperpycnite origination in the Late Triassic Ordos Basin, central China: Implications for unconventional petroleum development. *Aapg Bulletin,* 101**,** 95-117.

YANG, Y., LI, W. & MA, L. 2005. Tectonic and stratigraphic controls of hydrocarbon systems in the Ordos basin: A multicycle cratonic basin in central China. *AAPG bulletin,* 89**,** 255-269.

YARBUH, I. & CONTRERAS, J. 2017. The interplay between deformation, erosion and sedimentation in the deep-water Mexican Ridges foldbelt, western Gulf of Mexico basin. *Basin Research,* 29**,** 446-464.

YUNOV, A. Y. & MARTIROSYAN, B. N. 1996. Structure of the Outer Zone of the Turkmenistan Shelf of the South Caspian Based on Common Depth Point Seismic Data. *Petroleum Geology: A digest of Russian literature on Petroleum Geology.*

YUSIFOV, M. & RABINOWITZ, P. D. 2004. Classification of mud volcanoes in the South Caspian Basin, offshore Azerbaijan. *Marine and Petroleum Geology,* 21**,** 965-975.

ZAVALA, C., LIU, H., LI, X., ARCURI, M., DI MEGLIO, M., ZORZANO, A., OTHARÁN, G., HAO, B. & WANG, Y. 2022. Lacustrine sequence stratigraphy: New insights from the study of the Yanchang Formation (Middle-Late Triassic), Ordos Basin, China. *The Ordos Basin.* Elsevier.

ZAVALA, C., PONCE, J. J., ARCURI, M., DRITTANTI, D., FREIJE, H. & ASENSIO, M. 2006. Ancient lacustrine hyperpycnites: a depositional model from a case study in the Rayoso Formation (Cretaceous) of west-central Argentina. *Journal of Sedimentary Research,* 76**,** 41-59.

ZHANG, X. & SCHOLZ, C. A. 2015. Turbidite systems of lacustrine rift basins: Examples from the Lake Kivu and Lake Albert rifts, East Africa. *Sedimentary Geology,* 325**,** 177-191.

ZHAO, J., MOUNTNEY, N. P., LIU, C., QU, H. & LIN, J. 2015. Outcrop architecture of a fluvio-lacustrine succession: upper Triassic Yanchang Formation, Ordos Basin, China. *Marine and Petroleum Geology,* 68**,** 394-413.

ZHI-QIANG, F., CHENG-ZAO, J., XI-NONG, X., SHUN, Z., ZI-HUI, F. & CROSS, T. A. 2010. Tectonostratigraphic units and stratigraphic sequences of the nonmarine Songliao basin, northeast China. *Basin Research,* 22**,** 79-95.

ZONENSHAIN, L. P. & PICHON, X. 1986. Deep basins of the Black Sea and Caspian Sea as remnants of Mesozoic back-arc basins. *Tectonophysics,* 123**,** 181-211.

Appendix

Appendix A

The elasto-plastic overburden is modelled with non-linear Young's modulus and Poissons Ratio, which are defined as:

$$E_o = E_{ref}\left[\frac{p'+A}{B}\right]^n \phi^c \qquad \nu = \nu_{min} + (\nu_{max} - \nu_{min}) * \left(1 - e^{-mp'}\right)$$

where p' is effective mean stress.

Parameter	**value**
Youngs modulus (E)	0.25
Poissons ratio (ν_{min})	0.25
Poissons ratio (ν_{max})	0.40
A	-275862
B	-275862
C	-1.8
n	0
m	1e-8
Initial porosity (ϕ)	0.4
Ave. bulk density (kg/m^3)	2391

The visco-plastic shale is modelled under Hershell- Bulkley law, where shear stress (τ) is defined as:

$$\tau = \tau_0 + k(\gamma)^n$$

Parameter	**Value**
Yield Stress (τ_0)	500
Consistency factor (k)	Viscosity values as in Table 1.
Flow index (*n*)	1

By setting $T_0 = 0$ and n = 1 we recover a Newtonian model with *k* becoming viscosity. However, we set the yield stress to a low value to help stabilise at low equivalent viscosities.